PETROGENESIS OF LAVAS

FROM THE AXIS OF THE NORTHERN CHILE RIDGE

A THESIS SUBMITTED TO THE GRADUATE DIVISION OF THE
UNIVERSITY OF HAWAI‘I IN PARTIAL FULFILLMENT
OF THE REQUIREMENTS FOR THE DEGREE OF

MASTER OF SCIENCE

IN

GEOLOGY AND GEOPHYSICS

MAY 2002

By
Margaret S. Milman

Thesis Committee:

Jill L. Karsten, Chairperson
Margo Edwards
Michael O. Garcia

We certify that we have read this thesis and that, in our opinion, it is satisfactory in scope and quality as a thesis for the degree of Master of Science in Geology and Geophysics.

THESIS COMMITTEE

_____
Chairperson

_____

_____

To Wendy Calvin, Suzanne Mahlburg-Kay, Dennis Bernstein, my grandmother Charlotte Milman, and most especially Elizabeth Moore.

Also to my family, my friends, and to Brian who is in both categories.

ACKNOWLEDGMENTS

I owe a great debt to Vincent Beltran for operating the ICP-MS during the trace element analyses, and especially to Eric de Carlo for endless guidance in designing the ICP-MS analytical runs. I also owe more than the cookies I paid him with to Nathan Becker, for cheerful computer-related assistance at what were surely often inconvenient times.

Figure 30 includes previously existing samples from throughout the southeast Pacific, as reported in the PetDB online database maintained by Lamont-Doherty Earth Observatory (http://www.ldeo.columbia.edu/datarep/index.html). References are *Bach et al.* (1994), *Cohen and O'Nions* (1982), *Ferguson and Klein* (1993), *Hall and Sinton* (1996), *Hébert et al.* (1983), *Hékinian et al.* (1992, 1995, 1997, 1999), *Jambon et al.* (1995), *Melson* (Smithsonian Database), *Michael and Chase* (1987), *Michael* (1988, 1995), *Perfit et al.* (1994), *Puchelt and Emmermann* (1983), *Schiano et al.* (1997), *Sherman et al.* (1997), *Sinton et al.* (1991), and *Vlastélic et al.* (2000).

Figures 1, 2, 3a, 3b, 4, and 30 were generated in part using the Generic Mapping Tools (GMT) software (*Wessel and Smith*, 1998).

This study was funded by National Science Foundation grant OCE96-18401.

ABSTRACT

New major and trace element analyses are presented for axial lava samples recovered during the 1998 PANORAMA Expedition to the Northern Chile Ridge. These samples are MORBs that range from ultra-depleted N-MORBs to T-MORBs, as well as a few alkalic basalts that are among the few on-axis alkalic basalts in the Pacific not associated with a known hotspot.

Quantitative incompatible trace element models, as well as the presence of correlations between radiogenic isotope ratios and incompatible trace element ratios and the lack of correlations between incompatible trace element ratios and Na_8, suggest that the best explanation for the petrogenesis of pre-fractionation parent magmas for this suite of samples is mixing of < 5% of a primitive alkalic magma with primitive tholeiitic magmas that were formed by variable extents of melting (14-20%) of a depleted source. This mixing controls the radiogenic isotope and incompatible trace element content of the lavas, while the major element compositions of parental magmas probably reflect the extent of melting of the depleted mantle matrix. A likely situation for this petrogenetic scenario is melting of an upper mantle that contains ubiquitous heterogeneities of Pacific hotspot-type fertile mantle embedded in a depleted mantle matrix, similar to the "plum-pudding" mantle idea.

The Northern Chile Ridge lava population is more uniform and more depleted in incompatible trace elements (using K/Ti as a proxy) than lava populations at other southeast Pacific mid-ocean ridges. This may be due to a sparser distribution of fertile mantle heterogeneities in the Northern Chile Ridge mantle than in the rest of the

southeast Pacific mantle. A previous episode of melt extraction, which had been suggested by *Bach et al.* (1996), is not required.

No arc-like trace element signature is found in any of the Northern Chile Ridge samples, suggesting that the chemical heterogeneities introduced by recent subduction at the Chile Margin Triple Junction are small in geographic scale and are subordinate to larger regional patterns of mantle heterogeneity.

Northern Chile Ridge lavas are more primitive (higher Mg #) than lavas from intermediate spreading rate ridges near hotspots, suggesting that at intermediate spreading rates hotspots exert an important influence on the thermal budget controlling shallow crystallization and mechanisms of crustal accretion.

There are no obvious systematic effects of segmentation and transform offsets on the petrogenesis of the Northern Chile Ridge lavas. The presence of long-offset transforms does not affect the regional extent of melting at this site, except near the Valdivia Fracture Zone, where the segment-transform geometry approaches the extreme case of a fracture zone containing intra-transform spreading centers (ITSCs).

TABLE OF CONTENTS

LIST OF TABLES

LIST OF FIGURES

Figure Page

Figure Page

INTRODUCTION

Motivation

Mid-ocean ridges are divergent plate boundaries where new oceanic crust is created. As the rigid plates spread, the upper mantle upwells adiabatically to fill the void, and in doing so melts by decompression. The melts percolate upwards through the ascending mantle, coalesce, and migrate towards the oceanic crust. Some crystallize and freeze within the crust and others erupt at the ocean floor, to build a long, globe-encircling chain of underwater volcanoes.

This is arguably the simplest among all igneous petrologic systems. Scientific study of the petrogenesis of basalts found at mid-ocean ridges is entering its fifth decade, but there is still no consensus on many fundamental geologic issues.

Continuing issues include, firstly, questions about the fate of chemical heterogeneities introduced into the mantle by recycled oceanic crust. It has long been recognized that recycled subducted altered oceanic crust is one of the main sources of heterogeneities in the upper mantle, along with primitive mantle material (*e.g.*, *Sleep*, 1984). Previous studies of lavas erupted at the Southern Chile Ridge, near the site of present-day subduction of the active ridge, found contamination of the ridge-source mantle by subduction-related material (*Klein and Karsten*, 1995; Sherman, 1998; Sturm *et al.*, 1999). This suggested that in this tectonic setting, recently-subducted oceanic crust might get recycled into the uppermost mantle and asthenosphere, where spreading center

upwelling is occurring. However, it was unclear how far along the Chile Ridge axis such contamination from subduction might extend. It was furthermore unclear how the contribution of recently-subducted material fit in with other regional mantle heterogeneity in the southeast Pacific. Even at the Southern Chile Ridge, the geographic distribution of contaminated lavas is discontinuous (*Klein and Karsten*, 1995).

Secondly, morphological and geochemical features at mid-ocean ridges are observed to vary at different spreading rates. The classic example is a transition from an axial valley morphology at slow spreading rates to an axial ridge morphology at fast spreading rates (*e.g.*, *Macdonald*, 1986; *Small*, 1998), but spreading-rate dependent variations have also been observed in many other features such as flank roughness (*Small*, 1998) and geochemistry of erupted lavas (*Sinton and Detrick*, 1992; *Niu and Hékinian*, 1997; *Parmentier and Sinton*, 1998). Conceptual models exist to explain some of the variations (*e.g.*, *Chen and Morgan*, 1990), but no real consensus and no tests or evidence have emerged. It has been observed that the nature of the spreading-rate dependence of several different morphological features changes quickly and profoundly at intermediate rates of 50-80 km/My (full rate), so it is presumed that the mechanisms responsible for these changes must undergo a transition or encounter some sort of critical threshold at these intermediate spreading rates (*Small*, 1998). In this regard, the behavior of intermediate spreading rate ridges is particularly important in understanding the mechanisms for spreading rate dependence.

The only intermediate rate ridges that have been studied in detail previously, the Juan de Fuca Ridge (*e.g.*, *Delaney et al.*, 1981) and the Galapagos Spreading Center (*e.g.*,

Byerly, 1980; *Christie and Sinton*, 1986; *Clague et al.*, 1981; *Fornari et al.*, 1983; *Perfit et al.*, 1983), are proximal to mantle hotspots which are thought to cause excess magma supply (*e.g.*, *Sinton and Detrick*, 1992). It is considered likely that intermediate rate ridges away from hotspots behave quite differently, because most spreading rate-dependent features are closely linked with magma supply. There have been surveys of non-hotspot intermediate rate spreading centers at the northern Gorda Ridge (*e.g.*, *Davis and Clague*, 1987, 1990), the Southeast Indian Ridge 110-116º E (*Shah and Sempére*, 1998), and at the Pacific-Antarctic Ridge 56-66º S (*Vlastélic et al.*, 2000). However, there has been no synthesis of morphological or geochemical features at these ridges, or, until the present study, discussion of them in the context of their intermediate spreading rate.

Finally, it has been postulated that segmentation structure can affect the thermal structure and melt distribution patterns at spreading ridges, especially when segmentation is defined by long-offset transform boundaries. Previous studies of this effect have been either theoretical in nature (*e.g.*, *Phipps Morgan and Forsyth*, 1988; *Phipps Morgan and Chen*, 1993), or have depended heavily on geochemistry-based interpretations of extent and depth of melting (*e.g.*, *Langmuir and Bender*, 1984; *Lawson et al.*, 1996). The geochemistry-based studies have generally neglected to establish the fundamental systematics of petrogenesis that are in operation at their particular site, which must be done in order to make such interpretations with confidence. Taken as a whole, these studies have yielded ambiguous results.

The Northern Chile Ridge is a site where all the issues described above can be investigated: the geographic extent of chemical heterogeneities introduced into the mantle by subducted oceanic crust, the behavior of an intermediate spreading rate ridge with no hotspot nearby, and the control that segmentation exerts on thermal structure and melt distribution.

Chile Ridge Site Background

The Chile Ridge is the spreading center between the Nazca and Antarctic plates in the southeast Pacific ocean basin (*Ewing and Heezen*, 1956; *Menard et al.*, 1964) (Figure 1). It extends for more than 1000 km from the Juan Fernandez microplate and Chile Fracture Zone in the north, across the Valdivia Fracture Zone, to the Chile Margin Triple Junction in the south. At the Chile Margin Triple Junction, the active spreading center is being subducted into the Chile Trench at the edge of the South American continent (*e.g.*, *Herron et al.*, 1981; *Cande et al.*, 1987).

Tectonic History

The tectonic history of the southeast Pacific region including the Chile Ridge has been reconstructed based on shipboard magnetics data (*Herron et al.*, 1981; *Cande et al.*, 1982; *Pilger*, 1983) and aeromagnetics data (*Tebbens et al.*, 1997; *Tebbens and Cande*,

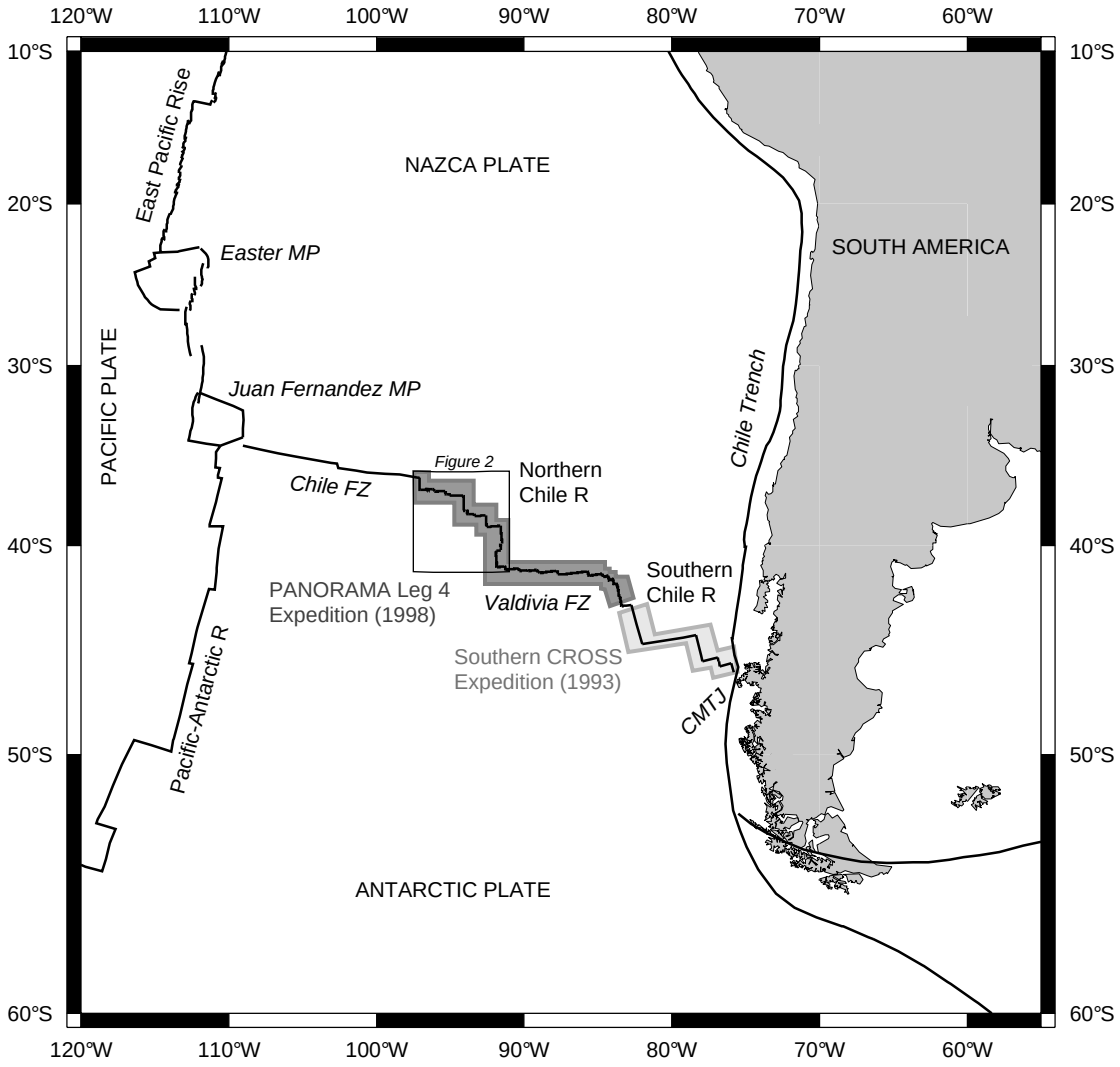

Figure 1: Locator map for the Northern Chile Ridge in the southeast Pacific. The study regions for the PANORAMA Leg 4 Expedition in 1998 and the Southern CROSS Expedition in 1993 are shown (shaded boxes). Abbreviations used are R, Ridge; MP, Microplate; FZ, Fracture Zone; CMTJ, Chile Margin Triple Junction.

1997). The following details were presented by *Tebbens et al.* (1997) and *Tebbens and Cande* (1997).

Prior to 12 Ma, the Chile Ridge extended only as far north as the Valdivia Fracture Zone. From approximately 12 to 9 Ma, the Chile Ridge propagated rapidly northward from the Valdivia Fracture Zone into the Nazca Plate, through crust formed 5 My earlier at the Pacific-Nazca Ridge. This event formed a Northern Chile Ridge province distinct from the Southern Chile Ridge. The present-day province of oceanic crust produced by spreading on the Northern Chile Ridge is bounded at magnetic chron 5A by the Friday Trough on the west and by the Crusoe Trough on the east. Outside of this region, the oceanic crust was produced by spreading at the Pacific-Nazca Ridge.

Since the cessation of ridge propagation at 9 Ma, the segment-transform geometry has been stable (*Tebbens et al.*, 1997; *Tebbens and Cande*, 1997). The only present-day tectonic instabilities that have been identified are two southward-propagating rifts (*e.g.*, *Hey*, 1978; *Hey et al.*, 1980), one on the Northern Chile Ridge at approximately 38º S (*e.g.*, *Phipps Morgan and Sandwell*, 1994; *Tebbens et al.*, 1997), and the other on the Southern Chile Ridge at approximately 43º 55' S (*Sherman et al.*, 1997).

Today the Northern Chile Ridge has a full spreading rate of 53 mm/yr, constant along the entire length of the ridge and symmetric on either side of the ridge. The spreading rate was higher in the past, and reached a maximum of 123 mm/yr at 23 Ma (*Tebbens et al.*, 1997).

Segmentation and Morphology

Early interpretations of axial morphology and segmentation geometry at the Chile Ridge were based on shipboard magnetic and aeromagnetic profiles, limited bathymetry, and satellite altimetry data (*e.g.*, *Herron*, 1972; *Klitgord et al.*, 1973; *Handschumacher*, 1976; *Herron et al.*, 1981; *Tebbens et al.*, 1997). The Chile Ridge was seen in bathymetry to have an axial valley morphology, with the ridge segments cut by numerous long-offset transforms (*e.g.*, *Herron and Hayes*, 1969; *Herron*, 1972; *Klitgord et al.*, 1973; *Herron et al.*, 1981).

In 1998, Leg 4 of the PANORAMA Expedition aboard the R/V *Melville* (*J. Karsten*, *E. Klein*, *F. Martinez*, Principal Investigators) collected samples and geophysical data along the axes of the Northern Chile Ridge (36.38-41.05º S, 97.09-91.85º W), the Valdivia Fracture Zone intra-transform spreading centers (ITSCs) (41.10-41.55º S, 91.27-84.67º W), and the northernmost three segments of the Southern Chile Ridge (41.58-43.02º S, 84.35-83.44º W) (Figure 1). In conjunction with the Southern Chile Ridge On-axis Survey and Sampling (CROSS) expedition in 1993 (*Klein and Karsten*, 1995; *Karsten et al.*, 1996; *Sherman et al.*, 1997; Figure 1), this expedition formed a complete sampling survey of the Chile Ridge from the Chile Fracture Zone to the Chile Margin Triple Junction.

Based on new high-resolution shipboard SeaBeam bathymetry acquired during the 1998 PANORAMA cruise, *Karsten et al.* (1999) and *Martinez et al.* (in preparation) gave the following description of Northern Chile Ridge segmentation geometry and segment

morphology. The Northern Chile Ridge consists of 10 first-order segments separated by transform offsets, named N1 through N10 from north to south (Figure 2). Depth inside the axial valley varies locally from ~3300 to 4000 m. The axial valley morphology of these segments is similar to what has been found at the Mid-Atlantic Ridge (*e.g.*, *Kong et al.*, 1988). The subsidence rate (depth on the flank) is symmetric on both sides of the axis. The average axial depth is constant along the length of the ridge (*i.e.*, there is no regional gradient in ridge depth), which is consistent with seismic tomography studies which show that under the Northern Chile Ridge there is no regional gradient in mantle temperature (*Anderson et al.*, 1992; *Zhang and Tanimoto*, 1993).

Segments at the Northern Chile Ridge are diverse in morphology (*Karsten et al.*, 1999; *Martinez et al.*, in preparation). Segments N1, N8, and N10 are medium length (55-90 km) hourglass type segments, shallow and narrow at the segment center, and wider and deeper at segment ends (Figures 3a and 3b). Narrow central ridges ~200 m high are visible inside the axial valleys, and are thought to be the neovolcanic zones of the spreading segments.

Segments N2, N3, and N4 are very short (< 15 km) intratransform spreading center (ITSC) -like segments, with deep, rhomboid-shaped axial valley basins (Figure 3a). These basins also contain median ridges ~200 m high.

Segments N5 and N6 make up the propagating rift and dying rift, respectively (Figure 3a). The northern end of segment N5 is characterized by a broad bathymetric high across the axis and flanks that extends approximately 30 km along the axis and shallows to 3100 m in the axial valley. A negative gravity “bull’s eye” anomaly (*e.g.*, *Kuo and Forsyth*,

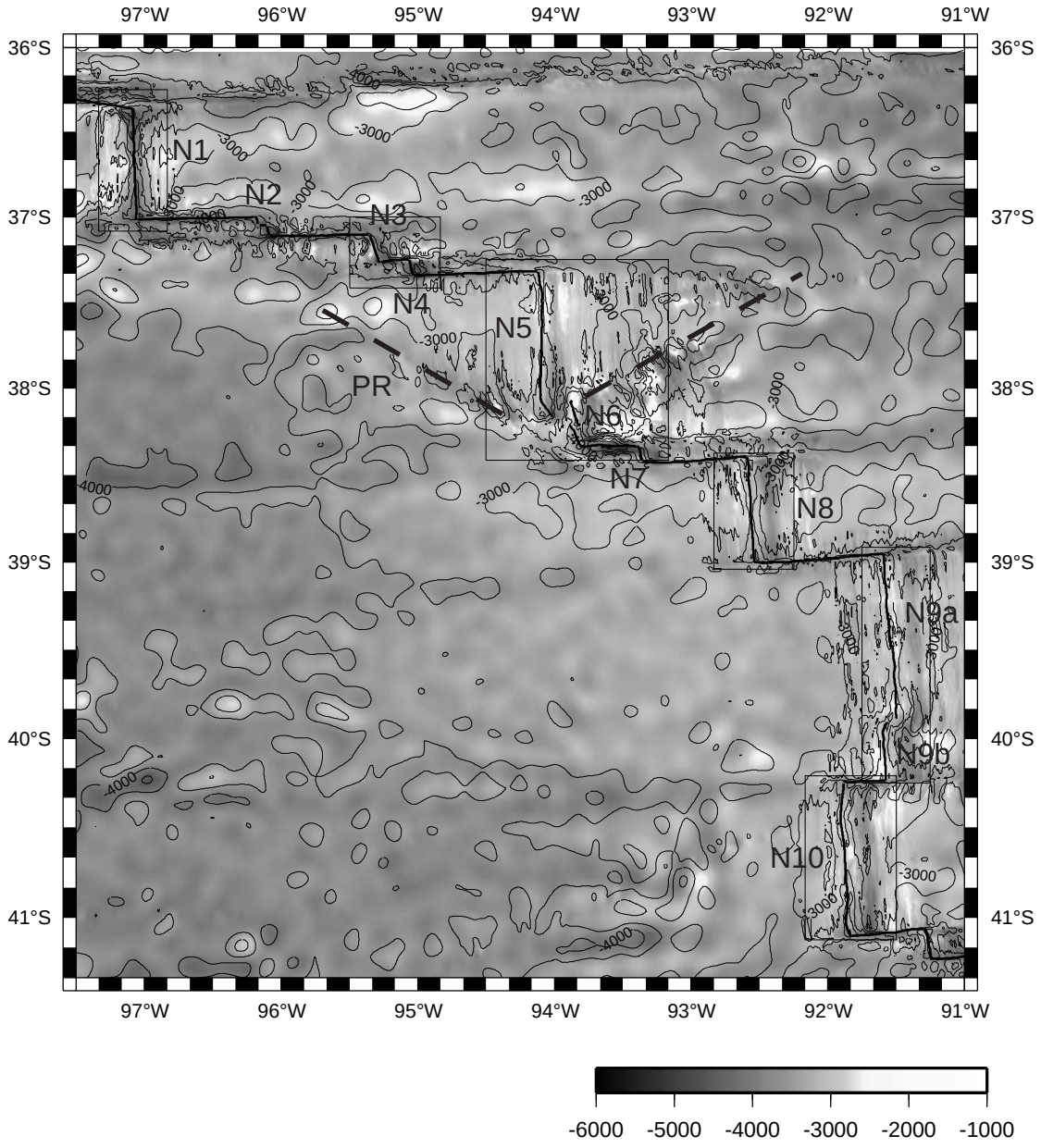

Figure 2: Bathymetry of the Northern Chile Ridge, showing segment locations. Near the ridge axis, bathymetry data are from the PANORAMA Expedition; farther from the ridge axis, data are estimated seafloor topography from *Smith and Sandwell* (1997). Spreading axes (trending roughly north-south) and transform offsets (striking roughly east-west) are outlined; segment names (N1 through N10) and the propagating rift (PR) are labelled. Boxes indicate regions shown in Figures 3a and 3b. Contour interval is 500 m.

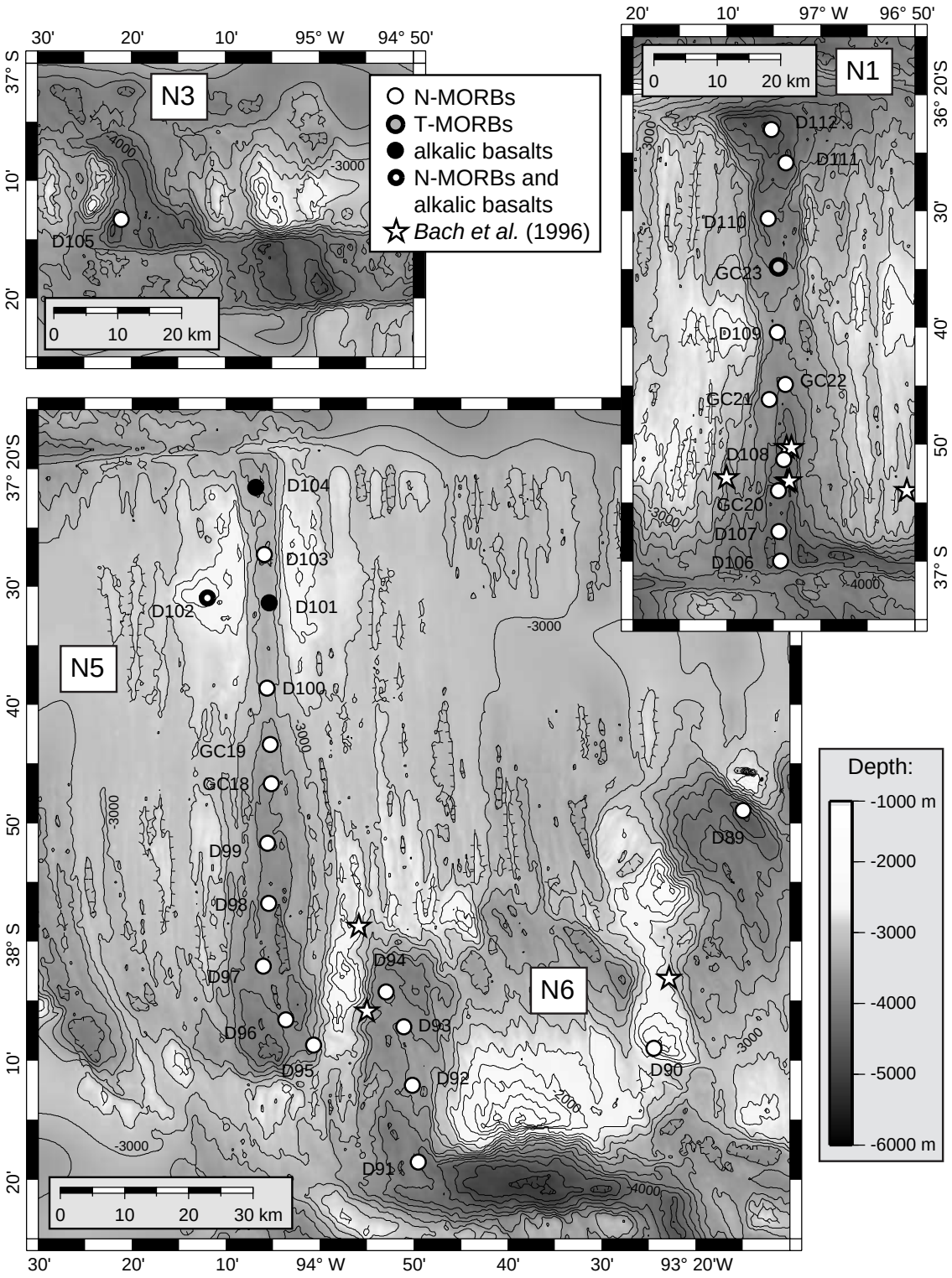

Figure 3a: Northern Chile Ridge segments N1, N3, N5, and N6, showing locations and petrologic types of samples recovered in this study, and by *Bach et al.* (1996). See legend for explanation of symbols. Bathymetry data as in Figure 2. Contour lines every 250 m.

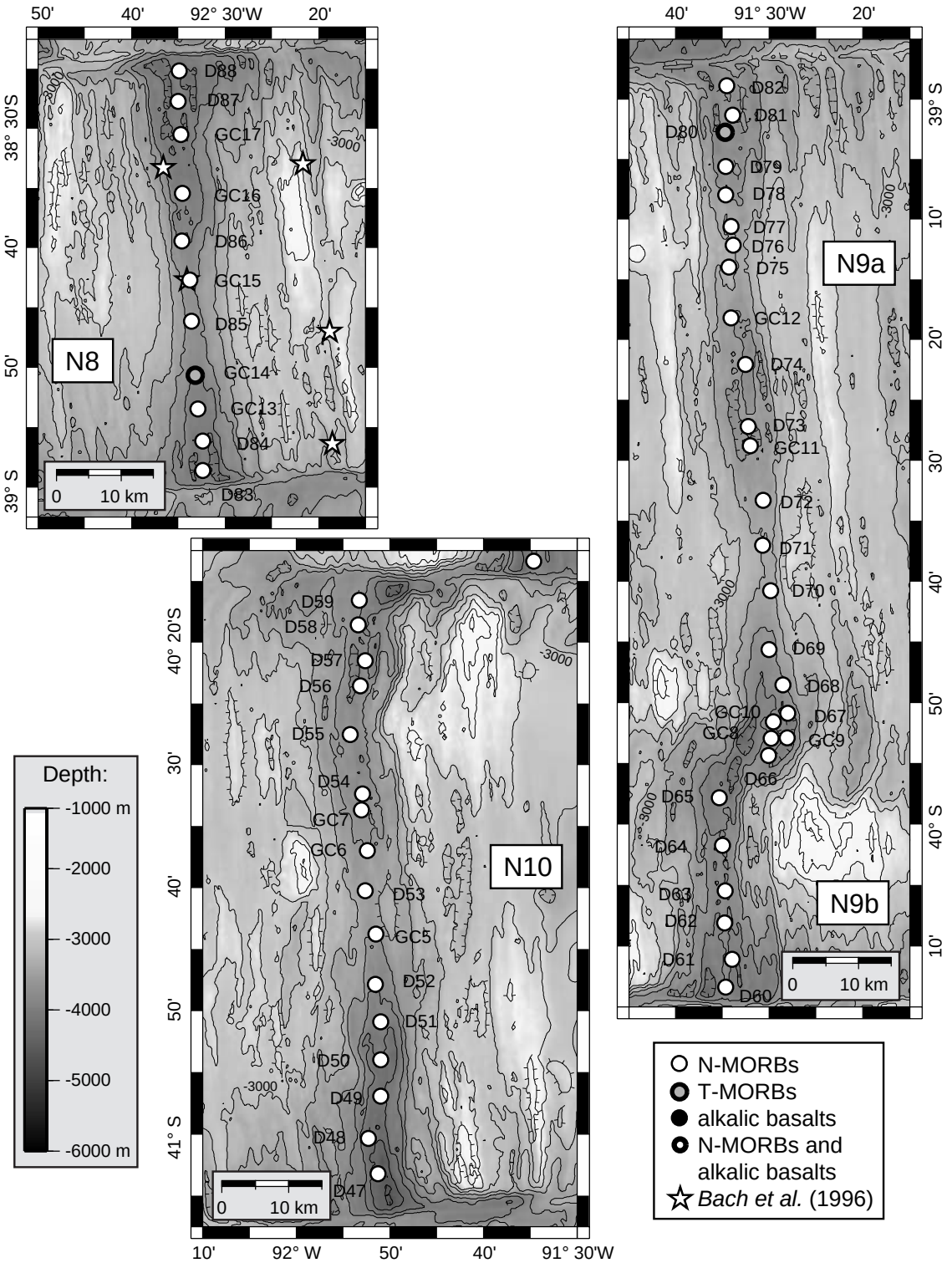

Figure 3b: Northern Chile Ridge segments N8, N9a, N9b, and N10, showing locations and petrologic types of samples recovered in this study, and by *Bach et al.* (1996), after Figure 3a. See legend for explanation of symbols. Bathymetry data as in Figure 2. Contour lines every 250 m.

1988; *Tolstoy et al.*, 1993) centered over the bathymetric high indicates that this is likely to be a region of thicker crust.

Segment N9 is a pinch-and-swell type segment, with undulating axial valley width and depth (Figure 3b). This segment is subdivided into N9a and N9b by a non-transform offset at 38º 55' S, and contains a DevAL (deviation from axial linearity) at 39º 28' S. None of the other segments is disrupted by smaller-order segmentation.

Karsten et al. (1999) and *Martinez et al.* (in preparation) also described Valdivia Fracture Zone and Southern Chile Ridge segmentation geometry and segment morphology. The Valdivia Fracture Zone contains six intra-transform spreading centers (ITSCs), named V1 through V6 from north to south, within the fracture zone system (Figure 4). The northern end of the Southern Chile Ridge consists of three first-order segments, named S5 through S7 from south to north. Segments S6 and S7 meet at an overlapping spreading center that appears from the bathymetry to be unstable (*Karsten et al.*, 1999; *Martinez et al.*, in preparation).

Prior Petrology Studies

The only previous sample recovery project at the Northern Chile Ridge was the So40 cruise conducted aboard the R/V *Sonne* in 1985 (*Bach et al.*, 1996). This cruise conducted a limited Hydrosweep bathymetry survey and dredged at 16 sites from 36º 50' to 38º 56' S, recovering 38 samples, all normal-type mid-ocean ridge basalts (N-MORBs) (*Bach et al*., 1996) (Figures 3a and 3b). Many of the N-MORBs recovered were a

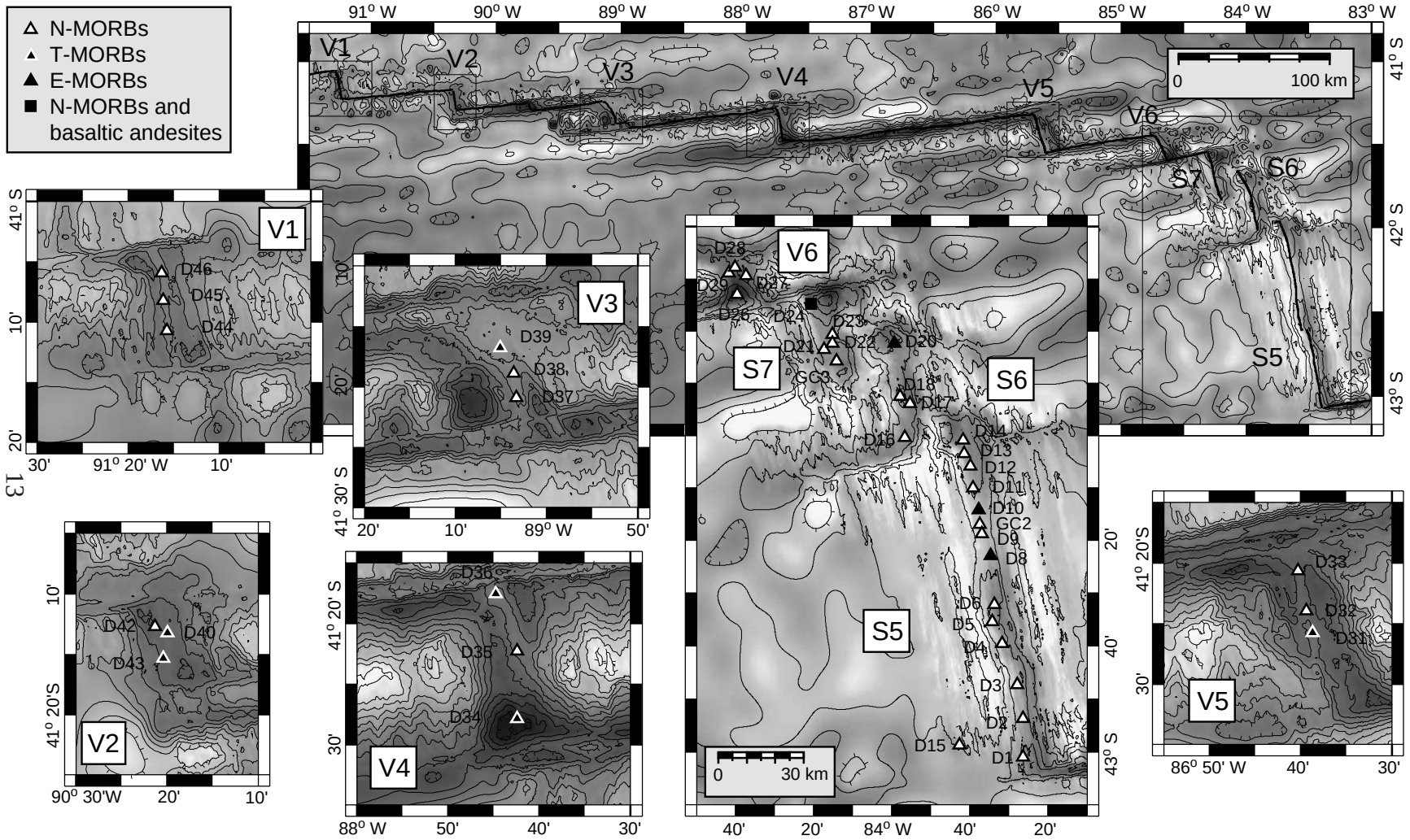

Figure 4: Valdivia Fracture Zone and Southern Chile Ridge segments S5-S7: regional segmentation geometry (top); segment morphology and locations and petrologic types of samples recovered in this study (bottom plots). Bathymetry data and depth scale as in Figure 2. Contour lines every 250 m for segments V1-V5 plots, and every 500 m for segments V6-S5 and regional plot.

species of "ultra-depleted" N-MORBs, with low abundances of incompatible trace elements (relative to the typical N-MORB composition in *Sun and McDonough*, 1989) but high abundances of the most highly incompatible trace elements (Th, U, Ba, Rb; Ba = 4.6-9.9 ppm, Rb = 0.23-61 ppm); the N-MORBs recovered also had higher Na_2O and TiO_2 and lower CaO contents than N-MORBs from other spreading centers in the east Pacific (the southern East Pacific Rise and the Galapagos Spreading Center) (*Bach et al.*, 1996). However, the spatial coverage of the So40 survey was insufficient to determine firstly whether these were really the dominant geochemical features at the entire Northern Chile Ridge, and secondly whether there were any systematic geochemical changes near transform offsets. The geographic coverage of the survey was restricted, and many of the sample sites were located off-axis or near fracture zones.

This Study

This study investigates the petrogenesis of the Northern Chile Ridge volcanic system based on the major element and trace element compositions of glasses from lavas erupted at the ridge axis, using the samples recovered during Leg 4 of the PANORAMA Expedition to the Chile Ridge in 1998. Nd, Sr, and Pb isotope analyses of 12 samples from the Northern Chile Ridge are in progress (*E. Klein*, personal communication). New major element analyses for glasses from the Valdivia Fracture Zone and Southern Chile Ridge (segments S5-S7) from the PANORAMA Expedition are presented where they are relevant to Northern Chile Ridge processes. However, their petrogenesis is not discussed

in detail here. Trace element geochemistry from these Valdivia Fracture Zone and Southern Chile Ridge segments was presented by *Sturm et al.* (1998) and *Klein et al.* (2001).

Sampling during Leg 4 of the 1998 PANORAMA Expedition to the Chile Ridge was by dredge haul and wax core, at an average sample spacing of approximately 7 km along axis. Volcanic rocks and glass fragments were recovered from 66 dredge sites and 19 wax core sites along the axes of the Northern Chile Ridge spreading segments N1, N3, N5, N6, N8, N9a, N9b, and N10, between 36º 20' and 41º 15' S (Figures 3a and 3b). All but three of the sampling sites were located along neovolcanic zones, identified in the bathymetry as narrow constructional highs running down the centers of the ridge axial valleys (*Karsten et al.*, 1999); two were located on off-axis seamounts, and one was located on the eastern pseudofault of the propagating rift. Additional samples were recovered from 23 dredge sites along the axes of Valdivia Fracture Zone Intra-Transform Spreading Centers V1 through V6 (41º 06'-41º 33' S), and from 27 dredge sites along Southern Chile Ridge segments S7, S6, and S5 (41º 35'-43º 02' S) (Figure 4). In total, 668 samples from these 135 locations were analyzed for major element compositions, and 50 samples from the Northern Chile Ridge were analyzed for trace element concentrations.

The Northern Chile Ridge samples are MORBs that range from ultra-depleted N-MORBs to T-MORBs, as well as a few alkalic basalts that are among the few on-axis alkalic basalts in the Pacific not associated with a known hotspot. This is a much more geochemically diverse suite of samples than had been previously reported for this region.

Quantitative incompatible trace element models, as well as the presence of correlations between radiogenic isotope ratios and incompatible trace element ratios and the lack of correlations between incompatible trace element ratios and Na_8, suggest that the best explanation for the petrogenesis of this suite of samples is mixing of < 5% of an alkalic magma with tholeiitic magmas, formed by variable extents of melting (14-20%) of a depleted source. Mixing controls the radiogenic isotope and incompatible trace element content of the lavas. However, since such a small amount of the alkalic magmas are added, and their major element compositions are similar, the major element compositions of the mixtures are not significantly affected, with the result that major element compositions of primitive parental magmas probably reflect the extent of melting of the depleted mantle matrix. Metasomatic addition of very small quantities of a fluid enriched in the most highly incompatible trace elements (Cs, Rb, Ba, Th, U, Nb, and Ta) may also occur, since these elements are observed to vary widely and not in relation to other incompatible trace elements. The most likely situation for this petrogenetic scenario is melting of an upper mantle that contains ubiquitous blobs of Pacific hotspot-type fertile mantle embedded in a depleted mantle matrix.

The Northern Chile Ridge lava population is more uniform and more depleted in incompatible trace elements (using K/Ti as a proxy) than lava populations at other southeast Pacific mid-ocean ridges. This may be due to a sparser distribution of fertile mantle blobs in the Northern Chile Ridge mantle than in the rest of the southeast Pacific mantle. A previous episode of melt extraction, which had been suggested by *Bach et al.* (1996), is not required.

No arc-like trace element signature is found in any of the Northern Chile Ridge samples, suggesting that chemical heterogeneities introduced by recent subduction at the Chile Margin Triple Junction are small in geographic scale and are subordinate to the larger regional patterns of mantle heterogeneity (even though regional patterns themselves are probably caused in part by ancient subduction).

Northern Chile Ridge lavas are more primitive (higher Mg #) than lavas from intermediate spreading rate ridges near hotspots, suggesting that at intermediate spreading rates hotspots exert an important influence on the thermal budget controlling shallow crystallization and mechanisms of crustal accretion.

Finally, at the Chile Ridge, the presence of long-offset transforms does not affect the extent of melting in a large-scale sense, except near the Valdivia Fracture Zone, where the segment-transform geometry approaches the extreme case of a fracture zone containing intra-transform spreading centers (ITSCs). There are no obvious systematic effects of segmentation and transform offsets on the petrogenesis of Northern Chile Ridge lavas.

METHODS FOR GEOCHEMICAL ANALYSIS

Lavas recovered from the Chile Ridge were analyzed for major elements by electron microprobe and for trace elements by inductively coupled plasma mass spectrometer (ICP-MS). In all cases, the sample consisted of fresh glass chips that were hand-picked using an optical microscope to avoid alteration and phenocrysts. For trace element analysis, sample digestion was preceded by a leaching step (5% HCl + 10% H_2O_2 in a 1:1 ratio for 10 minutes) and sonification to remove any invisible alteration.

Major Elements

Major elements were analyzed at the University of Hawai‘i at Mānoa on a 1992 Cameca SX50 electron microprobe, a fully automated microprobe with five wavelength dispersive spectrometers. The conditions of analysis were a beam current of 10 nA, a beam diameter of 10 μm, and an accelerating voltage of 15 KV. Count times were 20 s for Na and Ca; 30 s for Mg, Al, Si, and Ti; 40 s for Fe; 50 s for Mn; 60 s for K; and 110 s for P. For each sample, between three and ten point analyses were acquired on at least three different glass chips. Drift was corrected by normalizing analyses to the Lamont-Doherty Earth Observatory internal standard JdF D-2, a basalt glass (provided by J. Reynolds). Point analyses were discarded if they had sums lower than 98% or greater than 101.5%, or if they showed obvious phenocryst contamination.

Where several rock samples from the same dredge site all had the same major element composition (identical within analytical precision for all oxides), they were binned into a single average "rock type" composition. This "rock type" composition may represent the average composition of a single lava flow on the ocean floor, from which multiple fragments were recovered in a dredge (*e.g.*, *Sinton et al.*, 1991). From the Northern Chile Ridge spreading segments, 408 samples from 85 dredge sites were analyzed and binned into 193 rock types; from the Valdivia Fracture Zone ITSCs, 119 samples from 23 dredge sites were analyzed and binned into 50 rock types; from the Southern Chile Ridge segments, 141 samples from 27 dredge sites were analyzed and binned into 61 rock types.

Where errors are shown for major element rock type compositions, they are the 1σ standard deviation of all the analysis points for the samples in the bin. Relative errors are near 0.5% for SiO_2; near 1% for Al_2O_3, MgO, and CaO; near 2% for FeO* and Na_2O; near 3% for TiO_2; and near 15% for K_2O, P_2O_5, and MnO.

Trace Elements

Trace elements were analyzed for a subset of 50 Northern Chile Ridge samples on a VG Plasmaquad II+ ICP-MS at the University of Hawai'i at Mānoa, using the external standard calibration method (*e.g.*, *Skoog and Leary*, 1992; *Montaser*, 1998). The samples were chosen based on the results of the major element analyses, so that they included all different geochemical types observed, covered the range of lava differentiation, included

samples from every ridge segment and every tectonic setting within the segment, and included a densely-spaced profile of one of the ridge segments.

Samples were analyzed in two batches, the first in the fall of 1999 and the second in the summer of 2000. Each batch was run twice, once for trace elements that were expected to be present in high abundances, and once for trace elements that were expected to be present in low abundances. This was done to ensure that all the target nuclides during a data acquisition run were in detectable concentrations in the sample dilution. Digested sample solutions that were analyzed for low-abundance trace elements were diluted to approximately 1:1000. Digested sample solutions that were analyzed for high-abundance trace elements were diluted to approximately 1:3000 for low-K/Ti samples in the first batch, and 1:5000 for high-K/Ti samples in the first batch and all samples in the second batch. Dilutions were measured by weight. Sample solutions were refrigerated for the time between digestion and data acquisition.

The standards used during the first batch of analyses were the Hawaiian basalt BHVO-1 and the andesite AGV-1; during the second batch the standards were revised to BHVO-1 and the Icelandic basalt BIR-1. The standard compositions used to calibrate the data are shown in Table 1. During data acquisition, three repeated analyses were acquired for each sample, standard, and blank.

ICP-MS analytical runs were designed on the two premises that drift in the machine would vary both in time and over the mass range in an unpredictable way (*e.g.*, *Cheatham et al.*, 1993; *Cheatham*, 1995), and that interferences from oxidation of isotope nuclides in the sample and in the internal standard would vary in time. The internal standard

Table 1:
Working Values for Trace Element Concentrations
in Standards used in ICP-MS Analyses

	AGV-1	BHVO-1	BIR-1
(ppm)			
Sc	12.2	31.8	44
Cr	10.1	289	382
Ni	16	121	166
Cu	60	136	126
Zn	88	105	71
Rb	67.3	10.1	0.25
Sr	662	403	108
Y	20	27.6	16
Zr	227	179	15.5
Nb	15.3	19.7	0.6
Cs	1.28	0.1	0.005
Ba	1226	132.9	6.6
La	38	15.74	0.56
Ce	67	37.77	1.90
Pr	7.84	5.40	0.39
Nd	33	24.81	2.40
Sm	5.9	6.10	1.11
Eu	1.64	1.98	0.52
Gd	4.76	6.56	1.98
Tb	0.59	1.02	0.41
Dy	3.6	5.37	2.62
Ho	0.67	1.01	0.59
Er	1.7	2.38	1.71
Tm	0.26	0.33	0.27
Yb	1.72	2.01	1.70
Lu	0.27	0.29	0.26
Hf	5.32	4.38	0.6
Ta	0.90	1.23	0.04
Pb	36	2.08	2.91
Th	6.5	1.16	0.031
U	1.92	0.41	0.010

Values from *Cheatham et al.* (1993), *Garbe-Schönberg* (1993), *Govindaraju* (1994), *Jochum et al.* (1990), and *Korotev* (1996).

contained ^{67}Zn (for high-abundance elements only), ^{115}In, ^{147}Sm, and ^{209}Bi, which bracketed the mass range of the target nuclides (the nuclides of Sm that we measured in the samples were ^{149}Sm and ^{152}Sm). The internal standard was done by flow method.

In order to monitor changing interferences from the internal standard, HNO_3 blanks were inserted every 5-8 samples during the runs, in addition to the blanks from sample digestions. Blanks containing only 20 ppm Ba were inserted in the low-abundance run of the first batch, in order to constrain the magnitude of interferences to isotopes of Eu from the oxidation of Ba.

The set of all dilutions of the standards was analyzed at the beginning, middle, and end of each data acquisition run. Accordingly, during the calculation step, output from each acquisition was calculated as three separate sub-procedures, using the appropriate set of standard dilutions analyses as the calibration points. This was done to ensure that the calibration lines approximately kept apace with instrument drift.

The following corrections were made to the trace element data as part of the data processing. A blank subtraction was applied to correct for interferences from oxidation products from the internal standard, and to subtract out very low concentrations of ^{149}Sm and ^{152}Sm that were present in the internal standard. Blank concentrations at other mass numbers were consistently near zero, indicating that the sample analysis solutions were not contaminated.

Calibration lines were checked to ensure that all calibration points were collinear. Calibration points that were drastically off the calibration line for all isotopes of a standard dilution were assumed to be bad and were excluded from the calibration line;

after these exclusions, all calibration lines still had 3-4 good calibration points, went through zero, and were linear. Dead-timing (a deviation below linearity of calibration points at high concentrations caused by detector saturation) was not observed in any of the calibration lines.

Interference equations were applied in the calculation step of data processing, based on examination of the blank spectra and calibration lines. Corrections were necessary for an interference of Rb with ^{87}Sr, and for an interference in ^{67}Zn in the internal standard from Zn in the sample. In low-abundance acquisition runs, corrections were necessary for oxide interferences with the following rare earth elements: ^{139}La and ^{149}Sm (second batch only), ^{151}Eu, ^{153}Eu (first batch only), ^{152}Sm, ^{155}Gd, ^{157}Gd, ^{159}Tb, ^{160}Gd, ^{162}Dy, ^{163}Dy, ^{165}Ho, ^{166}Er, and ^{174}Yb.

Trace Element Data Quality

Several indicators of data quality demonstrate that the trace element analyses acquired in this study are accurate and precise. New analyses of two old Northern Chile Ridge samples (So40-07D and So40-08S, N-MORBs, *Bach et al.*, 1996) were compared to their published analyses (Table 2). Newly acquired trace element ratios are similar to the published ratios, especially for ratios of the rare earth elements (La/Sm, Sm/Yb).

The main problems with the data are that absolute concentrations of some elements don't compare well in the inter-laboratory comparison, and that for the most depleted samples and the elements that are in lowest abundance (Cs, U, and Rb), data acquisition

Table 2:
Inter-laboratory Comparison of Trace Element Analyses

	Bach et al.	This Study		inter-lab	*Bach et al.*	This Study		inter-lab	detection
	(1996)	*conc.*	*error*	ratio[†]	(1996)	*conc.*	*error*	ratio[†]	range (ppm)[*]
(ppm)	*sample So40-07D*				*sample So40-08S*				
Sc	--	40.9	0.4	--	--	43.6	2.8	--	0.5-50
Cr	298	332	5	1.12	--	422	43	--	5-500
Ni	117	114.0	2.8	0.97	113	120.1	11.6	1.06	2-200
Cu	61	66.7	1.9	1.09	69	77.3	8.6	1.12	1.6-160
Zn	75	71.5	2.9	0.95	71	68.4	6.6	0.96	2-200
Rb	0.23	0.116	0.010	0.50	0.47	0.589	0.056	1.25	0.14-14
Sr	89	93	3	1.05	97	108	6	1.11	5-500
Y	28.9	35.1	0.2	1.21	25.5	31.9	0.8	1.25	0.5-50
Zr	74	83.6	1.0	1.13	65	75.0	2.7	1.15	4.5-450
Nb	0.60	0.67	0.03	1.12	1.30	1.50	0.03	1.15	0.1-10
Cs	--	0.0015	0.0009	--	--	0.0049	0.0004	--	0.1-10
Ba	4.6	1.23	0.08	0.27	6.8	7.04	0.19	1.04	1.3-130
La	1.89	1.96	0.03	1.04	1.94	2.17	0.04	1.12	0.1-10
Ce	6.9	7.25	0.30	1.05	6.6	6.89	0.28	1.04	0.6-60
Pr	1.26	1.42	0.06	1.13	1.14	1.31	0.01	1.15	0.1-10
Nd	7.9	8.4	0.2	1.07	7.0	7.6	0.3	1.09	0.6-60
Sm	2.90	3.25	0.08	1.12	2.50	2.87	0.05	1.15	0.4-40
Eu	1.10	1.13	0.01	1.03	1.03	1.06	0.01	1.03	0.2-20
Gd	3.9	4.99	0.08	1.28	3.6	4.38	0.01	1.22	0.5-50
Tb	0.73	0.909	0.023	1.25	0.68	0.818	0.002	1.20	0.1-10
Dy	4.8	5.53	0.03	1.15	4.5	4.98	0.09	1.11	0.4-40
Ho	1.08	1.219	0.009	1.13	1.00	1.055	0.018	1.05	0.1-10
Er	3.0	3.65	0.06	1.22	2.8	3.21	0.02	1.15	0.3-30
Tm	0.45	0.582	0.011	1.29	0.41	0.507	0.002	1.24	0.1-10
Yb	3.0	3.45	0.04	1.15	2.7	3.04	0.06	1.12	0.3-30
Lu	0.45	0.549	0.005	1.22	0.40	0.484	0.008	1.21	0.1-10
Hf	2.28	2.34	0.05	1.03	1.85	2.03	0.06	1.10	0.4-40
Ta	0.04	0.062	0.003	1.55	0.08	0.109	0.003	1.36	0.1-10
Pb	0.27	0.29	0.02	1.08	0.27	0.64	0.03	2.36	0.2-20
Th	0.040	0.034	0.001	0.84	0.080	0.086	0.004	1.07	0.1-10
U	0.020	0.019	0.001	0.97	0.035	0.035	0.001	0.99	0.1-10
Nb/Ta	15	11	1	0.72	16	14	1	0.85	
Zr/Hf	32	36	1	1.10	35	37	3	1.05	
Nb/U	30	34	5	1.15	37	43	3	1.16	
Th/La	0.021	0.017	0.001	0.81	0.041	0.040	0.003	0.96	
Ba/Rb	20	11	2	0.53	14	12	2	0.83	
Ce/Pb	26	25	3	0.97	24	11	1	0.44	
Nb/La	0.32	0.34	0.02	1.08	0.67	0.69	0.03	1.03	
La/Sm	0.65	0.60	0.03	0.93	0.78	0.75	0.03	0.97	
Sm/Yb	0.97	0.94	0.04	0.98	0.93	0.95	0.04	1.02	
Sm/Gd	0.74	0.65	0.03	0.88	0.69	0.66	0.01	0.94	

[†] inter-laboratory ratio: This Study/*Bach et al.* (1996)

* Detection range is the range of theoretical minimum and maximum detectable concentrations for these samples.

was near or below the official detection limit (Table 2). Absolute concentrations of Ta especially are 30-50% higher in the data acquired in this study than in the published analyses. The inaccuracy may lie either in the analyses in this study, or in the analysis by *Bach et al.*, 1996.

However, as we will show in the results, systematic behavior of the rare earth elements and the more highly incompatible trace elements, as well as a good correlation between ratios of trace elements obtained by ICP-MS and K/Ti obtained by electron microprobe, attest to the high quality of this trace element dataset.

Error presented in the results are estimates based on counting statistics (*i.e.*, the standard deviation of repeated acquisitions) and weighing error. The estimated error is around 5% for most elements in most samples, but is higher for Rb, Cs, Pb, Th, and U. Additional error is expected to have been introduced in the calibration lines, but this was not accounted for in our reported error, due to the difficulty of estimating it. Therefore, the reported error must be regarded as an estimated minimum error. Approximately 5% additional error is introduced for Pb by not knowing appropriate isotopic ratios for standards or samples, since $^{206}Pb/^{204}Pb$ and $^{208}Pb/^{204}Pb$ vary widely in oceanic basalts.

RESULTS

Major Element Data

Major element compositions for the 193 Northern Chile Ridge sample bins are given in Table 3. Samples were classified as alkalic basalts or MORBs (low-K tholeiitic basalts) on a diagram of total alkalis vs. SiO_2, and further grouped into normal-type MORBs (N-MORBs), transitional-type MORBs (T-MORBs), and enriched-type MORBs (E-MORBs) according to K/Ti (Figure 5).

Samples recovered from the Northern Chile Ridge are predominantly N-MORBs, with rare T-MORBs and alkalic basalts. The N-MORBs constitute 96% of recovered samples and are found at all regions of all segments (Figures 3a and 3b). The T-MORBs have the same total alkali content as the N-MORBs, but with distinctly higher K_2O contents and K/Ti. T-MORBs constitute only 3% of recovered samples. They are not found in any consistent tectonic setting: T-MORBs occur mid-segment at segment N1, near the southern ridge-transform intersection of segment N8, and near the northern ridge-transform intersection of segment N9a (Figures 3a and 3b). The alkalic basalts have high K_2O and K/Ti and high Na_2O. Alkalic basalts constitute only 2% of recovered samples. They are found only at sites near the bathymetric high at the northern end of segment N5 (Figure 3a). Two were recovered in on-axis dredges, and one was recovered at an off-axis seamount.

Table 3: Major Element Compositions from the Northern Chile Ridge

sample	D112-a	D112-b	D111-a	D111-b	D111-c	D111-d	D110-a	D110-b	GC23-a	GC23-b	D109-a
segment	N1	N1	N1	N1	N1	N1	N1	N1	N1	N1	N1
latitude (^oS)	36.383	36.383	36.431	36.431	36.431	36.431	36.511	36.511	36.580	36.580	36.674
longitude (^oW)	97.088	97.088	97.062	97.062	97.062	97.062	97.093	97.093	97.075	97.075	97.077
depth (m)	4585	4585	4504	4504	4504	4504	3971	3971	3834	3834	3507
# samples	1	1	1	3	1	1	4	4	1	1	1
# points	5	5	5	14	5	5	20	18	4	5	5
lava type	N-MORB	N-MORB	N-MORB	N-MORB	N-MORB	N-MORB	N-MORB	N-MORB	T-MORB	T-MORB	N-MORB
K/Ti	0.05	0.06	0.09	0.09	0.08	0.09	0.06	0.06	0.21	0.22	0.07
SiO_2	50.09	50.13	49.47	49.51	49.64	49.71	50.28	50.40	49.86	49.66	50.84
TiO_2	1.73	1.72	1.32	1.44	1.41	1.37	1.34	1.40	1.15	1.14	1.23
Al_2O_3	15.36	15.43	16.88	16.45	16.63	16.58	15.90	15.81	16.49	16.24	15.26
FeO*	9.84	9.92	8.97	9.31	9.30	9.29	9.01	9.14	8.46	8.63	9.21
MnO	0.19	0.20	0.14	0.15	0.17	0.17	0.15	0.16	0.17	0.18	0.16
MgO	8.25	8.25	8.77	8.57	8.65	8.59	8.63	8.52	9.16	9.23	8.23
CaO	11.32	11.18	11.66	11.45	11.45	11.53	11.95	11.98	11.96	11.81	12.38
Na_2O	2.73	2.88	2.77	2.86	2.81	2.85	2.57	2.57	2.45	2.39	2.68
K_2O	0.07	0.08	0.09	0.09	0.08	0.09	0.06	0.06	0.18	0.18	0.07
P_2O_5	0.17	0.17	0.15	0.16	0.16	0.17	0.12	0.12	0.12	0.14	0.11
sum	99.75	99.97	100.23	99.99	100.30	100.35	100.03	100.16	99.99	99.60	100.16
	standard deviation (1 σ)										
SiO_2	0.63	0.78	0.13	0.13	0.25	0.26	0.29	0.26	0.23	0.18	0.12
TiO_2	0.04	0.03	0.05	0.03	0.01	0.03	0.04	0.04	0.04	0.04	0.04
Al_2O_3	0.09	0.11	0.03	0.09	0.10	0.09	0.06	0.13	0.02	0.39	0.05
FeO*	0.16	0.14	0.16	0.22	0.04	0.09	0.17	0.13	0.09	0.22	0.09
MnO	0.03	0.03	0.02	0.04	0.03	0.01	0.03	0.03	0.02	0.03	0.05
MgO	0.02	0.02	0.06	0.06	0.05	0.08	0.05	0.08	0.06	0.30	0.07
CaO	0.13	0.12	0.08	0.10	0.11	0.13	0.12	0.12	0.15	0.10	0.05
Na_2O	0.04	0.06	0.09	0.05	0.02	0.04	0.07	0.07	0.06	0.07	0.06
K_2O	0.01	0.01	0.01	0.01	0.01	0.01	0.01	0.01	0.01	0.01	0.01
P_2O_5	0.02	0.01	0.01	0.02	0.02	0.02	0.02	0.02	0.02	0.00	0.03

sample	D109-b	GC22	GC21	D108-a	D108-b	D108-c	D108-d	D108-e	GC20	D107-a	D107-b
segment	N1	N1	N1	N1	N1	N1	N1	N1	N1	N1	N1
latitude (^oS)	36.674	36.748	36.770	36.855	36.855	36.855	36.855	36.855	36.900	36.958	36.958
longitude (^oW)	97.077	97.063	97.092	97.066	97.066	97.066	97.066	97.066	97.075	97.075	97.075
depth (m)	3507	3769	3476	4209	4209	4209	4209	4209	4014	4098	4098
# samples	1	1	1	2	1	1	1	1	1	6	1
# points	5	5	5	10	4	6	5	5	5	30	5
lava type	N-MORB	N-MORB	N-MORB	N-MORB	N-MORB	N-MORB	N-MORB	N-MORB	N-MORB	N-MORB	N-MORB
K/Ti	0.07	0.05	0.04	0.05	0.05	0.05	0.05	0.04	0.05	0.05	0.04
SiO_2	50.71	51.15	50.81	50.36	50.84	50.76	50.62	50.91	50.59	50.24	50.09
TiO_2	1.33	1.39	1.29	2.20	1.91	1.97	2.07	1.82	1.35	1.34	1.17
Al_2O_3	15.23	14.89	15.41	14.11	14.58	14.46	14.26	14.63	15.25	15.91	16.55
FeO*	9.11	9.13	9.14	11.75	10.76	11.02	11.55	10.57	9.41	9.08	8.33
MnO	0.17	0.19	0.18	0.23	0.20	0.21	0.21	0.20	0.17	0.16	0.15
MgO	8.24	8.07	8.33	6.86	7.39	7.31	7.02	7.53	8.29	8.50	9.18
CaO	12.33	12.02	11.86	10.62	11.08	10.99	10.71	11.23	11.94	12.03	12.07
Na_2O	2.70	2.86	2.67	3.07	2.93	2.94	3.06	2.91	2.65	2.68	2.59
K_2O	0.07	0.05	0.04	0.08	0.07	0.07	0.08	0.06	0.05	0.05	0.03
P_2O_5	0.12	0.13	0.11	0.22	0.18	0.20	0.22	0.19	0.13	0.13	0.12
sum	100.01	99.90	99.84	99.50	99.94	99.93	99.82	100.05	99.84	100.12	100.29
	standard deviation (1 σ)										
SiO_2	0.30	0.09	0.08	0.47	0.10	0.12	0.21	0.15	0.12	0.26	0.14
TiO_2	0.06	0.05	0.03	0.05	0.02	0.05	0.05	0.04	0.08	0.04	0.02
Al_2O_3	0.32	0.12	0.08	0.09	0.07	0.08	0.04	0.05	0.10	0.08	0.08
FeO*	0.28	0.12	0.10	0.19	0.13	0.09	0.16	0.14	0.07	0.14	0.14
MnO	0.02	0.02	0.02	0.03	0.03	0.02	0.01	0.04	0.02	0.03	0.03
MgO	0.23	0.07	0.08	0.07	0.04	0.05	0.03	0.06	0.05	0.06	0.09
CaO	0.20	0.05	0.11	0.14	0.10	0.13	0.16	0.11	0.11	0.15	0.10
Na_2O	0.06	0.07	0.06	0.07	0.07	0.05	0.09	0.06	0.04	0.05	0.06
K_2O	0.01	0.01	0.01	0.01	0.01	0.00	0.01	0.01	0.01	0.01	0.01
P_2O_5	0.01	0.02	0.02	0.02	0.02	0.03	0.01	0.01	0.02	0.02	0.02

(Table 3 continued)

sample	D107-c	D107-d	D106-a	D106-b	D105-a	D105-b	D105-c	D104	D103-a	D103-b	D103-c
segment	N1	N1	N1	N1	N3	N3	N3	N5	N5	N5	N5
latitude (^{o}S)	36.958	36.958	37.000	37.000	37.222	37.222	37.222	37.360	37.455	37.455	37.455
longitude (^{o}W)	97.075	97.075	97.072	97.072	95.352	95.352	95.352	94.114	94.099	94.099	94.099
depth (m)	4098	4098	4135	4135	4404	4404	4404	3296	3271	3271	3271
# samples	3	1	1	1	4	1	1	1	2	1	1
# points	14	5	5	4	23	4	5	5	11	4	5
lava type	N-MORB	N-MORB	N-MORB	N-MORB	N-MORB	N-MORB	N-MORB	alkalic	N-MORB	N-MORB	N-MORB
K/Ti	0.05	0.05	0.05	0.04	0.02	0.02	0.03	0.55	0.05	0.05	0.05
SiO_2	50.02	50.06	50.18	50.73	50.11	50.03	50.62	50.62	49.72	49.72	49.59
TiO_2	1.13	1.22	1.39	1.79	1.42	1.37	2.52	2.13	1.24	1.24	1.24
Al_2O_3	16.75	16.64	16.01	14.67	15.34	15.74	14.13	15.86	16.61	16.67	16.63
FeO*	8.30	8.40	8.95	10.39	9.60	9.41	11.50	9.22	8.78	8.65	8.75
MnO	0.15	0.16	0.20	0.18	0.19	0.17	0.23	0.18	0.19	0.20	0.16
MgO	9.25	9.16	8.37	7.61	8.37	8.61	6.43	6.20	8.76	8.78	8.69
CaO	12.18	11.95	11.97	11.67	12.28	12.26	10.47	10.02	11.87	11.75	11.75
Na_2O	2.49	2.55	2.79	2.75	2.58	2.60	3.67	3.87	2.94	2.98	2.89
K_2O	0.04	0.05	0.05	0.05	0.02	0.02	0.06	0.85	0.04	0.04	0.04
P_2O_5	0.11	0.12	0.14	0.18	0.12	0.11	0.25	0.43	0.12	0.13	0.13
sum	100.41	100.30	100.05	100.03	100.03	100.31	99.89	99.38	100.28	100.16	99.87
	standard deviation (1 σ)										
SiO_2	0.18	0.16	0.13	0.51	0.35	0.33	0.13	0.08	0.16	0.10	0.08
TiO_2	0.04	0.05	0.03	0.06	0.04	0.06	0.05	0.06	0.04	0.06	0.03
Al_2O_3	0.06	0.08	0.02	0.10	0.24	0.06	0.14	0.07	0.09	0.06	0.09
FeO*	0.11	0.16	0.14	0.20	0.19	0.20	0.17	0.08	0.15	0.10	0.09
MnO	0.03	0.03	0.03	0.04	0.04	0.03	0.03	0.04	0.04	0.03	0.05
MgO	0.04	0.03	0.04	0.08	0.11	0.04	0.04	0.07	0.06	0.05	0.07
CaO	0.12	0.07	0.05	0.08	0.10	0.10	0.09	0.10	0.12	0.11	0.13
Na_2O	0.08	0.03	0.03	0.05	0.07	0.00	0.08	0.06	0.08	0.04	0.04
K_2O	0.01	0.01	0.00	0.00	0.01	0.01	0.01	0.01	0.01	0.00	0.01
P_2O_5	0.02	0.01	0.02	0.02	0.02	0.02	0.02	0.02	0.02	0.01	0.03

sample	D102-a	D102-b	D102-c	D101	D100	GC19	GC18	D99	D98	D97	D96
segment		N5 (off-axis)		N5	N5	N5	N5	N5	N5	N5	N5
latitude (^{o}S)	37.517	37.517	37.517	37.524	37.644	37.723	37.778	37.863	37.947	38.035	38.110
longitude (^{o}W)	94.200	94.200	94.200	94.090	94.094	94.089	94.087	94.093	94.091	94.101	94.061
depth (m)	2202	2202	2202	3160	3204	3148	3200	3616	3490	3432	3648
# samples	5	1	1	7	5	1	1	3	1	1	1
# points	24	5	5	35	23	3	5	15	5	8	7
lava type	N-MORB	alkalic	alkalic	alkalic	N-MORB	N-MORB	N-MORB	N-MORB	N-MORB	N-MORB	N-MORB
K/Ti	0.04	0.86	0.78	0.87	0.04	0.05	0.05	0.08	0.07	0.06	0.05
SiO_2	50.60	48.96	48.05	50.36	50.92	50.22	50.50	50.31	50.61	50.41	48.69
TiO_2	1.38	2.10	2.46	2.58	1.38	1.34	1.58	1.46	1.42	1.15	1.25
Al_2O_3	14.74	16.39	16.77	17.18	15.27	15.54	15.21	15.67	15.77	16.01	16.64
FeO*	10.06	8.99	9.78	8.21	9.37	9.34	9.82	9.45	9.38	8.70	10.75
MnO	0.22	0.16	0.18	0.16	0.19	0.16	0.20	0.18	0.19	0.16	0.21
MgO	7.88	7.46	6.81	4.93	8.14	8.64	8.02	8.16	8.31	8.81	8.52
CaO	12.22	9.61	9.59	8.57	12.05	11.61	11.46	11.71	11.68	12.20	11.30
Na_2O	2.80	3.80	4.00	4.65	2.84	2.56	2.81	2.92	2.82	2.56	2.66
K_2O	0.04	1.30	1.39	1.63	0.04	0.05	0.06	0.08	0.07	0.05	0.05
P_2O_5	0.12	0.58	0.60	0.61	0.11	0.13	0.14	0.14	0.14	0.12	0.11
sum	100.04	99.34	99.64	98.89	100.32	99.57	99.80	100.07	100.38	100.16	100.18
	standard deviation (1 σ)										
SiO_2	0.22	0.08	0.13	0.20	0.18	0.09	0.08	0.34	0.13	0.23	0.12
TiO_2	0.04	0.04	0.04	0.04	0.04	0.03	0.05	0.05	0.05	0.09	0.05
Al_2O_3	0.09	0.03	0.07	0.08	0.05	0.10	0.06	0.10	0.07	0.21	0.05
FeO*	0.16	0.18	0.14	0.14	0.19	0.09	0.14	0.14	0.12	0.14	0.15
MnO	0.04	0.03	0.03	0.03	0.03	0.01	0.03	0.03	0.04	0.03	0.04
MgO	0.07	0.05	0.03	0.07	0.07	0.08	0.06	0.06	0.05	0.28	0.05
CaO	0.13	0.07	0.04	0.10	0.10	0.08	0.10	0.14	0.11	0.17	0.08
Na_2O	0.08	0.09	0.09	0.08	0.06	0.06	0.07	0.05	0.09	0.15	0.04
K_2O	0.01	0.03	0.02	0.03	0.01	0.01	0.01	0.01	0.00	0.01	0.01
P_2O_5	0.02	0.03	0.04	0.03	0.02	0.03	0.01	0.02	0.02	0.02	0.01

(Table 3 continued)

sample	D95	D94-a	D94-b	D94-c	D94-d	D94-e	D93	D92	D91-a	D91-b	D91-c
segment	N5	N6	N6	N6	N6	N6	N6	N6	N6	N6	N6
latitude (°S)	38.146	38.071	38.071	38.071	38.071	38.071	38.120	38.202	38.309	38.309	38.309
longitude (°W)	94.012	93.883	93.883	93.883	93.883	93.883	93.852	93.837	93.825	93.825	93.825
depth (m)	3632	3524	3524	3524	3524	3524	3413	3369	3824	3824	3824
# samples	1	4	1	1	1	2	1	1	3	5	1
# points	5	20	5	5	5	10	5	5	15	25	5
lava type	N-MORB	N-MORB	N-MORB	N-MORB	N-MORB	N-MORB	N-MORB	N-MORB	N-MORB	N-MORB	N-MORB
K/Ti	0.04	0.09	0.09	0.10	0.10	0.09	0.06	0.04	0.05	0.07	0.08
SiO_2	50.25	50.92	51.10	50.87	50.93	50.93	50.31	50.80	51.14	50.79	50.50
TiO_2	1.42	1.38	1.39	1.34	1.36	1.33	1.16	1.72	1.35	1.51	1.51
Al_2O_3	15.45	15.07	15.49	15.11	15.15	15.15	15.39	15.13	15.03	15.11	15.16
FeO*	9.42	10.04	9.88	9.81	9.82	9.85	9.18	9.95	9.72	9.80	9.76
MnO	0.16	0.18	0.16	0.19	0.16	0.17	0.18	0.17	0.17	0.19	0.20
MgO	8.37	8.46	7.81	8.46	8.08	8.36	9.78	7.87	8.17	8.31	8.37
CaO	12.10	11.49	11.75	11.63	11.66	11.71	11.92	11.27	11.58	11.53	11.71
Na_2O	2.48	2.36	2.37	2.33	2.36	2.39	1.99	2.92	2.52	2.47	2.47
K_2O	0.04	0.09	0.09	0.09	0.09	0.09	0.05	0.04	0.05	0.08	0.09
P_2O_5	0.13	0.13	0.13	0.13	0.14	0.13	0.11	0.15	0.12	0.15	0.16
sum	99.83	100.12	100.18	99.96	99.75	100.10	100.08	100.03	99.85	99.94	99.92
	standard deviation (1 σ)										
SiO_2	0.34	0.21	0.17	0.21	0.21	0.15	0.11	0.22	0.22	0.15	0.11
TiO_2	0.04	0.05	0.03	0.04	0.03	0.06	0.02	0.05	0.04	0.05	0.05
Al_2O_3	0.08	0.10	0.12	0.08	0.08	0.07	0.09	0.04	0.06	0.09	0.07
FeO*	0.20	0.21	0.26	0.23	0.15	0.13	0.18	0.04	0.12	0.12	0.20
MnO	0.02	0.03	0.02	0.01	0.04	0.05	0.02	0.03	0.03	0.03	0.03
MgO	0.06	0.09	0.39	0.04	0.21	0.06	0.06	0.08	0.06	0.06	0.07
CaO	0.09	0.08	0.14	0.21	0.15	0.10	0.13	0.11	0.09	0.09	0.09
Na_2O	0.05	0.07	0.07	0.07	0.07	0.07	0.05	0.05	0.04	0.06	0.03
K_2O	0.01	0.01	0.01	0.01	0.01	0.01	0.00	0.01	0.01	0.01	0.01
P_2O_5	0.02	0.01	0.03	0.01	0.01	0.02	0.01	0.02	0.02	0.02	0.01

sample	D91-d	D90	D89	D88-a	D88-b	D87-a	D87-b	D87-c	D87-d	D87-e	GC17
segment	N6	N6 (off-axis)		N8	N8	N8	N8	N8	N8	N8	N8
latitude (°S)	38.309	38.150	37.817	38.420	38.420	38.462	38.462	38.462	38.462	38.462	38.508
longitude (°W)	93.825	93.407	93.250	92.582	92.582	92.584	92.584	92.584	92.584	92.584	92.579
depth (m)	3824	2158	4430	3981	3981	3819	3819	3819	3819	3819	3785
# samples	2	1	1	3	4	4	1	1	1	3	1
# points	9	5	5	14	19	20	5	5	4	15	5
lava type	N-MORB	N-MORB	N-MORB	N-MORB	N-MORB	N-MORB	N-MORB	N-MORB	N-MORB	N-MORB	N-MORB
K/Ti	0.08	0.04	0.05	0.06	0.06	0.05	0.04	0.05	0.07	0.05	0.05
SiO_2	50.59	49.95	50.73	50.58	50.53	50.62	49.75	50.66	51.21	50.55	50.24
TiO_2	1.52	1.19	1.21	1.45	1.47	1.21	1.38	1.25	1.48	1.22	1.36
Al_2O_3	15.14	16.59	15.32	15.51	15.50	15.35	16.01	15.43	15.74	15.37	15.82
FeO*	9.78	8.32	9.01	9.29	9.34	9.15	8.97	9.11	8.84	9.13	8.99
MnO	0.20	0.13	0.18	0.19	0.17	0.19	0.19	0.16	0.19	0.19	0.15
MgO	8.35	9.09	8.86	8.33	8.38	8.89	8.64	8.93	8.35	8.89	8.74
CaO	11.48	11.92	12.38	11.79	11.84	12.22	11.87	12.30	11.58	12.27	11.81
Na_2O	2.49	2.66	2.10	2.67	2.63	2.19	2.74	2.14	2.79	2.13	2.58
K_2O	0.09	0.04	0.05	0.06	0.07	0.05	0.04	0.04	0.08	0.05	0.05
P_2O_5	0.15	0.09	0.11	0.13	0.13	0.11	0.11	0.10	0.14	0.10	0.13
sum	99.77	99.97	99.95	100.00	100.06	99.98	99.70	100.12	100.38	99.89	99.87
	standard deviation (1 σ)										
SiO_2	0.09	0.09	0.08	0.18	0.18	0.24	0.27	0.10	0.14	0.26	0.08
TiO_2	0.04	0.03	0.04	0.04	0.04	0.04	0.03	0.02	0.06	0.04	0.08
Al_2O_3	0.05	0.09	0.08	0.06	0.08	0.09	0.09	0.02	0.06	0.05	0.08
FeO*	0.13	0.04	0.06	0.16	0.12	0.15	0.13	0.07	0.14	0.10	0.06
MnO	0.03	0.05	0.03	0.03	0.03	0.03	0.02	0.03	0.04	0.04	0.03
MgO	0.06	0.03	0.04	0.07	0.05	0.06	0.06	0.04	0.05	0.07	0.05
CaO	0.09	0.12	0.08	0.12	0.08	0.12	0.07	0.07	0.10	0.12	0.10
Na_2O	0.03	0.12	0.09	0.06	0.06	0.05	0.05	0.04	0.09	0.03	0.03
K_2O	0.01	0.01	0.01	0.01	0.01	0.01	0.02	0.01	0.01	0.01	0.01
P_2O_5	0.01	0.02	0.02	0.01	0.02	0.02	0.02	0.02	0.03	0.02	0.02

(Table 3 continued)

sample	GC16	D86-a	D86-b	GC15	D85-a	D85-b	D85-c	D85-d	D85-e	GC14	GC13
segment	N8	N8	N8	N8	N8	N8	N8	N8	N8	N8	N8
latitude (°S)	38.591	38.657	38.657	38.712	38.769	38.769	38.769	38.769	38.769	38.844	38.892
longitude (°W)	92.576	92.577	92.577	92.563	92.560	92.560	92.560	92.560	92.560	92.553	92.548
depth (m)	3850	3518	3518	3542	3520	3520	3520	3520	3520	3689	3841
# samples	1	7	1	1	3	1	1	2	2	1	1
# points	5	14	5	5	12	4	4	10	6	4	5
lava type	N-MORB	N-MORB	N-MORB	N-MORB	N-MORB	N-MORB	N-MORB	N-MORB	N-MORB	T-MORB	N-MORB
K/Ti	0.06	0.04	0.05	0.07	0.06	0.05	0.05	0.05	0.04	0.20	0.07
SiO_2	50.93	50.14	50.65	50.65	51.36	50.90	51.21	51.03	51.14	50.15	51.03
TiO_2	1.27	1.36	1.24	1.34	1.59	1.43	1.44	1.36	1.39	1.48	1.55
Al_2O_3	14.80	16.09	15.18	15.46	15.04	14.81	15.05	15.46	15.36	15.74	14.91
FeO*	9.30	8.96	9.16	9.08	9.52	9.35	9.29	8.98	9.21	9.21	9.44
MnO	0.20	0.15	0.20	0.21	0.17	0.19	0.15	0.16	0.13	0.17	0.20
MgO	8.51	8.64	8.86	8.55	7.97	8.08	8.31	8.51	8.36	8.23	7.85
CaO	12.42	11.79	12.31	12.00	11.37	11.97	12.18	11.93	11.87	11.51	11.72
Na_2O	2.35	2.72	2.21	2.57	2.82	2.65	2.63	2.67	2.59	2.80	2.83
K_2O	0.05	0.04	0.04	0.07	0.07	0.05	0.05	0.05	0.04	0.21	0.07
P_2O_5	0.10	0.11	0.11	0.10	0.11	0.10	0.09	0.10	0.10	0.17	0.15
sum	99.92	100.01	99.96	100.05	100.02	99.53	100.41	100.26	100.19	99.68	99.74
	standard deviation (1 σ)										
SiO_2	0.12	0.23	0.29	0.20	0.11	0.51	0.07	0.36	0.24	0.15	0.24
TiO_2	0.05	0.05	0.03	0.03	0.05	0.02	0.02	0.05	0.05	0.02	0.03
Al_2O_3	0.12	0.11	0.08	0.05	0.08	0.15	0.10	0.29	0.11	0.05	0.04
FeO*	0.18	0.11	0.11	0.07	0.12	0.04	0.23	0.16	0.09	0.19	0.10
MnO	0.04	0.02	0.02	0.03	0.03	0.05	0.04	0.03	0.03	0.03	0.03
MgO	0.11	0.06	0.08	0.09	0.05	0.06	0.04	0.07	0.06	0.02	0.06
CaO	0.15	0.08	0.10	0.08	0.15	0.13	0.11	0.18	0.15	0.07	0.10
Na_2O	0.07	0.07	0.07	0.08	0.05	0.09	0.05	0.07	0.12	0.07	0.07
K_2O	0.01	0.01	0.01	0.01	0.01	0.01	0.02	0.01	0.01	0.01	0.01
P_2O_5	0.01	0.01	0.01	0.02	0.01	0.01	0.02	0.01	0.01	0.02	0.02

sample	D84	D83	D82-a	D82-b	D81-a	D81-b	D81-c	D80-a	D80-b	D80-c	D79
segment	N8	N8	N9a	N9a	N9a	N9a	N9a	N9a	N9a	N9a	N9a
latitude (°S)	38.936	38.977	38.982	38.982	39.023	39.023	39.023	39.046	39.046	39.046	39.094
longitude (°W)	92.540	92.540	91.575	91.575	91.565	91.565	91.565	91.579	91.579	91.579	91.577
depth (m)	3846	3823	3407	3407	3501	3501	3501	3578	3578	3578	3553
# samples	1	1	1	2	5	1	1	1	1	1	1
# points	4	5	3	7	21	5	5	5	5	5	5
lava type	N-MORB	N-MORB	N-MORB	N-MORB	N-MORB	N-MORB	N-MORB	T-MORB	T-MORB	T-MORB	N-MORB
K/Ti	0.04	0.06	0.08	0.08	0.07	0.07	0.08	0.16	0.16	0.16	0.08
SiO_2	50.37	50.79	51.05	50.88	50.88	50.75	50.87	50.62	50.59	50.51	50.99
TiO_2	1.18	1.23	1.48	1.43	1.72	1.71	1.72	1.23	1.20	1.19	1.53
Al_2O_3	16.36	15.39	15.51	15.70	15.15	15.17	14.91	16.24	16.28	16.29	15.29
FeO*	8.50	9.09	9.09	8.98	9.72	9.69	9.82	8.48	8.37	8.40	9.28
MnO	0.15	0.20	0.16	0.18	0.20	0.17	0.18	0.17	0.17	0.17	0.19
MgO	9.26	8.93	8.38	8.41	7.91	7.91	7.78	8.96	9.06	8.99	7.99
CaO	12.01	12.32	11.65	11.55	11.38	11.33	11.41	11.78	11.60	11.76	11.27
Na_2O	2.46	2.19	2.81	2.82	2.84	2.73	2.82	2.50	2.49	2.48	2.90
K_2O	0.04	0.05	0.09	0.08	0.09	0.08	0.09	0.14	0.14	0.14	0.08
P_2O_5	0.08	0.09	0.13	0.13	0.15	0.14	0.16	0.13	0.12	0.12	0.14
sum	100.41	100.29	100.36	100.17	100.02	99.69	99.76	100.25	100.01	100.06	99.67
	standard deviation (1 σ)										
SiO_2	0.31	0.10	0.20	0.18	0.11	0.11	0.15	0.14	0.23	0.18	0.20
TiO_2	0.04	0.03	0.03	0.02	0.04	0.03	0.04	0.02	0.03	0.04	0.07
Al_2O_3	0.07	0.11	0.05	0.09	0.10	0.09	0.12	0.06	0.06	0.08	0.05
FeO*	0.11	0.06	0.10	0.12	0.10	0.13	0.17	0.09	0.11	0.09	0.13
MnO	0.03	0.02	0.03	0.03	0.04	0.04	0.02	0.03	0.03	0.05	0.04
MgO	0.08	0.06	0.05	0.06	0.08	0.07	0.08	0.06	0.08	0.05	0.04
CaO	0.10	0.10	0.07	0.05	0.08	0.10	0.08	0.09	0.03	0.08	0.17
Na_2O	0.05	0.08	0.03	0.05	0.07	0.04	0.01	0.06	0.04	0.06	0.04
K_2O	0.01	0.00	0.01	0.01	0.01	0.01	0.01	0.00	0.01	0.01	0.01
P_2O_5	0.01	0.01	0.02	0.02	0.01	0.01	0.02	0.02	0.02	0.01	0.01

(Table 3 continued)

sample	D78-a	D78-b	D78-c	D77-a	D77-b	D77-c	D77-d	D77-e	D77-f	D77-g	D76
segment	N9a	N9a	N9a	N9a	N9a	N9a	N9a	N9a	N9a	N9a	N9a
latitude (°S)	39.133	39.133	39.133	39.177	39.177	39.177	39.177	39.177	39.177	39.177	39.203
longitude (°W)	91.578	91.578	91.578	91.568	91.568	91.568	91.568	91.568	91.568	91.568	91.564
depth (m)	3451	3451	3451	3339	3339	3339	3339	3339	3339	3339	3260
# samples	4	1	2	1	3	1	1	1	1	1	4
# points	18	5	10	5	15	4	5	4	4	5	16
lava type	N-MORB	N-MORB	N-MORB	N-MORB	N-MORB	N-MORB	N-MORB	N-MORB	N-MORB	N-MORB	N-MORB
K/Ti	0.07	0.08	0.07	0.07	0.07	0.08	0.07	0.07	0.07	0.06	0.09
SiO_2	50.30	50.32	50.25	50.87	50.86	50.55	50.48	50.43	50.38	50.84	50.46
TiO_2	1.75	1.78	1.73	1.95	1.96	1.71	1.82	1.73	1.84	1.44	1.10
Al_2O_3	15.29	15.39	15.41	14.79	14.83	15.50	15.34	15.38	15.20	15.28	16.52
FeO*	9.76	9.67	9.80	9.95	10.20	9.46	9.76	9.65	9.94	8.92	7.75
MnO	0.19	0.20	0.22	0.19	0.18	0.18	0.20	0.16	0.21	0.18	0.17
MgO	7.97	8.07	8.08	7.46	7.53	8.08	7.91	8.00	7.79	8.06	9.21
CaO	11.30	11.15	11.19	11.02	11.16	11.40	11.21	11.37	11.19	11.62	11.95
Na_2O	2.79	2.79	2.74	2.92	2.94	2.84	2.83	2.86	2.88	2.84	2.65
K_2O	0.09	0.10	0.09	0.10	0.10	0.09	0.10	0.09	0.10	0.06	0.07
P_2O_5	0.16	0.15	0.16	0.18	0.18	0.15	0.18	0.16	0.17	0.14	0.10
sum	99.62	99.61	99.66	99.45	99.94	99.97	99.84	99.84	99.71	99.38	99.96
	standard deviation (1 σ)										
SiO_2	0.22	0.12	0.28	0.24	0.17	0.12	0.11	0.17	0.33	0.18	0.19
TiO_2	0.05	0.03	0.03	0.02	0.06	0.03	0.03	0.05	0.05	0.03	0.04
Al_2O_3	0.07	0.10	0.09	0.09	0.08	0.02	0.07	0.07	0.13	0.07	0.09
FeO*	0.09	0.12	0.14	0.10	0.15	0.13	0.08	0.11	0.12	0.14	0.12
MnO	0.03	0.06	0.04	0.02	0.03	0.02	0.02	0.02	0.03	0.03	0.04
MgO	0.05	0.05	0.05	0.04	0.06	0.08	0.07	0.06	0.04	0.06	0.09
CaO	0.12	0.11	0.12	0.13	0.11	0.09	0.12	0.13	0.07	0.10	0.12
Na_2O	0.08	0.03	0.07	0.05	0.04	0.05	0.06	0.07	0.04	0.05	0.07
K_2O	0.01	0.01	0.01	0.00	0.01	0.01	0.01	0.01	0.02	0.01	0.01
P_2O_5	0.01	0.02	0.01	0.03	0.02	0.02	0.01	0.02	0.02	0.02	0.02

sample	D75-a	D75-b	GC12	D74-a	D74-b	D74-c	D73-a	D73-b	D73-c	D73-d	D73-e
segment	N9a	N9a	N9a	N9a	N9a	N9a	N9a	N9a	N9a	N9a	N9a
latitude (°S)	39.233	39.233	39.303	39.368	39.368	39.368	39.453	39.453	39.453	39.453	39.453
longitude (°W)	91.572	91.572	91.568	91.542	91.542	91.542	91.537	91.537	91.537	91.537	91.537
depth (m)	3109	3109	3377	3360	3360	3360	3426	3426	3426	3426	3426
# samples	4	4	1	2	1	2	1	1	1	1	1
# points	18	18	5	10	5	10	5	2	2	2	5
lava type	N-MORB	N-MORB	N-MORB	N-MORB	N-MORB	N-MORB	N-MORB	N-MORB	N-MORB	N-MORB	N-MORB
K/Ti	0.08	0.08	0.05	0.07	0.07	0.06	0.08	0.08	0.07	0.08	0.09
SiO_2	50.57	50.77	50.50	50.56	50.55	50.74	50.83	50.88	50.89	50.75	50.76
TiO_2	1.53	1.51	1.03	1.48	1.32	1.39	1.55	1.51	1.54	1.63	1.53
Al_2O_3	15.70	15.70	16.05	15.76	15.72	15.76	15.49	15.78	15.73	15.57	15.73
FeO*	8.99	8.89	8.28	9.14	8.95	9.03	9.20	9.44	9.15	9.39	9.14
MnO	0.18	0.18	0.15	0.19	0.20	0.18	0.17	0.17	0.19	0.20	0.16
MgO	8.42	8.32	9.39	8.56	8.68	8.55	8.01	8.21	8.17	8.17	8.17
CaO	11.55	11.55	12.22	11.51	11.75	11.64	11.51	11.34	11.32	11.30	11.34
Na_2O	2.86	2.87	2.30	2.79	2.71	2.77	2.91	2.95	2.87	2.90	2.94
K_2O	0.09	0.09	0.04	0.08	0.06	0.07	0.09	0.08	0.08	0.09	0.09
P_2O_5	0.14	0.15	0.08	0.13	0.13	0.10	0.13	0.14	0.13	0.17	0.17
sum	100.02	100.03	100.03	100.18	100.08	100.21	99.90	100.51	100.06	100.19	100.02
	standard deviation (1 σ)										
SiO_2	0.20	0.15	0.07	0.19	0.21	0.13	0.14	0.04	0.04	0.04	0.11
TiO_2	0.04	0.05	0.05	0.05	0.05	0.03	0.04	0.00	0.02	0.05	0.04
Al_2O_3	0.08	0.08	0.03	0.08	0.07	0.07	0.06	0.02	0.06	0.21	0.06
FeO*	0.16	0.15	0.09	0.10	0.16	0.16	0.12	0.06	0.24	0.16	0.10
MnO	0.03	0.03	0.02	0.04	0.02	0.04	0.03	0.06	0.03	0.02	0.02
MgO	0.06	0.07	0.02	0.04	0.05	0.04	0.05	0.09	0.02	0.07	0.05
CaO	0.11	0.11	0.10	0.07	0.16	0.09	0.14	0.06	0.03	0.02	0.04
Na_2O	0.05	0.05	0.05	0.07	0.09	0.06	0.09	0.04	0.00	0.04	0.05
K_2O	0.01	0.01	0.01	0.01	0.01	0.01	0.01	0.01	0.00	0.01	0.01
P_2O_5	0.02	0.01	0.02	0.02	0.02	0.05	0.01	0.01	0.01	0.02	0.02

(Table 3 continued)

sample	D73-f	D73-g	D73-h	GC11	D72-a	D72-b	D72-c	D71-a	D71-b	D71-c	D71-d
segment	N9a	N9a	N9a	N9a	N9a	N9a	N9a	N9a	N9a	N9a	N9a
latitude (^{o}S)	39.453	39.453	39.453	39.480	39.556	39.556	39.556	39.617	39.617	39.617	39.617
longitude (^{o}W)	91.537	91.537	91.537	91.533	91.511	91.511	91.511	91.512	91.512	91.512	91.512
depth (m)	3426	3426	3426	3353	3214	3214	3214	3243	3243	3243	3243
# samples	2	3	2	1	10	2	1	5	4	2	2
# points	10	12	9	4	50	10	5	25	20	10	10
lava type	N-MORB	N-MORB	N-MORB	N-MORB	N-MORB	N-MORB	N-MORB	N-MORB	N-MORB	N-MORB	N-MORB
K/Ti	0.08	0.09	0.08	0.06	0.07	0.06	0.08	0.07	0.06	0.06	0.06
SiO_2	50.72	50.62	50.72	50.70	50.80	51.07	50.87	51.22	51.09	51.12	50.91
TiO_2	1.62	1.62	1.55	1.44	1.67	1.67	1.54	1.78	1.79	1.77	1.75
Al_2O_3	15.63	15.60	15.66	15.34	14.90	14.96	15.68	14.86	15.02	15.02	15.07
FeO*	9.45	9.47	9.23	8.90	9.84	9.77	9.24	9.93	9.85	9.92	9.91
MnO	0.17	0.18	0.19	0.17	0.20	0.19	0.21	0.16	0.18	0.19	0.18
MgO	8.08	8.21	8.24	8.44	7.91	7.98	8.29	7.63	7.69	7.60	7.82
CaO	11.21	11.27	11.42	11.78	11.45	11.50	11.46	11.25	11.22	11.20	11.21
Na_2O	2.92	2.88	2.89	2.54	2.81	2.85	2.89	2.92	2.94	2.92	2.91
K_2O	0.10	0.11	0.09	0.06	0.08	0.07	0.09	0.09	0.08	0.07	0.08
P_2O_5	0.17	0.16	0.14	0.12	0.15	0.16	0.14	0.16	0.16	0.16	0.15
sum	100.06	100.12	100.13	99.50	99.80	100.23	100.42	100.01	100.02	99.97	100.01
	standard deviation (1 σ)										
SiO_2	0.21	0.22	0.20	0.24	0.39	0.16	0.20	0.17	0.15	0.15	0.18
TiO_2	0.05	0.03	0.05	0.05	0.04	0.03	0.03	0.05	0.04	0.03	0.05
Al_2O_3	0.10	0.09	0.06	0.05	0.09	0.09	0.06	0.08	0.06	0.08	0.06
FeO*	0.11	0.08	0.10	0.18	0.17	0.13	0.10	0.12	0.11	0.15	0.18
MnO	0.04	0.03	0.02	0.03	0.03	0.04	0.01	0.03	0.03	0.03	0.03
MgO	0.07	0.07	0.06	0.03	0.06	0.05	0.05	0.09	0.07	0.07	0.05
CaO	0.10	0.12	0.07	0.09	0.11	0.10	0.12	0.10	0.10	0.09	0.11
Na_2O	0.07	0.07	0.07	0.08	0.07	0.07	0.05	0.06	0.05	0.05	0.07
K_2O	0.01	0.01	0.01	0.01	0.01	0.01	0.01	0.01	0.01	0.01	0.01
P_2O_5	0.03	0.02	0.02	0.02	0.02	0.01	0.02	0.02	0.02	0.02	0.02

sample	D71-e	D71-f	D71-g	D71-h	D70-a	D70-b	D69-a	D69-b	D68-a	D68-b	D68-c
segment	N9a	N9a	N9a	N9a	N9a	N9a	N9a	N9a	N9a	N9a	N9a
latitude (^{o}S)	39.617	39.617	39.617	39.617	39.680	39.680	39.761	39.761	39.809	39.809	39.809
longitude (^{o}W)	91.512	91.512	91.512	91.512	91.497	91.497	91.500	91.500	91.476	91.476	91.476
depth (m)	3243	3243	3243	3243	3337	3337	3593	3593	3571	3571	3571
# samples	1	2	1	1	2	2	1	2	1	1	1
# points	5	10	5	5	10	15	5	10	5	5	5
lava type	N-MORB	N-MORB	N-MORB	N-MORB	N-MORB	N-MORB	N-MORB	N-MORB	N-MORB	N-MORB	N-MORB
K/Ti	0.07	0.06	0.06	0.06	0.06	0.06	0.06	0.05	0.07	0.07	0.07
SiO_2	50.91	51.00	51.16	50.92	50.85	51.11	51.47	50.08	50.69	50.79	50.89
TiO_2	1.79	1.78	1.85	1.77	1.43	1.58	1.64	1.01	1.60	1.64	1.50
Al_2O_3	15.03	15.08	14.81	14.93	15.46	14.87	14.38	16.67	15.22	15.13	15.17
FeO*	10.09	9.88	10.10	9.90	9.29	9.86	10.06	8.02	9.42	9.42	9.34
MnO	0.15	0.18	0.19	0.19	0.17	0.17	0.17	0.15	0.14	0.16	0.17
MgO	7.68	7.76	7.56	7.72	8.39	7.96	7.39	9.40	7.97	7.93	7.98
CaO	11.26	11.12	11.28	11.04	11.87	11.68	11.77	12.28	11.62	11.60	11.89
Na_2O	2.89	2.95	2.92	2.88	2.56	2.71	3.00	2.34	2.87	2.83	2.78
K_2O	0.09	0.08	0.08	0.08	0.06	0.07	0.07	0.03	0.08	0.08	0.08
P_2O_5	0.15	0.17	0.17	0.15	0.12	0.14	0.15	0.09	0.14	0.13	0.14
sum	100.04	99.98	100.12	99.59	100.21	100.14	100.09	100.08	99.74	99.73	99.93
	standard deviation (1 σ)										
SiO_2	0.09	0.15	0.14	0.14	0.20	0.14	0.13	0.17	0.07	0.08	0.18
TiO_2	0.05	0.05	0.06	0.02	0.03	0.03	0.06	0.05	0.02	0.04	0.05
Al_2O_3	0.05	0.09	0.06	0.08	0.07	0.06	0.08	0.07	0.05	0.06	0.04
FeO*	0.10	0.10	0.15	0.13	0.18	0.10	0.08	0.06	0.08	0.13	0.13
MnO	0.04	0.04	0.02	0.02	0.03	0.03	0.03	0.03	0.04	0.03	0.03
MgO	0.04	0.07	0.08	0.03	0.06	0.07	0.07	0.03	0.10	0.06	0.05
CaO	0.11	0.11	0.05	0.05	0.09	0.13	0.20	0.13	0.09	0.15	0.08
Na_2O	0.15	0.08	0.06	0.04	0.04	0.06	0.07	0.09	0.08	0.03	0.06
K_2O	0.01	0.01	0.01	0.01	0.01	0.01	0.01	0.01	0.01	0.01	0.01
P_2O_5	0.02	0.01	0.01	0.01	0.02	0.02	0.02	0.01	0.01	0.02	0.01

(Table 3 continued)

sample	D67-a	D67-b	D67-c	GC10	GC9	GC8	D66	D65-a	D65-b	D65-c	D65-d
segment	N9a	N9a	N9a	N9a	N9a	N9a	N9a	N9b	N9b	N9b	N9b
latitude (°S)	39.860	39.860	39.860	39.848	39.882	39.882	39.906	39.964	39.964	39.964	39.964
longitude (°W)	91.492	91.492	91.492	91.467	91.468	91.497	91.502	91.589	91.589	91.589	91.589
depth (m)	3627	3627	3627	3551	3678	3584	3637	3787	3787	3787	3787
# samples	2	10	4	1	1	1	5	1	3	4	1
# points	10	46	20	5	5	5	25	5	15	20	5
lava type	N-MORB	N-MORB	N-MORB	N-MORB	N-MORB	N-MORB	N-MORB	N-MORB	N-MORB	N-MORB	N-MORB
K/Ti	0.06	0.06	0.06	0.07	0.08	0.06	0.07	0.09	0.09	0.09	0.09
SiO_2	50.40	50.40	50.14	50.53	50.54	50.30	50.73	50.58	50.57	50.39	50.60
TiO_2	1.63	1.63	1.65	1.35	1.90	1.41	1.73	1.86	1.80	1.79	1.79
Al_2O_3	15.68	15.58	15.49	15.74	15.42	15.61	14.65	15.04	15.23	15.23	15.22
FeO*	9.74	9.68	9.67	9.00	9.62	9.26	9.89	9.85	9.78	9.77	9.92
MnO	0.18	0.17	0.19	0.17	0.19	0.18	0.18	0.18	0.20	0.20	0.17
MgO	8.38	8.32	8.24	8.59	8.04	8.73	7.55	7.64	7.81	7.96	7.87
CaO	11.40	11.43	11.41	11.83	11.07	11.88	11.59	11.08	10.98	10.92	10.92
Na_2O	2.65	2.68	2.64	2.59	2.85	2.41	2.85	2.94	2.97	2.95	2.94
K_2O	0.07	0.07	0.07	0.07	0.11	0.06	0.08	0.13	0.11	0.12	0.12
P_2O_5	0.14	0.14	0.14	0.11	0.18	0.12	0.15	0.17	0.18	0.18	0.18
sum	100.27	100.09	99.64	99.98	99.92	99.97	99.41	99.47	99.62	99.50	99.72
	standard deviation (1 σ)										
SiO_2	0.21	0.22	0.19	0.11	0.09	0.17	0.28	0.17	0.23	0.19	0.23
TiO_2	0.06	0.05	0.04	0.02	0.07	0.02	0.04	0.05	0.05	0.04	0.06
Al_2O_3	0.07	0.09	0.07	0.08	0.07	0.07	0.10	0.09	0.06	0.09	0.05
FeO*	0.12	0.13	0.10	0.22	0.14	0.18	0.14	0.09	0.14	0.14	0.19
MnO	0.02	0.03	0.03	0.02	0.03	0.01	0.03	0.05	0.04	0.02	0.02
MgO	0.07	0.08	0.08	0.07	0.05	0.07	0.06	0.06	0.04	0.08	0.05
CaO	0.09	0.13	0.10	0.09	0.11	0.12	0.09	0.10	0.08	0.13	0.06
Na_2O	0.04	0.06	0.07	0.06	0.04	0.07	0.06	0.08	0.03	0.07	0.06
K_2O	0.01	0.01	0.01	0.01	0.01	0.01	0.01	0.01	0.01	0.01	0.01
P_2O_5	0.02	0.02	0.02	0.01	0.02	0.01	0.02	0.02	0.02	0.02	0.02

sample	D65-e	D65-f	D65-g	D64-a	D64-b	D64-c	D63-a	D63-b	D63-c	D63-d	D63-e
segment	N9b	N9b	N9b	N9b	N9b	N9b	N9b	N9b	N9b	N9b	N9b
latitude (°S)	39.964	39.964	39.964	40.029	40.029	40.029	40.092	40.092	40.092	40.092	40.092
longitude (°W)	91.589	91.589	91.589	91.584	91.584	91.584	91.578	91.578	91.578	91.578	91.578
depth (m)	3787	3787	3787	3752	3752	3752	3704	3704	3704	3704	3704
# samples	1	1	2	4	1	3	4	1	1	1	1
# points	5	5	10	18	4	15	10	2	4	4	5
lava type	N-MORB	N-MORB	N-MORB	N-MORB	N-MORB	N-MORB	N-MORB	N-MORB	N-MORB	N-MORB	N-MORB
K/Ti	0.09	0.08	0.08	0.08	0.08	0.08	0.08	0.08	0.09	0.08	0.09
SiO_2	50.48	50.52	50.40	50.63	50.51	50.58	50.83	51.17	50.83	50.93	50.84
TiO_2	1.86	1.79	1.87	1.36	1.32	1.31	1.47	1.39	1.45	1.43	1.39
Al_2O_3	15.22	15.24	15.17	15.54	15.70	15.65	15.11	15.20	15.08	15.05	15.23
FeO*	9.98	9.87	10.07	9.02	8.84	8.88	9.12	9.26	9.23	9.09	9.12
MnO	0.15	0.16	0.17	0.16	0.15	0.17	0.17	0.21	0.18	0.16	0.18
MgO	7.60	7.92	7.77	8.52	8.56	8.49	8.24	8.26	8.33	8.08	8.27
CaO	10.92	10.98	10.85	11.81	11.87	11.87	11.72	11.58	11.69	11.84	11.63
Na_2O	3.05	3.06	3.02	2.44	2.38	2.39	2.58	2.54	2.54	2.55	2.61
K_2O	0.12	0.11	0.11	0.08	0.08	0.07	0.09	0.08	0.09	0.09	0.09
P_2O_5	0.21	0.20	0.18	0.13	0.14	0.11	0.14	0.10	0.15	0.14	0.14
sum	99.58	99.84	99.63	99.70	99.55	99.52	99.46	99.79	99.57	99.37	99.48
	standard deviation (1 σ)										
SiO_2	0.17	0.18	0.15	0.15	0.07	0.15	0.25	0.30	0.09	0.12	0.14
TiO_2	0.04	0.06	0.05	0.05	0.07	0.04	0.05	0.00	0.05	0.05	0.06
Al_2O_3	0.14	0.09	0.10	0.07	0.08	0.07	0.11	0.11	0.21	0.08	0.02
FeO*	0.15	0.13	0.07	0.12	0.12	0.16	0.17	0.07	0.29	0.03	0.09
MnO	0.05	0.03	0.02	0.03	0.02	0.03	0.02	0.01	0.03	0.01	0.02
MgO	0.08	0.05	0.05	0.08	0.09	0.10	0.06	0.12	0.15	0.02	0.08
CaO	0.12	0.11	0.15	0.09	0.08	0.11	0.06	0.00	0.05	0.14	0.11
Na_2O	0.08	0.12	0.07	0.05	0.03	0.05	0.06	0.01	0.06	0.03	0.03
K_2O	0.00	0.02	0.01	0.01	0.01	0.01	0.01	0.01	0.02	0.01	0.02
P_2O_5	0.02	0.02	0.02	0.02	0.02	0.02	0.01	0.00	0.02	0.02	0.01

(Table 3 continued)

sample	D62	D61-a	D61-b	D61-c	D60-a	D60-b	D59-a	D59-b	D59-c	D58-a	D58-b
segment	N9b	N9b	N9b	N9b	N9b	N9b	N10	N10	N10	N10	N10
latitude (°S)	40.135	40.185	40.185	40.185	40.223	40.223	40.276	40.276	40.276	40.310	40.310
longitude (°W)	91.580	91.566	91.566	91.566	91.578	91.578	91.888	91.888	91.888	91.889	91.889
depth (m)	3681	3651	3651	3651	3714	3714	3590	3590	3590	3672	3672
# samples	3	3	2	1	2	4	1	3	1	2	1
# points	6	15	9	1	11	17	4	15	5	10	5
lava type	N-MORB	N-MORB	N-MORB	N-MORB	N-MORB	N-MORB	N-MORB	N-MORB	N-MORB	N-MORB	N-MORB
K/Ti	0.07	0.07	0.07	0.06	0.09	0.08	0.07	0.06	0.05	0.07	0.06
SiO_2	50.48	50.83	50.79	50.83	50.62	50.78	49.80	49.72	50.32	50.49	50.92
TiO_2	1.51	1.51	1.46	1.67	1.53	1.93	1.25	1.22	1.69	1.49	1.20
Al_2O_3	15.14	15.35	15.51	15.08	15.27	14.88	16.20	16.36	15.23	15.18	15.17
FeO*	9.31	9.16	9.00	9.28	9.26	9.83	9.12	9.02	9.85	9.77	9.22
MnO	0.15	0.16	0.16	0.16	0.16	0.18	0.18	0.19	0.19	0.16	0.17
MgO	8.10	8.04	8.22	8.06	7.88	7.29	8.79	8.90	7.89	8.27	8.53
CaO	11.79	11.55	11.60	11.64	11.45	10.94	11.77	11.87	11.22	11.70	12.48
Na_2O	2.62	2.77	2.72	2.71	2.86	3.13	2.59	2.58	2.90	2.60	2.27
K_2O	0.08	0.08	0.08	0.07	0.10	0.12	0.06	0.06	0.06	0.08	0.05
P_2O_5	0.14	0.15	0.13	0.12	0.16	0.21	0.12	0.11	0.15	0.15	0.11
sum	99.32	99.61	99.66	99.63	99.30	99.28	99.90	100.03	99.50	99.87	100.13
	standard deviation (1 σ)										
SiO_2	0.34	0.15	0.17	N/A	0.16	0.15	0.19	0.13	0.19	0.13	0.15
TiO_2	0.04	0.06	0.05	N/A	0.04	0.05	0.04	0.04	0.02	0.03	0.04
Al_2O_3	0.08	0.10	0.08	N/A	0.15	0.10	0.04	0.08	0.08	0.11	0.04
FeO*	0.09	0.17	0.19	N/A	0.14	0.14	0.14	0.12	0.07	0.13	0.17
MnO	0.02	0.03	0.02	N/A	0.02	0.02	0.02	0.03	0.03	0.04	0.04
MgO	0.05	0.09	0.08	N/A	0.07	0.04	0.07	0.04	0.05	0.05	0.05
CaO	0.14	0.11	0.14	N/A	0.07	0.09	0.09	0.13	0.13	0.06	0.05
Na_2O	0.06	0.06	0.07	N/A	0.09	0.07	0.06	0.10	0.08	0.04	0.04
K_2O	0.01	0.01	0.01	N/A	0.01	0.01	0.01	0.01	0.01	0.01	0.02
P_2O_5	0.02	0.02	0.01	N/A	0.02	0.02	0.02	0.02	0.01	0.01	0.01

sample	D58-c	D57	D56-a	D56-b	D56-c	D56-d	D55-a	D55-b	D54	GC7	GC6
segment	N10	N10	N10	N10	N10	N10	N10	N10	N10	N10	N10
latitude (°S)	40.310	40.358	40.393	40.393	40.393	40.393	40.459	40.459	40.540	40.562	40.617
longitude (°W)	91.889	91.877	91.885	91.885	91.885	91.885	91.904	91.904	91.882	91.884	91.873
depth (m)	3672	3674	3613	3613	3613	3613	3569	3569	3566	3606	3293
# samples	2	6	6	1	4	1	1	1	5	1	1
# points	9	29	30	5	20	4	5	5	25	4	5
lava type	N-MORB	N-MORB	N-MORB	N-MORB	N-MORB	N-MORB	N-MORB	N-MORB	N-MORB	N-MORB	N-MORB
K/Ti	0.06	0.07	0.06	0.07	0.06	0.07	0.04	0.04	0.07	0.07	0.07
SiO_2	50.80	50.76	50.69	50.75	50.79	51.04	50.32	50.14	49.98	50.56	50.93
TiO_2	1.20	1.54	1.32	1.34	1.30	1.37	1.07	1.03	1.13	1.56	1.52
Al_2O_3	15.24	14.98	15.20	14.84	15.13	14.81	15.78	15.98	16.43	15.34	15.07
FeO*	9.11	9.94	9.33	9.60	9.34	9.55	8.80	8.64	8.63	9.66	9.43
MnO	0.17	0.17	0.17	0.17	0.17	0.19	0.20	0.17	0.16	0.18	0.17
MgO	8.68	7.98	8.36	8.26	8.40	8.18	8.89	9.12	9.43	8.12	7.92
CaO	12.36	11.66	12.12	12.20	12.18	12.18	12.54	12.48	12.18	11.64	11.65
Na_2O	2.32	2.72	2.40	2.38	2.42	2.40	2.29	2.24	2.25	2.67	2.71
K_2O	0.05	0.08	0.06	0.07	0.06	0.07	0.03	0.03	0.06	0.08	0.08
P_2O_5	0.10	0.14	0.11	0.10	0.12	0.12	0.10	0.08	0.09	0.12	0.12
sum	100.03	99.97	99.75	99.71	99.92	99.91	100.01	99.91	100.34	99.92	99.60
	standard deviation (1 σ)										
SiO_2	0.17	0.17	0.22	0.14	0.17	0.19	0.19	0.23	0.22	0.13	0.11
TiO_2	0.05	0.03	0.04	0.02	0.04	0.05	0.03	0.05	0.04	0.04	0.01
Al_2O_3	0.07	0.09	0.16	0.11	0.05	0.05	0.09	0.11	0.12	0.51	0.11
FeO*	0.15	0.15	0.17	0.18	0.09	0.16	0.14	0.25	0.11	0.41	0.13
MnO	0.03	0.02	0.04	0.03	0.03	0.02	0.04	0.01	0.03	0.02	0.02
MgO	0.07	0.06	0.08	0.10	0.07	0.08	0.03	0.05	0.09	0.05	0.03
CaO	0.07	0.12	0.14	0.15	0.12	0.04	0.09	0.09	0.09	0.05	0.11
Na_2O	0.04	0.07	0.07	0.03	0.06	0.06	0.01	0.04	0.05	0.07	0.02
K_2O	0.01	0.01	0.01	0.01	0.01	0.01	0.01	0.01	0.01	0.01	0.01
P_2O_5	0.02	0.02	0.02	0.02	0.02	0.02	0.01	0.01	0.02	0.02	0.02

(Table 3 continued)

sample	D53	GC5	D52	D51-a	D51-b	D51-c	D50	D49-a	D49-b	D49-c	D48-a
segment	N10	N10	N10	N10	N10	N10	N10	N10	N10	N10	N10
latitude (^{o}S)	40.671	40.730	40.798	40.848	40.848	40.848	40.900	40.949	40.949	40.949	41.006
longitude (^{o}W)	91.877	91.858	91.859	91.849	91.849	91.849	91.850	91.850	91.850	91.850	91.871
depth (m)	3391	3345	3770	3822	3822	3822	3916	3952	3952	3952	3809
# samples	10	1	4	3	7	1	5	3	1	7	4
# points	51	5	19	15	34	6	23	15	5	35	19
lava type	N-MORB	N-MORB	N-MORB	N-MORB	N-MORB	N-MORB	N-MORB	N-MORB	N-MORB	N-MORB	N-MORB
K/Ti	0.06	0.07	0.03	0.07	0.06	0.07	0.06	0.07	0.07	0.07	0.10
SiO_2	50.62	50.56	49.42	50.79	50.96	50.91	50.86	50.74	50.55	50.48	50.28
TiO_2	1.12	1.38	0.76	1.44	1.47	1.48	1.52	1.61	1.59	1.58	1.34
Al_2O_3	15.95	15.52	17.28	15.10	15.10	15.13	14.34	15.20	15.20	15.17	15.94
FeO*	8.60	9.62	7.93	9.70	9.77	9.72	10.63	10.01	10.16	9.98	8.97
MnO	0.16	0.15	0.16	0.18	0.19	0.17	0.19	0.21	0.21	0.19	0.17
MgO	8.84	8.40	10.31	8.08	8.13	8.16	7.71	8.05	8.25	8.16	8.68
CaO	12.42	11.70	12.52	11.76	11.74	11.79	11.91	11.16	11.13	11.22	11.72
Na_2O	2.50	2.54	1.98	2.47	2.48	2.47	2.40	2.72	2.75	2.72	2.52
K_2O	0.05	0.07	0.02	0.07	0.07	0.07	0.06	0.08	0.08	0.08	0.10
P_2O_5	0.09	0.13	0.06	0.12	0.13	0.12	0.14	0.15	0.14	0.15	0.13
sum	100.34	100.07	100.44	99.71	100.04	100.01	99.76	99.93	100.07	99.75	99.86
	standard deviation (1 σ)										
SiO_2	0.18	0.17	0.21	0.20	0.16	0.11	0.18	0.16	0.08	0.28	0.22
TiO_2	0.04	0.03	0.03	0.04	0.04	0.02	0.04	0.03	0.06	0.04	0.04
Al_2O_3	0.13	0.11	0.07	0.09	0.08	0.10	0.07	0.10	0.10	0.08	0.11
FeO*	0.14	0.13	0.15	0.11	0.11	0.17	0.18	0.20	0.07	0.11	0.13
MnO	0.03	0.04	0.03	0.02	0.03	0.02	0.03	0.04	0.02	0.03	0.03
MgO	0.10	0.04	0.07	0.08	0.05	0.07	0.05	0.14	0.04	0.07	0.05
CaO	0.10	0.13	0.12	0.09	0.12	0.05	0.13	0.12	0.14	0.11	0.11
Na_2O	0.06	0.04	0.05	0.04	0.07	0.07	0.06	0.06	0.10	0.08	0.06
K_2O	0.01	0.01	0.01	0.01	0.01	0.01	0.01	0.01	0.01	0.01	0.01
P_2O_5	0.02	0.01	0.02	0.02	0.02	0.02	0.02	0.02	0.02	0.02	0.01

sample	D48-b	D48-c	D48-d	D48-e	D47-a	D47-b
segment	N10	N10	N10	N10	N10	N10
latitude (^{o}S)	41.006	41.006	41.006	41.006	41.053	41.053
longitude (^{o}W)	91.871	91.871	91.871	91.871	91.854	91.854
depth (m)	3809	3809	3809	3809	4313	4313
# samples	1	1	1	1	2	1
# points	5	5	5	5	10	5
lava type	N-MORB	N-MORB	N-MORB	N-MORB	N-MORB	N-MORB
K/Ti	0.10	0.10	0.09	0.10	0.07	0.08
SiO_2	49.86	50.45	50.35	49.69	49.90	50.05
TiO_2	1.32	1.37	1.39	1.35	1.32	1.27
Al_2O_3	15.83	16.01	16.02	15.81	15.99	16.00
FeO*	8.63	9.12	9.00	8.74	9.34	9.27
MnO	0.20	0.16	0.13	0.18	0.20	0.17
MgO	8.71	8.73	8.77	8.61	8.69	8.76
CaO	11.52	11.79	11.72	11.38	11.73	11.48
Na_2O	2.52	2.48	2.58	2.51	2.47	2.52
K_2O	0.10	0.10	0.10	0.10	0.07	0.07
P_2O_5	0.13	0.11	0.13	0.13	0.12	0.11
sum	98.81	100.32	100.19	98.49	99.82	99.70
	standard deviation (1 σ)					
SiO_2	0.16	0.08	0.14	0.16	0.10	0.17
TiO_2	0.03	0.02	0.03	0.03	0.03	0.03
Al_2O_3	0.04	0.08	0.07	0.11	0.10	0.09
FeO*	0.10	0.18	0.23	0.09	0.13	0.10
MnO	0.04	0.05	0.03	0.04	0.03	0.04
MgO	0.05	0.03	0.03	0.06	0.04	0.13
CaO	0.13	0.11	0.08	0.12	0.09	0.10
Na_2O	0.05	0.09	0.02	0.03	0.10	0.09
K_2O	0.01	0.01	0.01	0.01	0.01	0.01
P_2O_5	0.02	0.02	0.02	0.01	0.01	0.02

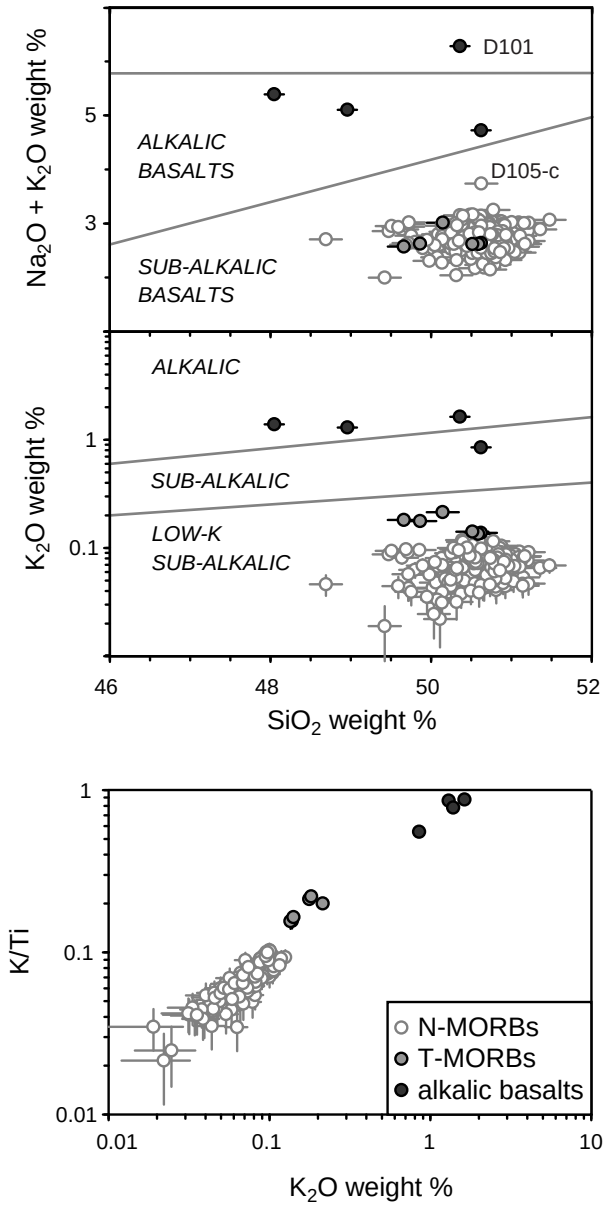

Figure 5: Petrologic classification of lavas recovered from the Northern Chile Ridge, based on alkali content and K/Ti. Classifications after *Middlemost* (1975) and *Cox et al.* (1979).

Major element compositions of sample bins from the Valdivia Fracture Zone intra-transform spreading centers and Southern Chile Ridge segments S5-S7 are given in Table 4. These samples are all MORBs (Figure 6). Valdivia Fracture Zone samples fall into N-MORB and T-MORB groups based on their K_2O and K/Ti contents, while Southern Chile Ridge samples fall into N-MORB and E-MORB groups. The same value of K/Ti that *Sherman et al.* (1997) found for the N-MORB/E-MORB boundary at Southern Chile Ridge segments S1-S4 is also a clear boundary for segments S5-S7 sampled in this study. However, the Southern Chile Ridge N-MORBs span a range of K/Ti that would include the T-MORBs of the Valdivia Fracture Zone and the Northern Chile Ridge. Southern Chile Ridge samples D24-d and D24-e have SiO_2 contents greater than 52.0 weight % and are therefore classified as basaltic andesites. These two samples are from the northernmost dredge site on Southern Chile Ridge segment S7, proximal to the Valdivia Fracture Zone. This dredge site also yielded N-MORBs.

The Northern Chile Ridge samples are primitive to moderately evolved. The N-MORBs are very primitive to moderate (mean and 1σ standard deviation MgO = 8.3 ± 0.5 weight %). N-MORB sample D105-c has higher Na_2O than the others because it is more evolved (MgO = 6.4 weight %). The T-MORBs are in general more primitive (MgO = 8.2-9.2 weight %), and the alkalic basalts are more evolved (MgO = 4.9-7.5 weight %).

The MORB lavas at the Northern Chile Ridge show coherent trends in major element compositions (Figure 7). As MgO content in these samples decreases, Al_2O_3 and CaO contents decrease, and SiO_2, FeO*, TiO_2, Na_2O, and K_2O increase. The major element

Table 4: Major Element Compositions from the Valdivia Fracture Zone ITSCs and the Southern Chile Ridge

sample	D46	D45-a	D45-b	D44	D43	D42	D40-a	D40-b	D40-c	D40-d
segment	V1	V1	V1	V1	V2	V2	V2	V2	V2	V2
latitude (°S)	41.099	41.137	41.137	41.179	41.256	41.212	41.221	41.221	41.221	41.221
longitude (°W)	91.273	91.270	91.270	91.263	90.340	90.355	90.333	90.333	90.333	90.333
depth (m)	3949	3914	3914	3941	4250	4342	4282	4282	4282	4282
# samples	1	1	7	5	1	4	4	1	1	1
# points	5	3	21	15	5	14	13	2	3	3
lava type	N-MORB	N-MORB	N-MORB	N-MORB	T-MORB	N-MORB	T-MORB	T-MORB	T-MORB	T-MORB
K/Ti	0.08	0.07	0.08	0.09	0.25	0.10	0.27	0.20	0.21	0.20
SiO_2	50.07	50.12	50.26	50.24	50.67	50.29	50.22	50.62	50.54	50.69
TiO_2	2.01	1.74	1.95	2.31	1.67	1.66	1.53	1.62	1.77	1.77
Al_2O_3	15.25	15.89	15.55	14.71	16.12	15.58	16.24	16.94	15.71	15.65
FeO*	9.88	9.24	9.69	10.94	8.60	9.65	8.53	8.53	9.24	9.12
MnO	0.19	0.22	0.20	0.23	0.15	0.19	0.15	0.14	0.15	0.13
MgO	7.41	7.92	7.46	6.78	7.69	7.58	7.91	6.70	7.28	7.23
CaO	10.75	11.00	10.78	10.38	10.75	11.27	10.99	11.15	10.97	10.87
Na_2O	3.42	3.43	3.59	3.46	3.09	3.09	3.17	3.42	3.44	3.36
K_2O	0.12	0.09	0.11	0.14	0.30	0.12	0.29	0.24	0.26	0.26
P_2O_5	0.21	0.17	0.21	0.23	0.23	0.17	0.19	0.22	0.19	0.19
sum	99.31	99.81	99.79	99.42	99.27	99.62	99.23	99.58	99.54	99.28
	standard deviation (1 σ)									
SiO_2	0.31	0.22	0.25	0.19	0.11	0.20	0.17	0.14	0.32	0.05
TiO_2	0.09	0.01	0.06	0.06	0.03	0.05	0.05	0.12	0.04	0.04
Al_2O_3	0.05	0.03	0.07	0.07	0.04	0.08	0.09	1.62	0.15	0.04
FeO*	0.11	0.11	0.14	0.16	0.10	0.09	0.11	1.07	0.16	0.20
MnO	0.03	0.02	0.03	0.04	0.03	0.04	0.02	0.05	0.02	0.01
MgO	0.07	0.01	0.08	0.04	0.03	0.05	0.06	0.83	0.06	0.05
CaO	0.09	0.05	0.09	0.11	0.08	0.10	0.10	0.31	0.03	0.12
Na_2O	0.03	0.07	0.06	0.05	0.06	0.07	0.08	0.01	0.11	0.00
K_2O	0.01	0.02	0.01	0.01	0.01	0.01	0.01	0.03	0.01	0.01
P_2O_5	0.02	0.01	0.01	0.02	0.02	0.02	0.02	0.02	0.02	0.00

sample	D39-a	D39-b	D39-c	D39-d	D38-a	D38-b	D38-c	D38-d	D38-e	D38-f
segment	V3	V3	V3	V3	V3	V3	V3	V3	V3	V3
latitude (°S)	41.280	41.280	41.280	41.280	41.315	41.315	41.315	41.315	41.315	41.315
longitude (°W)	89.085	89.085	89.085	89.085	89.060	89.060	89.060	89.060	89.060	89.060
depth (m)	3520	3520	3520	3520	3827	3827	3827	3827	3827	3827
# samples	2	2	3	3	5	1	1	2	1	3
# points	8	6	10	10	15	2	3	4	3	10
lava type	T-MORB	T-MORB	T-MORB	T-MORB	N-MORB	N-MORB	N-MORB	N-MORB	N-MORB	N-MORB
K/Ti	0.16	0.16	0.15	0.16	0.09	0.09	0.09	0.08	0.09	0.09
SiO_2	51.00	50.84	50.40	50.40	50.20	50.59	50.64	50.41	50.62	50.64
TiO_2	1.77	1.81	1.81	1.83	1.38	1.52	1.55	1.63	1.53	1.56
Al_2O_3	15.52	15.77	15.63	15.56	16.29	15.96	16.06	15.44	15.94	16.00
FeO*	9.33	9.37	9.28	9.25	8.60	9.09	9.14	9.23	8.93	9.04
MnO	0.20	0.21	0.17	0.18	0.18	0.18	0.20	0.16	0.21	0.19
MgO	8.24	8.18	8.29	8.24	8.16	7.92	7.96	7.59	7.92	7.91
CaO	10.45	10.30	10.55	10.46	11.43	11.26	11.44	11.36	11.45	11.37
Na_2O	3.22	3.31	3.25	3.27	3.20	3.22	3.24	3.25	3.27	3.19
K_2O	0.20	0.20	0.20	0.21	0.09	0.10	0.10	0.10	0.10	0.10
P_2O_5	0.23	0.23	0.23	0.22	0.14	0.15	0.15	0.17	0.16	0.15
sum	100.15	100.22	99.82	99.62	99.66	99.99	100.47	99.34	100.14	100.14
	standard deviation (1 σ)									
SiO_2	0.13	0.14	0.19	0.17	0.19	0.09	0.34	0.50	0.01	0.16
TiO_2	0.02	0.03	0.05	0.05	0.03	0.01	0.09	0.05	0.02	0.04
Al_2O_3	0.08	0.26	0.14	0.16	0.10	0.05	0.13	0.12	0.10	0.11
FeO*	0.16	0.19	0.14	0.15	0.13	0.01	0.24	0.17	0.04	0.14
MnO	0.05	0.02	0.03	0.04	0.03	0.03	0.02	0.04	0.03	0.02
MgO	0.05	0.26	0.17	0.12	0.03	0.00	0.08	0.08	0.09	0.09
CaO	0.12	0.24	0.23	0.09	0.11	0.04	0.03	0.06	0.20	0.10
Na_2O	0.07	0.15	0.08	0.07	0.07	0.04	0.01	0.08	0.10	0.10
K_2O	0.00	0.01	0.01	0.01	0.01	0.01	0.00	0.01	0.01	0.01
P_2O_5	0.02	0.02	0.02	0.02	0.02	0.04	0.02	0.02	0.01	0.01

(Table 4 continued)

sample	D37-a	D37-b	D37-c	D37-d	D37-e	D37-f	D36	D35-a	D35-b	D35-c
segment	V3	V3	V3	V3	V3	V3	V4	V4	V4	V4
latitude (^{o}S)	41.349	41.349	41.349	41.349	41.349	41.349	41.292	41.371	41.371	41.371
longitude (^{o}W)	89.055	89.055	89.055	89.055	89.055	89.055	87.746	87.707	87.707	87.707
depth (m)	3887	3887	3887	3887	3887	3887	3970	4140	4140	4140
# samples	4	1	2	1	1	2	3	5	2	1
# points	12	3	6	3	3	6	9	15	6	5
lava type	N-MORB	N-MORB	N-MORB	N-MORB	N-MORB	N-MORB	T-MORB	N-MORB	N-MORB	N-MORB
K/Ti	0.05	0.08	0.04	0.04	0.06	0.06	0.24	0.10	0.10	0.10
SiO_2	49.32	50.94	49.33	49.29	49.33	50.12	50.31	50.77	50.64	50.68
TiO_2	1.37	1.56	1.36	1.32	1.30	1.72	1.62	1.56	1.58	1.52
Al_2O_3	17.36	15.49	17.53	17.52	17.49	15.75	16.73	15.81	15.83	15.71
FeO*	8.33	9.54	8.27	8.33	8.25	9.32	8.57	9.04	8.93	9.03
MnO	0.16	0.20	0.15	0.15	0.17	0.21	0.17	0.17	0.17	0.18
MgO	8.37	7.79	8.40	8.34	8.34	7.17	7.72	8.10	8.08	8.06
CaO	11.34	11.20	11.30	11.39	11.29	11.29	10.69	10.92	11.00	11.02
Na_2O	3.62	3.15	3.60	3.56	3.59	3.88	3.64	3.34	3.27	3.30
K_2O	0.05	0.10	0.04	0.04	0.06	0.08	0.28	0.11	0.11	0.11
P_2O_5	0.15	0.17	0.17	0.15	0.18	0.25	0.23	0.15	0.15	0.16
sum	100.05	100.12	100.17	100.10	100.00	99.80	99.97	99.98	99.76	99.76
	standard deviation (1 σ)									
SiO_2	0.27	0.20	0.35	0.14	0.19	0.16	0.29	0.24	0.17	0.14
TiO_2	0.04	0.06	0.03	0.01	0.03	0.05	0.04	0.04	0.03	0.04
Al_2O_3	0.08	0.10	0.03	0.04	0.02	0.14	0.05	0.07	0.08	0.04
FeO*	0.13	0.03	0.11	0.20	0.10	0.15	0.10	0.12	0.21	0.13
MnO	0.03	0.03	0.03	0.03	0.03	0.03	0.03	0.03	0.03	0.03
MgO	0.07	0.07	0.03	0.03	0.10	0.03	0.06	0.06	0.06	0.06
CaO	0.12	0.07	0.07	0.08	0.10	0.14	0.09	0.10	0.12	0.05
Na_2O	0.06	0.04	0.05	0.01	0.03	0.03	0.04	0.09	0.08	0.09
K_2O	0.01	0.02	0.01	0.01	0.00	0.01	0.01	0.01	0.01	0.01
P_2O_5	0.01	0.02	0.03	0.01	0.00	0.03	0.02	0.02	0.03	0.01

sample	D35-d	D35-e	D34	D33-a	D33-b	D33-c	D32	D31	D29-a	D29-b
segment	V4	V4	V4	V5	V5	V5	V5	V5	V6	V6
latitude (^{o}S)	41.371	41.371	41.465	41.345	41.345	41.345	41.399	41.430	41.481	41.481
longitude (^{o}W)	87.707	87.707	87.707	85.672	85.672	85.672	85.656	85.644	84.696	84.696
depth (m)	4140	4140	5495	4314	4314	4314	4312	4199	4083	4083
# samples	2	3	9	1	1	1	1	1	4	3
# points	6	9	28	3	3	5	5	5	14	9
lava type	N-MORB	N-MORB	T-MORB	N-MORB	N-MORB	N-MORB	N-MORB	T-MORB	N-MORB	N-MORB
K/Ti	0.10	0.10	0.15	0.09	0.08	0.08	0.12	0.15	0.10	0.09
SiO_2	50.75	50.73	51.10	50.02	50.17	50.16	50.78	50.33	51.31	51.24
TiO_2	1.56	1.53	1.85	1.52	1.50	1.60	1.92	1.92	1.65	1.64
Al_2O_3	15.83	15.85	15.20	16.05	16.13	15.91	15.00	15.53	15.90	15.83
FeO*	9.04	9.06	9.84	8.92	8.66	9.20	10.14	9.71	8.91	9.03
MnO	0.16	0.16	0.18	0.16	0.18	0.18	0.18	0.17	0.17	0.18
MgO	8.07	8.08	7.25	8.11	8.16	7.96	7.08	7.16	7.51	7.43
CaO	10.87	10.97	10.36	11.07	11.32	11.04	10.36	10.27	10.61	10.49
Na_2O	3.31	3.31	3.46	3.02	2.96	2.99	3.28	3.52	3.50	3.55
K_2O	0.11	0.11	0.20	0.10	0.09	0.10	0.17	0.21	0.12	0.11
P_2O_5	0.16	0.17	0.25	0.18	0.17	0.19	0.21	0.25	0.19	0.17
sum	99.87	99.98	99.69	99.15	99.34	99.32	99.12	99.07	99.86	99.66
	standard deviation (1 σ)									
SiO_2	0.20	0.18	0.41	0.37	0.42	0.32	0.32	0.15	0.32	0.73
TiO_2	0.03	0.04	0.04	0.06	0.04	0.02	0.09	0.03	0.05	0.04
Al_2O_3	0.10	0.06	0.08	0.08	0.08	0.10	0.14	0.09	0.11	0.13
FeO*	0.09	0.13	0.17	0.08	0.18	0.19	0.14	0.18	0.14	0.15
MnO	0.02	0.03	0.03	0.02	0.01	0.03	0.04	0.02	0.04	0.02
MgO	0.04	0.05	0.06	0.04	0.07	0.06	0.03	0.07	0.06	0.05
CaO	0.12	0.07	0.11	0.04	0.08	0.08	0.08	0.10	0.11	0.09
Na_2O	0.07	0.05	0.09	0.09	0.15	0.07	0.06	0.07	0.17	0.05
K_2O	0.01	0.01	0.02	0.01	0.01	0.01	0.01	0.01	0.01	0.01
P_2O_5	0.03	0.02	0.02	0.01	0.01	0.02	0.01	0.03	0.02	0.02

(Table 4 continued)

sample	D29-c	D29-d	D29-e	D29-f	D28-a	D28-b	D28-c	D27-a	D27-b	D26
segment	V6	V6	V6	V6	V6	V6	V6	V6	V6	V6
latitude (^{o}S)	41.481	41.481	41.481	41.481	41.464	41.464	41.464	41.491	41.491	41.550
longitude (^{o}W)	84.696	84.696	84.696	84.696	84.669	84.669	84.669	84.622	84.622	84.660
depth (m)	4083	4083	4083	4083	3910	3910	3910	4048	4048	5064
# samples	4	4	3	3	1	5	2	1	1	1
# points	12	12	9	9	5	15	6	5	5	5
lava type	N-MORB	N-MORB	N-MORB	N-MORB	N-MORB	N-MORB	N-MORB	N-MORB	N-MORB	N-MORB
K/Ti	0.10	0.11	0.10	0.10	0.06	0.06	0.07	0.03	0.06	0.09
SiO_2	51.02	51.36	51.37	51.26	51.53	51.60	51.30	49.91	51.05	51.84
TiO_2	1.66	1.62	1.63	1.69	1.41	1.40	1.38	1.17	1.64	1.79
Al_2O_3	15.86	15.82	15.91	15.65	15.69	15.61	15.68	17.59	15.64	15.72
FeO*	8.94	9.05	8.88	9.20	8.83	8.84	8.84	8.02	9.18	9.00
MnO	0.17	0.16	0.16	0.17	0.17	0.18	0.18	0.16	0.19	0.16
MgO	7.42	7.45	7.52	7.46	7.85	7.87	7.93	8.62	7.28	7.05
CaO	10.58	10.57	10.58	10.37	11.08	11.15	11.25	11.14	10.80	9.96
Na_2O	3.51	3.57	3.50	3.57	3.04	3.01	2.95	3.38	3.69	4.02
K_2O	0.12	0.12	0.12	0.12	0.06	0.06	0.07	0.03	0.07	0.11
P_2O_5	0.17	0.19	0.19	0.22	0.13	0.12	0.14	0.08	0.16	0.19
sum	99.46	99.91	99.87	99.73	99.80	99.83	99.72	100.10	99.70	99.85
	standard deviation (1 σ)									
SiO_2	0.50	0.27	0.35	0.32	0.27	0.36	0.25	0.21	0.35	0.23
TiO_2	0.05	0.06	0.05	0.05	0.05	0.05	0.05	0.02	0.02	0.03
Al_2O_3	0.08	0.15	0.13	0.08	0.08	0.08	0.06	0.10	0.09	0.09
FeO*	0.14	0.20	0.14	0.15	0.14	0.13	0.25	0.10	0.22	0.05
MnO	0.03	0.02	0.04	0.03	0.02	0.04	0.04	0.04	0.04	0.03
MgO	0.07	0.08	0.06	0.05	0.04	0.08	0.05	0.06	0.05	0.09
CaO	0.05	0.14	0.12	0.11	0.17	0.12	0.09	0.09	0.09	0.11
Na_2O	0.04	0.07	0.21	0.08	0.12	0.07	0.10	0.06	0.04	0.09
K_2O	0.01	0.01	0.01	0.01	0.00	0.01	0.01	0.01	0.01	0.01
P_2O_5	0.02	0.02	0.01	0.02	0.02	0.02	0.03	0.01	0.02	0.02

sample	D24-a	D24-b	D24-c	D24-d	D24-e	D24-f	D23-a	D23-b	D22-a	D22-b
segment	S7	S7	S7	S7	S7	S7	S7	S7	S7	S7
latitude (^{o}S)	41.580	41.580	41.580	41.580	41.580	41.580	41.678	41.678	41.708	41.708
longitude (^{o}W)	84.345	84.345	84.345	84.345	84.345	84.345	84.253	84.253	84.253	84.253
depth (m)	4121	4121	4121	4121	4121	4121	3349	3349	3607	3607
# samples	3	1	2	3	1	3	1	1	1	4
# points	8	5	6	9	3	11	5	2	4	14
lava type	N-MORB	N-MORB	N-MORB	b. andesite	b. andesite	N-MORB	N-MORB	N-MORB	N-MORB	N-MORB
K/Ti	0.08	0.08	0.09	0.08	0.08	0.09	0.06	0.05	0.11	0.12
SiO_2	51.15	51.58	51.73	52.06	52.31	51.86	50.92	50.52	50.63	50.84
TiO_2	1.36	1.42	1.39	1.41	1.32	1.41	1.25	1.22	1.61	1.61
Al_2O_3	15.37	15.58	15.46	15.38	15.07	15.42	15.67	15.54	15.76	15.85
FeO*	8.60	8.90	8.89	8.85	8.64	8.78	8.87	8.49	9.11	9.15
MnO	0.17	0.15	0.17	0.18	0.15	0.16	0.20	0.18	0.18	0.19
MgO	8.18	8.22	8.29	8.13	8.02	8.13	8.18	8.18	7.61	7.62
CaO	10.94	11.21	11.19	11.04	11.62	11.11	11.28	11.15	10.01	10.22
Na_2O	2.83	2.91	2.87	2.88	2.68	2.86	2.90	2.94	3.59	3.53
K_2O	0.08	0.09	0.09	0.09	0.08	0.09	0.05	0.04	0.13	0.14
P_2O_5	0.14	0.15	0.15	0.14	0.13	0.14	0.10	0.11	0.20	0.19
sum	98.82	100.21	100.23	100.13	100.03	99.96	99.44	98.38	98.84	99.34
	standard deviation (1 σ)									
SiO_2	0.27	0.31	0.30	0.19	0.14	0.25	0.08	0.11	0.31	0.26
TiO_2	0.02	0.04	0.02	0.03	0.03	0.04	0.04	0.03	0.05	0.03
Al_2O_3	0.22	0.04	0.04	0.07	0.10	0.08	0.08	0.09	0.06	0.10
FeO*	0.08	0.12	0.09	0.13	0.22	0.14	0.15	0.06	0.12	0.13
MnO	0.04	0.02	0.04	0.03	0.04	0.02	0.02	0.04	0.04	0.02
MgO	0.07	0.05	0.03	0.05	0.09	0.06	0.07	0.00	0.06	0.04
CaO	0.18	0.14	0.13	0.07	0.06	0.10	0.08	0.03	0.05	0.11
Na_2O	0.07	0.05	0.04	0.05	0.04	0.08	0.02	0.03	0.10	0.05
K_2O	0.01	0.01	0.01	0.01	0.01	0.01	0.01	0.01	0.00	0.01
P_2O_5	0.02	0.03	0.02	0.02	0.01	0.03	0.03	0.01	0.02	0.02

(Table 4 continued)

sample	D21-a	D21-b	GC3	D20-a	D20-b	D20-c	D18	D17	D16-a	D16-b
segment	S7	S7	S7	S6	S6	S6	S6	S6	S6	S6
latitude (^{o}S)	41.727	41.727	41.763	41.707	41.707	41.707	41.876	41.901	42.008	42.008
longitude (^{o}W)	84.290	84.290	84.237	83.990	83.990	83.990	83.964	83.923	83.945	83.945
depth (m)	3590	3590	3706	3616	3616	3616	4084	3908	3670	3670
# samples	1	1	1	1	1	1	1	1	1	1
# points	5	5	5	3	3	4	5	5	3	4
lava type	N-MORB	N-MORB	N-MORB	E-MORB	E-MORB	E-MORB	N-MORB	N-MORB	N-MORB	N-MORB
K/Ti	0.07	0.07	0.11	0.35	0.34	0.35	0.09	0.10	0.10	0.11
SiO_2	51.82	50.99	50.94	51.22	51.10	50.97	50.88	51.08	50.30	49.78
TiO_2	1.28	1.15	1.59	1.52	1.49	1.51	1.83	1.36	1.58	1.53
Al_2O_3	14.51	15.50	15.86	15.96	15.75	15.80	14.87	15.76	15.98	16.02
FeO*	9.54	8.92	9.14	9.46	9.22	9.50	10.27	8.77	9.98	9.83
MnO	0.21	0.17	0.18	0.23	0.20	0.19	0.24	0.18	0.21	0.21
MgO	7.92	8.53	7.21	8.06	7.98	8.07	7.05	7.88	7.92	7.81
CaO	12.16	12.06	10.79	9.11	8.97	9.06	10.52	11.31	10.36	10.29
Na_2O	2.52	2.51	3.67	3.38	3.45	3.44	3.38	2.87	3.10	3.10
K_2O	0.07	0.06	0.12	0.38	0.36	0.38	0.12	0.10	0.12	0.13
P_2O_5	0.12	0.09	0.16	0.18	0.19	0.20	0.21	0.14	0.18	0.19
sum	100.15	99.97	99.67	99.49	98.72	99.12	99.37	99.45	99.72	98.90
	standard deviation (1 σ)									
SiO_2	0.13	0.20	0.14	0.07	0.09	0.32	0.14	0.38	0.12	0.08
TiO_2	0.04	0.06	0.03	0.06	0.05	0.03	0.01	0.12	0.01	0.07
Al_2O_3	0.12	0.08	0.06	0.05	0.06	0.03	0.08	0.59	0.05	0.03
FeO*	0.09	0.16	0.14	0.10	0.04	0.26	0.16	0.56	0.15	0.17
MnO	0.07	0.04	0.05	0.02	0.03	0.01	0.05	0.01	0.05	0.05
MgO	0.05	0.05	0.10	0.01	0.10	0.07	0.05	0.71	0.05	0.05
CaO	0.08	0.10	0.15	0.05	0.01	0.10	0.06	0.24	0.11	0.11
Na_2O	0.08	0.02	0.11	0.02	0.03	0.04	0.09	0.09	0.04	0.06
K_2O	0.01	0.01	0.01	0.02	0.01	0.02	0.01	0.01	0.00	0.01
P_2O_5	0.02	0.01	0.01	0.02	0.01	0.01	0.03	0.02	0.02	0.01

sample	D15-a	D15-b	D14-a	D14-b	D13-a	D13-b	D12-a	D12-b	D12-c	D12-d
segment	S5	S5	S5	S5	S5	S5	S5	S5	S5	S5
latitude (^{o}S)	42.980	42.980	42.015	42.015	42.060	42.060	42.099	42.099	42.099	42.099
longitude (^{o}W)	83.711	83.711	83.696	83.696	83.692	83.692	83.665	83.665	83.665	83.665
depth (m)	3918	3918	3751	3751	3700	3700	3694	3694	3694	3694
# samples	1	1	1	1	1	10	1	6	1	3
# points	5	5	4	3	2	30	6	19	3	6
lava type	N-MORB	N-MORB	N-MORB	N-MORB	N-MORB	N-MORB	N-MORB	N-MORB	N-MORB	N-MORB
K/Ti	0.15	0.17	0.16	0.15	0.16	0.14	0.13	0.13	0.12	0.12
SiO_2	50.26	50.38	50.91	50.44	49.99	50.45	49.67	49.88	50.62	49.89
TiO_2	0.99	1.03	1.09	1.07	0.87	0.97	1.09	1.09	1.19	1.06
Al_2O_3	15.79	15.75	15.05	15.47	15.59	15.68	15.65	15.76	15.20	15.75
FeO*	8.59	8.58	9.43	9.20	8.41	8.70	8.86	9.08	9.27	8.79
MnO	0.16	0.20	0.23	0.21	0.18	0.19	0.15	0.15	0.18	0.15
MgO	8.72	8.74	7.91	8.27	8.74	8.66	8.22	8.27	8.01	8.30
CaO	12.34	12.34	12.19	12.26	12.01	12.33	11.54	11.61	11.81	11.50
Na_2O	2.21	2.22	2.48	2.43	2.39	2.29	2.70	2.68	2.64	2.64
K_2O	0.11	0.12	0.12	0.12	0.10	0.10	0.10	0.10	0.10	0.09
P_2O_5	0.11	0.11	0.11	0.11	0.09	0.09	0.10	0.10	0.10	0.10
sum	99.27	99.48	99.52	99.59	98.37	99.46	98.09	98.72	99.12	98.29
	standard deviation (1 σ)									
SiO_2	0.34	0.29	0.13	0.29	0.15	0.18	0.13	0.22	0.16	0.25
TiO_2	0.04	0.02	0.01	0.04	0.04	0.04	0.06	0.03	0.07	0.05
Al_2O_3	0.05	0.07	0.09	0.10	0.02	0.08	0.10	0.11	0.09	0.07
FeO*	0.13	0.11	0.13	0.14	0.06	0.12	0.10	0.15	0.08	0.05
MnO	0.05	0.04	0.03	0.02	0.04	0.04	0.02	0.02	0.01	0.03
MgO	0.03	0.05	0.08	0.02	0.04	0.08	0.05	0.08	0.03	0.05
CaO	0.07	0.09	0.13	0.11	0.14	0.10	0.08	0.14	0.06	0.10
Na_2O	0.05	0.04	0.05	0.05	0.03	0.07	0.04	0.06	0.03	0.04
K_2O	0.01	0.01	0.02	0.00	0.01	0.01	0.01	0.01	0.00	0.01
P_2O_5	0.01	0.02	0.02	0.03	0.02	0.02	0.02	0.02	0.01	0.01

(Table 4 continued)

sample	D12-e	D11-a	D11-b	D11-c	D10	GC2	D9-a	D9-b	D8-a	D8-b
segment	S5	S5	S5	S5	S5	S5	S5	S5	S5	S5
latitude (^{o}S)	42.099	42.168	42.168	42.168	42.238	42.283	42.313	42.313	42.384	42.384
longitude (^{o}W)	83.665	83.655	83.655	83.655	83.630	83.625	83.617	83.617	83.579	83.579
depth (m)	3694	3562	3562	3562	3211	3160	3161	3161	3169	3169
# samples	13	1	1	5	3	1	1	1	3	3
# points	37	8	10	17	18	5	6	5	11	9
lava type	N-MORB	N-MORB	N-MORB	N-MORB	E-MORB	N-MORB	N-MORB	N-MORB	E-MORB	E-MORB
K/Ti	0.12	0.14	0.15	0.14	0.38	0.14	0.13	0.13	0.36	0.35
SiO_2	50.06	50.72	50.69	50.51	48.91	50.84	50.80	50.79	49.62	49.74
TiO_2	1.10	1.18	1.16	1.14	1.00	0.96	1.11	1.10	1.23	1.25
Al_2O_3	15.87	15.05	15.00	15.08	16.18	15.76	14.63	14.80	15.30	15.15
FeO*	9.13	9.16	9.09	9.25	9.19	8.71	9.18	9.28	9.62	9.69
MnO	0.16	0.18	0.17	0.17	0.17	0.16	0.21	0.19	0.20	0.19
MgO	8.33	7.89	7.89	8.06	8.31	8.65	7.61	7.75	7.72	7.58
CaO	11.73	11.74	11.66	11.71	11.75	12.32	11.84	11.82	11.73	11.79
Na_2O	2.70	2.51	2.53	2.50	2.45	2.37	2.69	2.69	2.54	2.56
K_2O	0.09	0.12	0.13	0.12	0.27	0.09	0.10	0.11	0.32	0.31
P_2O_5	0.10	0.10	0.12	0.12	0.14	0.09	0.13	0.10	0.16	0.16
sum	99.28	98.64	98.43	98.66	98.37	99.96	98.32	98.63	98.43	98.40
	standard deviation (1 σ)									
SiO_2	0.26	0.27	0.29	0.14	0.13	0.17	0.18	0.07	0.17	0.25
TiO_2	0.04	0.03	0.02	0.03	0.04	0.04	0.04	0.03	0.02	0.02
Al_2O_3	0.07	0.09	0.12	0.08	0.11	0.08	0.09	0.07	0.05	0.18
FeO*	0.18	0.15	0.19	0.14	0.15	0.14	0.05	0.13	0.13	0.20
MnO	0.03	0.05	0.03	0.03	0.03	0.02	0.04	0.03	0.03	0.03
MgO	0.06	0.05	0.06	0.08	0.07	0.03	0.06	0.08	0.05	0.06
CaO	0.11	0.11	0.13	0.11	0.12	0.10	0.13	0.04	0.09	0.15
Na_2O	0.06	0.06	0.07	0.06	0.06	0.07	0.04	0.06	0.04	0.07
K_2O	0.01	0.02	0.01	0.01	0.01	0.01	0.01	0.01	0.01	0.01
P_2O_5	0.02	0.02	0.02	0.02	0.02	0.01	0.01	0.02	0.02	0.01

sample	D8-c	D8-d	D6-a	D6-b	D6-c	D6-d	D6-e	D6-f	D6-g	D6-h
segment	S5	S5	S5	S5	S5	S5	S5	S5	S5	S5
latitude (^{o}S)	42.384	42.384	42.538	42.538	42.538	42.538	42.538	42.538	42.538	42.538
longitude (^{o}W)	83.579	83.579	83.563	83.563	83.563	83.563	83.563	83.563	83.563	83.563
depth (m)	3169	3169	3626	3626	3626	3626	3626	3626	3626	3626
# samples	1	5	1	2	4	1	1	2	2	4
# points	4	12	2	3	6	5	7	6	5	11
lava type	E-MORB	E-MORB	N-MORB	N-MORB	N-MORB	N-MORB	N-MORB	N-MORB	N-MORB	N-MORB
K/Ti	0.37	0.35	0.05	0.06	0.06	0.04	0.05	0.08	0.04	0.05
SiO_2	49.63	49.57	48.53	48.80	48.81	48.64	48.65	49.13	48.71	48.32
TiO_2	1.21	1.24	0.68	0.67	0.73	0.71	0.70	0.73	0.70	0.70
Al_2O_3	15.13	15.24	17.11	17.17	17.08	17.30	17.30	17.23	17.26	17.02
FeO*	9.67	9.68	10.15	10.09	10.13	10.04	10.01	9.47	10.09	9.98
MnO	0.17	0.19	0.17	0.16	0.18	0.19	0.18	0.14	0.20	0.16
MgO	7.66	7.62	10.01	10.12	9.90	10.04	9.94	9.63	9.82	10.03
CaO	11.71	11.74	11.48	11.65	11.65	11.52	11.66	11.82	11.47	11.42
Na_2O	2.58	2.58	1.82	1.77	1.81	1.75	1.75	1.89	1.79	1.74
K_2O	0.32	0.32	0.02	0.03	0.03	0.02	0.03	0.04	0.02	0.03
P_2O_5	0.16	0.16	0.06	0.05	0.04	0.03	0.04	0.06	0.05	0.05
sum	98.23	98.34	100.04	100.49	100.37	100.25	100.25	100.15	100.11	99.44
	standard deviation (1 σ)									
SiO_2	0.21	0.14	0.02	0.20	0.19	0.16	0.12	0.08	0.12	0.32
TiO_2	0.06	0.06	0.02	0.06	0.02	0.03	0.05	0.04	0.04	0.03
Al_2O_3	0.06	0.10	0.11	0.13	0.03	0.11	0.07	0.05	0.15	0.19
FeO*	0.02	0.14	0.02	0.14	0.08	0.05	0.09	0.09	0.29	0.19
MnO	0.04	0.03	0.00	0.03	0.02	0.03	0.02	0.02	0.03	0.02
MgO	0.08	0.06	0.02	0.06	0.25	0.08	0.08	0.07	0.28	0.19
CaO	0.09	0.14	0.05	0.08	0.10	0.09	0.13	0.07	0.07	0.09
Na_2O	0.05	0.06	0.04	0.06	0.05	0.05	0.06	0.05	0.11	0.06
K_2O	0.01	0.01	0.00	0.01	0.01	0.01	0.01	0.01	0.01	0.01
P_2O_5	0.01	0.02	0.02	0.01	0.02	0.02	0.01	0.02	0.02	0.02

(Table 4 continued)

sample	D6-i	D6-j	D6-k	D6-l	D5	D4	D3	D2-a	D2-b	D2-c	D1
segment	S5	S5	S5	S5	S5	S5	S5	S5	S5	S5	S5
latitude (^{o}S)	42.538	42.538	42.538	42.538	42.592	42.660	42.790	42.897	42.897	42.897	43.017
longitude (^{o}W)	83.563	83.563	83.563	83.563	83.572	83.530	83.466	83.441	83.441	83.441	83.440
depth (m)	3626	3626	3626	3626	3970	3726	3860	3820	3820	3820	4207
# samples	5	1	3	1	1	3	4	4	2	1	5
# points	15	3	9	3	6	14	7	17	11	5	21
lava type	N-MORB	N-MORB	N-MORB	N-MORB	N-MORB	N-MORB	N-MORB	N-MORB	N-MORB	N-MORB	N-MORB
K/Ti	0.06	0.06	0.08	0.05	0.18	0.18	0.08	0.14	0.13	0.14	0.13
SiO_2	47.92	48.14	48.36	48.23	50.89	50.93	48.63	51.44	51.52	51.59	51.38
TiO_2	0.68	0.65	0.71	0.70	1.06	1.24	0.93	1.02	1.03	1.02	1.09
Al_2O_3	16.79	16.92	16.89	16.73	15.78	15.38	16.84	14.97	15.38	15.21	15.34
FeO*	9.90	10.00	9.54	9.91	9.23	9.83	10.12	8.99	8.71	8.84	8.77
MnO	0.18	0.19	0.18	0.16	0.18	0.16	0.17	0.15	0.15	0.16	0.18
MgO	10.14	9.84	9.60	9.95	8.51	8.04	9.21	8.34	8.61	8.44	8.38
CaO	11.27	11.26	11.52	11.28	11.61	11.43	11.94	12.39	11.98	11.91	12.05
Na_2O	1.71	1.79	1.80	1.66	2.51	2.54	2.23	2.22	2.32	2.31	2.45
K_2O	0.03	0.03	0.04	0.03	0.14	0.16	0.05	0.10	0.10	0.11	0.11
P_2O_5	0.04	0.04	0.05	0.05	0.11	0.12	0.07	0.10	0.11	0.11	0.11
sum	98.64	98.86	98.70	98.69	100.00	99.82	100.21	99.72	99.92	99.70	99.85
	standard deviation (1 σ)										
SiO_2	0.11	0.14	0.20	0.03	0.12	0.20	0.23	0.22	0.20	0.06	0.19
TiO_2	0.03	0.03	0.03	0.04	0.09	0.03	0.01	0.05	0.02	0.02	0.03
Al_2O_3	0.10	0.13	0.07	0.06	0.25	0.10	0.06	0.12	0.08	0.10	0.12
FeO*	0.14	0.08	0.20	0.06	0.40	0.16	0.14	0.16	0.15	0.07	0.16
MnO	0.03	0.05	0.03	0.02	0.04	0.02	0.04	0.04	0.04	0.04	0.03
MgO	0.16	0.07	0.15	0.20	0.27	0.09	0.03	0.10	0.08	0.05	0.17
CaO	0.10	0.19	0.17	0.17	0.13	0.10	0.10	0.11	0.13	0.16	0.13
Na_2O	0.04	0.04	0.07	0.03	0.07	0.10	0.14	0.05	0.05	0.07	0.06
K_2O	0.01	0.01	0.01	0.00	0.01	0.02	0.01	0.01	0.01	0.01	0.01
P_2O_5	0.02	0.04	0.02	0.01	0.02	0.02	0.01	0.02	0.01	0.02	0.02

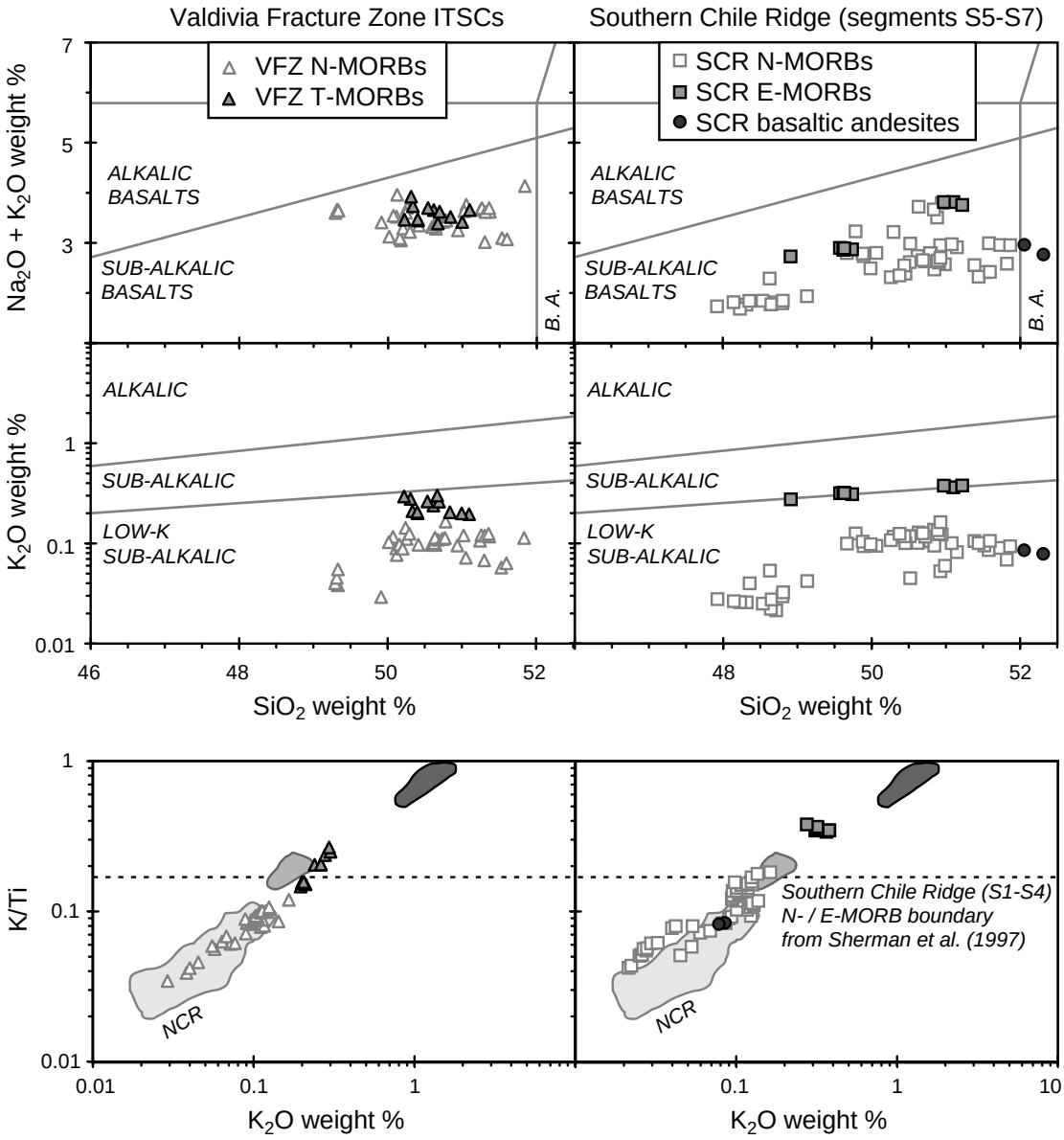

Figure 6: Petrologic classification of lavas recovered from the Valdivia Fracture Zone intra-transform spreading centers and the Southern Chile Ridge (segments S5-S7), based on alkali content and K/Ti as in Figure 5. All samples are tholeiitic. Fields enclose the observed compositional ranges for Northern Chile Ridge N-MORBs (light grey), T-MORBs (intermediate), and alkalic basalts (dark grey) for comparison.

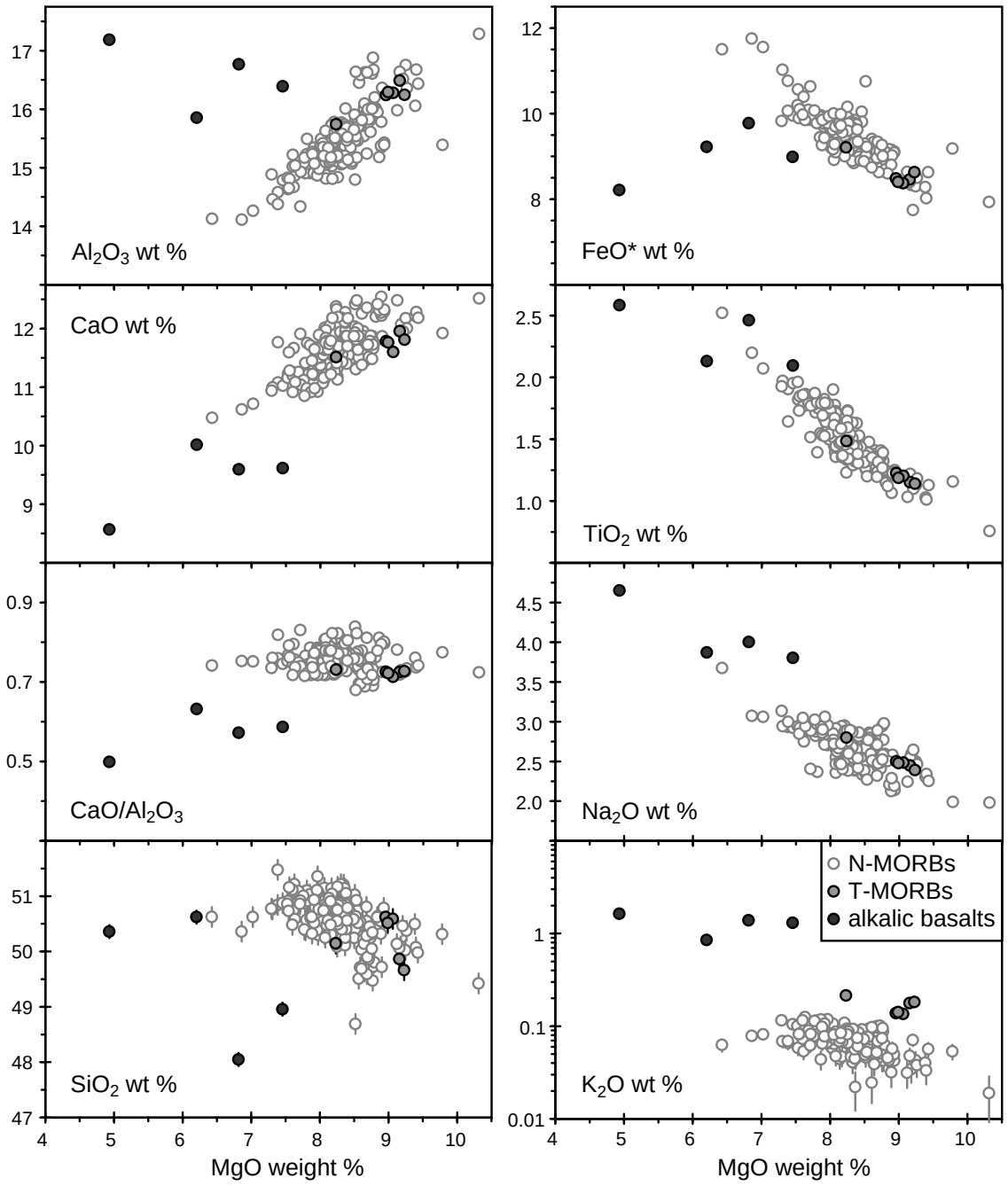

Figure 7: Major element oxides vs. MgO for N-MORBs, T-MORBs, and alkalic basalts from the Northern Chile Ridge. Error bars in SiO_2 and K_2O indicate 1 standard deviation of repeated analyses.

compositions of T-MORB samples fall within the fields defined by the N-MORBs for all elements except K_2O. The alkalic basalts have higher Al_2O_3 and K_2O and lower FeO* and CaO than would be expected if the trend defined by N-MORB and T-MORB compositions continued to low MgO values.

Samples from the Valdivia Fracture Zone and Southern Chile Ridge segments S5-S7 exhibit major element trends similar to those of lavas from the Northern Chile Ridge, except that there is no clear trend in CaO vs. MgO (Figure 8). In general, major element trends at the Valdivia Fracture Zone and Southern Chile Ridge segments S5-S7 are looser and more scattered than those at the Northern Chile Ridge. Major element trends in Valdivia Fracture Zone and Southern Chile Ridge samples are offset from each other and from the trends in Northern Chile Ridge MORBs (Figure 8). Valdivia Fracture Zone samples are clearly offset to higher Na_2O and Al_2O_3 contents and lower FeO* contents than Northern Chile Ridge and Southern Chile Ridge MORBs at the same MgO content. Southern Chile Ridge samples are offset to lower TiO_2 contents than Northern Chile Ridge and Valdivia Fracture Zone samples at the same MgO content.

Among Valdivia Fracture Zone samples, the major element compositions of T-MORBs fall roughly within the fields defined by N-MORBs for all elements except for K_2O (Figure 9). The same is true for Southern Chile Ridge E-MORBs and N-MORBs (Figure 10). The Southern Chile Ridge basaltic andesites have MgO contents similar to those of the N-MORBs; in fact, the basaltic andesite compositions fall within the fields defined by N-MORBs for all elements except SiO_2 (Figure 10). A group of Southern

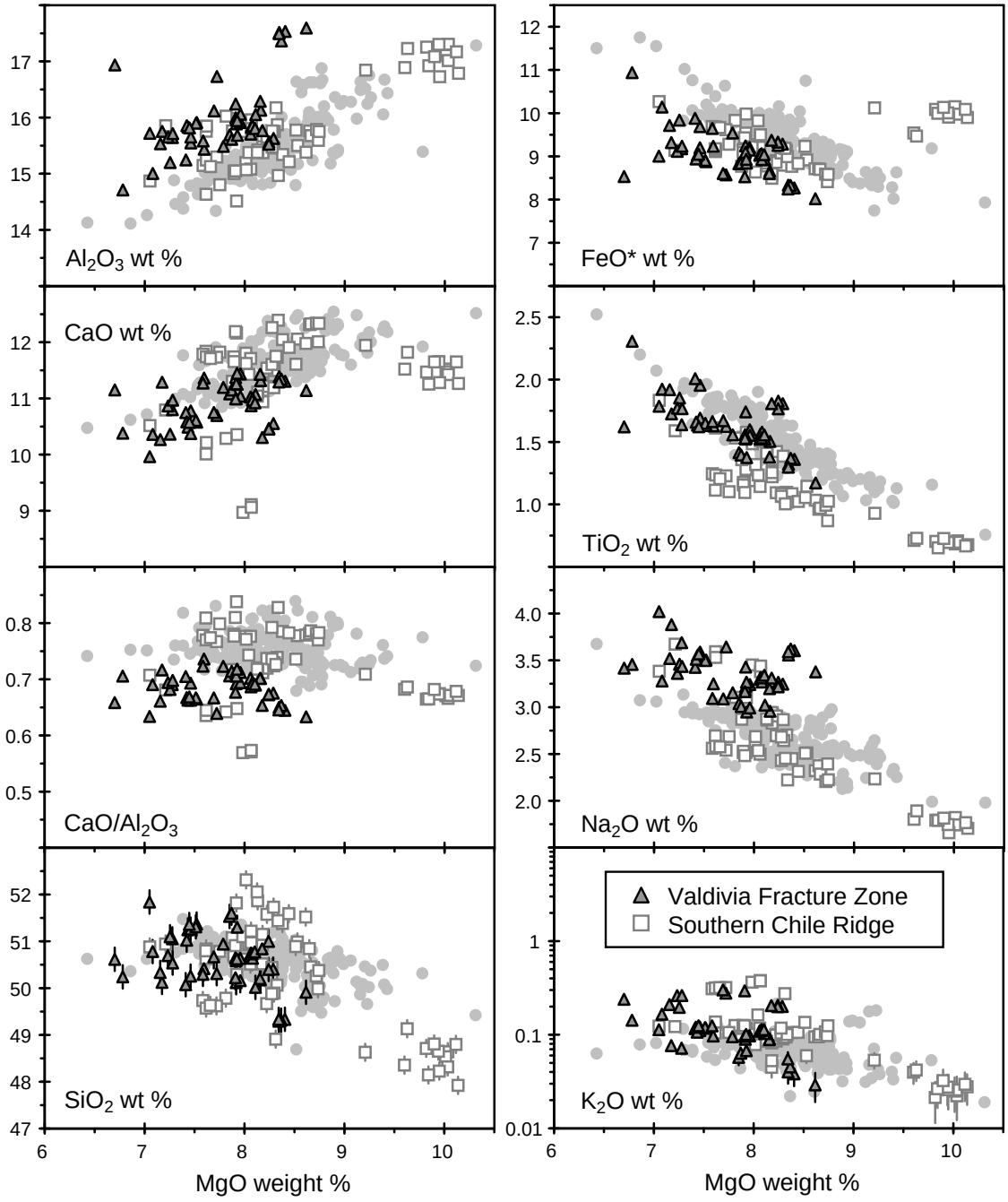

Figure 8: Major element oxides vs. MgO for samples from Valdivia Fracture Zone ITSCs (grey triangles) and the Southern Chile Ridge (segments S5-S7; white squares), compared to Northern Chile Ridge MORBs (grey dots). Error bars in SiO_2 and K_2O indicate 1 standard deviation of repeated analyses.

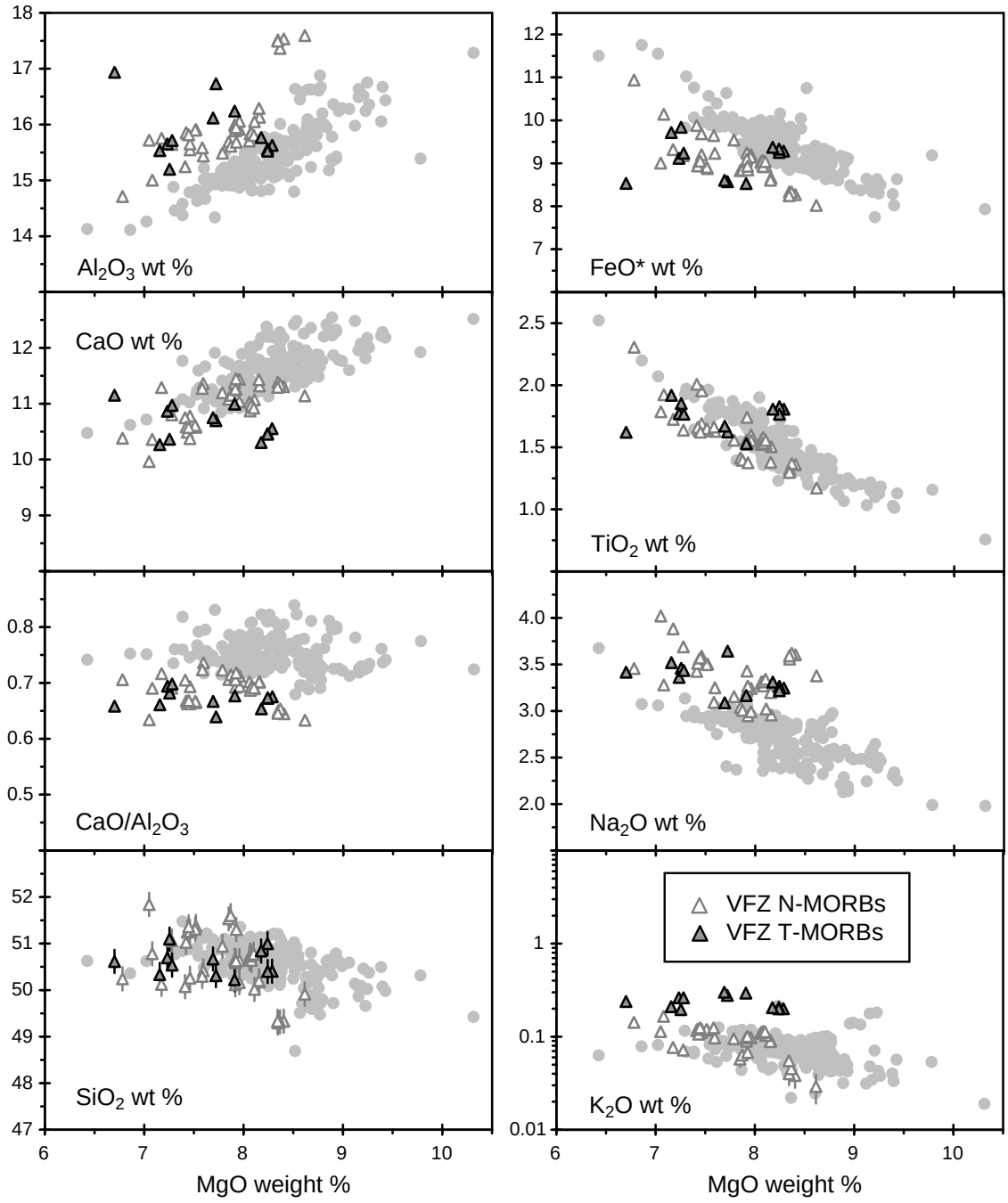

Figure 9: Major element oxides vs. MgO for N-MORBs and T-MORBs from Valdivia Fracture Zone ITSCs, compared to Northern Chile Ridge MORBs (grey dots). Error bars in SiO_2 and K_2O indicate 1 standard deviation of repeated analyses.

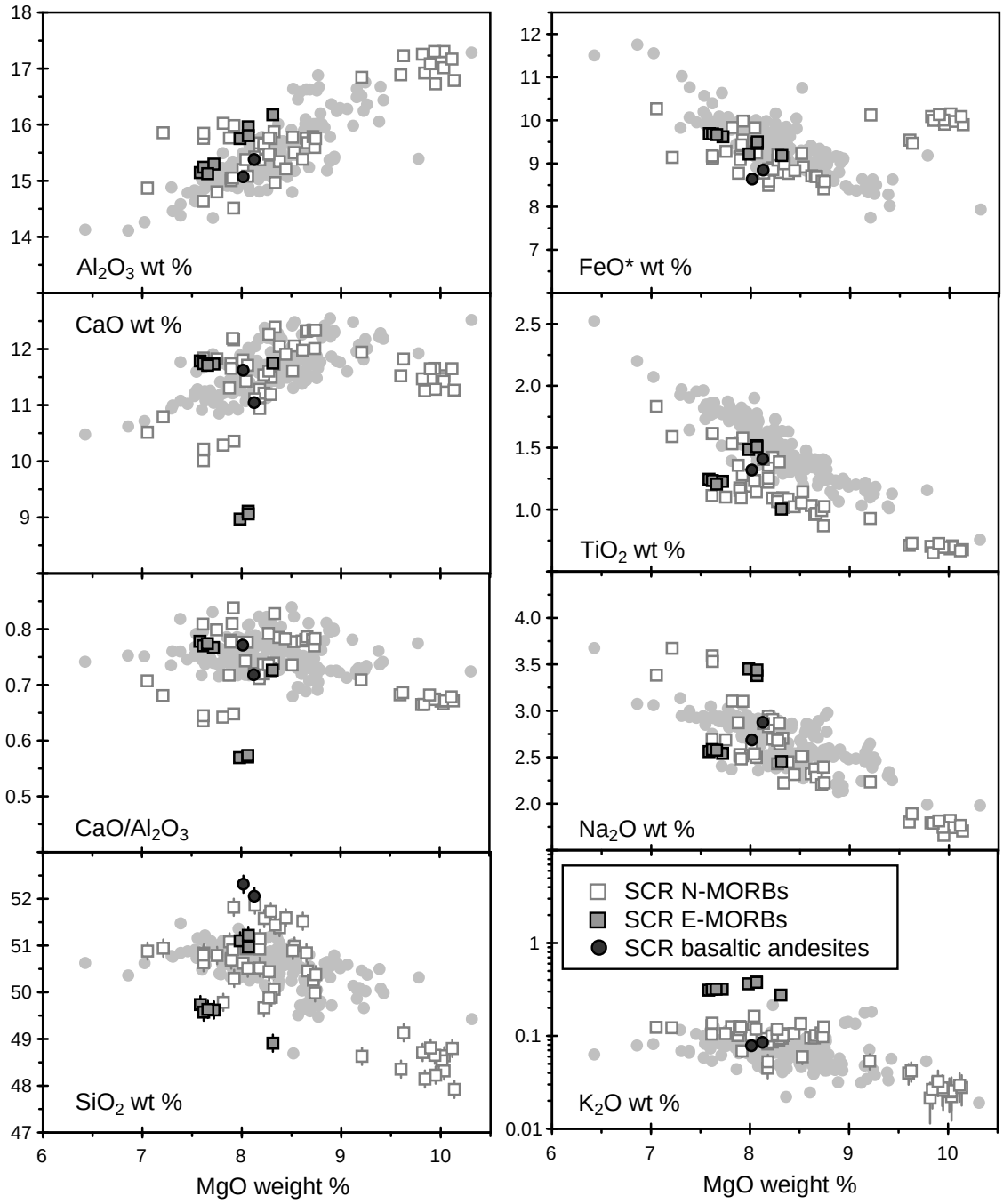

Figure 10: Major element oxides vs. MgO for N-MORBs, E-MORBs, and basaltic andesites from the Southern Chile Ridge (segments S5-S7), compared to Northern Chile Ridge MORBs (grey dots). Error bars in SiO_2 and K_2O indicate 1 standard deviation of repeated analyses.

Chile Ridge samples with MgO contents greater than 9 weight % (Figure 10) are all found at a single dredge site (D6) at segment S5 (Figure 11).

There is no regional gradient in the MgO content of recovered lavas along the 550 km span of the Northern Chile Ridge (Figure 11). In contrast, there is a pronounced southward increase in the MgO content of recovered lavas over the shorter distance of approximately 200 km between the Valdivia Fracture Zone and the southernmost extent of the study region at Southern Chile Ridge segment S5.

Trace Element Data

Trace element concentrations for the subset of 50 Northern Chile Ridge samples are given in Table 5. The minimum estimated error in trace element concentrations, as described in the Methods section, is given in Table 6.

The incompatible trace element contents of the Northern Chile Ridge MORBs span a spectrum from N-MORBs to T-MORBs (Figure 12). Many of the N-MORBs are depleted in incompatible trace elements relative to the typical N-MORB composition described in *Sun and McDonough* (1989). Some of these are similar to the "ultra-depleted" N-MORBs found previously at the Northern Chile Ridge by *Bach et al.* (1996). Alkalic basalts display typical enrichments in incompatible trace elements (*Sun and McDonough*, 1989) (Figure 12).

Among the "ultra-depleted" N-MORBs there are two independent types of depletions: depletion in the rare earth elements and other trace elements with similar incompatibility

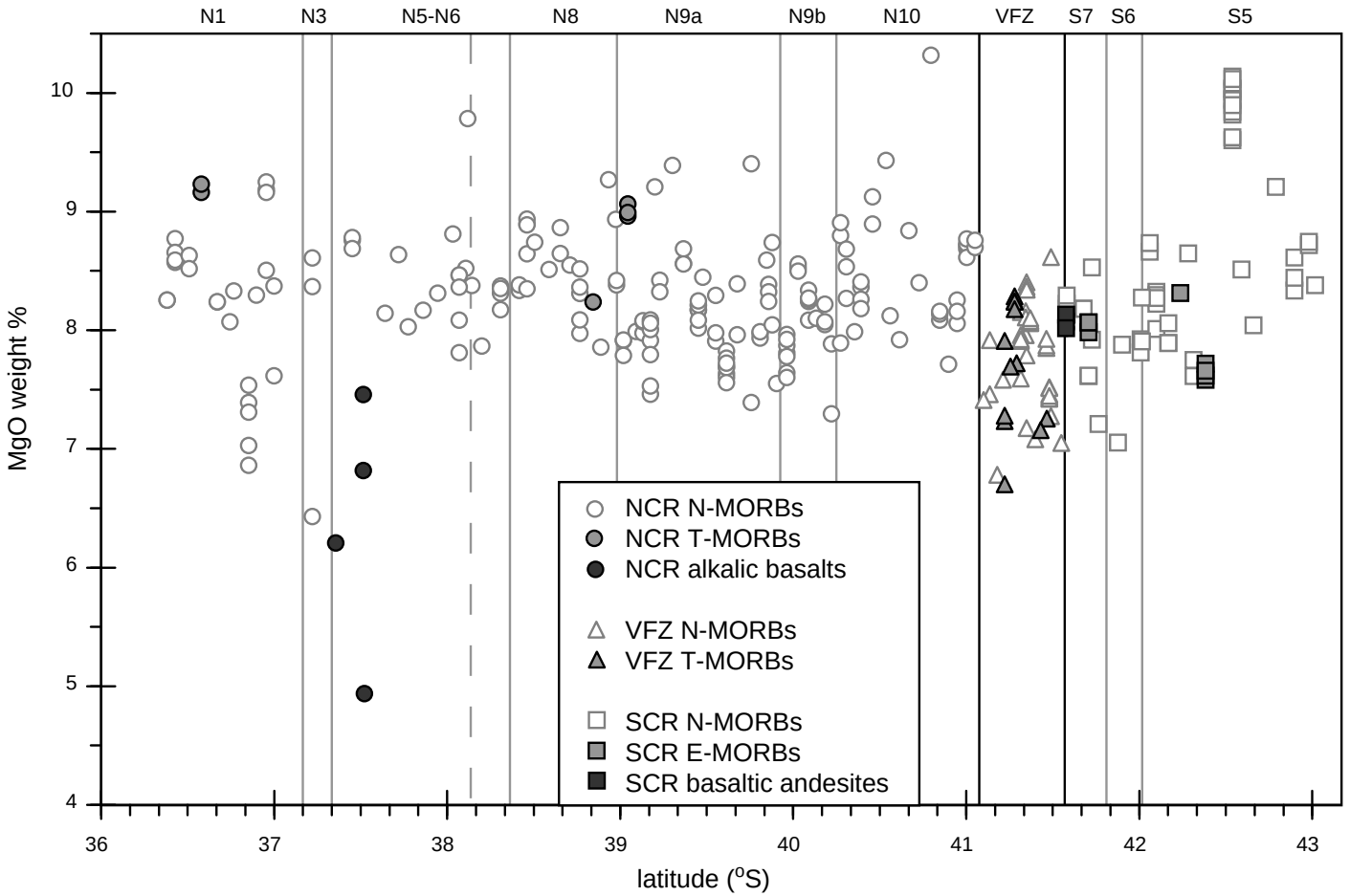

Figure 11: MgO content vs. latitude along the Northern Chile Ridge (NCR), Valdivia Fracture Zone ITSCs (VFZ), and Southern Chile Ridge segments S5-S7 (SCR). All data are from this study. Different petrologic rock types are shown with different symbols. Segment boundaries are shown as grey lines and segments are labelled along the top. The tip of the propagating rift between segments N5 and N6 is shown as a dashed line.

Table 5: Trace Element Abundances from the Northern Chile Ridge

sample	D112-3	D111-1	D110-6	GC23-1	D109-1	GC22	D108-1	D107-12	D106-1	D105-2
segment	N1	N1	N1	N1	N1	N1	N1	N1	N1	N3
latitude (^{o}S)	36.383	36.431	36.511	36.580	36.674	36.748	36.855	36.958	37.000	37.222
longitude (^{o}W)	97.088	97.062	97.093	97.075	97.077	97.063	97.066	97.075	97.072	95.352
depth (m)	4585	4504	3971	3834	3507	3769	4209	4098	4135	4404
lava type	N-MORB	N-MORB	N-MORB	T-MORB	N-MORB	N-MORB	N-MORB	N-MORB	N-MORB	N-MORB
K/Ti	0.06	0.09	0.05	0.21	0.07	0.05	0.05	0.05	0.05	0.02
	major element composition (weight %)									
# points	5	5	4	4	5	5	5	5	5	6
SiO_2	50.13	49.47	50.42	49.86	50.84	51.15	50.31	50.25	50.18	50.05
TiO_2	1.72	1.32	1.38	1.15	1.23	1.39	2.17	1.33	1.39	1.39
Al_2O_3	15.43	16.88	15.77	16.49	15.26	14.89	14.17	15.87	16.01	15.42
FeO*	9.92	8.97	9.15	8.46	9.21	9.13	11.86	9.11	8.95	9.46
MnO	0.20	0.14	0.17	0.17	0.16	0.19	0.22	0.13	0.20	0.18
MgO	8.25	8.77	8.50	9.16	8.23	8.07	6.89	8.54	8.37	8.38
CaO	11.18	11.66	11.95	11.96	12.38	12.02	10.60	12.02	11.97	12.28
Na_2O	2.88	2.77	2.59	2.45	2.68	2.86	3.06	2.64	2.79	2.58
K_2O	0.08	0.09	0.05	0.18	0.07	0.05	0.07	0.05	0.05	0.02
P_2O_5	0.17	0.15	0.12	0.12	0.11	0.13	0.22	0.15	0.14	0.12
sum	99.97	100.23	100.10	99.99	100.16	99.90	99.57	100.09	100.05	99.88
	trace element composition (ppm)									
Sc	37.1	40.6	38.0	35.7	40.9	43.8	44.6	36.7	35.5	40.5
Cr	325	311	383	367	396	371	182	346	366	417
Ni	139.3	163.9	151.3	168.6	122.2	89.0	73.9	121.5	125.4	154.9
Cu	65.2	72.0	67.1	67.2	82.6	73.6	62.4	69.3	75.5	73.2
Zn	90.0	65.0	65.4	61.6	69.4	67.8	110.9	65.5	77.3	73.2
Rb	0.702	0.682	0.704	3.106	0.726	0.420	0.541	0.384	0.355	0.097
Sr	111	161	112	124	88	120	118	116	133	94
Y	41.0	29.7	31.0	27.6	29.1	32.4	54.1	30.8	32.1	31.8
Zr	113.8	99.7	84.6	71.7	62.8	91.2	163.5	88.8	92.3	77.9
Nb	2.04	1.93	1.55	5.93	1.74	1.16	1.88	1.10	1.20	0.36
Cs	0.0101	0.0073	0.0067	0.0341	0.0081	0.0047	0.0064	0.0045	0.0037	0.0013
Ba	7.41	6.56	7.64	37.21	8.71	4.89	5.76	3.91	3.96	0.85
La	3.27	3.63	2.62	4.62	1.92	2.43	4.64	2.78	2.72	1.83
Ce	11.18	10.71	8.63	11.39	6.22	8.49	15.48	8.55	9.26	7.09
Pr	1.99	1.78	1.48	1.65	1.16	1.58	2.70	1.58	1.64	1.35
Nd	11.6	9.4	8.3	8.4	6.9	8.9	14.9	8.7	9.3	8.0
Sm	3.89	3.12	2.98	2.71	2.52	3.24	5.03	3.10	3.13	2.83
Eu	1.30	1.09	1.06	0.98	0.95	1.13	1.63	1.09	1.11	1.03
Gd	5.42	4.49	4.47	4.21	3.52	4.79	7.08	4.62	4.24	3.99
Tb	0.997	0.808	0.802	0.748	0.677	0.869	1.309	0.831	0.781	0.764
Dy	6.13	4.86	4.90	4.51	4.23	5.23	7.99	5.06	4.77	4.73
Ho	1.403	1.020	1.041	0.988	0.950	1.114	1.855	1.071	1.089	1.071
Er	3.67	3.13	3.16	2.96	2.48	3.37	4.85	3.22	2.92	2.83
Tm	0.558	0.495	0.501	0.479	0.378	0.534	0.737	0.515	0.438	0.430
Yb	3.70	2.94	2.96	2.82	2.50	3.16	4.90	3.06	2.90	2.83
Lu	0.562	0.468	0.466	0.444	0.383	0.500	0.754	0.482	0.453	0.426
Hf	2.90	2.29	2.09	1.97	1.67	2.34	3.84	2.21	2.28	1.97
Ta	0.141	0.149	0.113	0.380	0.103	0.096	0.145	0.093	0.086	0.037
Pb	0.39	0.44	0.32	0.35	0.22	0.34	0.53	0.36	0.35	0.27
Th	0.125	0.105	0.091	0.431	0.106	0.069	0.117	0.061	0.070	0.020
U	0.046	0.044	0.034	0.134	0.033	0.030	0.046	0.027	0.028	0.009

(Table 5 continued)

sample	D104-SG	D103-1	D102-1	D101-2	D99-3	D97-SG	D93-1	D92-1	D88-1	D87-2
segment	N5	N5	N5 off-axis	N5	N5	N5	N6	N6	N8	N8
latitude (^{o}S)	37.360	37.455	37.517	37.524	37.863	38.035	38.120	38.202	38.420	38.462
longitude (^{o}W)	94.114	94.099	94.200	94.090	94.093	94.101	93.852	93.837	92.582	92.584
depth (m)	3296	3271	2202	3160	3616	3432	3413	3369	3981	3819
lava type	alkalic	N-MORB	N-MORB	alkalic	N-MORB	N-MORB	N-MORB	N-MORB	N-MORB	N-MORB
K/Ti	0.55	0.05	0.03	0.87	0.08	0.06	0.06	0.04	0.07	0.05
	major element composition (weight %)									
# points	5	6	4	5	5	8	5	5	4	5
SiO_2	50.62	49.65	50.76	50.43	50.33	50.41	50.31	50.80	50.56	50.48
TiO_2	2.13	1.23	1.38	2.57	1.47	1.15	1.16	1.72	1.45	1.21
Al_2O_3	15.86	16.64	14.67	17.22	15.71	16.01	15.39	15.13	15.51	15.33
FeO*	9.22	8.76	10.04	8.16	9.46	8.70	9.18	9.95	9.28	9.18
MnO	0.18	0.20	0.21	0.16	0.18	0.16	0.18	0.17	0.18	0.18
MgO	6.20	8.77	7.89	4.97	8.17	8.81	9.78	7.87	8.29	8.87
CaO	10.02	11.86	12.19	8.56	11.75	12.20	11.92	11.27	11.77	12.27
Na_2O	3.87	2.96	2.86	4.60	2.93	2.56	1.99	2.92	2.62	2.18
K_2O	0.85	0.05	0.03	1.61	0.08	0.05	0.05	0.04	0.07	0.05
P_2O_5	0.43	0.12	0.12	0.61	0.14	0.12	0.11	0.15	0.14	0.12
sum	99.38	100.23	100.15	98.89	100.22	100.16	100.08	100.03	99.87	99.87
	trace element composition (ppm)									
Sc	34.4	39.0	48.1	22.8	41.0	36.8	35.1	43.7	40.7	40.5
Cr	211	336	261	141	343	401	421	302	347	408
Ni	74.7	113.4	67.6	82.6	114.2	139.1	191.6	111.9	112.7	128.1
Cu	60.3	84.8	87.1	50.2	72.8	79.3	59.7	63.8	72.1	71.0
Zn	82.7	66.7	89.6	90.5	76.0	75.0	64.8	87.4	74.6	73.4
Rb	19.673	0.435	0.348	32.303	0.664	0.374	0.637	0.111	0.501	0.338
Sr	304	162	102	518	128	99	71	101	102	78
Y	39.8	27.0	36.2	36.1	35.1	29.2	30.8	41.8	35.7	29.7
Zr	193.8	88.7	82.6	244.8	98.8	67.7	64.3	112.6	94.2	66.1
Nb	29.03	1.12	0.97	53.68	1.71	1.02	1.39	0.86	1.45	1.09
Cs	0.2317	0.0056	0.0047	0.4255	0.0079	0.0045	0.0083	0.0030	0.0044	0.0040
Ba	204	5.19	3.98	378	6.33	4.04	6.71	1.06	4.34	3.51
La	17.75	2.83	2.10	29.12	2.90	1.83	1.93	2.75	2.60	1.91
Ce	36.47	9.29	7.26	56.42	9.35	6.40	6.38	10.08	8.56	6.46
Pr	4.76	1.59	1.39	6.85	1.63	1.19	1.12	1.92	1.62	1.19
Nd	21.3	8.7	8.0	29.6	9.4	7.2	6.6	11.3	9.1	7.0
Sm	5.29	2.69	3.02	6.65	3.35	2.60	2.44	4.01	3.45	2.57
Eu	1.80	0.99	1.13	2.17	1.17	0.96	0.88	1.36	1.23	0.93
Gd	7.44	3.55	4.44	7.12	4.93	3.66	3.59	5.77	4.62	3.82
Tb	1.178	0.662	0.833	1.086	0.891	0.691	0.700	1.089	0.956	0.755
Dy	6.62	4.05	5.15	6.04	5.45	4.23	4.37	6.71	5.70	4.70
Ho	1.358	0.917	1.194	1.167	1.158	0.987	1.024	1.512	1.258	1.107
Er	4.01	2.37	3.18	2.91	3.47	2.56	2.74	3.96	3.52	2.92
Tm	0.610	0.368	0.475	0.418	0.561	0.388	0.416	0.605	0.553	0.448
Yb	3.59	2.37	3.18	2.70	3.28	2.58	2.77	3.94	3.42	2.94
Lu	0.548	0.367	0.486	0.408	0.520	0.396	0.430	0.606	0.555	0.454
Hf	4.34	1.94	2.08	5.10	2.37	1.79	1.71	3.05	2.51	1.85
Ta	1.668	0.082	0.072	2.854	0.123	0.073	0.096	0.087	0.113	0.087
Pb	1.17	0.37	0.29	1.71	0.37	0.26	0.23	0.38	0.32	0.30
Th	1.873	0.067	0.058	3.594	0.094	0.059	0.086	0.047	0.088	0.062
U	0.538	0.023	0.026	0.976	0.039	0.023	0.034	0.023	0.035	0.023

(Table 5 continued)

sample	GC17	GC16	D86-5	GC15	D85-9	GC14	GC13	D84-1	D83-1	D82-2
segment	N8	N8	N8	N8	N8	N8	N8	N8	N8	N9a
latitude (^{o}S)	38.508	38.591	38.657	38.712	38.769	38.844	38.892	38.936	38.977	38.982
longitude (^{o}W)	92.579	92.576	92.577	92.563	92.560	92.553	92.548	92.540	92.540	91.575
depth (m)	3785	3850	3518	3542	3520	3689	3841	3846	3823	3407
lava type	N-MORB	N-MORB	N-MORB	N-MORB	N-MORB	T-MORB	N-MORB	N-MORB	N-MORB	N-MORB
K/Ti	0.05	0.06	0.03	0.07	0.05	0.20	0.07	0.04	0.06	0.08
	major element composition (weight %)									
# points	5	5	1	5	3	4	5	4	5	4
SiO_2	50.24	50.93	49.90	50.65	50.94	50.15	51.03	50.37	50.79	50.94
TiO_2	1.36	1.27	1.36	1.34	1.35	1.48	1.55	1.18	1.23	1.43
Al_2O_3	15.82	14.80	16.28	15.46	15.38	15.74	14.91	16.36	15.39	15.70
FeO*	8.99	9.30	8.98	9.08	9.27	9.21	9.44	8.50	9.09	9.02
MnO	0.15	0.20	0.14	0.21	0.12	0.17	0.20	0.15	0.20	0.20
MgO	8.74	8.51	8.70	8.55	8.40	8.23	7.85	9.26	8.93	8.41
CaO	11.81	12.42	11.72	12.00	11.92	11.51	11.72	12.01	12.32	11.55
Na_2O	2.58	2.35	2.73	2.57	2.61	2.80	2.83	2.46	2.19	2.82
K_2O	0.05	0.05	0.03	0.07	0.05	0.21	0.07	0.04	0.05	0.08
P_2O_5	0.13	0.10	0.10	0.10	0.10	0.17	0.15	0.08	0.09	0.13
sum	99.87	99.92	99.95	100.05	100.13	99.68	99.74	100.41	100.29	100.27
	trace element composition (ppm)									
Sc	39.0	43.2	36.2	38.7	40.3	41.6	42.9	37.7	40.0	39.0
Cr	353	435	333	423	336	311	329	371	351	393
Ni	145.7	103.9	131.5	116.7	102.1	121.5	93.4	161.2	117.3	126.8
Cu	67.5	74.0	68.5	80.1	70.6	61.4	65.2	75.7	69.3	74.1
Zn	69.0	66.6	69.9	78.6	69.2	68.1	68.7	70.1	68.8	80.4
Rb	0.420	0.497	0.203	0.630	0.320	3.201	0.686	0.158	0.289	0.285
Sr	98	92	96	106	103	157	107	102	128	130
Y	33.1	31.3	31.6	31.5	32.5	33.6	35.6	28.4	34.7	33.9
Zr	85.9	71.4	82.1	71.7	83.3	103.7	93.8	66.8	102.0	94.4
Nb	1.23	1.28	0.78	1.76	1.05	6.13	1.78	0.77	1.50	1.50
Cs	0.0030	0.0047	0.0019	0.0074	0.0031	0.0269	0.0076	0.0022	0.0032	0.0033
Ba	4.13	4.84	1.75	7.96	3.32	36.46	6.63	1.81	3.23	3.22
La	2.28	2.03	2.07	2.23	2.22	5.19	2.78	1.75	2.99	2.77
Ce	7.47	6.55	7.20	7.17	7.72	13.49	9.12	6.14	9.50	9.29
Pr	1.44	1.28	1.41	1.29	1.44	2.18	1.71	1.16	1.79	1.64
Nd	8.6	7.3	8.2	7.7	8.4	11.2	9.6	6.6	9.7	9.5
Sm	3.25	2.87	3.14	2.78	3.07	3.63	3.56	2.44	3.49	3.24
Eu	1.15	1.03	1.15	1.02	1.15	1.26	1.25	0.90	1.24	1.14
Gd	4.94	4.49	4.33	4.00	4.31	5.33	5.30	3.53	4.68	4.48
Tb	0.900	0.823	0.870	0.743	0.872	0.939	0.950	0.670	0.934	0.814
Dy	5.37	5.00	5.15	4.65	5.19	5.56	5.78	4.19	5.51	5.02
Ho	1.158	1.085	1.162	1.077	1.162	1.193	1.226	0.977	1.231	1.144
Er	3.52	3.30	3.21	2.80	3.23	3.60	3.71	2.55	3.35	3.00
Tm	0.549	0.531	0.502	0.422	0.502	0.565	0.585	0.396	0.526	0.458
Yb	3.27	3.12	3.09	2.77	3.13	3.35	3.47	2.59	3.30	3.00
Lu	0.524	0.486	0.499	0.435	0.502	0.547	0.543	0.392	0.527	0.465
Hf	2.38	2.00	2.28	1.94	2.23	2.70	2.48	1.73	2.56	2.33
Ta	0.098	0.102	0.070	0.117	0.084	0.380	0.126	0.056	0.118	0.108
Pb	0.31	0.27	0.29	0.27	0.31	0.48	0.35	0.24	0.38	0.35
Th	0.072	0.076	0.045	0.093	0.058	0.398	0.097	0.041	0.076	0.080
U	0.031	0.030	0.019	0.036	0.025	0.125	0.037	0.019	0.035	0.036

(Table 5 continued)

sample	D80-2	D76-2	GC12	D73-1	D71-14	D66-1	D64-3	D63-1	D62-2	D61-5
segment	N9a	N9a	N9a	N9a	N9a	N9a	N9b	N9b	N9b	N9b
latitude (^{o}S)	39.046	39.203	39.303	39.453	39.617	39.906	40.029	40.092	40.135	40.185
longitude (^{o}W)	91.579	91.564	91.568	91.537	91.512	91.502	91.584	91.578	91.580	91.566
depth (m)	3578	3260	3377	3426	3243	3637	3752	3704	3681	3651
lava type	T-MORB	N-MORB	N-MORB	N-MORB	N-MORB	N-MORB	N-MORB	N-MORB	N-MORB	N-MORB
K/Ti	0.16	0.10	0.05	0.08	0.06	0.06	0.08	0.08	0.07	0.08
	major element composition (weight %)									
# points	5	5	5	5	5	5	5	1	3	5
SiO_2	50.59	50.49	50.50	50.83	50.83	50.59	50.64	50.90	50.62	50.83
TiO_2	1.20	1.10	1.03	1.55	1.79	1.74	1.38	1.44	1.51	1.52
Al_2O_3	16.28	16.53	16.05	15.49	15.05	14.65	15.54	15.14	15.19	15.32
FeO*	8.37	7.76	8.28	9.20	9.87	10.00	8.92	8.91	9.31	9.21
MnO	0.17	0.17	0.15	0.17	0.17	0.19	0.16	0.14	0.15	0.14
MgO	9.06	9.28	9.39	8.01	7.82	7.50	8.52	8.18	8.11	7.97
CaO	11.60	11.95	12.22	11.51	11.22	11.59	11.81	11.68	11.73	11.49
Na_2O	2.49	2.65	2.30	2.91	2.91	2.86	2.44	2.54	2.63	2.80
K_2O	0.14	0.08	0.04	0.09	0.08	0.08	0.07	0.08	0.08	0.08
P_2O_5	0.12	0.09	0.08	0.13	0.16	0.16	0.14	0.14	0.13	0.15
sum	100.01	100.10	100.03	99.90	99.89	99.36	99.62	99.16	99.46	99.51
	trace element composition (ppm)									
Sc	36.5	33.9	33.9	38.7	40.1	43.2	40.8	41.3	42.7	43.7
Cr	404	396	353	360	273	344	381	352	367	367
Ni	167.0	166.2	134.5	122.9	109.7	91.2	139.1	116.7	111.8	110.7
Cu	66.1	68.4	64.8	72.0	60.5	70.7	69.1	64.3	72.1	70.2
Zn	65.6	53.7	54.9	81.8	83.2	82.1	73.4	68.8	75.5	75.8
Rb	1.053	0.229	0.160	0.300	0.300	0.283	0.500	0.643	0.521	0.408
Sr	135	143	99	136	117	121	111	117	122	127
Y	28.3	25.0	26.7	35.7	40.4	38.9	31.6	34.3	35.6	36.3
Zr	86.6	79.5	65.7	102.0	114.2	111.9	88.7	96.8	101.1	107.1
Nb	2.87	1.20	0.79	1.63	1.62	1.56	1.79	1.87	1.65	1.63
Cs	0.0105	0.0029	0.0015	0.0033	0.0040	0.0030	0.0063	0.0079	0.0057	0.0036
Ba	10.97	2.46	1.67	3.45	3.30	3.11	4.55	5.75	4.46	3.83
La	3.38	2.62	2.01	3.03	3.22	3.15	2.89	3.03	3.03	3.28
Ce	9.58	8.11	6.61	10.05	10.94	10.65	9.24	9.53	9.58	10.32
Pr	1.54	1.37	1.12	1.77	1.98	1.93	1.59	1.67	1.71	1.82
Nd	8.2	7.4	6.8	10.2	11.1	10.8	8.9	9.3	9.4	10.1
Sm	2.79	2.45	2.22	3.43	3.82	3.66	2.94	3.38	3.37	3.56
Eu	1.01	0.91	0.84	1.20	1.31	1.27	1.02	1.21	1.22	1.26
Gd	3.81	3.28	3.10	4.70	5.23	5.05	4.13	4.60	4.60	4.76
Tb	0.745	0.623	0.593	0.857	0.987	0.949	0.786	0.922	0.924	0.961
Dy	4.48	3.76	3.69	5.33	6.05	5.85	4.88	5.45	5.50	5.62
Ho	1.005	0.847	0.849	1.212	1.353	1.300	1.122	1.232	1.239	1.264
Er	2.81	2.18	2.22	3.19	3.55	3.43	2.94	3.38	3.40	3.48
Tm	0.445	0.326	0.341	0.473	0.543	0.521	0.452	0.536	0.534	0.549
Yb	2.77	2.21	2.26	3.13	3.63	3.44	2.97	3.32	3.32	3.37
Lu	0.445	0.335	0.335	0.480	0.554	0.524	0.458	0.535	0.523	0.545
Hf	2.09	1.76	1.52	2.50	2.81	2.67	2.19	2.45	2.48	2.56
Ta	0.185	0.091	0.058	0.116	0.117	0.109	0.120	0.139	0.128	0.126
Pb	0.32	0.30	0.23	0.39	0.42	0.45	0.87	0.39	0.39	0.44
Th	0.165	0.060	0.038	0.089	0.078	0.082	0.105	0.114	0.092	0.084
U	0.062	0.030	0.019	0.040	0.036	0.036	0.042	0.042	0.039	0.038

(Table 5 continued)

sample	D60-3	D59-1	D58-1	D57-1	D56-5	D55-2	D53-6	D52-1	D48-1	D47-1
segment	N9b	N10	N10	N10	N10	N10	N10	N10	N10	N10
latitude (^{o}S)	40.223	40.276	40.310	40.358	40.393	40.459	40.671	40.798	41.006	41.053
longitude (^{o}W)	91.578	91.888	91.889	91.877	91.885	91.904	91.877	91.859	91.871	91.854
depth (m)	3714	3590	3672	3674	3613	3569	3391	3770	3809	4313
lava type	N-MORB	N-MORB	N-MORB	N-MORB	N-MORB	N-MORB	N-MORB	N-MORB	N-MORB	N-MORB
K/Ti	0.08	0.07	0.07	0.06	0.07	0.04	0.06	0.03	0.11	0.07
	major element composition (weight %)									
# points	2	4	5	5	5	5	5	4	5	2
SiO_2	50.72	49.80	50.41	50.65	50.75	50.14	50.55	49.46	50.21	49.43
TiO_2	1.93	1.25	1.47	1.55	1.34	1.03	1.09	0.76	1.35	1.25
Al_2O_3	14.77	16.20	15.21	15.00	14.84	15.98	15.93	17.27	15.99	15.60
FeO*	9.79	9.12	9.72	9.89	9.60	8.64	8.76	7.99	8.88	8.91
MnO	0.18	0.18	0.17	0.16	0.17	0.17	0.16	0.15	0.15	0.19
MgO	7.30	8.79	8.28	7.94	8.26	9.12	8.90	10.28	8.66	8.52
CaO	10.93	11.77	11.66	11.60	12.20	12.48	12.42	12.47	11.74	11.60
Na_2O	3.10	2.59	2.59	2.72	2.38	2.24	2.49	2.00	2.50	2.51
K_2O	0.11	0.06	0.08	0.07	0.07	0.03	0.05	0.02	0.10	0.06
P_2O_5	0.22	0.12	0.14	0.13	0.10	0.08	0.10	0.06	0.14	0.12
sum	99.05	99.90	99.72	99.70	99.71	99.91	100.44	100.45	99.72	98.20
	trace element composition (ppm)									
Sc	43.0	38.2	43.2	43.1	42.8	39.2	39.0	33.5	40.5	41.5
Cr	320	340	304	315	370	424	406	397	379	335
Ni	102.1	149.4	118.1	110.8	123.0	135.3	129.4	192.5	137.6	139.9
Cu	68.0	72.2	67.9	67.7	70.3	80.1	78.7	82.3	71.5	68.3
Zn	93.8	65.2	79.1	80.2	73.1	62.0	65.4	53.9	72.1	72.5
Rb	0.612	0.281	0.570	0.613	0.403	0.161	0.242	0.096	0.942	0.551
Sr	146	115	109	109	94	83	96	68	109	102
Y	44.6	28.8	37.0	38.6	32.7	26.6	26.9	21.0	30.7	33.3
Zr	139.6	74.3	94.4	95.8	76.8	51.5	59.6	32.6	79.8	80.8
Nb	2.47	1.22	1.80	1.80	1.30	0.60	0.95	0.31	2.98	1.68
Cs	0.0081	0.0032	0.0055	0.0063	0.0035	0.0021	0.0030	0.0005	0.0108	0.0055
Ba	5.70	3.39	5.98	6.87	4.56	1.76	2.86	1.00	12.17	6.34
La	4.40	2.24	2.83	2.86	2.17	1.30	1.60	0.70	2.93	2.42
Ce	14.17	7.59	8.88	9.68	7.31	4.59	5.62	2.74	8.96	7.95
Pr	2.41	1.35	1.64	1.70	1.35	0.90	1.07	0.56	1.53	1.39
Nd	13.6	7.6	9.3	9.7	7.6	5.3	6.3	3.6	8.7	7.9
Sm	4.35	2.67	3.32	3.48	2.90	2.14	2.37	1.57	2.89	2.86
Eu	1.45	0.97	1.21	1.24	1.06	0.83	0.89	0.65	1.02	1.05
Gd	5.91	3.68	4.64	4.78	4.04	3.10	3.29	2.36	4.07	3.90
Tb	1.097	0.708	0.954	0.978	0.834	0.638	0.639	0.506	0.774	0.817
Dy	6.54	4.39	5.65	5.78	4.98	3.89	3.98	3.02	4.75	4.84
Ho	1.509	1.015	1.275	1.297	1.118	0.889	0.904	0.691	1.073	1.109
Er	3.97	2.65	3.54	3.59	3.13	2.45	2.35	1.95	2.84	3.08
Tm	0.593	0.401	0.560	0.565	0.492	0.389	0.354	0.308	0.432	0.484
Yb	3.91	2.69	3.46	3.51	3.06	2.37	2.36	1.91	2.87	3.04
Lu	0.603	0.413	0.556	0.570	0.494	0.381	0.359	0.308	0.442	0.492
Hf	3.33	1.85	2.40	2.44	1.97	1.40	1.58	0.95	2.07	1.97
Ta	0.165	0.085	0.139	0.139	0.103	0.051	0.062	0.036	0.182	0.132
Pb	0.54	0.32	0.38	0.39	0.30	0.20	0.24	0.11	0.32	0.32
Th	0.142	0.065	0.091	0.090	0.064	0.028	0.046	0.015	0.150	0.081
U	0.056	0.024	0.036	0.036	0.026	0.013	0.018	0.006	0.053	0.031

Table 6: Estimated Minimum Error in Trace Elements from the Northern Chile Ridge

sample	D112-3	D111-1	D110-6	GC23-1	D109-1	GC22	D108-1	D107-12	D106-1	D105-2
	major element standard deviation (1 σ, weight %)									
SiO_2	0.78	0.13	0.13	0.23	0.12	0.09	0.58	0.22	0.13	0.17
TiO_2	0.03	0.05	0.03	0.04	0.04	0.05	0.03	0.02	0.03	0.03
Al_2O_3	0.11	0.03	0.05	0.02	0.05	0.12	0.10	0.11	0.02	0.08
FeO*	0.14	0.16	0.04	0.09	0.09	0.12	0.08	0.12	0.14	0.10
MnO	0.03	0.02	0.04	0.02	0.05	0.02	0.03	0.02	0.03	0.06
MgO	0.02	0.06	0.03	0.06	0.07	0.07	0.07	0.03	0.04	0.09
CaO	0.12	0.08	0.07	0.15	0.05	0.05	0.15	0.18	0.05	0.05
Na_2O	0.06	0.09	0.05	0.06	0.06	0.07	0.09	0.02	0.03	0.03
K_2O	0.01	0.01	0.01	0.01	0.01	0.01	0.01	0.01	0.00	0.01
P_2O_5	0.01	0.01	0.02	0.02	0.03	0.02	0.02	0.01	0.02	0.02
	trace element estimated minimum error (ppm)									
Sc	0.3	0.1	0.3	0.7	0.3	0.6	0.7	0.5	0.2	0.1
Cr	2	2	13	5	6	6	4	4	4	6
Ni	1.2	2.0	3.9	3.7	1.7	0.7	1.0	1.6	0.3	1.0
Cu	0.7	0.5	3.0	0.6	1.4	0.3	0.9	0.3	0.4	0.4
Zn	0.8	0.7	2.3	0.3	1.5	0.2	1.5	0.3	0.3	0.7
Rb	0.015	0.074	0.050	0.172	0.013	0.014	0.016	0.061	0.019	0.008
Sr	1	4	3	2	1	1	1	2	2	1
Y	0.3	0.3	0.4	0.1	0.1	0.2	0.7	0.6	0.1	0.1
Zr	0.9	0.3	1.6	0.6	0.8	1.3	1.3	2.8	0.9	0.2
Nb	0.11	0.09	0.13	0.25	0.04	0.05	0.06	0.12	0.03	0.02
Cs	0.0009	0.0003	0.0004	0.0047	0.0008	0.0008	0.0007	0.0001	0.0006	0.0000
Ba	0.24	0.35	0.41	0.30	0.11	0.12	0.20	0.60	0.12	0.03
La	0.04	0.13	0.10	0.11	0.01	0.06	0.04	0.11	0.01	0.02
Ce	0.05	0.14	0.02	0.37	0.06	0.32	0.09	0.30	0.11	0.12
Pr	0.07	0.07	0.06	0.06	0.02	0.03	0.05	0.10	0.07	0.07
Nd	0.4	0.3	0.3	0.4	0.2	0.2	0.4	0.2	0.2	0.2
Sm	0.08	0.05	0.05	0.12	0.03	0.08	0.05	0.02	0.05	0.11
Eu	0.03	0.01	0.02	0.02	0.01	0.00	0.02	0.02	0.03	0.04
Gd	0.09	0.04	0.02	0.07	0.01	0.03	0.02	0.14	0.07	0.07
Tb	0.010	0.002	0.003	0.030	0.013	0.006	0.015	0.005	0.015	0.016
Dy	0.13	0.03	0.07	0.22	0.10	0.01	0.07	0.05	0.07	0.09
Ho	0.035	0.015	0.004	0.026	0.019	0.016	0.019	0.014	0.024	0.021
Er	0.06	0.01	0.03	0.10	0.04	0.03	0.05	0.07	0.04	0.03
Tm	0.006	0.006	0.003	0.015	0.002	0.003	0.012	0.004	0.004	0.012
Yb	0.07	0.05	0.05	0.13	0.06	0.08	0.13	0.07	0.05	0.07
Lu	0.007	0.001	0.004	0.019	0.009	0.002	0.011	0.003	0.003	0.004
Hf	0.09	0.02	0.04	0.06	0.07	0.08	0.11	0.04	0.07	0.05
Ta	0.002	0.006	0.006	0.022	0.002	0.005	0.003	0.000	0.003	0.001
Pb	0.02	0.02	0.01	0.01	0.02	0.01	0.04	0.01	0.02	0.02
Th	0.002	0.003	0.002	0.004	0.003	0.002	0.002	0.001	0.001	0.001
U	0.003	0.003	0.004	0.002	0.002	0.001	0.001	0.001	0.003	0.002

(Table 6 continued)

sample	D104-SG	D103-1	D102-1	D101-2	D99-3	D97-SG	D93-1	D92-1	D88-1	D87-2
	major element standard deviation (1 σ, weight %)									
SiO_2	0.08	0.18	0.12	0.21	0.34	0.23	0.11	0.22	0.07	0.32
TiO_2	0.06	0.04	0.03	0.04	0.07	0.09	0.02	0.05	0.05	0.05
Al_2O_3	0.07	0.08	0.04	0.08	0.08	0.21	0.09	0.04	0.05	0.07
FeO*	0.08	0.15	0.10	0.12	0.15	0.14	0.18	0.04	0.11	0.22
MnO	0.04	0.03	0.04	0.03	0.03	0.03	0.02	0.03	0.04	0.03
MgO	0.07	0.06	0.09	0.09	0.04	0.28	0.06	0.08	0.05	0.03
CaO	0.10	0.11	0.21	0.09	0.05	0.17	0.13	0.11	0.07	0.19
Na_2O	0.06	0.08	0.05	0.07	0.04	0.15	0.05	0.05	0.07	0.05
K_2O	0.01	0.01	0.00	0.04	0.01	0.01	0.00	0.01	0.01	0.01
P_2O_5	0.02	0.02	0.02	0.03	0.01	0.02	0.01	0.02	0.01	0.02
	trace element estimated minimum error (ppm)									
Sc	0.3	0.4	0.6	0.3	0.5	0.3	0.1	0.5	0.5	0.7
Cr	2	6	3	5	2	1	1	6	10	5
Ni	0.4	1.1	1.1	1.2	0.4	0.8	2.4	1.0	4.2	1.4
Cu	1.1	1.0	0.4	0.3	2.5	0.4	0.5	0.4	0.2	0.7
Zn	0.3	1.1	0.6	0.9	0.2	1.1	0.9	0.7	1.5	1.1
Rb	0.689	0.011	0.039	0.390	0.053	0.008	0.003	0.010	0.002	0.016
Sr	3	1	1	7	1	1	1	1	1	1
Y	0.5	0.1	0.1	0.3	0.2	0.1	0.6	0.4	0.1	0.2
Zr	2.5	0.4	1.2	2.0	3.0	1.1	1.5	0.4	0.9	0.5
Nb	0.63	0.04	0.04	0.56	0.10	0.06	0.02	0.05	0.04	0.04
Cs	0.0041	0.0003	0.0007	0.0045	0.0007	0.0008	0.0005	0.0008	0.0003	0.0005
Ba	2.2	0.15	0.22	8.5	0.55	0.20	0.25	0.02	0.44	0.27
La	0.26	0.03	0.05	0.23	0.08	0.02	0.09	0.05	0.04	0.03
Ce	0.52	0.04	0.12	0.24	0.01	0.14	0.14	0.16	0.02	0.04
Pr	0.14	0.08	0.04	0.35	0.09	0.03	0.03	0.13	0.06	0.04
Nd	0.5	0.1	0.1	0.6	0.2	0.3	0.1	0.2	0.3	0.1
Sm	0.06	0.07	0.04	0.13	0.15	0.03	0.03	0.04	0.05	0.02
Eu	0.02	0.02	0.01	0.03	0.02	0.02	0.02	0.02	0.01	0.02
Gd	0.15	0.07	0.06	0.14	0.00	0.02	0.05	0.05	0.02	0.04
Tb	0.003	0.009	0.010	0.032	0.003	0.008	0.006	0.017	0.018	0.004
Dy	0.10	0.05	0.05	0.05	0.03	0.06	0.02	0.09	0.07	0.05
Ho	0.024	0.018	0.010	0.022	0.021	0.022	0.008	0.006	0.004	0.019
Er	0.17	0.08	0.01	0.02	0.01	0.06	0.04	0.03	0.06	0.03
Tm	0.007	0.011	0.014	0.004	0.005	0.006	0.010	0.012	0.014	0.002
Yb	0.08	0.09	0.08	0.06	0.04	0.06	0.07	0.06	0.06	0.04
Lu	0.004	0.006	0.018	0.002	0.014	0.012	0.005	0.013	0.006	0.011
Hf	0.05	0.05	0.07	0.10	0.04	0.04	0.03	0.10	0.04	0.03
Ta	0.014	0.002	0.004	0.051	0.000	0.001	0.002	0.002	0.003	0.002
Pb	0.06	0.02	0.01	0.10	0.01	0.02	0.01	0.03	0.01	0.02
Th	0.024	0.001	0.004	0.036	0.003	0.003	0.002	0.004	0.002	0.004
U	0.007	0.002	0.002	0.024	0.003	0.001	0.001	0.001	0.001	0.002

(Table 6 continued)

sample	GC17	GC16	D86-5	GC15	D85-9	GC14	GC13	D84-1	D83-1	D82-2
	major element standard deviation (1 σ, weight %)									
SiO_2	0.08	0.12	N/A	0.20	0.14	0.15	0.24	0.31	0.10	0.21
TiO_2	0.08	0.05	N/A	0.03	0.01	0.02	0.03	0.04	0.03	0.03
Al_2O_3	0.08	0.12	N/A	0.05	0.01	0.05	0.04	0.07	0.11	0.07
FeO*	0.06	0.18	N/A	0.07	0.06	0.19	0.10	0.11	0.06	0.13
MnO	0.03	0.04	N/A	0.03	0.03	0.03	0.03	0.03	0.02	0.02
MgO	0.05	0.11	N/A	0.09	0.05	0.02	0.06	0.08	0.06	0.05
CaO	0.10	0.15	N/A	0.08	0.13	0.07	0.10	0.10	0.10	0.06
Na_2O	0.03	0.07	N/A	0.08	0.07	0.07	0.07	0.05	0.08	0.04
K_2O	0.01	0.01	N/A	0.01	0.01	0.01	0.01	0.01	0.00	0.01
P_2O_5	0.02	0.01	N/A	0.02	0.02	0.02	0.02	0.01	0.01	0.02
	trace element estimated minimum error (ppm)									
Sc	0.5	0.5	0.2	0.6	0.7	0.5	0.9	0.3	0.5	0.3
Cr	5	1	7	6	5	11	2	8	2	2
Ni	0.1	3.5	2.2	1.7	1.6	3.0	0.9	2.3	3.1	0.3
Cu	0.1	1.8	0.3	1.1	1.3	0.6	2.6	1.0	2.2	0.5
Zn	0.7	0.4	0.6	1.1	0.6	0.7	3.6	0.7	2.2	0.2
Rb	0.009	0.022	0.006	0.017	0.016	0.057	0.052	0.011	0.021	0.006
Sr	1	2	1	1	2	2	2	1	3	2
Y	0.4	0.1	0.3	0.4	0.8	0.4	0.1	0.2	0.3	0.2
Zr	1.9	1.7	0.7	0.3	0.6	2.2	0.3	0.8	2.5	0.7
Nb	0.03	0.04	0.01	0.07	0.05	0.08	0.10	0.03	0.10	0.05
Cs	0.0010	0.0003	0.0005	0.0008	0.0003	0.0036	0.0001	0.0004	0.0003	0.0004
Ba	0.11	0.34	0.18	0.30	0.16	1.14	0.56	0.10	0.12	0.07
La	0.05	0.06	0.02	0.03	0.02	0.18	0.11	0.02	0.08	0.03
Ce	0.18	0.11	0.15	0.08	0.04	0.12	0.15	0.10	0.22	0.12
Pr	0.12	0.08	0.07	0.08	0.05	0.06	0.02	0.02	0.03	0.07
Nd	0.4	0.4	0.2	0.1	0.3	0.5	0.3	0.2	0.2	0.2
Sm	0.04	0.04	0.04	0.04	0.06	0.05	0.05	0.10	0.11	0.04
Eu	0.02	0.02	0.02	0.01	0.02	0.02	0.00	0.02	0.02	0.02
Gd	0.16	0.06	0.09	0.04	0.07	0.11	0.02	0.05	0.16	0.11
Tb	0.009	0.022	0.009	0.006	0.014	0.023	0.006	0.011	0.031	0.010
Dy	0.01	0.07	0.02	0.09	0.03	0.09	0.02	0.08	0.09	0.10
Ho	0.013	0.018	0.007	0.009	0.027	0.041	0.011	0.011	0.016	0.017
Er	0.01	0.01	0.04	0.03	0.01	0.06	0.04	0.02	0.10	0.02
Tm	0.008	0.013	0.001	0.006	0.008	0.005	0.008	0.007	0.009	0.003
Yb	0.09	0.06	0.04	0.06	0.06	0.12	0.07	0.06	0.09	0.07
Lu	0.015	0.007	0.005	0.003	0.005	0.007	0.003	0.009	0.004	0.007
Hf	0.06	0.08	0.02	0.06	0.06	0.07	0.06	0.03	0.09	0.06
Ta	0.001	0.003	0.000	0.003	0.004	0.018	0.000	0.001	0.004	0.007
Pb	0.02	0.02	0.01	0.02	0.01	0.03	0.01	0.02	0.01	0.01
Th	0.002	0.001	0.004	0.007	0.000	0.007	0.007	0.004	0.005	0.005
U	0.003	0.001	0.003	0.002	0.000	0.001	0.002	0.000	0.001	0.002

(Table 6 continued)

sample	D80-2	D76-2	GC12	D73-1	D71-14	D66-1	D64-3	D63-1	D62-2	D61-5
	major element standard deviation (1 σ, weight %)									
SiO_2	0.23	0.19	0.07	0.14	0.12	0.18	0.08	N/A	0.08	0.12
TiO_2	0.03	0.01	0.05	0.04	0.03	0.02	0.07	N/A	0.04	0.08
Al_2O_3	0.06	0.06	0.03	0.06	0.07	0.07	0.07	N/A	0.05	0.08
FeO*	0.11	0.15	0.09	0.12	0.11	0.13	0.15	N/A	0.13	0.11
MnO	0.03	0.03	0.02	0.03	0.02	0.01	0.02	N/A	0.01	0.03
MgO	0.08	0.05	0.02	0.05	0.03	0.06	0.08	N/A	0.03	0.06
CaO	0.03	0.16	0.10	0.14	0.10	0.10	0.07	N/A	0.16	0.10
Na_2O	0.04	0.06	0.05	0.09	0.09	0.09	0.03	N/A	0.02	0.08
K_2O	0.01	0.01	0.01	0.01	0.00	0.02	0.02	N/A	0.02	0.01
P_2O_5	0.02	0.03	0.02	0.01	0.03	0.00	0.03	N/A	0.03	0.02
	trace element estimated minimum error (ppm)									
Sc	0.4	0.7	0.6	0.3	0.3	0.3	0.6	1.1	0.5	0.2
Cr	7	7	8	4	3	2	5	10	7	7
Ni	2.0	1.9	0.9	1.1	1.2	0.2	2.1	4.2	1.8	1.2
Cu	0.7	2.0	0.7	0.6	0.5	0.6	1.5	2.5	1.0	0.9
Zn	1.8	1.4	0.6	0.3	0.8	0.3	1.3	2.3	1.1	0.4
Rb	0.059	0.005	0.002	0.006	0.002	0.006	0.015	0.002	0.021	0.005
Sr	2	5	2	2	1	1	2	1	2	1
Y	0.2	0.0	0.2	0.4	0.4	0.1	0.3	0.1	0.3	0.7
Zr	0.4	1.5	0.4	1.5	1.0	0.3	1.4	0.9	1.7	2.0
Nb	0.10	0.02	0.02	0.07	0.03	0.02	0.02	0.04	0.03	0.05
Cs	0.0002	0.0001	0.0003	0.0006	0.0003	0.0000	0.0007	0.0002	0.0006	0.0005
Ba	0.54	0.07	0.12	0.24	0.19	0.13	0.14	0.27	0.20	0.15
La	0.10	0.01	0.06	0.07	0.02	0.02	0.06	0.04	0.06	0.06
Ce	0.35	0.03	0.15	0.17	0.11	0.05	0.07	0.33	0.15	0.20
Pr	0.01	0.01	0.03	0.09	0.04	0.02	0.08	0.10	0.03	0.05
Nd	0.4	0.4	0.2	0.3	0.3	0.2	0.3	0.2	0.6	0.5
Sm	0.09	0.05	0.03	0.10	0.11	0.04	0.07	0.04	0.07	0.08
Eu	0.06	0.02	0.01	0.02	0.03	0.01	0.01	0.03	0.01	0.02
Gd	0.05	0.05	0.05	0.14	0.14	0.07	0.03	0.04	0.07	0.03
Tb	0.010	0.007	0.005	0.017	0.026	0.005	0.008	0.004	0.001	0.009
Dy	0.07	0.03	0.08	0.07	0.13	0.02	0.05	0.04	0.03	0.04
Ho	0.029	0.013	0.014	0.010	0.033	0.014	0.016	0.013	0.006	0.008
Er	0.04	0.02	0.03	0.08	0.05	0.01	0.00	0.05	0.03	0.01
Tm	0.017	0.010	0.005	0.022	0.010	0.010	0.010	0.001	0.005	0.006
Yb	0.09	0.07	0.04	0.11	0.12	0.07	0.09	0.06	0.08	0.06
Lu	0.003	0.004	0.005	0.018	0.013	0.010	0.007	0.007	0.007	0.003
Hf	0.14	0.05	0.04	0.05	0.10	0.04	0.04	0.06	0.02	0.04
Ta	0.007	0.001	0.002	0.003	0.006	0.002	0.000	0.005	0.001	0.001
Pb	0.04	0.01	0.02	0.02	0.03	0.03	0.04	0.02	0.01	0.01
Th	0.010	0.002	0.001	0.006	0.002	0.003	0.002	0.001	0.003	0.004
U	0.003	0.001	0.001	0.004	0.001	0.002	0.001	0.000	0.001	0.002

(Table 6 continued)

sample	D60-3	D59-1	D58-1	D57-1	D56-5	D55-2	D53-6	D52-1	D48-1	D47-1
	major element standard deviation (1 σ, weight %)									
SiO_2	0.16	0.19	0.13	0.13	0.14	0.23	0.18	0.17	0.08	0.28
TiO_2	0.03	0.04	0.02	0.04	0.02	0.05	0.04	0.03	0.03	0.02
Al_2O_3	0.02	0.04	0.07	0.08	0.11	0.11	0.08	0.03	0.08	0.15
FeO*	0.06	0.14	0.10	0.13	0.18	0.25	0.18	0.11	0.10	0.15
MnO	0.01	0.02	0.02	0.03	0.03	0.01	0.05	0.02	0.04	0.04
MgO	0.02	0.07	0.04	0.04	0.10	0.05	0.08	0.06	0.05	0.14
CaO	0.01	0.09	0.05	0.17	0.15	0.09	0.07	0.14	0.17	0.00
Na_2O	0.04	0.06	0.06	0.03	0.03	0.04	0.04	0.05	0.06	0.05
K_2O	0.00	0.01	0.01	0.01	0.01	0.01	0.01	0.00	0.01	0.00
P_2O_5	0.01	0.02	0.01	0.02	0.02	0.01	0.01	0.03	0.02	0.01
	trace element estimated minimum error (ppm)									
Sc	0.6	0.2	0.3	0.6	0.4	0.3	0.1	0.4	1.2	0.6
Cr	5	5	3	6	9	6	2	4	11	1
Ni	0.9	1.0	0.8	2.4	3.1	1.2	1.0	1.0	4.5	2.5
Cu	0.7	0.8	0.7	1.1	1.7	0.2	0.4	0.4	2.0	0.7
Zn	1.8	0.7	0.3	2.2	2.1	0.8	0.5	0.6	1.6	0.8
Rb	0.011	0.003	0.028	0.019	0.012	0.009	0.010	0.010	0.014	0.021
Sr	3	1	1	2	1	2	0	1	2	1
Y	0.4	0.1	0.9	0.8	0.0	0.3	0.2	0.1	0.5	0.4
Zr	1.9	0.7	1.6	1.0	0.8	1.1	0.6	0.6	1.5	0.7
Nb	0.11	0.03	0.01	0.04	0.06	0.03	0.03	0.01	0.07	0.10
Cs	0.0005	0.0006	0.0005	0.0001	0.0002	0.0001	0.0001	0.0003	0.0008	0.0002
Ba	0.19	0.07	0.03	0.31	0.08	0.13	0.08	0.06	0.19	0.22
La	0.05	0.06	0.04	0.02	0.03	0.01	0.02	0.01	0.03	0.05
Ce	0.15	0.10	0.18	0.07	0.25	0.09	0.03	0.02	0.05	0.18
Pr	0.12	0.03	0.03	0.03	0.03	0.01	0.02	0.01	0.10	0.02
Nd	0.3	0.2	0.4	0.4	0.3	0.1	0.1	0.3	0.3	0.5
Sm	0.06	0.04	0.03	0.07	0.05	0.02	0.04	0.06	0.02	0.04
Eu	0.02	0.02	0.02	0.02	0.02	0.01	0.02	0.01	0.01	0.01
Gd	0.02	0.07	0.07	0.07	0.05	0.06	0.05	0.04	0.04	0.05
Tb	0.017	0.005	0.008	0.007	0.011	0.001	0.010	0.013	0.005	0.008
Dy	0.10	0.04	0.01	0.01	0.02	0.04	0.03	0.05	0.05	0.02
Ho	0.017	0.013	0.021	0.012	0.004	0.018	0.014	0.003	0.019	0.008
Er	0.05	0.04	0.02	0.03	0.07	0.04	0.02	0.04	0.06	0.02
Tm	0.004	0.006	0.007	0.005	0.004	0.001	0.004	0.003	0.005	0.008
Yb	0.07	0.06	0.07	0.10	0.06	0.06	0.05	0.02	0.07	0.04
Lu	0.009	0.007	0.009	0.003	0.010	0.003	0.011	0.003	0.007	0.001
Hf	0.07	0.06	0.02	0.06	0.08	0.05	0.07	0.04	0.04	0.05
Ta	0.007	0.001	0.000	0.004	0.003	0.001	0.001	0.001	0.002	0.002
Pb	0.03	0.02	0.01	0.01	0.02	0.01	0.02	0.00	0.02	0.01
Th	0.003	0.001	0.001	0.001	0.002	0.001	0.002	0.002	0.001	0.001
U	0.002	0.001	0.003	0.001	0.001	0.001	0.001	0.000	0.003	0.000

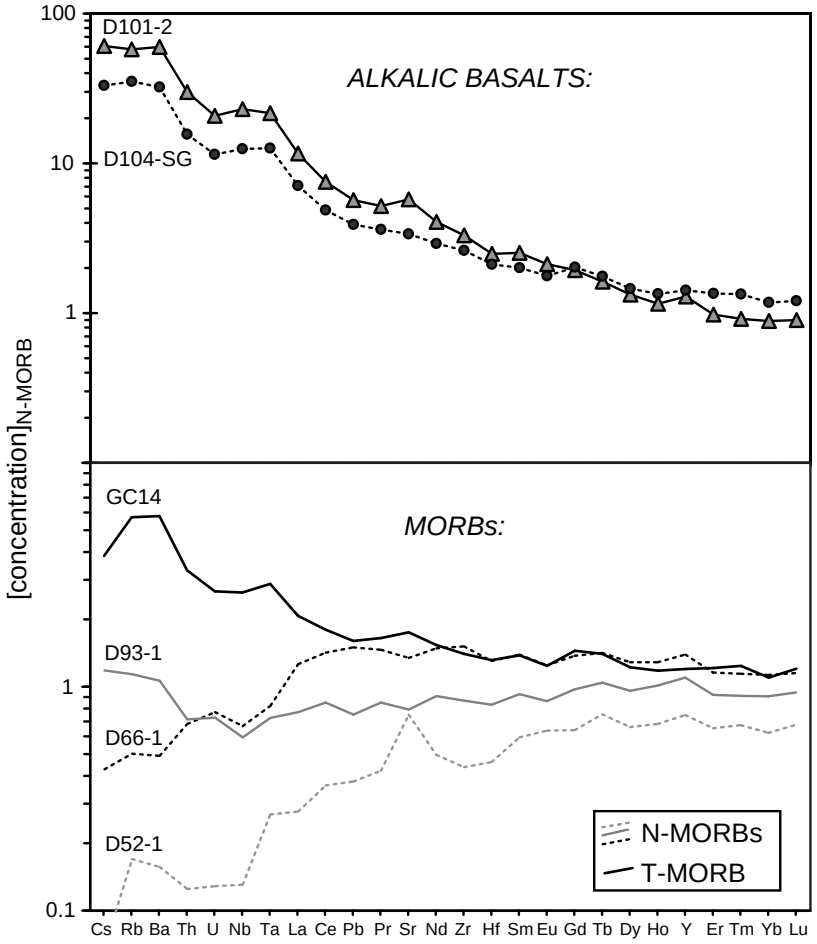

Figure 12: Incompatible trace element contents of alkalic basalts and representative MORBs from the Northern Chile Ridge, normalized to N-MORB from *Sun and McDonough* (1989), and using their order of incompatibility (increasing towards the left). Cs, Rb, and Ba are thought to have similar incompatibilities and behave the same geochemically, as are U, Nb, and Ta (*Sun and McDonough*, 1989).

(*e.g.*, sample D52-1 on Figure 13), and depletion in the trace elements more incompatible than La (*e.g.*, sample D66-1 on Figure 12). Geochemical behavior among the rare earth elements is coherent, and also is coherent among the trace elements more incompatible than La (Figures 13 and 14). However, there is no correlation between the occurrence of one type of depletion and the occurrence of the other type of depletion in the N-MORBs (Figure 14). These two groups of incompatible trace elements define two independent types of depletions (depletion in the rare earth elements, and depletion in the trace elements more highly incompatible than La) in the N-MORB samples.

N-MORBs exhibiting extreme depletions of either type (the "ultra-depleted" samples) are not found in any consistent geographic location or tectonic setting. Sample D92-1, which has the steepest decrease in highly incompatible trace elements (*i.e.*, the lowest Ba/Nb and Ba/Th), was found mid-segment on segment N6, the dying rift. However, sample D66-1, another low Ba/Nb sample, was found at the end of N9a, a pinch-and-swell type segment, proximal to the non-transform offset with N9b. Samples D52-1 and D105-2, the most light-rare-earth depleted samples (*i.e.*, the lowest La/Sm), were found mid-segment on segment N10, an hourglass-shaped segment adjacent to the Valdivia Fracture Zone, and at segment N3, a short ITSC-like segment, respectively.

In general, there are no large-scale regional gradients in incompatible trace element contents along the Northern Chile Ridge (Figure 15). There are subtle differences in trace element character between segments (*e.g.*, segment N8 is more heterogeneous than segment N9a in Ba/Nb and Th/La; segment N3 is more depleted than the other

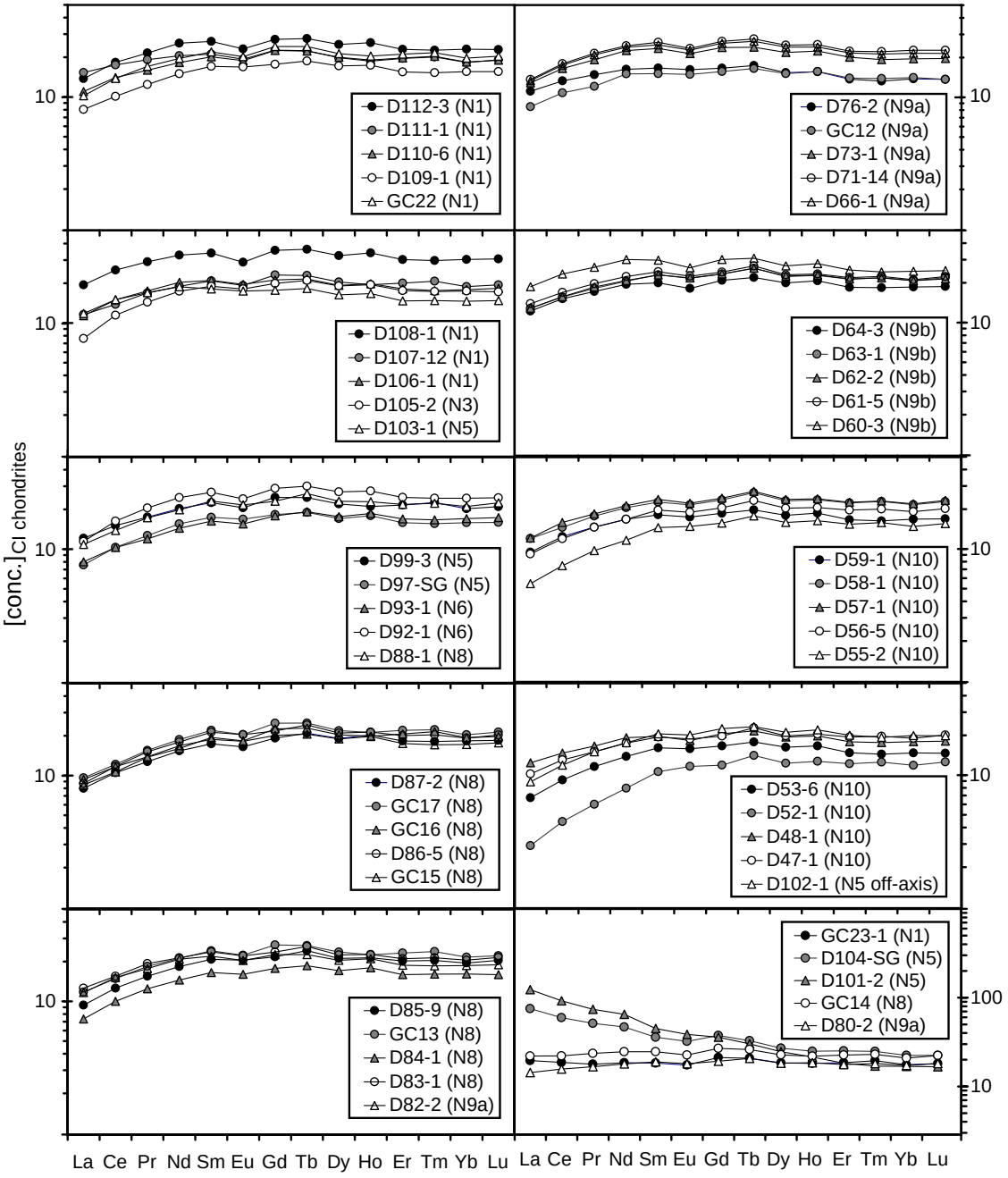

Figure 13: Rare earth element abundances in Northern Chile Ridge samples, normalized to concentrations in CI chondrites (*McDonough and Sun*, 1995). The segment at which each sample was found is listed in parentheses after the sample name.

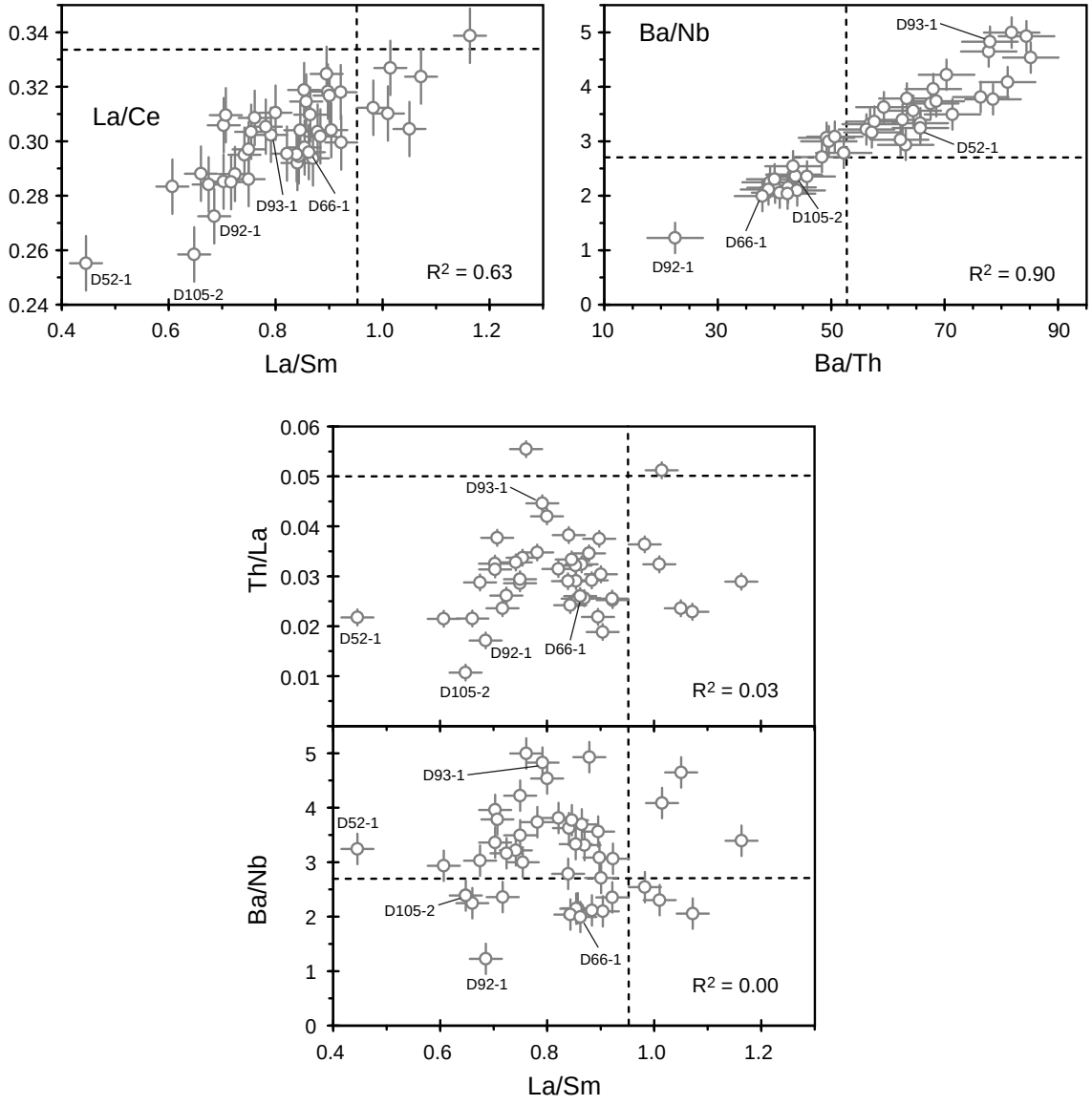

Figure 14: Covarying ratios of incompatible trace elements in Northern Chile Ridge N-MORBs. Top, correlations within the group of rare earth elements (La/Ce vs. La/Sm), and within the group of the more highly incompatible trace elements (Ba/Nb vs. Ba/Th). Bottom, independent behavior between these two groups. The most depleted samples in each group are labeled. $R^2 = \{n(XY)-(X)(Y)\}^2/\{[n X^2-(X)^2][n Y^2-(Y)^2]\}$, the square of the Pearson product moment correlation coefficient. Dotted lines show the values for typical N-MORB from *Sun and McDonough* (1989): La/Ce = 0.33, La/Sm = 0.95, Ba/Nb = 2.7, Ba/Th = 52.5, Th/La = 0.05. See text for discussion.

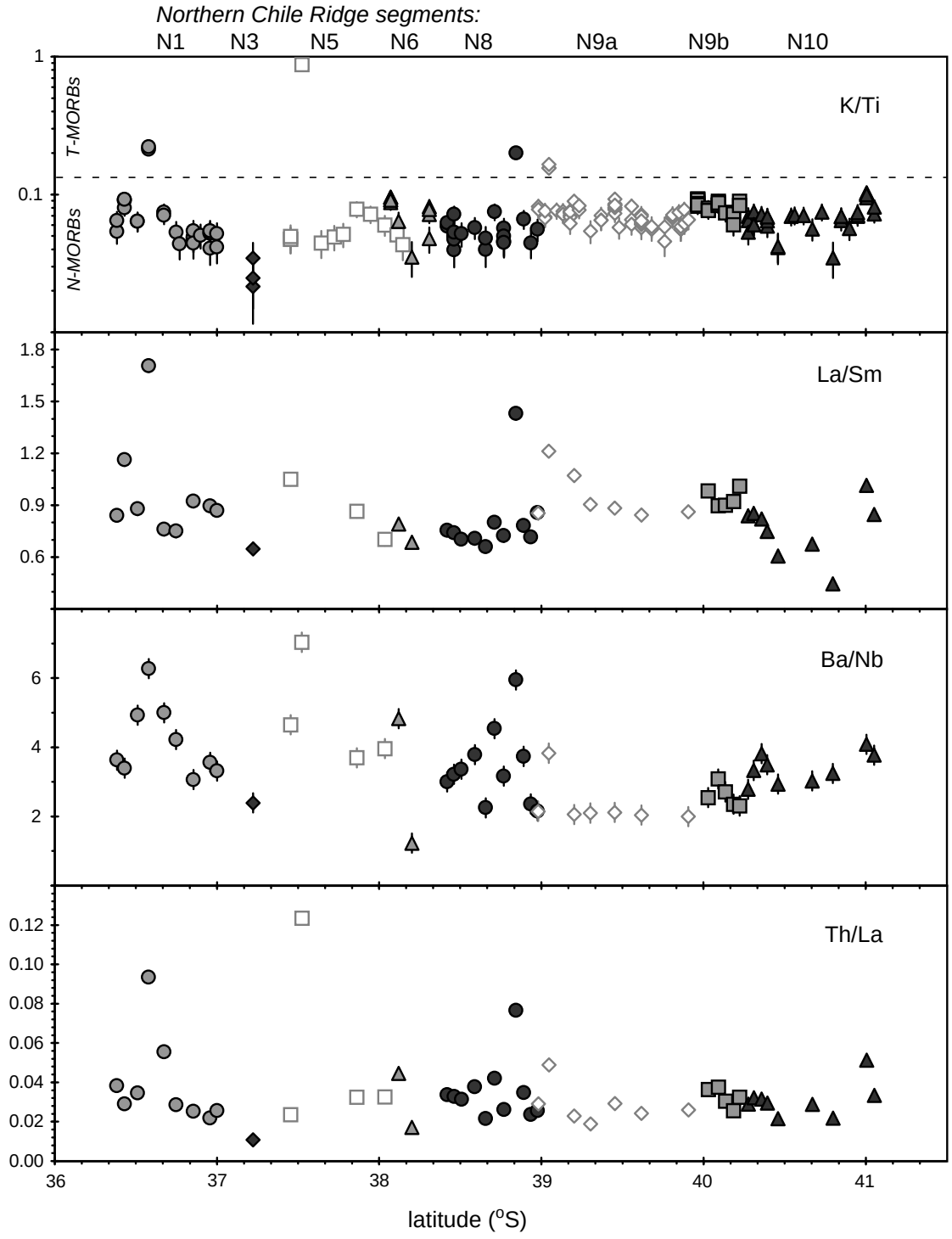

Figure 15: Geographic variations in incompatible trace elements of Northern Chile Ridge samples. Each segment is shown with a different symbol, and labeled along the top of the figure.

segments). However, the only differences that consistently appear in all trace elements are those that distinguish T-MORBs from N-MORBs.

Crystallinity

Many of the samples are phyric in hand specimen. Phenocrysts and microlites were identified in thin section by optical microscopy for 42 samples (Table 7).

Most samples contained a plagioclase+olivine±clinopyroxene±spinel phenocryst assemblage. Clinopyroxene phenocrysts were recognizable by their hourglass twinning, brownish color in plane light, and lack of a distinct crystal habit. Spinel phenocrysts were dark brown isotropic euhedra. Samples commonly contained two populations of plagioclase phenocrysts, one which consisted of large rounded or resorbed crystals, and one which consisted of slightly smaller euhedral or skeletal crystals. Smaller plagioclase phenocrysts are usually intergrown with olivine.

The microlite assemblage was generally the same as the phenocryst assemblage, except that spinel was not observed as a microlite phase (a microlite spinel phase may have been present, but too small to detect with an optical microscope). Samples D94-1, D94-5, D91-4, D91-12, and D91-11, all from segment N6, were unusual in that they contained a plagioclase+olivine microlite assemblage but only olivine as a phenocryst phase. Sample D93-1, a primitive N-MORB (MgO = 9.78 weight %) also from segment N6, contained only olivine as microlites, and olivine+spinel as phenocrysts.

Table 7:
Phenocryst Phases Observed in Thin Sections

sample bin	sample name	segment	lava type	phenocryst phases†	microlite phases†
D112-b	D112-3	N1	N-MORB	plag, ol, sp	plag, ol
D110-b	D110-5	N1	N-MORB	plag, ol, sp	plag, ol
D108-e	D108-7	N1	N-MORB	cpx, plag, ol	cpx?, plag, ol
D107-b	D107-6	N1	N-MORB	plag, ol, sp	plag, ol
D105-a	D105-2	N3	N-MORB	plag, ol; sp/glass inclusions	cpx?, plag, ol
D105-c	D105-6	N3	N-MORB	cpx, plag, ol	cpx,plag,ol
D104	D104-SG	N5	alkalic	plag,ol	glassy
D101	D101-4	N5	alkalic	aphyric	plag, ol
D100	D100-3	N5	N-MORB	plag	cpx?,plag, ol
GC18	GC18	N5	N-MORB	plag,ol	plag,ol
D99	D99-3	N5	N-MORB	cpx?, plag, ol	cpx?, plag, ol
D95	D95-1	N5	N-MORB	plag,ol	cpx?,plag, ol
D94-a	D94-1	N6	N-MORB	ol	plag,ol
D94-a	D94-5	N6	N-MORB	ol	cpx,plag,ol
D93	D93-1	N6	N-MORB	ol,sp	ol
D92	D92-1	N6	N-MORB	plag, ol	plag, ol, oxides?
D91-a	D91-1	N6	N-MORB	plag,ol	plag,ol
D91-b	D91-4	N6	N-MORB	ol	plag,ol
D91-b	D91-8	N6	N-MORB	plag,ol	plag,ol
D91-c	D91-12	N6	N-MORB	ol	plag,ol
D91-d	D91-11	N6	N-MORB	ol	plag,ol
GC16	GC16	N8	N-MORB	plag,ol	glassy
D88-b	D88-5	N8	N-MORB	plag,ol	plag,ol
D85-b	D85-3	N8	N-MORB	plag,ol	plag,ol
D84	D84-1	N8	N-MORB	plag,ol	plag,ol
D80-a	D80-1	N9a	T-MORB	plag,ol,sp	plag,ol
D77-a	D77-1	N9a	N-MORB	plag,ol,sp	plag,ol
D76	D76-2	N9a	N-MORB	plag,ol,sp	plag,ol
D65-f	D65-14	N9b	N-MORB	plag,ol	plag,ol
D65-c	D65-7	N9b	N-MORB	plag,ol,sp	plag,ol
D64-a	D64-3	N9b	N-MORB	plag,ol	plag
D63-a	D63-4	N9b	N-MORB	cpx,plag,ol	
D61-a	D61-5	N9b	N-MORB	plag,ol	
D60-b	D60-6	N9b	N-MORB	plag,ol	
D59-c	D59-5	N10	N-MORB	plag,ol	plag,ol,cpx
D57	D57-4	N10	N-MORB	plag,ol	
D54	D54-4	N10	N-MORB	plag,ol	plag,ol
D52	D52-1	N10	N-MORB	plag,ol,sp	plag,ol
D50	D50-1	N10	N-MORB	cpx,plag,ol,sp	
D49-b	D49-5	N10	N-MORB	aphyric	
D48-b	D48-4	N10	N-MORB	plag,ol	plag
D48-c	D48-5	N10	N-MORB	plag,ol	plag

† cpx, clinopyroxene; plag, plagioclase; ol, olivine; sp, spinel.

PETROGENESIS

The sample yield from the PANORAMA Expedition at the Northern Chile Ridge is more chemically and petrologically diverse than that which had been found previously by *Bach et al.* (1996). There is a large suite of MORBs surrounding a geographically restricted region of alkalic basalt recovery. It is important to constrain the petrogeneses of both the MORBs and the alkalic basalts, and to find the petrogenetic relationship between the two groups of samples. This will allow inferences about regional-scale mantle processes at the ridge, and furthermore will allow preliminary evaluation of whether a systematic transform fault effect (TFE) is present.

This section first discusses evidence for the petrogenesis of the MORB suite, starting with quantitative models of low-pressure crystallization controls on major element compositions in the MORB glasses. Then partial melting and magma mixing processes among the MORBs are discussed, again relying on quantitative models. The petrogenetic origin of the alkalic basalts is given separate attention, for even though the rareness of these samples renders interpretation of many petrogenetic details difficult, there are fundamental conclusions that can be drawn which are important for understanding the ridge as a whole. Finally, the models are summarized in a specific hypothesis for the petrogenesis of the ridge, accounting for both the MORBs and the alkalic basalts.

Crystal Fractionation

The coherent major element trends in the Northern Chile Ridge MORBs, described in the Results section (Figure 7), are typical of progressive differentiation by crystal fractionation at low pressures in oceanic tholeiitic basalts. Specifically, this pattern is consistent with fractionation of a clinopyroxene+plagioclase+olivine phase assemblage on a low-pressure cotectic (*e.g.*, *Stolper*, 1980). This is generally thought to happen as magma cools and differentiates in a shallow magma chamber or melt lens (*e.g.*, *Sinton and Detrick*, 1992). As described previously, the T-MORBs and N-MORBs define essentially the same trends, indicating that their parent magma major element compositions and conditions of differentiation were indistinguishable (except in K_2O).

Forward models of crystal fractionation using the MELTS software (*Ghiorso and Sack*, 1995) provide quantitative constraints on the differentiation of Northern Chile Ridge MORBs (Figure 16). MELTS draws on a database of experimental mineral-melt thermodynamics data to model crystallization of a given parent magma composition at specified conditions of pressure and oxygen fugacity (*Ghiorso and Sack*, 1995). The pressure at which crystal fractionation occurred in a suite of samples can be constrained because it controls the MgO content at which clinopyroxene joins the crystallizing phase assemblage (*Grove et al.*, 1992). The H_2O content in the magma similarly affects the MgO content at which clinopyroxene, and also plagioclase, join the crystallizing assemblage, but to a much lesser degree than does pressure.

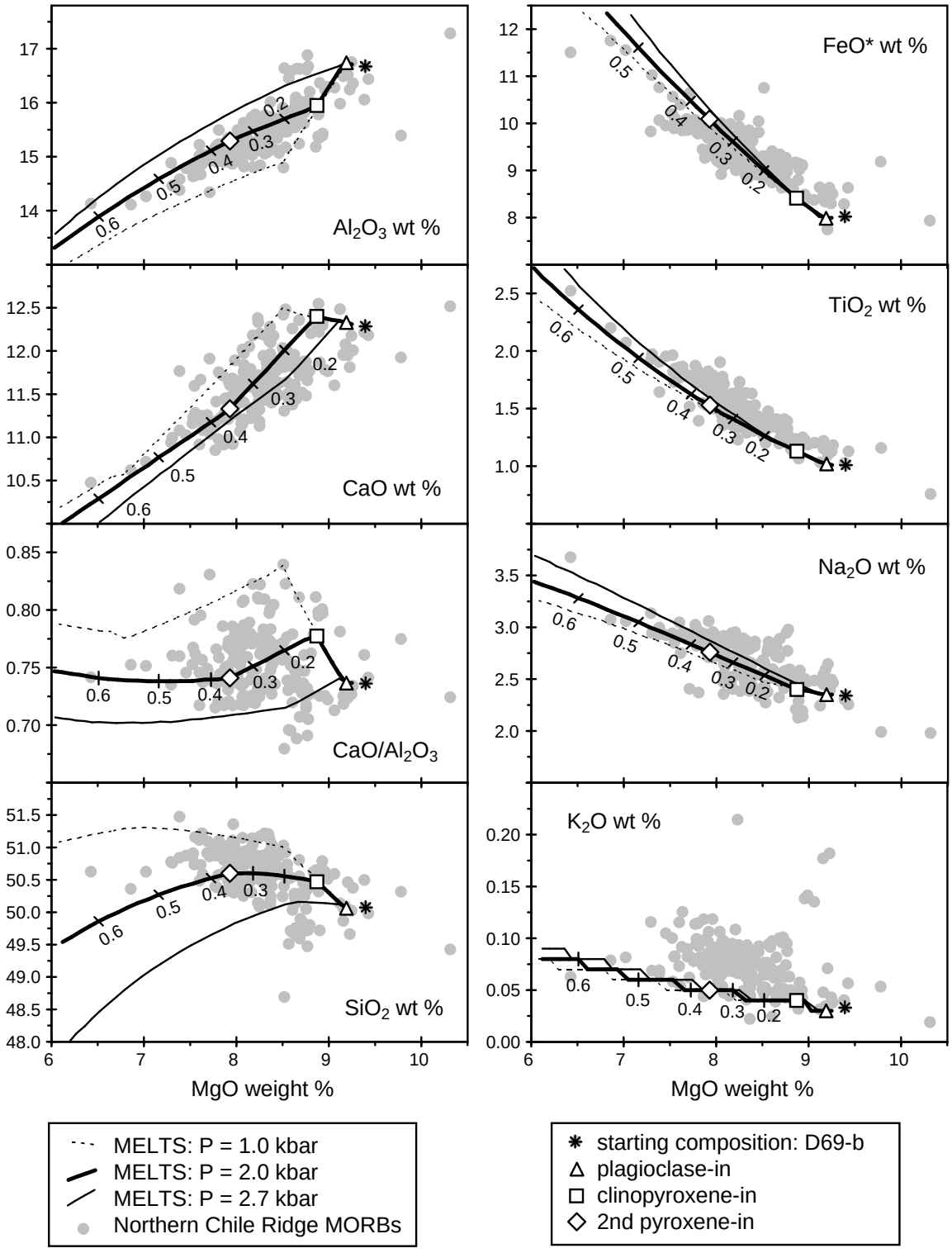

Figure 16: MELTS crystal fractionation model for Northern Chile Ridge MORBs at P = 2.0 kbar. Constraining models (P = 1.0, 2.7 kbar) shown for comparison. Phase-in points (open symbols) and extents of crystallization (tick marks) are shown. See text for details.

The models were performed using MELTS Version 3.0.0, Revision 3.6. All models were of isobaric fractionation of solids. The oxygen fugacity buffer was set at QFM-2. Oxygen fugacity is thought not to vary much at mid-ocean ridges (*Christie et al.*, 1986) and not to have a significant effect on crystallization (*Michael and Chase*, 1987). The starting composition, or the parent magma in the model, was Northern Chile Ridge sample D69-b. This primitive N-MORB from segment N9a, with Mg # = 69.9 and MgO = 9.40 weight %, is one of the highest-MgO samples in the main body of the data, and is on the main trend in all major element oxides.

A H_2O content of 0.01 weight % was assumed for the parent magma in the model, although the MELTS models are not sensitive to even moderate differences in the H_2O content of the parent magma. Low H_2O contents are expected for the depleted samples at the Northern Chile Ridge, since H_2O behaves in basaltic magmas as an incompatible trace element (*e.g.*, *Michael*, 1988; *Danyushevsky et al.*, 2000). H_2O contents of 0.09-0.23 weight % were found in the N-MORB samples of *Bach et al.* (1996), but many of their samples were located off-axis in old crust, and may have been affected by alteration.

The best-fit crystal fractionation model to the main trends of Northern Chile Ridge MORBs is at a pressure of 2.0 kbar. Figure 16 shows the path as the magma composition changes during the crystal fractionation process; this path is called the liquid line of descent (LLD). The model predicts that the most evolved lavas in the suite experienced up to 40-60% crystallization relative to the primitive lavas. Plagioclase-in occurs at an MgO content of 9.2 weight % (essentially on the liquidus), and clinopyroxene-in occurs at an MgO content of 8.9 weight %.

The pressure of crystallization is constrained between 1.0 and 2.7 kbar by the Al_2O_3 and CaO contents in the lavas (Figure 16). The lavas cannot have crystallized at pressures greater than approximately 3.0 kbar, because at that pressure clinopyroxene begins crystallizing before plagioclase does. When this happens, the crystallizing assemblage removes so much SiO_2 that the liquid lines of descent (LLDs) fall off drastically below the observed MgO-SiO_2 trend of the data.

The range of K_2O in Northern Chile Ridge MORBs can't be reproduced by Rayliegh crystal fractionation from parent magmas with uniform K_2O content, even as a perfectly incompatible trace element (which is essentially how MELTS models it). K_2O in most samples is higher than the liquid line of descent (Figure 16). This suggests that K_2O is enriched to different degrees in the parent magmas. Parent magmas may be approximately uniform in major elements, and still have different K_2O contents, because the abundance of K_2O is so low that it behaves essentially as a trace element. The addition of small amounts of enriched melts would affect K_2O, while the abundance of the other major elements is high enough that the addition of small amounts of melt would not change them. This will be discussed in more detail at the end of this section.

The possibility that high K_2O contents are from *in-situ* crystallization (*Langmuir*, 1989) cannot be ruled out. In this model, instead of evolving the whole magma batch, a portion of the magma is isolated, evolves to a high degree, and then re-integrates into the rest of the batch. The net effect is that the incompatible elements are over-enriched with respect to the degree of evolution, or that the liquid line of descent is steeper than it should be. However, given the correlation between K/Ti and radiogenic isotope ratios

that will be discussed shortly, it is most likely that K_2O variations are inherited from the parent magmas.

The only segment at which magmas seem to have crystallized at a different pressure is segment N1. At this segment there are two groups of lavas, one which is fit by a lower-pressure (1.0 kbar) MELTS crystal fractionation model, and one which is expected to be fit by a higher-pressure (3.0 kbar) model due to low CaO and SiO_2 contents (Figure 17). The MELTS models for segment N1 use sample D107-c as a parent magma. Sample D107-c has a higher Na_2O content than sample D69-b (2.50 weight %, compared with 2.34 weight %), and is one of the highest-Na_2O samples at that MgO content. The high Na_2O content of this parent may mean that the onset of plagioclase crystallization is later in lavas descended from it than in lavas descended from D69-b (*e.g.*, *Biggar and Humphries*, 1981).

Group 1, which is fit by a 1.0 kbar model, contains samples from dredge sites D106 through D110 and GC20-GC22 (cf. Figure 3a). This spans the entire segment south of the northern ridge-transform intersection (RTI) basin. Group 2, which is expected to be fit by a 3.0 kbar model, contains samples only from dredge sites D111 and D112. These are the two northernmost dredge sites, in the broad, deep axial basin near the northern RTI. Along all the other segments of the Northern Chile Ridge the pressure of crystal fractionation seems to have been constant at approximately P = 2.0 kbar (Figures 18 and 19).

Compatible trace element data for Northern Chile Ridge MORB samples is consistent with crystal fractionation at P=2.0 kbar (Figure 20). To model this, the crystallization

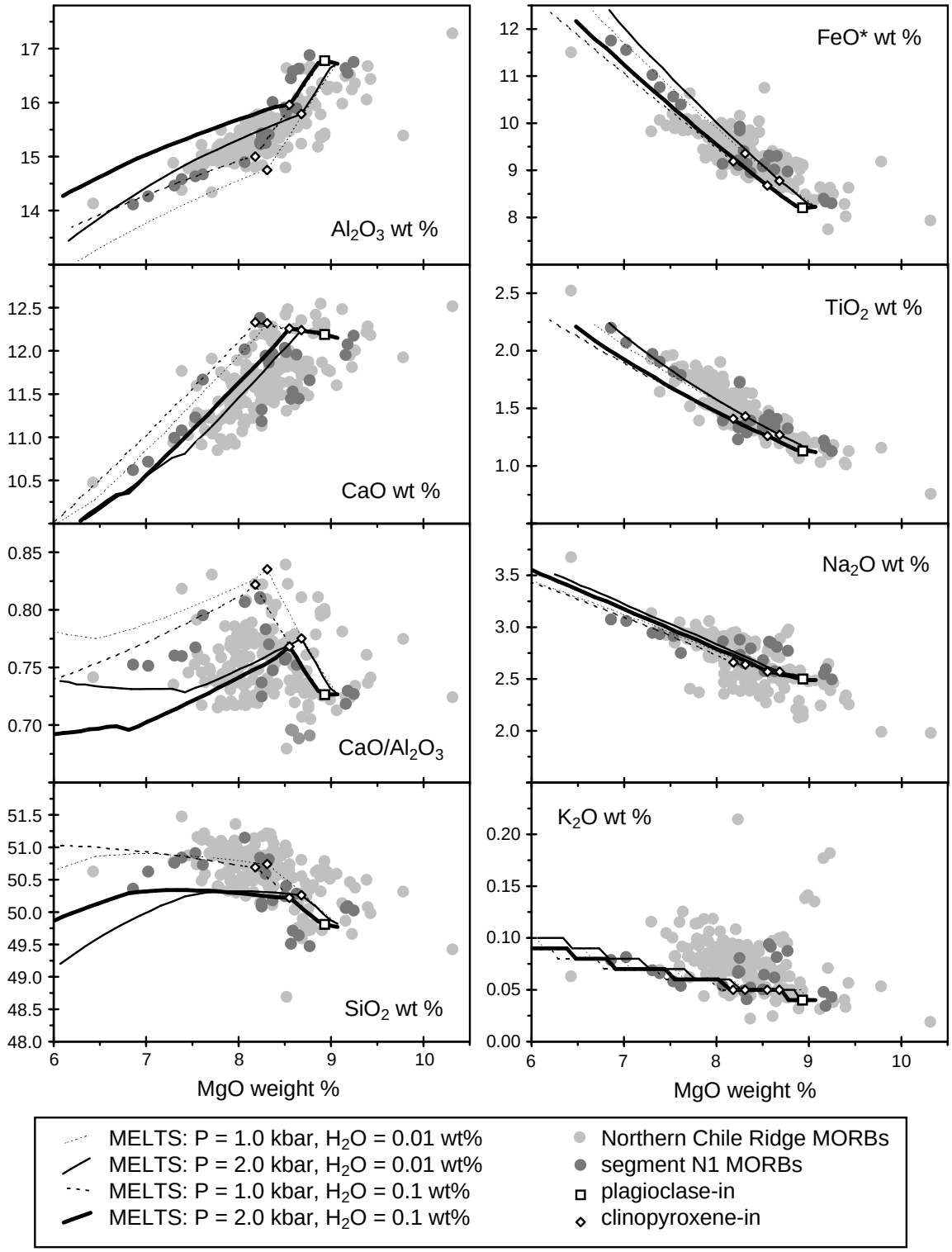

Figure 17: MELTS models for segment N1 MORBS, starting from D107-c: P = 1.0 and 2.0 kbar; H_2O = 0.01 and 0.1 wt %; QFM-2; phase-in points are shown.

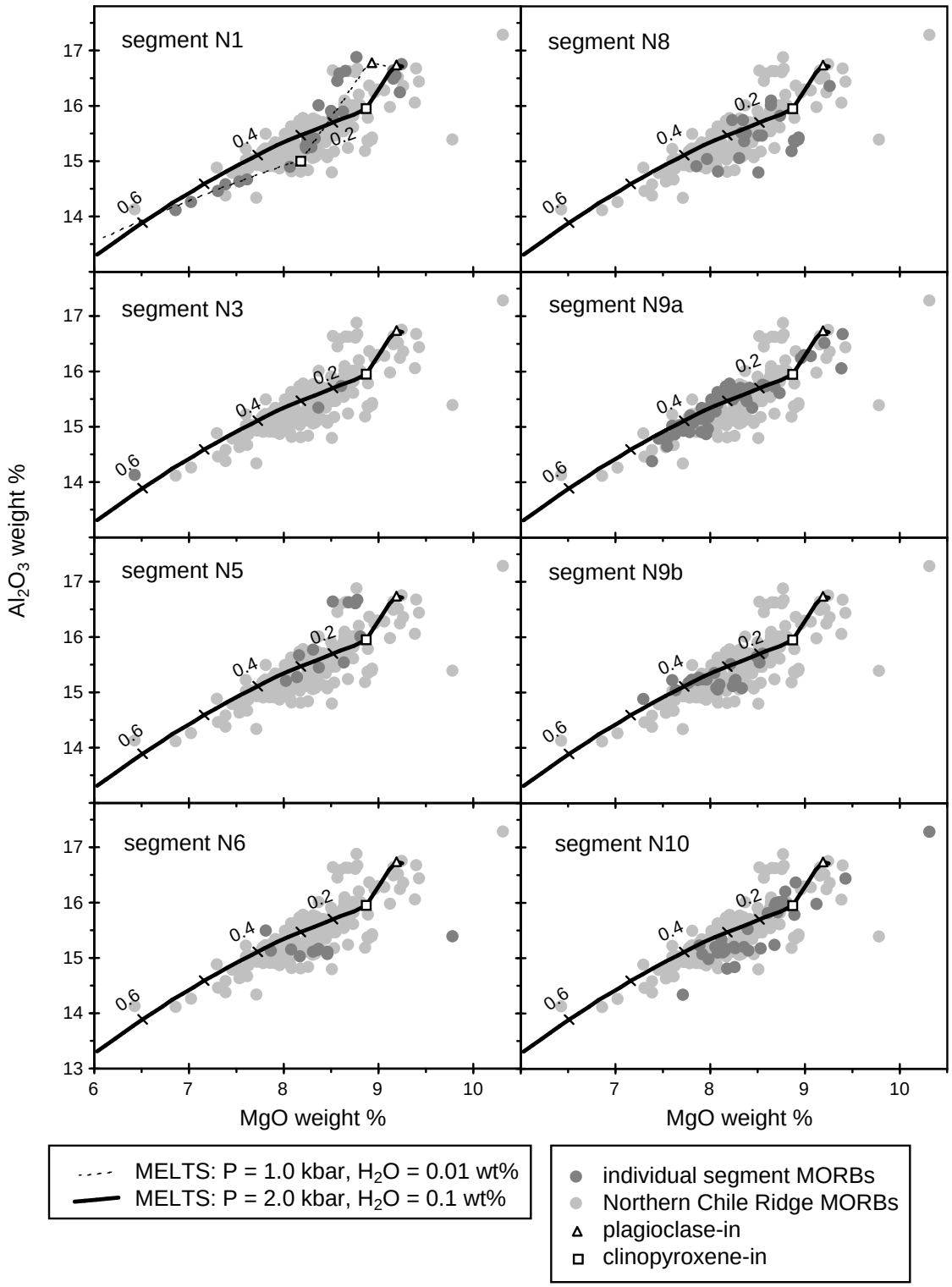

Figure 18: Al_2O_3 vs. MgO and MELTS crystal fractionation models for Northern Chile Ridge segments. Phase-in points (open symbols) and extents of crystallization (tick marks) are shown.

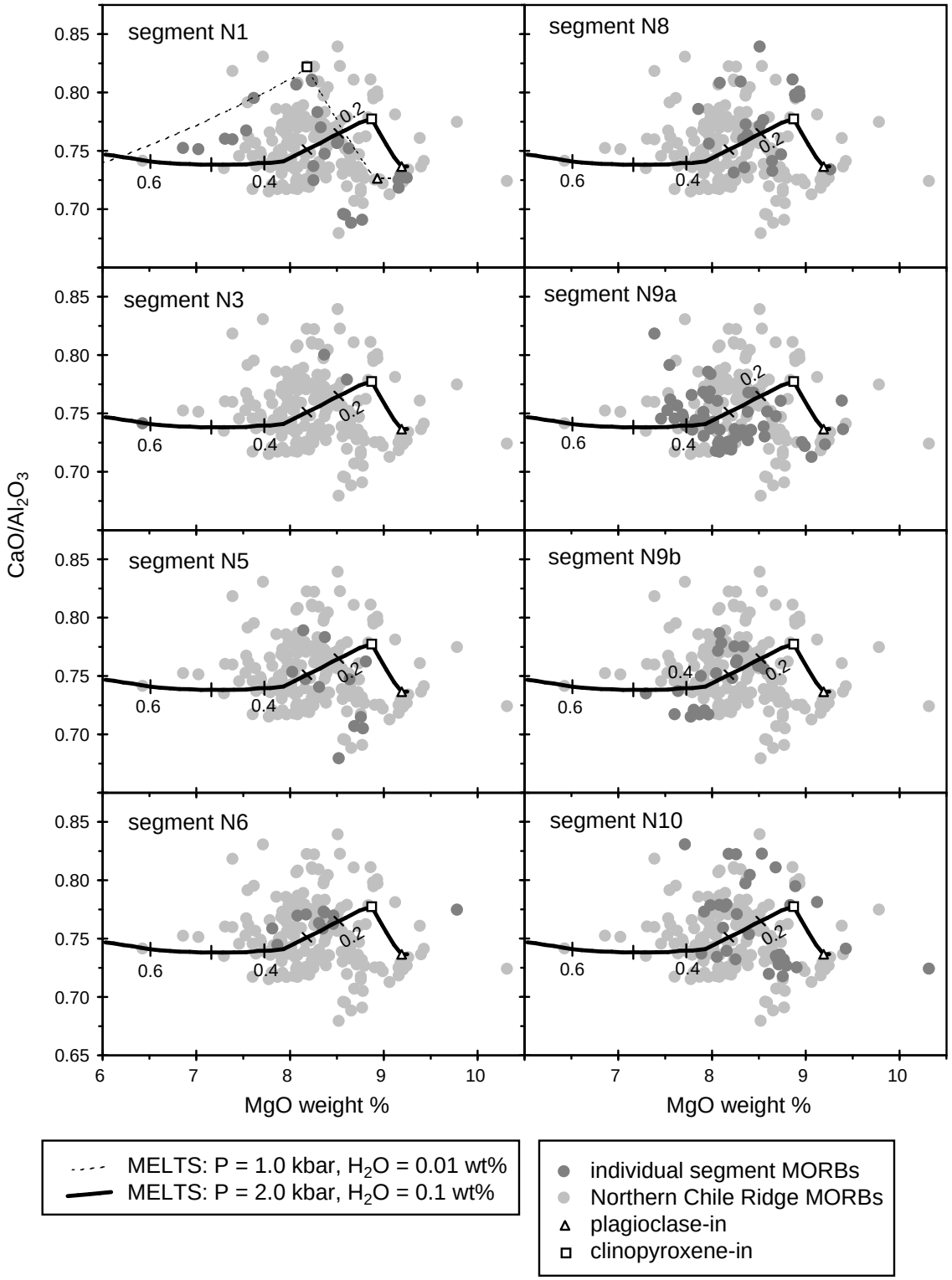

Figure 19: CaO/Al_2O_3 vs. MgO and MELTS crystal fractionation models for Northern Chile Ridge segments. Phase-in points (open symbols) and extents of crystallization (tick marks) are shown.

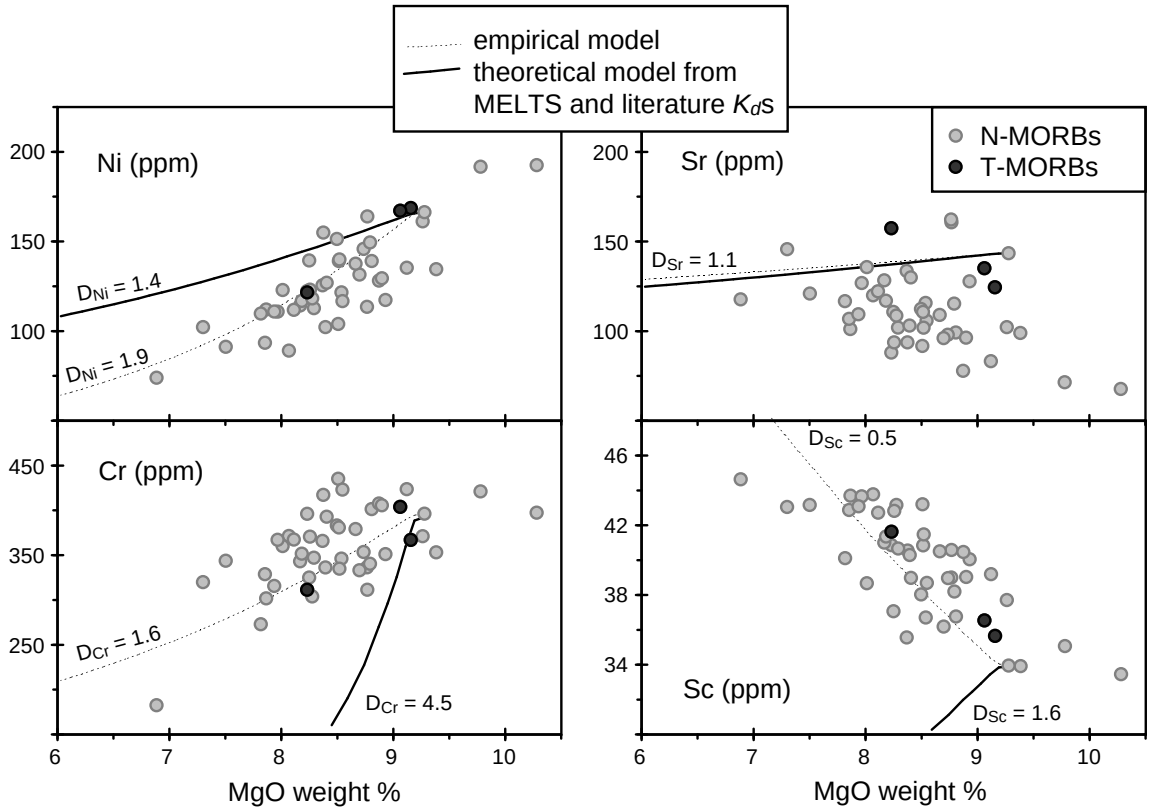

Figure 20: Crystal fractionation models for compatible trace elements, compared to Northern Chile Ridge MORB samples. Shown is an empirical model calculated from values of the bulk distribution coefficient *D* that best fit the sample data (dashed lines), and a theoretical model (solid lines) calculated according to the phase proportions predicted by MELTS and mineral-melt partition coefficients K_d from the literature (cf. Table 8).

parameters given by the best fit MELTS liquid line of descent were used as constraints in a model of compatible trace element concentrations during crystal fractionation.

There were several steps to this model (Figure 21). Step 1: Bulk distribution coefficients D were calculated for each compatible trace element (Sc, Cr, Ni, and Sr), using literature values of the mineral-melt partition coefficients K_D and the crystallizing phase proportions predicted by the best-fit MELTS model (Table 8). The MELTS model was constrained by the major element compositions of the samples, as discussed above.

Step 2: The concentration C_L of each element in a crystallizing liquid was calculated over a range of extent of crystallization F, using the Rayliegh fractionation equation $C_L = C_0F^{(D-1)}$ (*e.g.*, *Philpotts*, 1990) with the bulk distribution coefficients from Step 1, and using sample D76-2 (MgO = 9.3 weight %) as a parent (C_0).

Step 3: For each element, concentration as a function of extent of crystallization F was translated into concentration as a function of MgO, using the F-MgO relationship predicted by the MELTS liquid line of descent. This was compared to the real concentrations of compatible trace elements and MgO in the samples (Figure 20).

Step 4: Empirical best-fit values for the bulk distribution coefficients D for each element were also found: the bulk distribution coefficients were allowed to vary in Step 2, and the concentration as a function of MgO was found and compared to the samples as in Step 3. These empirical values for D were compared to the bulk distribution coefficients calculated from literature values of K_D in Step 1.

For Ni and Sr, the empirical values for the bulk distribution coefficient D that best fit the data are similar to those calculated from MELTS and the literature K_Ds (Figure 20).

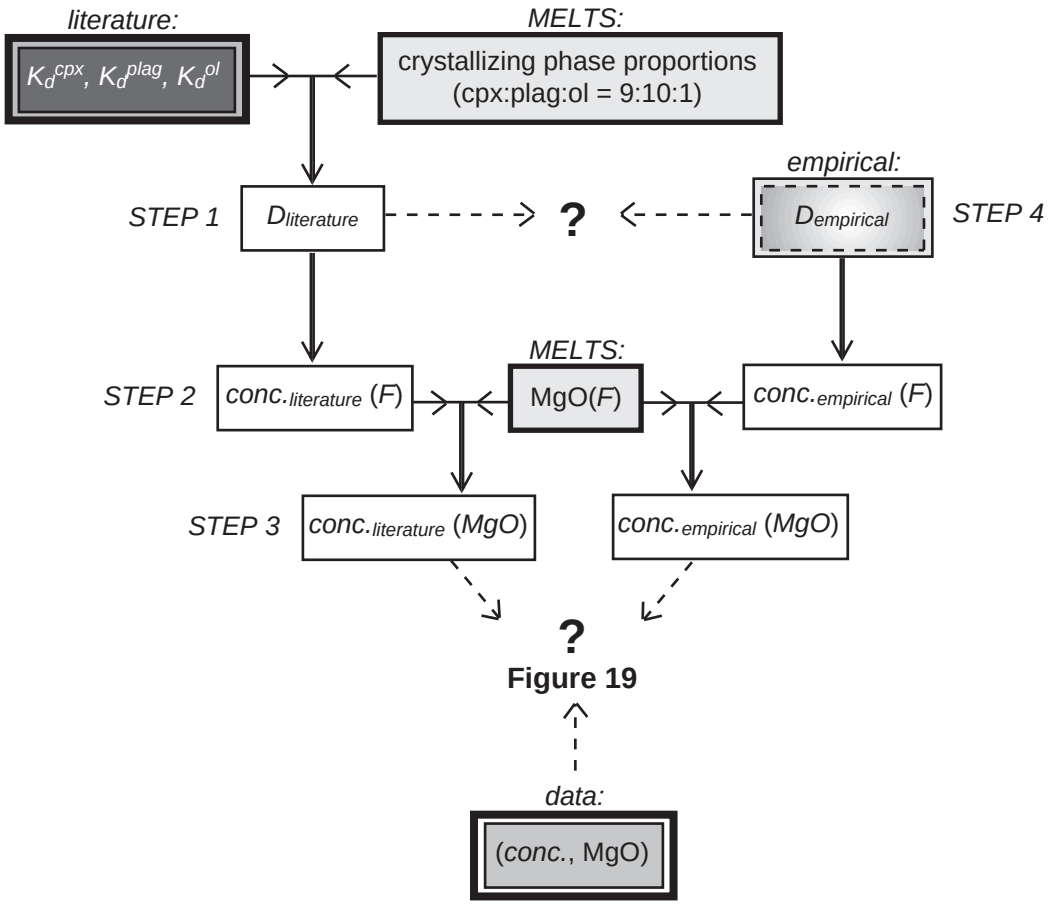

Figure 19

Figure 21: Flow chart for the compatible trace element model. Cpx, clinpyroxene; plag, plagioclase; ol, olivine. "STEP 1" *etc*. refer to the description of the model in the text. Solid arrows indicate the logical progression of the model; dashed arrows and question marks indicate quantities that are compared to each other.

Table 8: Mineral-melt Partition Coefficients and Distribution Coefficients for Compatible Trace Elements

	Sc	Cr†	Ni†	Sr†
	mineral-melt partition coefficients from the literature:			
K_d^{spinel}	0.45[a]	10	5	0.01
$K_d^{olivine}$	3[b], 0.23[c]	0.2	10	0.001
$K_d^{plagioclase}$	0.1[d]	0.01	0.01	2.2
$K_d^{clinopyroxene}$	3[d]	10	2	0.07
	bulk distribution coefficients (D):			
empirical best-fit to samples*	0.5	1.6	1.9	1.1
MELTS crystallizing phase proportions (approximate):				
MgO = 8.9-9.2 weight %:				
plag:ol = 5:2	0.9	0.1	2.9	1.6
MgO = 7.9-8.9 weight %:				
cpx:plag:ol = 9:10:1*	1.6	4.5	1.4	1.1
MgO < 7.9 weight %:				
px:plag = 1:1	1.6	5.0	1.0	1.1

mineral abbreviations: ol, olivine; plag, plagioclase; cpx, clinopyroxene; px, pyroxene.

[a]from *Horn et al.* (1994)

[b]from *Villemant* (1988)

[c]from *Klöck and Palme* (1988)

[d]from *Villemant et al.* (1981)

†from *Cox et al.* (1979)

*shown in Figure F138a.

However, for Cr and Sc, the values of D calculated from the literature and MELTS are much higher than the empirical values and cannot reproduce the data. This may indicate that there cannot be as much clinopyroxene in the crystallizing assemblage as MELTS predicts, since D_{Cr} and D_{Sc} are dominated by the contribution from $K_D^{clinopyroxene}$. MELTS predicts that clinopyroxene constitutes roughly half the fractionating assemblage (by mass) once it enters at MgO = 8.9 weight %. If the composition of the clinopyroxene predicted by MELTS were inaccurate, then the phase proportions would also be inaccurate, in order to fit the constraints of the major element data. Alternately, the discrepancy in D may indicate that the values of $K_d^{Cr}{}_{cpx}$ and $K_d^{Sc}{}_{cpx}$ were much lower during crystallization of these samples than those reported in the literature. Values of K_D are thought to vary depending on temperature, pressure, and melt composition.

However, in general, the fact that the MELTS model, which was derived from major element compositional trends, is also consistent with the compatible trace element contents in the samples lends support to the conclusion that crystal fractionation is the process responsible for the main compositional trends of the data. It also indicates that the crystallizing phase proportions, the relation between F and MgO, and the range of F values predicted by the best-fit MELTS model are accurate.

The fact that the trends of major elements can be approximately modeled by a single crystal fractionation path indicates that the parent magmas to the entire Northern Chile Ridge MORB suite were similar in major element composition to sample D69-b, and crystallized under similar pressure conditions. This suggests that the MORB source mantle under the entire ridge has a largely uniform major element and modal

composition. The pressure of crystallization, 2.0 kbar, is equivalent to a depth of 6 km, which is approximately at the base of the crust in a mid-ocean ridge setting. The pressure of crystallization for Group 1 lavas at segment N1, 1.0 kbar, is equivalent to 3 km.

Variation in Backtracked Major Elements

The major element compositions of Northern Chile Ridge MORBs exhibit scatter outside of error around the general crystal fractionation trend (Figure 16). Such scatter is often considered to have been inherited directly from small compositional variations in the parent magmas (*e.g.*, *Klein and Langmuir*, 1987), but in theory it could also have been caused by differences in the low-pressure crystal fractionation paths. During low-pressure crystal fractionation, liquid lines of descent from identical parent magmas can be offset by movements in the kinks that mark the onset of plagioclase and clinopyroxene crystallization. This can be caused by different pressures of crystallization (*e.g.*, Figure 16), different H_2O contents in the parent magmas, or different Na_2O contents in the parent magmas (*e.g.*, *Biggar and Humphries*, 1981; *Michael and Chase*, 1987; *Grove et al.*, 1992; *Shen and Forsyth*, 1995). Compositional variations in the parent magmas themselves are thought to arise from differences in extent of melting, pressure of melting, patterns of melt extraction, or mantle source heterogeneity (*e.g.*, *Hess*, 1992).

Each mechanism for changing the low-pressure crystal fractionation path causes the liquid line of descent in all the major elements to be offset in a predictable sense. This was calculated using MELTS (Figure 22). An affected suite of samples, when corrected

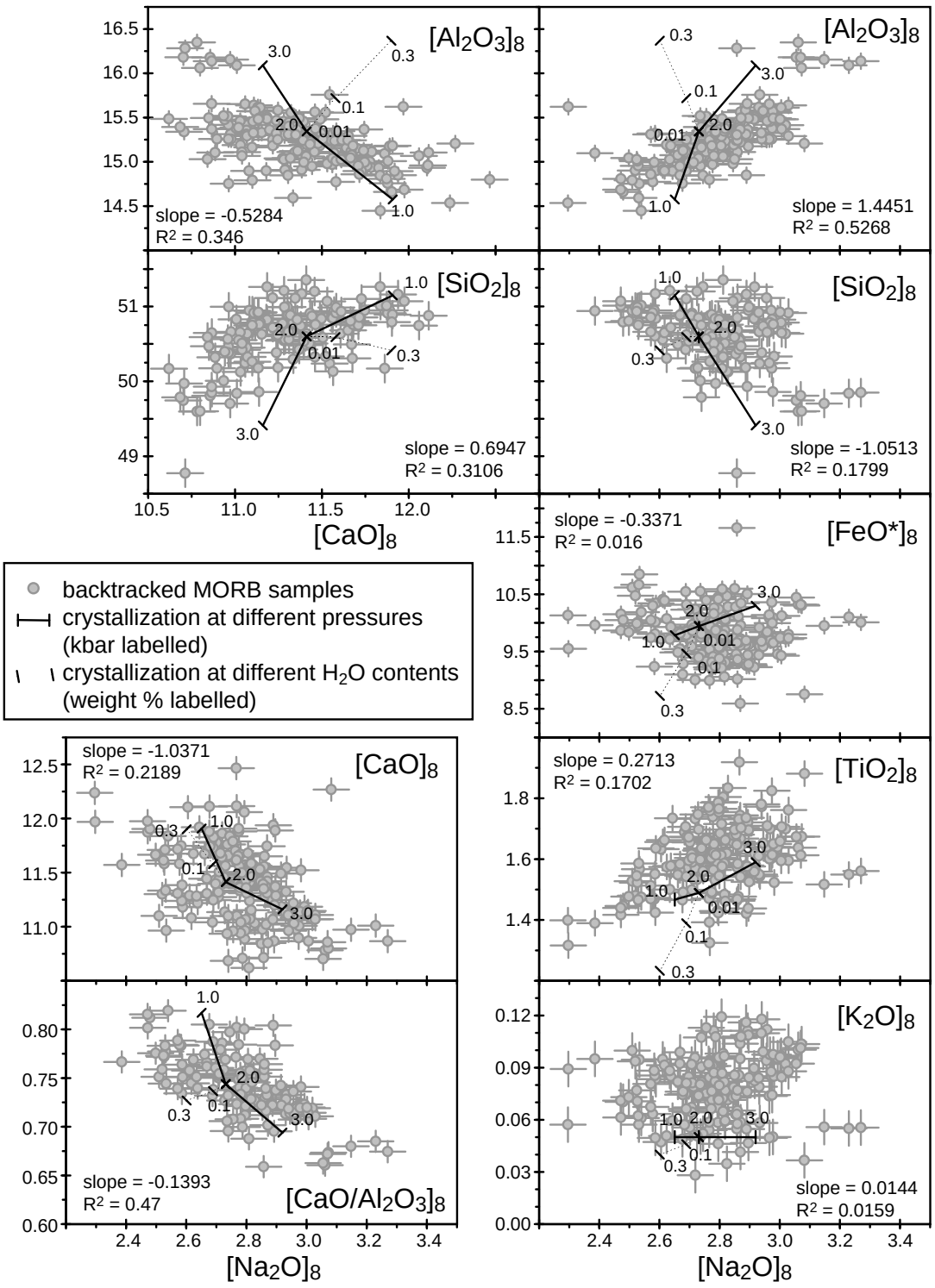

Figure 22: Covariations in MORB major element compositions backtracked to the same MgO content, with correlation slopes and R^2 values. The expected effects of crystallization at different pressures and with different H_2O contents, from MELTS models, are shown for comparison (dotted lines). Error bars are average standard deviations of major element analyses. See text for details. R^2 as in Figure 14.

to a common extent of fractionation, would exhibit consistent covariations in major element abundances. The Northern Chile Ridge samples were corrected for the known general crystal fractionation trend of the suite by backtracking the samples to a common MgO value of 8 weight %, after *Klein and Langmuir* (1987). However, instead of backtracking as they did along a regression to the data points, the backtracking was done along the best-fit MELTS liquid line of descent shown in Figure 16. Backtracked oxide abundances are represented in brackets, *e.g.*, $[Al_2O_3]_8$.

For Al_2O_3, CaO, FeO*, TiO_2, Na_2O, and K_2O, there is a kink in the liquid line of descent when clinopyroxene appears, but no kink when the second pyroxene appears. Therefore, in order to include only samples that were crystallizing either a clinopyroxene+plagioclase+olivine or a two-pyroxene+plagioclase phase assemblage, only samples with MgO < 8.87 weight % were included. This included 88% of the set of MORB samples. In addition, for K_2O we excluded the T-MORBs. For SiO_2 and CaO/Al_2O_3, there is a kink in the liquid line of descent when the second pyroxene appears, so for these oxides an additional restriction was imposed such that samples must have MgO > 7.93 weight %. This included 67 % of the set of MORB samples.

The covariations in backtracked major elements for Northern Chile Ridge MORB lavas are not simple trends easily attributable to any one of the processes described above (Figure 22). In particular, MELTS models show that low-pressure crystallization artifacts alone cannot account for the observed covariations. While the $[Al_2O_3]_8$ and $[SiO_2]_8$ variations are approximately bracketed by the models of crystallization at different pressures, the $[Na_2O]_8$ variations greatly exceed what's expected for the same

pressures. Even a reasonably large change in H_2O content, from 0.01 to 0.3 weight %, is expected to have only a relatively small effect on backtracked Na_2O contents. At the very least, some variation in primary magma Na_2O contents is required. This is most easily produced by variations in extent of melting (*e.g.*, *Klein and Langmuir*, 1987).

A complete and quantitative interpretation of backtracked major element trends to find extent of melting, pressure of melting, source heterogeneity, style of melting, and style of melt extraction is beyond the scope of this paper. This sort of interpretation was done roughly by *Klein and Langmuir* (1987), but since then it has become recognized that the subject is much more complex than originally envisioned because the behavior of the major element oxides during melting is not simple (*e.g.*, *Asimow et al.*, 2001).

Patterns in Trace Elements and Isotopes

In this section, the petrogenesis of the parent magmas to the Northern Chile Ridge MORB suite is discussed. The most common influences on primary magma compositions at mid-ocean ridges are thought to be mantle compositional heterogeneity, variation in extent of partial melting, and mixing between primary melts that are compositionally distinct as a result of either or both of the former two conditions. As was shown in the previous section, the operation of these processes could not be detected in the major element compositions of Northern Chile Ridge erupted MORB lavas, because the major element compositions are too strongly dominated by the effects of crystal fractionation, except to say that there must have been some amount of variation in

parent magma Na_2O contents ($[Na_2O]_8$). Instead, incompatible trace element ratios and radiogenic isotope ratios are used to investigate petrogenetic processes that occurred prior to crystal fractionation, because these ratios are not affected by crystal fractionation.

Mantle compositional heterogeneities affect incompatible trace element ratios, $[Na_2O]_8$, and radiogenic isotope ratios. Partial melting of a uniform mantle source, on the other hand, does not affect radiogenic isotope ratios, except in the case where fractionated parent-daughter ratios can lead to differences in radiogenic ingrowth after very long periods of time (100's of My for the isotope ratios considered in this study). Ratios of incompatible trace elements (when the more-incompatible element is in the numerator) decrease in the liquid as melting of a uniform mantle source progresses. Na_2O behaves like an incompatible trace element during mantle melting in a mid-ocean ridge setting, so as extent of melting increases, $[Na_2O]_8$ decreases. In addition, lower extents of melting result in lower melt production and a thinner crust, which isostatically compensates the axis at a deeper depth. Covariations between these species (incompatible trace element ratios, radiogenic isotope ratios, and $[Na_2O]_8$) are suggestive of which petrogenetic process dominated the compositions of Northern Chile Ridge parent magmas.

The absence of any correlation between incompatible trace element ratios and major element indicators of extent of melting in Northern Chile Ridge erupted lavas suggests that melting variations were not the dominant influence on MORB parent magma compositions. The population of N-MORB samples shows no correlation between incompatible trace element ratios (demonstrated by La/Sm) and $[Na_2O]_8$, either at the

scale of the whole ridge (Figure 23), or within individual segments (Figure 24). Correlations were judged by the R^2 value of the population, where $R^2 = \{n(\Sigma XY)-(\Sigma X)(\Sigma Y)\}^2/\{[n\Sigma X^2-(\Sigma X)^2][n\Sigma Y^2-(\Sigma Y)^2]\}$, the square of the Pearson product moment correlation coefficient. An exception to this generalization is a strong positive correlation among the three samples from segment N5 ($R^2 = 0.9743$). The strong positive correlation at segment N5 is unusual; this is the site of the bathymetric and gravity anomaly high, and exhibits along-axis gradients in $[Na_2O]_8$, with decreasing $[Na_2O]_8$ away from the gravity high. This probably reflects mixing, not extent of melting.

The extent of melting was estimated quantitatively using the empirical equation of *Niu and Batiza* (1991), $F = 19.202 - 5.175*[Na_2O]_8 + 15.537*[CaO]_8/[Al_2O_3]_8$. This calculation requires the assumption that the major element composition of the mantle source is homogeneous within the range of a depleted MORB mantle, as described by *Niu and Batiza* (1991). The fact that the erupted lavas are MORBs demonstrates that this is indeed the case. The equation also makes use of the variation in magmatic CaO/Al_2O_3 content as extent of melting progresses (*Niu and Batiza*, 1991), although it has recently been suggested that if differences in mantle source CaO/Al_2O_3 exist due to mantle heterogeneity, that they could overwhelm changes in CaO/Al_2O_3 due to melting (*Asimow et al.*, 2001). In addition, CaO/Al_2O_3 liquid lines of descent are in general distorted by the influence of magmatic Na_2O content on the point of onset of plagioclase crystallization.

Among Northern Chile Ridge MORBs, there is no correlation between the incompatible trace element ratios Nb/Zr or La/Sm and extent of melting F ($R^2 = 0.0178$

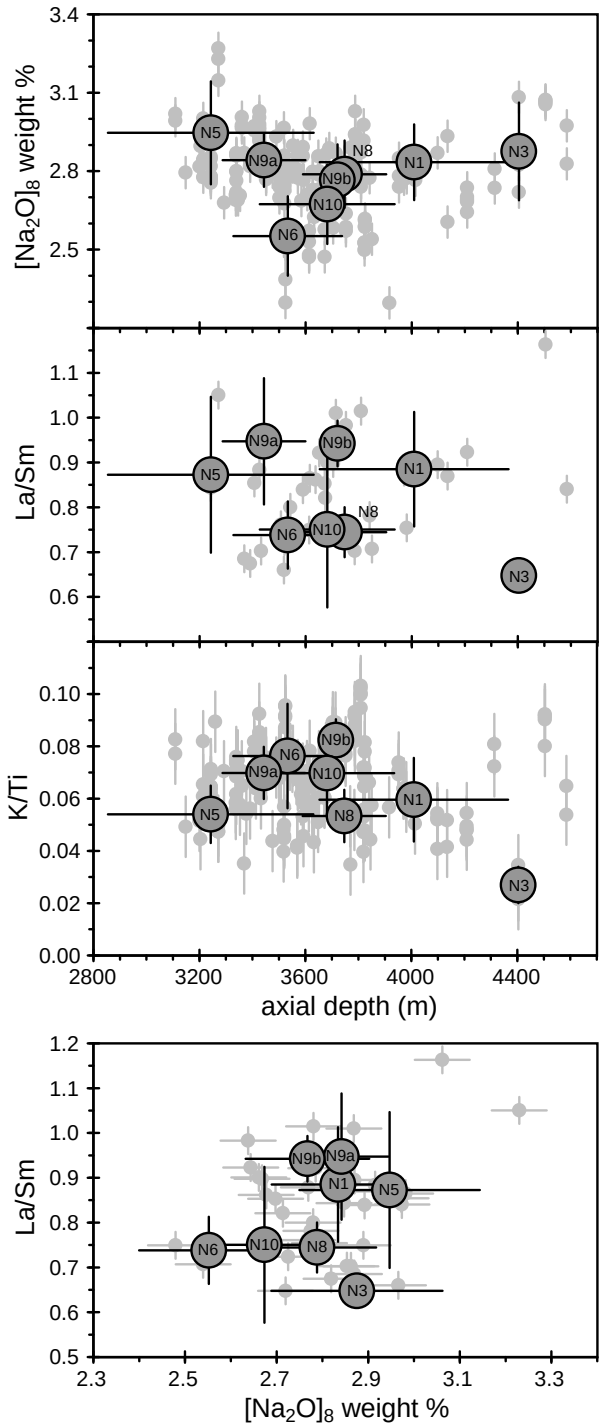

Figure 23: $[Na_2O]_8$, La/Sm, K/Ti, and axial depth for Northern Chile Ridge MORBs. Segment averages are shown as large dark circles (labelled by segment name), with bars showing the standard deviation of samples in each segment. Individual samples in the population of Northern Chile Ridge MORBs are shown as light grey points in the background. La/Sm and K/Ti averages include N-MORBs only. Average axial depth was calculated as the average of the depths of the dredge stations.

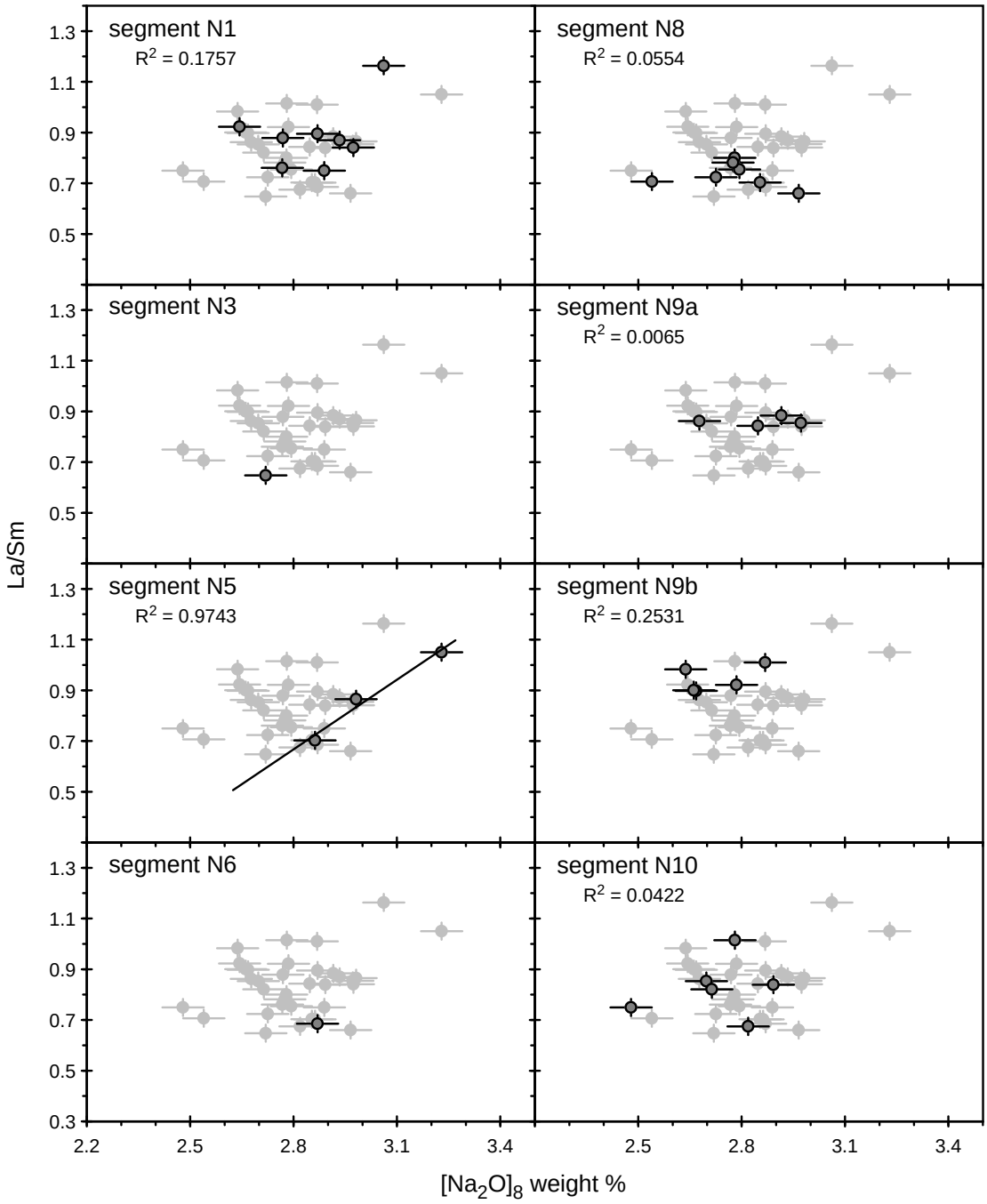

Figure 24: La/Sm vs. $[Na_2O]_8$ among Northern Chile Ridge N-MORBs for each segment (dark grey points), shown with the whole NCR population for comparison (light grey points). R^2 values for each segment calculated as in Figure 14.

and 0.1326, respectively) (Figure 25). The highest extent of melting at the ridge is F = 20.4 %, calculated for sample D50 at segment N10; excluding segment N5, the lowest extent of melting is F = 13.6 %, calculated for sample D111-1 at segment N1. Variations of this magnitude (14-20%) in the extent of melting under the length of a mid-ocean ridge are commonly thought to be geologically reasonable and, indeed, likely. At the Mid-Atlantic Ridge 26º S, *Niu and Batiza* (1991) found that extent of melting varied between 16-18%. High $[Na_2O]_8$ contents at segment N5 are probably not due to anomalously low extents of melting; the correlation at this segment between $[Na_2O]_8$ and La/Sm discussed above suggests that they are probably due to contamination by a high-Na_2O, high-La/Sm melt associated with the alkalic basalts.

Stronger correlations exist between incompatible trace element ratios and radiogenic isotope ratios in Northern Chile Ridge erupted lavas, suggesting that mixing between two compositionally distinct primitive magmas was a more important influence on MORB parent magma compositions. Among N-MORBs, there are subtle variations in radiogenic isotope ratios ($^{143}Nd/^{144}Nd$, $^{87}Sr/^{86}Sr$, $^{206}Pb/^{204}Pb$, $^{207}Pb/^{204}Pb$, and $^{208}Pb/^{204}Pb$), that correlate with the variations in incompatible trace element ratios (K/Ti and La/Sm) (Figure 26). No reliable isotope data exist yet for the new samples from the PANORAMA Expedition, so the data of *Bach et al.* (1996) were re-examined. R^2 for these correlations ranges from 0.1382 to 0.7197. The incompatible element enriched end-member has low $^{143}Nd/^{144}Nd$, high $^{87}Sr/^{86}Sr$, and high $^{206}Pb/^{204}Pb$, $^{207}Pb/^{204}Pb$, and $^{208}Pb/^{204}Pb$, trending towards hotspot-type ocean island alkalic basalts found throughout the Pacific (Figure 26). The incompatible element depleted end-member has high

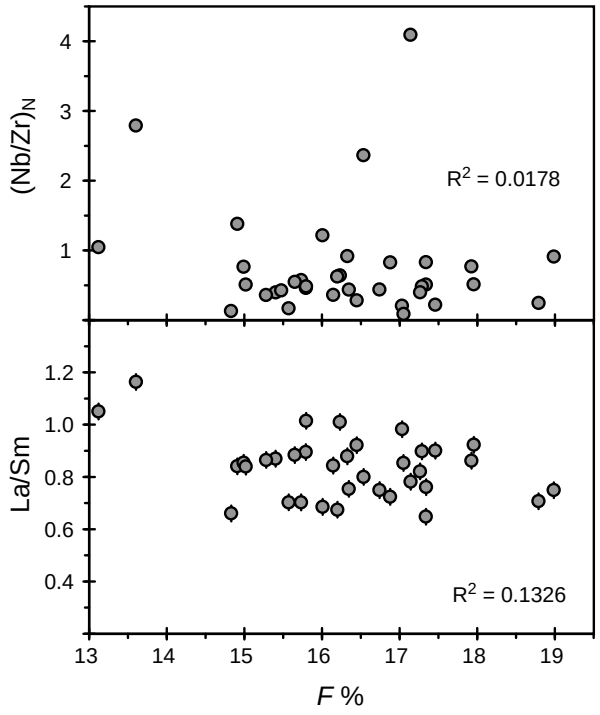

Figure 25: Incompatible trace element ratios vs. extent of melting, for all Northern Chile Ridge MORBs (N-MORBs and T-MORBs). *F* is the extent of melting calculated as in *Niu and Batiza* (1991), $F = 19.202\text{-}5.175*[Na_2O]_8+15.537*[CaO]_8/[Al_2O_3]_8$. Note the extremely low R^2 values, indicating that no statistically significant correlation is present. Compare to the *Vlastélic et al*. (2000) study of the Pacific-Antarctic Ridge 56-66º S, where these quantites are strongly correlated. $(Nb/Zr)_N = Nb/Zr*(5.13/0.465)$. R^2 calculated as in Figure 14.

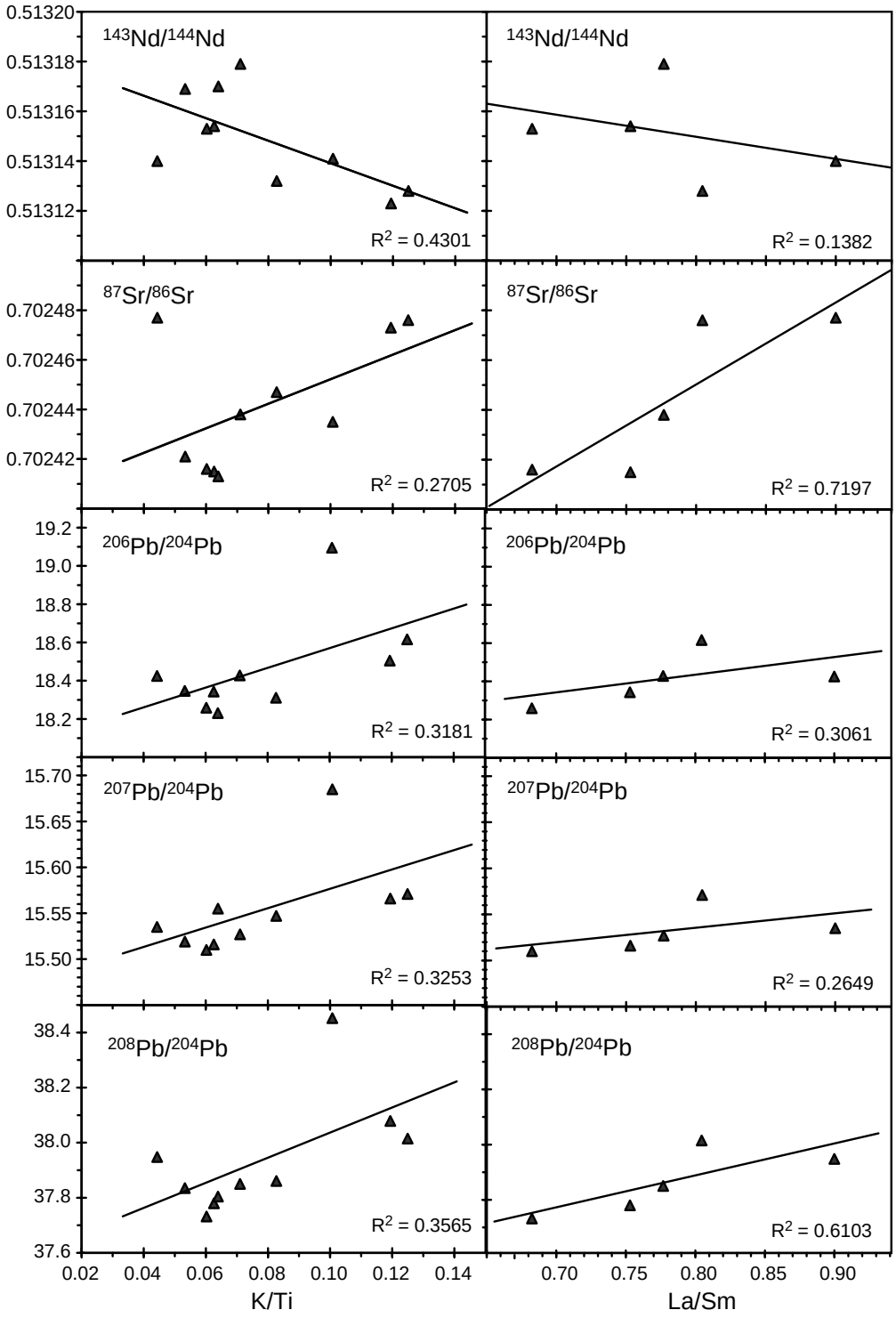

Figure 26: Incompatible trace element and radiogenic isotope ratio data from the previous Northern Chile Ridge survey of *Bach et al.* (1996). Published error estimates for isotope ratios are < 0.003% for Sr, < 0.004% for Nd, and 0.1% for Pb (*Bach et al.*, 1996). Correlations are indicated by regression lines and R^2 values for each plot. R^2 calculated as in Figure 14.

$^{143}Nd/^{144}Nd$, low $^{87}Sr/^{86}Sr$, and low $^{206}Pb/^{204}Pb$, $^{207}Pb/^{204}Pb$, and $^{208}Pb/^{204}Pb$, similar to MORBs worldwide. The sense of the trace element-isotope correlation is consistent with binary mixing between melts from a depleted MORB mantle source and a small amount of contamination from an enriched plume-type mantle source.

Previously, ocean-basin-scale covariations among isotopes in Pacific MORBs have been ascribed to parent-daughter ratios behaving coherently during the fractionating events that created heterogeneity in the depleted mantle reservoir, and the subsequent evolution of these parent-daughter ratios over time (*White et al.*, 1987). However, at the Northern Chile Ridge, the correlation of isotopes with trace elements, as well as the presence of trends in all isotope ratios including Nd and Sr, is strong evidence that the isotope trends are indeed caused, at least in large part, by binary mixing.

Whether the correlations observed in the Northern Chile Ridge N-MORBs extend to the newly recovered alkalic basalts or T-MORBs cannot be evaluated at this time, because isotope data for those samples do not yet exist. *Bach et al.* (1996) recovered three T-MORB lavas (K/Ti = 0.21-0.34), but did not identify them as such, and did not report isotope or trace element data for them. Similarly, $[Na_2O]_8$ values (and therefore also calculated values of F) are not defined for the alkalic basalts, since they depend on backtracking along crystal fractionation trends and on the assumption that the mantle has a depleted MORB mantle composition.

Quantitative models show that variations in the incompatible trace element compositions of the Northern Chile Ridge MORB suite are better explained by magma mixing than by variation in extent of partial melting of a uniform MORB source (Figure

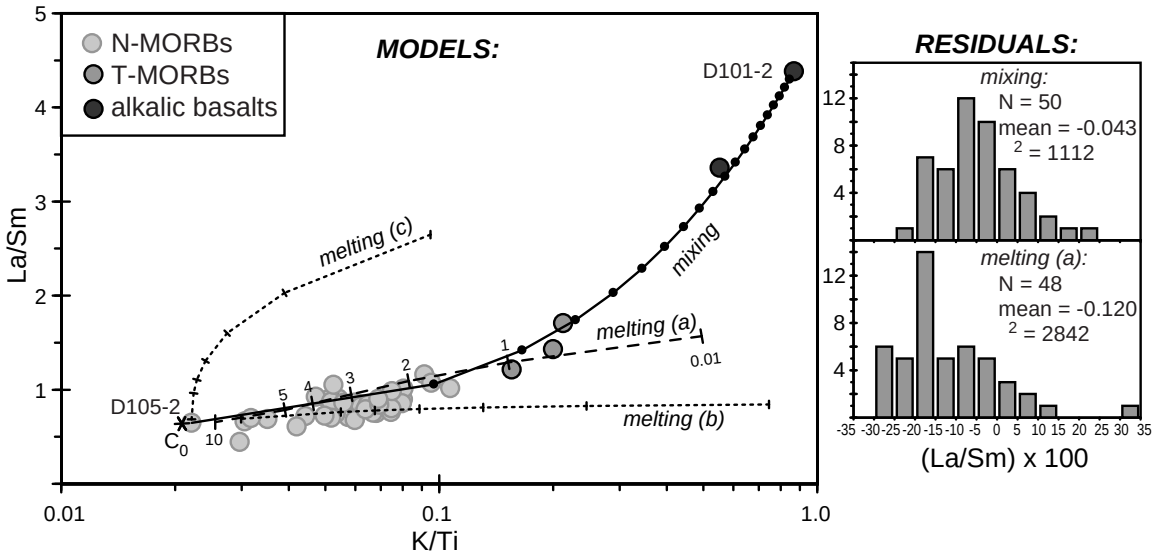

Figure 27: Mixing and partial melting models for generating the incompatible trace element contents of Northern Chile Ridge samples. The most robust model is a mixing hyperbola (solid line) between the most depleted sample (N-MORB D105-2) and the most enriched sample (alkalic basalt D101-2); dots show every 5% mixing. Also shown are three melting models that encompass the range of trajectories that can be generated by varying the mineral-melt distribution coeffeicients (K_d) within the range of values reported in the literature. "Melting (a)" (dashed line) fits the data reasonably well, but "melting (b)" and "melting (c)" (dotted lines) do not; these models differ only in $K_d^{La\text{-}olivine}$ and $K_d^{Ti\text{-}olivine}$. Numbers indicate % melting (0.01% through 10%); tick marks in "melting (b)" and "melting (c)" indicate the same % melting as in "melting (a)". Details of melting models are discussed in the text. Also shown are histograms and statistics for the residuals for the mixing and melting models. The residual (La/Sm) is $(La/Sm)_{sample}-(La/Sm)_{calculated}$. The ^{2} value is calculated as $\sum_{samples}[(La/Sm)_i/\ _i]^2$.

27). Mixing was modeled by calculating a mixing hyperbola, after *Langmuir et al.* (1978), using the most depleted N-MORB sample (sample D105-2) and the most enriched alkalic basalt sample (D101-2) as mixing end-members.

Partial melting of a uniform mantle source was modeled using the non-modal accumulated fractional melting equation: $C_L = (C_0/F) * \{1 - (1\text{-}PF/D_0)^{1/P}\}$. For the melting equation, the bulk distribution coefficients (D) and non-modal melting parameters (P) for each element were calculated from mineral-melt partition coefficients (K_d) for that element. These were obtained from the online GERM website (database maintained by Anthony Koppers), compiled as the "Kd's Database". The values of partition coefficients can vary by up to an order of magnitude, and are thought to depend on temperature, pressure, and the composition of the melt. The bulk distribution coefficient for an element in the mantle source rock is $D_i = \Sigma K_{di\alpha} X_\alpha$, where X_α is the fraction of mineral α in the melting rock. The mantle source mode was assumed to have the characteristics of spinel peridotite: 60% olivine, 10% clinopyroxene, 25% orthopyroxene, 5% spinel (*Hess*, 1992). The non-modal melting parameter for an element is $P_i = \Sigma K_{di\alpha} Y_\alpha$, where Y_α is the fractional contribution of mineral α to the melt. The mode entering the melt was assumed to be 70% clinopyroxene, 20% orthopyroxene, and 10% spinel.

The concentrations of the trace elements in the mantle source were estimated by choosing fixed values of C_L and F, and combining them with D_i and P_i to back-calculate C_0 from the equation above. The most depleted member of the sample suite must be the one generated by the greatest extent of partial melting, since incompatible element

concentrations decrease and approach the source concentrations as partial melting progresses. Therefore, a maximum extent of partial melting was estimated at $F = 15\%$ to coincide with the concentration C_L of the most depleted sample in the suite (D105-2). Models calculated for this study showed that generally by approximately 20-30% melting trace element concentrations decrease to the levels they were in the mantle source. The exact extent of partial melting at which this occurs depends on the bulk distribution coefficients.

The calculated source concentration (C_0) was then used with the calculated values of D and P to predict the trace element concentrations of melts produced at values of F ranging from very small ($F = 0.0001$) to reasonably large ($F = 0.15$) (Figure 27). At very small melt fractions, the enrichment of trace element concentrations relative to the mantle source reaches a finite limit. For the batch melting equation, this is $C_{Li}/C_{Lj} = D_j/D_i$ for trace elements i and j; for the accumulated fractional melting equation, the maximum enrichment limit is approximately the same.

The model is most sensitive to variations in the K_ds, which translate to variations in D and P. Because olivine and clinopyroxene are the dominant minerals in the mantle mode and melting mode, respectively, the fit of the model is especially sensitive to the K_d of elements in these minerals. If the extent of melting assumed for the most depleted sample, the mantle mode, or the mode entering the melt are varied within what is thought to be reasonable, the results and the fit of the model are not affected very much.

Using this approach, there is a wide range of partial melting models that are based on geologically likely estimates of the parameters. Three such models are shown in Figure

27. However, only a few of these reproduce the data in question. In this sense, the melting models are not statistically robust. The best-fit melting trajectory, "melting (a)", is produced when intermediate K_d for olivine and clinopyroxene are used. The shallowest melting trajectory, "melting (b)", and the steepest melting trajectory, "melting (c)", are produced when the maximum and minimum reasonable K_d for olivine and clinopyroxene, respectively, are used. Neither of these reproduce the data.

The two possibilities represented by the models are these. The entire lava suite could be generated by mixing between the most depleted N-MORB sample and the most enriched alkalic basalt sample. In this case, N-MORBs would all be generated by mixing of < 5% of the alkalic end-member; T-MORBs would be generated by mixing of 9-15% of the alkalic end-member (Figure 27). Alternately, the suite of MORBs (N-MORBs and T-MORBs, but not alkalic basalts) could be generated by variable degrees of partial melting of a depleted mantle source. In this case, N-MORBs would be generated by 1.5-15% melting; T-MORBs would require 1% melting or less.

Considering only these two possibilities, a statistical error analysis shows that the mixing model is better than the melting model, although it is noted that neither model on its own is complete. As is true for most geological systems, the trace element compositions of the Northern Chile Ridge MORB samples were probably affected by processes other than those described by the idealized models above. It is likely that that the depleted component of the mantle source was slightly chemically heterogeneous, and it is also likely that small differences in extent of melting created small differences in the depleted end-member of magma mixing, especially if the true parameters of melting were

similar to a model such as "melting (b)" in Figure 27. The purpose of a statistical analysis for this study is to determine which of the two models above was more important as the main process operating during Northern Chile Ridge petrogenesis.

The value of χ^2 for the mixing model, where $\chi^2 = \Sigma_{samples}[\Delta(La/Sm)_i/\sigma_i]^2$ (*Press et al.*, 1995), is half that for the melting model. In addition, the residual distribution of the mixing model is centered closer to zero and has a more natural, Gaussian shape than the distribution of residuals from the melting model (Figure 27). The mean of the residuals from the mixing model is –0.043, while the mean of the residuals from the melting model is –0.120. For a statistically good fit, the quantity χ^2 should have a value on the order of 1 to 10 (*Press et al.*, 1995); it is noted that the value of χ^2 is 1112 for the mixing model, and 2842 for the melting model (a) (Figure 27). In addition to the complexity of the real geological systems discussed above, a factor contributing to the poor statistical fit of the models may be that the error was underestimated in those elements that were obtained by ICP-MS (*i.e.,* La and Sm), as discussed in the Methods section.

There are additional reasons that the mixing model should be favored over the melting model. Firstly, as discussed above, the mixing model is much more robust than the melting model. By robust, it is meant that the model is "insensitive to small departures from the idealized assumptions for which the estimator is optimized" (*Press et al.*, 1995).

Secondly, the mixing model explains the trace element compositions of all the Northern Chile Ridge samples, including the alkalic basalts. The melting model shows that the Northern Chile Ridge alkalic basalts cannot be generated via melting of the

depleted source (Figure 27). Therefore it can only account for the N-MORBs and T-MORBs, and cannot explain the relationship of the alkalic basalts.

Lastly, the melting model predicts that the Northern Chile Ridge T-MORBs were generated by very small extents of melting (<1%). It may not be physically reasonable to invoke extraction of such small quantities of melt. Furthermore, such low extents of melting contradict estimates based on $[Na_2O]_8$ contents discussed above, in which T-MORBs were generated by intermediate extents of melting (14-20%).

It is certain that whether the depleted mantle produced melts that constitute one end-member of mixing, or was the parent to variable degrees of melt, it had a fairly uniform trace element composition in the rare earth elements and elements with similar incompatibilities. This composition is probably close to that of the most depleted N-MORB sample D105-2.

Origin of Alkalic Basalts

The alkalic basalts recovered at the Northern Chile Ridge require a different mantle source than the MORBs. These samples require an enriched, hotspot-like mantle source, but are not located near any known hotspot. Other common interpretations of the origin of alkalic basalts at oceanic islands can be definitively ruled out.

As discussed earlier, the alkalic basalts recovered at the Northern Chile Ridge have higher Al_2O_3 and K_2O and lower FeO* and CaO than would be expected if the trend defined by differentiation among the N-MORB and T-MORB samples continued to low

MgO contents (Figure 7). This indicates that the alkalic basalts cannot be generated by low-pressure crystal fractionation of a primitive N-MORB parent magma.

Although *Naumann and Geist* (1999) concluded that alkalic basalts at Cerro Azul in the Galapagos were derived by high-pressure crystal fractionation from a primitive tholeiitic parent magma, this cannot be the case for Northern Chile Ridge alkalic basalts. The large difference in K/Ti and incompatible trace element ratios between the Northern Chile Ridge alkalic basalts and the MORBs (Figures 5 and 12) cannot be produced by crystal fractionation. In addition, as discussed previously, MELTS models have shown that fractionation in MORBs at pressures higher than 2.7 kbar causes a decrease in SiO_2 content (Figure 16); however, the alkalic samples do not have SiO_2 contents significantly lower than the MORBs (Figure 7).

Even without isotopic data for the alkalic basalts, it is clear that they cannot have been generated by smaller extents of partial melting of the same source as the MORBs, as has been a common interpretation for the origin of alkalic basalts (*e.g.*, *Frey et al*., 1978; *Chen and Frey*, 1985; *Lanphere and Frey*, 1987). The quantitative models discussed above clearly show that incompatible trace element enrichments in the alkalic basalts are too great to have been produced by partial melting of a depleted mantle source (Figure 27). In addition, the observed negative gravity anomaly and swollen bathymetry at the northern end of segment N5 suggest that this region is in general characterized by unusually high extents of partial melting. Although it is not known if the alkalic basalts constitute a large fraction of total magma production throughout the swollen region, it is difficult to reconcile a high-melt-production region with low-degree melts.

Alkalic lavas are common at off-axis seamounts. However, it is uncommon among Pacific ridges to erupt alkalic basalts at the ridge axis, and is even rare worldwide. At most ridges, on-axis enriched samples (E-MORBs) are still tholeiitic (Figure 28). Previously, on-axis alkalic basalts have only been observed at sites where interaction with a hotspot is discernable, *e.g.* where the Foundation Hotspot is interacting with the Pacific-Antarctic Ridge near 36º S (*Hékinian et al.*, 1997, 1999), or where the Galapagos Hotspot is interacting with the Galapagos Spreading Center. The Northern Chile Ridge on-axis alkalic basalts are therefore unusual in a global sense.

Petrogenetic Model

The best explanation for the petrogenesis of Northern Chile Ridge lavas is mixing between primitive depleted (MORB) magmas and variable amounts of primitive alkalic magmas. The amount of the primitive alkalic end-member mixed in is <5% for the N-MORBs and 9-15% for the T-MORBs. Mixing occurs among primitive magmas, prior to low-pressure crystal fractionation.

The primitive depleted (MORB) magmas are generated by variable extents of melting (14-20%, based on $[Na_2O]_8$ contents and the *Niu and Batiza*, 1991, equation) of a depleted mantle source. The depleted mantle source has a trace element composition similar to that of the most depleted N-MORB sample (D105-2), and an isotopic composition with high $^{143}Nd/^{144}Nd$ (~0.51317) and low $^{87}Sr/^{86}Sr$ (~0.70241), $^{206}Pb/^{204}Pb$ (~18.2), $^{207}Pb/^{204}Pb$ (15.51), and $^{208}Pb/^{204}Pb$ (37.8). The primitive alkalic magmas are

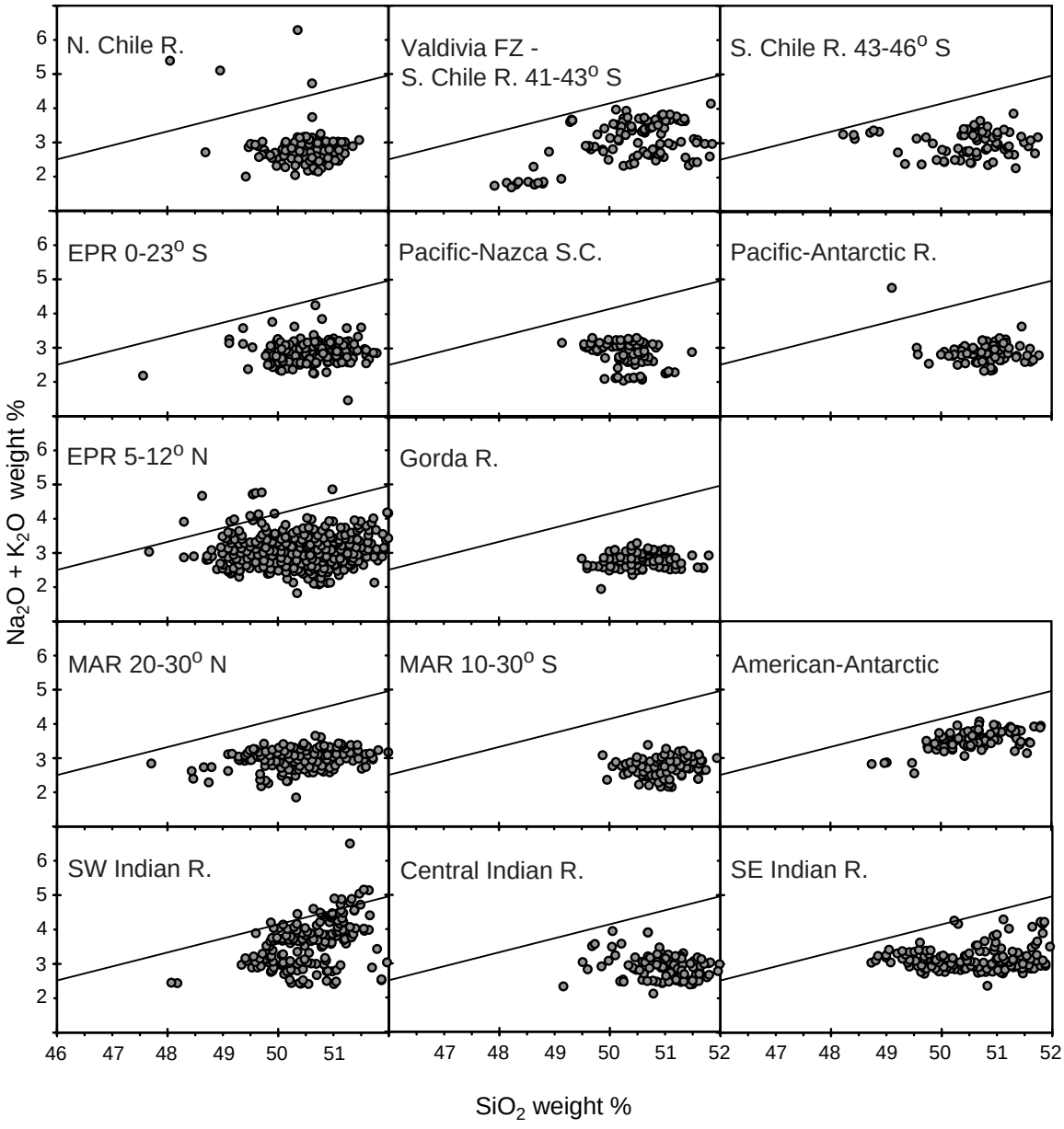

Figure 28: Populations worldwide of mid-ocean ridge basalt samples, showing their alkalic basalt (upper field) or tholeiitic basalt (lower field) classification, based on total alkalis vs. SiO_2. All samples with $SiO_2 < 52$ weight % that were reported as of August 2001 on the PetDB database maintained by Lamont-Doherty Earth Observatory are shown, as well as samples from this study from the Northern Chile Ridge, Valdivia Fracture Zone ITSCs, and Southern Chile Ridge segments S5-S7 (41-43° S).

generated by melting of a distinct fertile mantle source. The primitive alkalic magma end-member has a trace element composition similar to the most enriched alkalic basalt sample (D101-2) erupted at segment N5. The fertile mantle source must be enriched in incompatible trace elements relative to the depleted mantle source and is expected to have an isotopic composition with low $^{143}Nd/^{144}Nd$ and high $^{87}Sr/^{86}Sr$, $^{206}Pb/^{204}Pb$, $^{207}Pb/^{204}Pb$, and $^{208}Pb/^{204}Pb$, but the exact composition is not known. When isotope data for the alkalic basalt samples are obtained, the isotopic composition of the fertile mantle source can be quantitatively assessed and compared to the enriched end-member of mixing among the MORBs shown in Figure 26. Variability in extent of melting produces primary magmas that vary slightly in trace element composition, and is one cause of the scatter around the mixing curve in Figure 27.

The amount of alkalic primitive magma in the mixture controls the incompatible trace element content (including K_2O and K/Ti), but doesn't significantly affect major element content. This is because the addition of small amounts of material affects low-abundance species more than it affects high-abundance species, and because the major element compositions of the mixing end-members are not as different from each other as the trace element concentrations are. For example, Na_2O in the depleted N-MORB D105-2 is 2.58 weight %, and in the alkalic basalt D101-2 is 4.60 weight %, a difference of less than a factor of two. However, La/Sm in D105-2 is 0.65, in D101-2 is 4.38, a difference of more than a factor of six; K/Ti in D105-2 is 0.022, in D101-2 is 0.869, a difference of almost a factor of 40.

Metasomatic addition of very small quantities of a fluid enriched only in the most highly incompatible trace elements (Cs, Rb, Ba, Th, U, Nb, and Ta) may also occur. Observed depletions and enrichments in these elements do not correlate with depletions in the rare earth elements (Figure 14), and therefore cannot be attributed to the same alkalic mixing end-member.

Parent magmas to Northern Chile Ridge MORBs are uniform in major element composition compared to the different types of oceanic basalts observed globally, suggesting that the depleted mantle under this ridge has a generally uniform major element composition and underwent broadly uniform extents of melting. However, scatter in the trends of backtracked major elements cannot be fully explained by low-pressure crystallization effects, either varying pressure of crystallization or varying H_2O content (Figure 22). The subtle covariations may arise from combinations of different extents of melting, different styles of melt aggregation in the melt column, and different styles of segregation to the crust, in addition to the effect of Na_2O content on offsetting the LLDs in the other oxides. Furthermore, even though the effect of mixing on major element compositions would be small, it would be present, and it is likely to be yet another process responsible for these variations. In modern conceptualizations of magma production at mid-ocean ridges, variations in extent of melting are coupled with variations in depth of melting (*Klein and Langmuir*, 1987; *Langmuir et al.*, 1992) and variations in depletion of a basaltic component in the mantle source, *e.g.* the idea of column melting.

The most likely scenario by which mixing as described above might occur is melting of an upper mantle that contains ubiquitous blobs of fertile mantle embedded in a depleted mantle matrix, similar to the "plum pudding" mantle idea (*e.g.*, *Sleep*, 1984; *Allègre and Turcotte*, 1986). The exact shape of the fertile mantle blobs is unknown. The early-formed melts would preferentially sample the fertile mantle blobs and would have an enriched composition. After a certain temperature, the depleted mantle matrix would begin to melt and the fertile mantle blobs would stop melting, so that the later-formed melts would have a depleted composition (*Phipps Morgan*, 2001). *Langmuir et al.* (1992) described a similar scenario for the mantle under the East Pacific Rise system (including the Pacific-Nazca Ridge and the Pacific-Antarctic Ridge).

The Northern Chile Ridge fertile mantle component must be distributed relatively uniformly under the ridge as small heterogeneities ("blobs"). The mantle heterogeneity cannot be centralized under one segment, producing enriched melts that migrate away and contaminate the rest of the ridge as is observed near hotspots at the Mid-Atlantic Ridge (*Schilling*, 1985), because there are no patterns of decreasing enrichment in incompatible trace elements away from segment N5 (Figure 15). However, it seems that segment-scale along-axis redistribution, from the site where magma segregates from the mantle to the site of eruption, is widespread within the Northern Chile Ridge segments. The population of MORB samples shows no correlation between $[Na_2O]_8$ and axial depth, either at the scale of the whole ridge (Figure 23), or within individual segments (Figure 29).

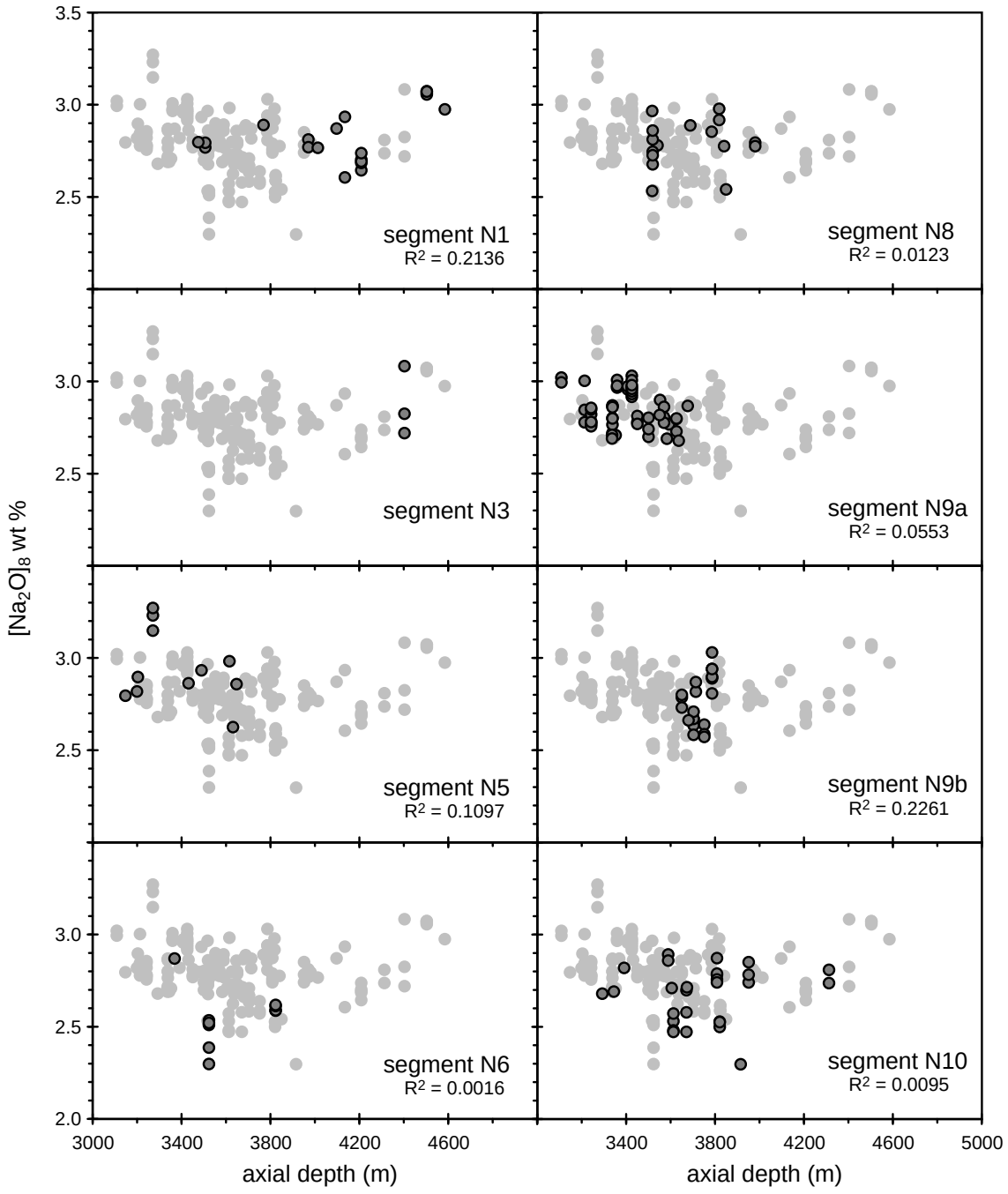

Figure 29: $[Na_2O]_8$ vs. axial depth (indicative of crustal thickness) among Northern Chile Ridge MORBs for each segment (dark grey points), with the whole NCR MORB population shown for comparison (light grey points). $[Na_2O]_8$ values were calculated by backtracking the sample composition along the best-fit MELTS model, and includes only those samples with MgO < 8.97 weight %. R^2 values for each segment calculated as in Figure 14.

DISCUSSION

Using the understanding of Northern Chile Ridge petrogenesis that was developed above, issues of regional interaction between the mantle and tectonics can be addressed. First, the regional mantle heterogeneity of the southeast Pacific ocean basin will be explored. Then, the Northern Chile Ridge will be used as a guidepost for understanding the behavior of non-hotspot intermediate rate ridges. Finally, a preliminary assessment of the effects of segmentation and transform offsets on petrogenetic processes and mantle thermal structure will be described.

Regional Chemical Heterogeneity of the Southeast Pacific Mantle

The Northern Chile Ridge lava population is more uniform and more depleted in incompatible trace elements (using K/Ti as a proxy) than lava populations at other southeast Pacific mid-ocean ridges (Figure 30). The Northern Chile Ridge lava population has the lowest mean K/Ti (0.071) and the smallest standard deviation in K/Ti ($1\sigma = 0.027$) of all the ridges in the southeast Pacific. However, the Northern Chile Ridge lava population has the same lower bound (near K/Ti = 0.02) as other southeast Pacific ridge populations; this likely indicates that the depleted component of the mantle source has the same composition at the Northern Chile Ridge as at other southeast Pacific ridges. It is possible that a lower bound in K_2O is due to a common detection limit during analysis, but it is unlikely that this would affect TiO_2 contents, or K/Ti ratios in

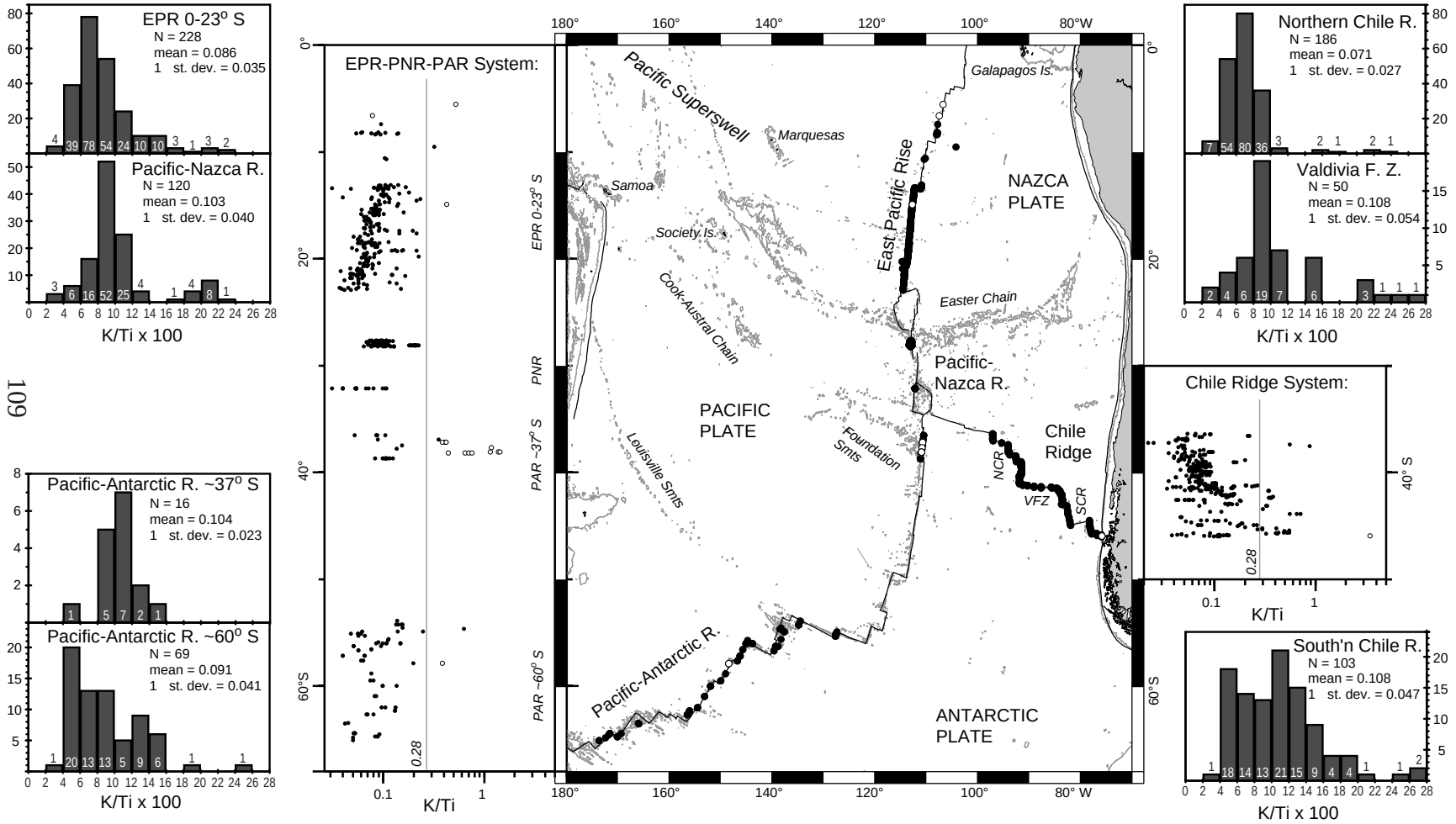

Figure 30: K/Ti as a proxy for trace element enrichment in lavas from southeast Pacific mid-ocean ridge systems. Samples are from this study and from others reported in the PetDB online database (see Acknowledgements for references). Map shows locations of samples along the mid-ocean ridge axes: black dots are basalts (SiO_2 < 52 weight %), white dots are evolved lavas (andesites and dacites, SiO_2 > 52 weight %). Also shown is the 2500 m contour of ocean floor bathymetry. Flanking latitudinal plots show the geographic distribution of enriched samples at the same scale as the map. Histograms show statistics of K/Ti in populations of lavas at each ridge. Note that while the K/Ti vs. latitude plots show all samples, the histograms show only depleted basalts (K/Ti < 0.28).

evolved samples with higher K_2O and TiO_2. *Bach et al.* (1996) gave their Northern Chile Ridge lava samples the blanket characterization of "unusually depleted", but in fact, a more accurate assessment is that while not all Northern Chile Ridge lavas are excessively depleted, the population as a whole is more depleted than other ridges in the southeast Pacific.

A likely explanation for the low mean K/Ti in the Northern Chile Ridge lava population is that the Northern Chile Ridge mantle contains fewer fertile mantle blobs than does the rest of the southeast Pacific mantle (Figure 31). This is a natural extension of the "plum-pudding" mantle concept. In this case, melting would produce a smaller percentage of enriched melts among the total melt products, and the mixtures that are the erupted lavas would reflect a lower contribution from enriched melts.

A competing idea from *Bach et al.* (1996) to explain the occurrence of "ultra-depleted" samples is that the mantle source of present-day Northern Chile Ridge erupted lavas was itself the residue of an even earlier episode of partial melting. They suggested that the previous melt extraction episode might have occurred as mantle upwelled at the East Pacific Rise to the west of the present-day Northern Chile Ridge, or, alternately, that it might have occurred during upwelling at the fossil Pacific-Farallon Ridge. In either case, they pointed out, the double episodes of melt extraction would be unique to the formation of the Northern Chile Ridge by rift propagation, as discussed earlier (*Bach et al*., 1996). This interpretation is buttressed by evidence from noble gas isotopes that suggests a previous episode of degassing (*Niedermann and Bach*, 1998).

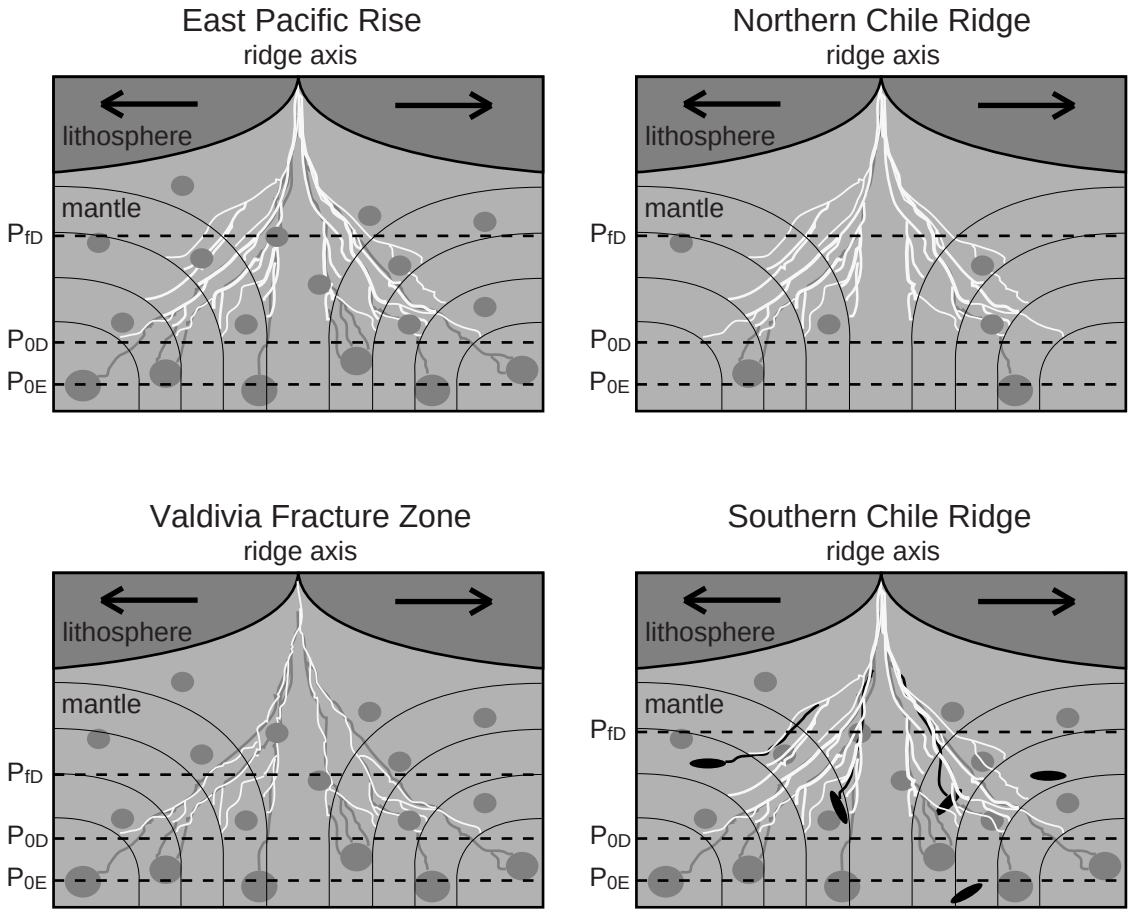

Figure 31: Conceptual illustration of differences in the mantle under the East Pacific Rise, Northern Chile Ridge, Valdivia Fracture Zone, and Southern Chile Ridge. The Northern Chile Ridge has a sparser distribution of enriched mantle heterogeneities (dark grey) embedded in the depleted mantle (light grey), which results in a lesser contribution of alkalic melts (grey lines) to the depleted MORB melts (white lines). The Valdivia Fracture Zone has lower extents of melting of the depleted mantle, which results in a lesser contribution of depleted MORB melts. The Southern Chile Ridge mantle contains an additional type of arc-like heterogeneity (black ellipses) that contributes arc-like melts (black lines). The shapes of all mantle heterogeneities shown are arbitrary. Dashed lines indicate the pressure at which the enriched mantle heterogeneities begin melting (P_{0E}), the pressure at which the depleted mantle begins melting and the enriched mantle heterogeneities stop melting (P_{0D}), and pressure at which the depleted mantle stops melting (P_{fD}). Solid curves indicate paths of upwelling mantle flow.

However, there are problems with this hypothesis. Firstly, it is unlikely that the Northern Chile Ridge is currently drawing from the lid of mantle that was previously depleted: assuming vertical mantle upwelling, at an upwelling rate of 26.5 km/My (half the full spreading rate of 53 mm/yr), in the 12 My the Northern Chile Ridge has been spreading, it would have drawn a column of mantle 318 km long. The thickness of a lid of previously-melted mantle residue would be approximately the same as the depth of the melting region, which is thought to be only 40-100 km. Secondly, this hypothesis assumes that the Northern Chile Ridge "ultra-depleted" samples were generated from a mantle source that was also ultra-depleted; however, the K/Ti data indicate that the depleted mantle component at the Northern Chile Ridge has a trace element composition similar to the depleted mantle component at other ridges.

A previous melting episode is not required to explain the incompatible trace element depletion of the Northern Chile Ridge lava population. In a plum-pudding type mantle, the effect of a previous melt extraction event might be to reduce the number of fertile mantle blobs, which would result in an erupted lava population with lower K/Ti; but this result is indistinguishable from the case where the number of fertile mantle blobs is reduced by any other mechanism. An alternate reason why the mantle under the Northern Chile Ridge would contain fewer blobs of enriched mantle than does the rest of the southeast Pacific mantle is that the Northern Chile Ridge may be sheltered from the South Pacific Superswell. In this case, an explanation is required for why Valdivia Fracture Zone and Southern Chile Ridge lavas are not observed to be as depleted as the Northern Chile Ridge lavas.

The K/Ti data for the Northern Chile Ridge lava population require that the Northern Chile Ridge be sampling a mantle that is geochemically distinct from its surroundings. Other explanations for the geochemical differences fail. The difference in mean K/Ti between the Northern Chile Ridge and other southeast Pacific ridges is not due solely to the slower spreading rate of the Northern Chile Ridge. While the Northern Chile Ridge spreads at an intermediate full spreading rate of 53 mm/yr, the East Pacific Rise/Pacific-Nazca Ridge/Pacific-Antarctic Ridge system spreads at superfast (> 100 mm/yr) rates, to intermediate rates (74-54 mm/yr) only in the southernmost regions (56-66° S). However, at lower extents of melting, if the mantle were geochemically the same, lavas at the Northern Chile Ridge would be more enriched than lavas at other southeast Pacific ridges, not more depleted as is observed.

Similarly, the difference in standard deviation in K/Ti, or uniformity of the lava population, is a real characteristic of the mantle. *Hess* (1992) suggested that homogeneous lava populations might be the result of large-scale mixing in a persistent and extended low porosity zone in the mantle during upwelling (*e.g.*, *Sparks and Parmentier*, 1991). However, the lateral scale of trace element homogeneity at the Northern Chile Ridge, 550 km, is quite large compared to the probable depth of the melting zone. It is unlikely that melts from disparate ends of this large study region could homogenize effectively.

Other chemical differences exist in the southeast Pacific mantle. *Klein and Karsten* (1995) reported that incompatible trace elements in some Southern Chile Ridge lavas near the Chile Margin Triple Junction were more characteristic of arc lavas than MORB

lavas. The geographic distribution of contaminated lavas near the Chile Margin Triple Junction is discontinuous. Lavas with subduction signatures were found at the ridge segment currently being subducted (S1) and a segment farther north (S3), but not at the intermediate segment (S2). However, there is no evidence at the Northern Chile Ridge for the arc-like contaminant that was seen near the site of Southern Chile Ridge subduction (Figure 32). Neither Northern Chile Ridge T-MORBs nor alkalic basalts are like Southern Chile Ridge "type II" E-MORBs. Northern Chile Ridge samples all have Nb/U greater than 37, Rb/Cs greater than 60, Ce/Pb greater than 20, and Th/La lower than 0.13. The one sample with low Ce/Pb is one that we suspect has artificially high Pb contents due to anthropogenic Pb contamination. Enriched samples from the Valdivia Fracture Zone and the northernmost segments of the Southern Chile Ridge also do not exhibit this arc-like contaminant (*Sturm et al.*, 1998; *Klein et al.*, 2001). This indicates that the reach of metasomatic fluids from the recycled slab is limited to the very southernmost portion of the Southern Chile Ridge, within a few 100's of km from the site of ridge subduction.

There is a stark contrast between the homogeneity and depletion of lavas at the Northern Chile Ridge, and the heterogeneity and enrichment of lavas at the Valdivia Fracture Zone and Southern Chile Ridge (Figure 31). The reason for this contrast is unclear. In other respects, the Northern Chile Ridge and Southern Chile Ridge are very similar: both have the same spreading rate of 53 km/My, both have an axial morphology of pronounced axial valleys, and both have a segmentation geometry that is cut by large-offset transforms.

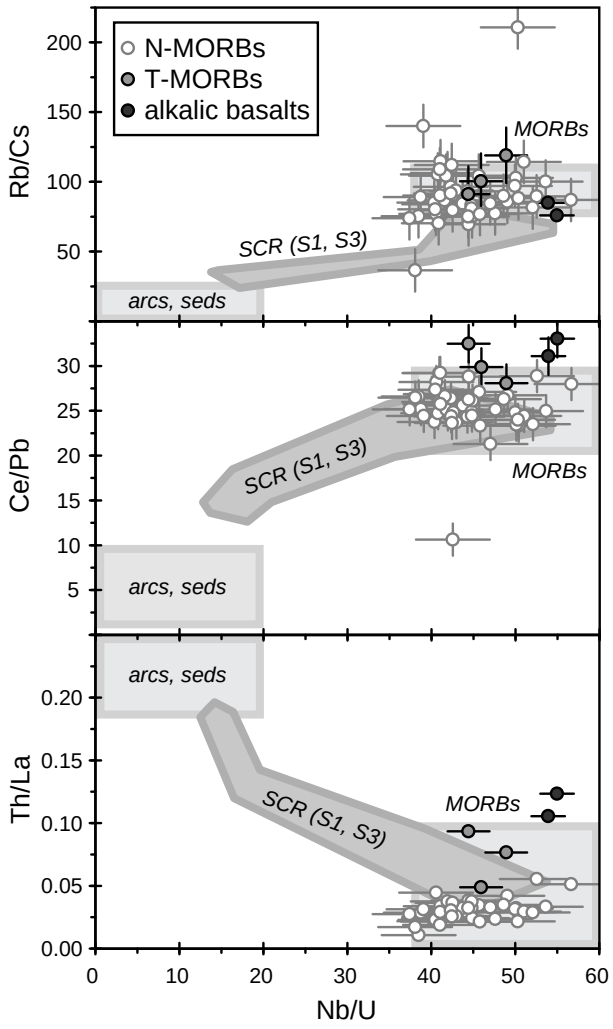

Figure 32: Mantle component fingerprints in Northern Chile Ridge samples, compared to Southern Chile Ridge segments S1 and S3 (grey fields, from *Klein and Karsten,* 1995). Light grey boxes indicate regions where trace element compositions typically lie for lavas recovered in arc settings and sediments ("arcs, seds") and for MORBs and ocean island basalts ("MORBs").

The contrast in heterogeneity is different from the subduction contamination discussed above, which is confined to the region near the Chile Margin Triple Junction. *Bach et al.* (1996) suggested that the Northern Chile Ridge and Southern Chile Ridge sample compositionally distinct mantles. However, sampling in their study, which included only widely spaced sites on the Northern Chile Ridge, could not present a complete characterization of the Northern Chile Ridge, and could not expose the regional change in lava compositions at the Valdivia Fracture Zone and the northernmost Southern Chile Ridge. Lavas from the Valdivia Fracture Zone and Southern Chile Ridge are the most heterogeneous population of any ridge in the southeast Pacific (Figure 30). The only other site with great amounts of heterogeneity is along the Pacific-Antarctic Ridge near 37º S, where the Farallon hotspot is thought to be contributing material to the spreading center (*Hékinian et al.*, 1997, 1999). However, no hotspot is thought to exist near the Valdivia Fracture Zone or Southern Chile Ridge.

Heterogeneous lavas at the Valdivia Fracture Zone intra-transform spreading centers may be due to low extents of melting resulting from the tectonic-dominated nature of spreading (Figure 31). In this case, there would not be as much depleted melt to dilute the enriched melts during mixing. $[Na_2O]_8$ contents of recovered lavas indicate that extents of melting are indeed lower at the Valdivia Fracture Zone than at the Northern Chile Ridge. In addition, a megamullion, which has been interpreted as a sign of amagmatic extension at the Mid-Atlantic Ridge (*e.g.*, *Tucholke et al.*, 1998), was found at Valdivia Fracture Zone segment V6 (*Martinez et al.*, 1998; *Karsten et al.*, 1999).

However, there also is evidence that regional mantle heterogeneity in the southeast Pacific cannot be completely characterized simply by greater or lesser contributions of Pacific hotspot-type fertile mantle blobs, but is of a different character unique to the southeast Pacific. *Vlastélic et al.* (1999) found that the Pacific ocean basin is generally divided into two isotopic provinces, with a boundary at the Easter Microplate (25º S along the East Pacific Rise): lavas from the northern province are offset to higher $^{143}Nd/^{144}Nd$, higher $^{87}Sr/^{86}Sr$, and lower $^{206}Pb/^{204}Pb$ along the Pacific Nd-Sr-Pb trends, while lavas from the southern province are offset to lower $^{143}Nd/^{144}Nd$, lower $^{87}Sr/^{86}Sr$, and higher $^{206}Pb/^{204}Pb$. Lower $^{87}Sr/^{86}Sr$ and higher $^{206}Pb/^{204}Pb$ point to a depleted MORB-like mantle source, but lower $^{143}Nd/^{144}Nd$ would be characteristic of a greater contribution of enriched plume-like mantle.

The Northern Chile Ridge (using isotope data from *Bach et al.*, 1996) and Southern Chile Ridge are in regions of the Pacific with different isotopic affinities. While the Northern Chile Ridge has "southern" type isotopes (low $^{143}Nd/^{144}Nd$, low $^{87}Sr/^{86}Sr$, and high $^{206}Pb/^{204}Pb$), the Southern Chile Ridge has "northern" type isotopes (high $^{143}Nd/^{144}Nd$, high $^{87}Sr/^{86}Sr$, and low $^{206}Pb/^{204}Pb$), although both ridges are geographically south of the boundary and should be in the "southern" isotopic province (*Vlastélic et al.*, 1999).

A definitive conclusion to this issue must await isotope data for the Northern Chile Ridge alkalic basalt samples, and trace element and isotope data for the Valdivia Fracture Zone intra-transform spreading centers and Southern Chile Ridge segments S5-S7.

Intermediate spreading rate

It has long been known that there is a gradual transition from large (1-2 km deep) axial valley morphology at slow spreading rates, to shallow (50-200 m deep) axial valley morphology at intermediate spreading rates, to axial rise morphology at fast spreading rates (*Macdonald*, 1986). In addition, it has been found that zero-age depth, relief of axial morphology, asymmetry, and stochastic roughness all depend on spreading rate at axial valley ridges, but are independent of spreading rate at axial rise ridges (*Small*, 1998). It is thought that this occurs because the mechanisms responsible for morphology at mid-ocean ridges undergo a transition that is coincident with the transition from axial valley to axial rise morphology (*Small*, 1998). It has been shown that there is overlap between axial valley and axial rise morphologies at intermediate spreading rates of ~53-67 km/My (full rate). This excludes the Australian-Antarctic Discordance (AAD) and the Reykjanes Ridge which are thought to be affected by deep mantle temperature anomalies (*Small*, 1998).

All of the morphological observations point to control of morphological features by magma supply and mantle temperature (*Small*, 1998). Therefore it is important to understand the spreading rate dependence of the thermal budget controlling shallow crystallization, as part of crustal accretion. This thermal budget is thought to depend on magma supply, on the residence time for magma storage such as occurs in subaxial melt lenses and mush zones, and on heat loss through eruption and hydrothermal circulation. An examination of Northern Chile Ridge lavas shows that at intermediate spreading rates,

these factors are susceptible to being affected by tectonic and geologic factors, in particular the presence of hotspots, but also including small fluctuations in spreading rate and deep mantle temperature variations.

The thermal budget controlling shallow crystallization is better known at fast spreading rates and at slow spreading rates than it is at intermediate spreading rates. Using a compilation of Mg # = Mg/(Mg + Fe^{2+}) for ridges at different spreading rates, *Sinton and Detrick* (1992) showed that lavas recovered from ridges with spreading rates slower than 50 km/My (full rate) are more primitive than lavas recovered from ridges with spreading rates faster than 80 km/My, which are more evolved. They interpreted this observation in terms of a spreading-rate-dependent magma supply rate and the presence of an axial magma chamber. At fast spreading rates, they suggested that narrow but continuous melt lenses, which are required by geophysical evidence, allow moderate extents of crystallization to occur between magma recharge events. At slow spreading rates, they suggested that the absence of any steady-state magma chamber, which is also required by geophysical evidence, hastens the magma freezing process in the crust and prevents any magmas except primitive magmas from erupting (*Sinton and Detrick*, 1992).

The population of intermediate-rate (50-80 km/My) ridge lavas in that study was heavily biased by samples from the Juan de Fuca and Galapagos Ridges, which are influenced by hotspots. They found that these lavas were the most variable in Mg # and extended to the most evolved (low Mg #) extremes. To explain this observation, *Sinton and Detrick* (1992) predicted that at intermediate spreading rates, small, discontinuous

melt lenses should exist, because they considered this environment to be the most favorable for extensive differentiation.

The Northern Chile Ridge samples show that the *Sinton and Detrick* (1992) description of the thermal budget at intermediate spreading rate ridges is highly affected by the hotspots, *i.e.*, there are differences in the shallow thermal budget at hotspot-influenced and non-hotspot-influenced ridges. A histogram of Mg # for the population of Northern Chile Ridge samples (full spreading rate is 53 km/My; Figure 33) shows that the Northern Chile Ridge erupted lavas are more primitive than the "intermediate" population of *Sinton and Detrick* (1992), and even more primitive than their "slow" population. The same is true for samples from the northern section of the Gorda Ridge (full spreading rate is 55 km/My) and the Pacific-Antarctic Ridge 56-66° S (full spreading rate is 54-74 km/My).

At propagating rifts also, the geochemistry that has been previously thought to be typical of that environment may in fact be affected by the presence of hotspots. At the Northern Chile Ridge segment N5 propagating rift, highly differentiated lavas are absent (Figure 34), even though advanced differentiation products of MORBs (FeTi basalts and rare andesites and dacites) have been found previously at four propagating rift tips at the Galapagos Spreading Center and the Juan de Fuca Ridge, and have been considered to be a normal product of the fluctuating magma plumbing system in a propagating rift setting (*Christie and Sinton*, 1981; *Sinton et al.*, 1983). The only other place where andesites and silicic lavas have been found in the southeast Pacific is on the Pacific-Antarctic Ridge near 37° S, where there are no propagating rifts, but the Foundation Hotspot

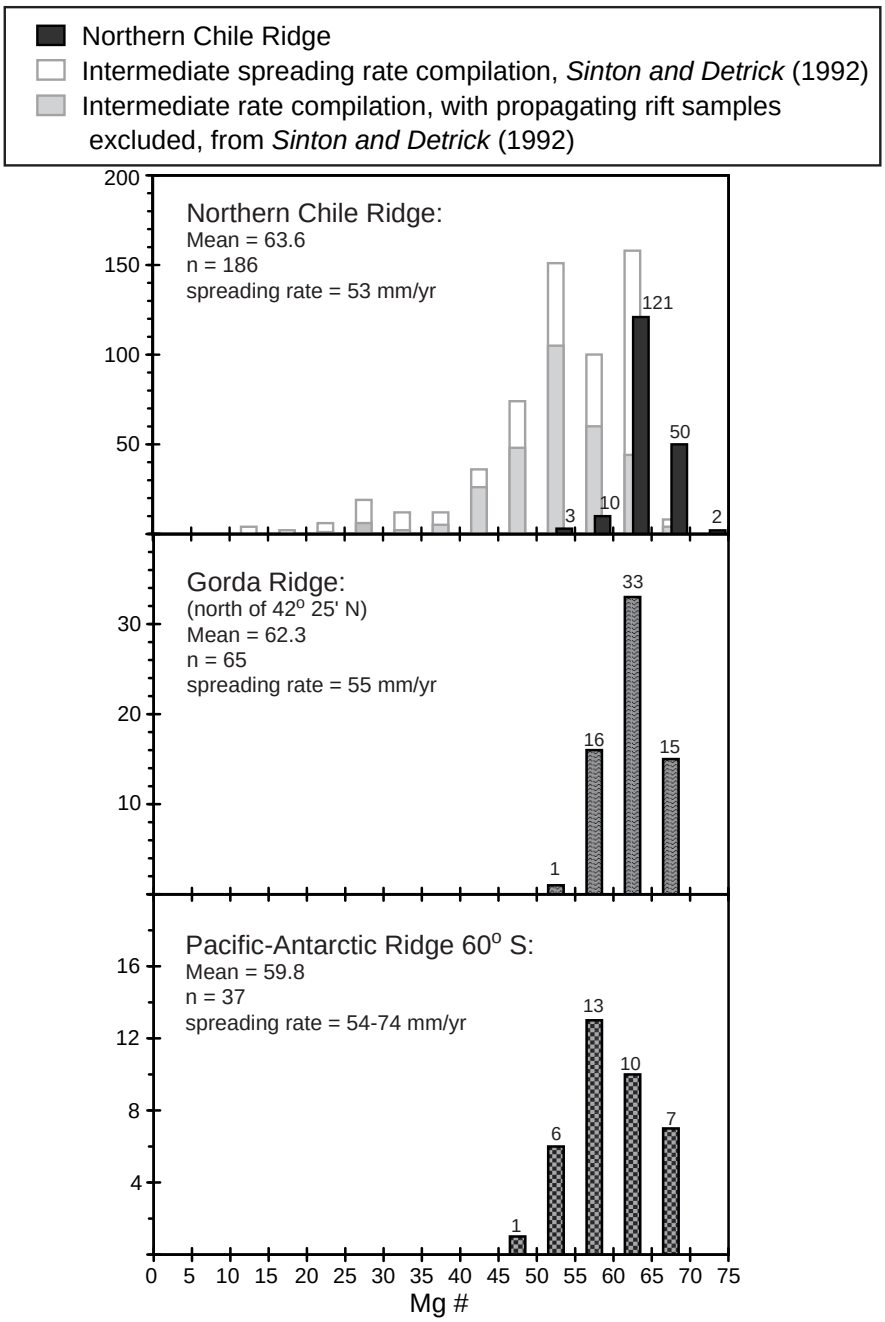

Figure 33: Histogram of Mg # for Northern Chile Ridge MORBs, compared to the histogram for intermediate rate ridges compiled by *Sinton and Detrick* (1992) (top); that compilation was biased towards samples from hotspot-influenced regions of the Juan de Fuca Ridge and the Galapagos Spreading Center. Also shown are two other non-hotspot intermediate spreading rate ridges, the Gorda Ridge (center; data from *Clague et al.*, 1984; *Clague and Holmes*, 1989; *Davis and Clague*, 1987, 1990) and the Pacific-Antarctic Ridge near 60° S (bottom; data from *Vlastélic et al.*, 2000). The two Northern Chile Ridge samples with Mg # > 70 are D76 (segment N9a, Mg # = 70.2) and D52 (segment N10, Mg # = 72.0).Mg # = Mg / (Mg + Fe^{2+}), assuming 90% of the total Fe is Fe^{2+}.

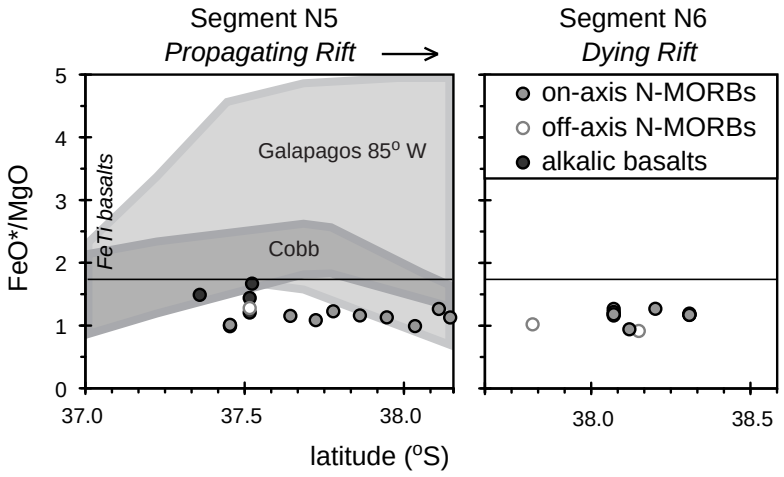

Figure 34: Comparison of lavas found at the Northern Chile Ridge propagating rift (segments N5 and N6, data points) to lavas found at propagating rifts at the Galapagos Spreading Center 85° W and the Cobb Fracture Zone (Juan de Fuca Ridge) (grey fields, from *Sinton et al.*, 1983). FeO*/MgO in all Northern Chile Ridge samples is lower than 1.67; FeO*/MgO at the Galapagos Spreading Center 85° W propagating rift reaches 5. *Sinton et al.* (1983) considered samples with FeO*/MgO > 1.75 to be FeTi basalts.

interacts with the ridge (*Hékinian et al.*, 1997, 1999). At the Galapagos and Juan de Fuca propagating rifts, the maximum extent of differentiation has been found to occur within 50 km of the propagating rift tip, and the signal of anomalous differentiation has been found to extend 100-200 km along the ridge behind the propagating rift tip (*Sinton et al.*, 1983). However, at the tip of the Northern Chile Ridge propagating rift, only relatively primitive basalts are found (Figure 34). Sample spacing at segment N5 was approximately 5km, which is dense enough to have recovered differentiated lavas if they occur in a pattern similar to the Galapagos Spreading Center and the Juan de Fuca Ridge. The absence of any high-amplitude magnetic (HAM) zone in the Northern Chile Ridge magnetics data acquired on the PANORAMA Expedition also suggests the absence of FeTi basalts.

At intermediate spreading rates there may be differences in the role of shallow melt lenses at hotspot-influenced and non-hotspot-influenced ridges. The non-hotspot-influenced lava populations (Northern Chile Ridge, Pacific-Antarctic Ridge, and northern Gorda Ridge) may have been products of an environment where shallow melt lenses are absent, less long-lived, or not important in controlling the extent of magma differentiation.

This could be the result of the combination of a shorter length of time for crystal growth and a slower crystal growth rate. The time for crystal growth might be shorter at a non-hotspot ridge because a cooler ambient crust does not allow melt to migrate out of the crystal mush zone, where most crystallization is thought to occur (*Sinton and Detrick*, 1992), and there is a very short residence time for magma in the melt body before

freezing occurs. Crystal growth rate for a given magma composition is mainly dependent on temperature. The crystal growth rate might be slower at an intermediate spreading rate ridge than at a slow-spreading ridge because magma supply is a little higher, melt bodies entering the crust are a little larger and have lost less heat during ascent, and the magmatic temperature is a little higher.

In general, the tectonic and geologic controls that are important for petrogenesis at the Northern Chile Ridge are different from those at two other non-hotspot intermediate rate ridges, the Pacific-Antarctic Ridge 56-66° S, and the Southeast Indian Ridge 110-166° E. At the Northern Chile Ridge, the geochemistry of erupted lavas is dominated by magma mixing and the distribution of chemical heterogeneities in the source mantle, but at these other sites the geochemistry of erupted lavas has been shown to be dominated by extent of melting. Extent of melting at the Pacific-Antarctic Ridge 56-66º S is controlled by variations in spreading rate from 74 mm/yr in the north to 54 mm/yr in the south. There are no appreciable ridge-scale mantle temperature variations at this site (*Vlastélic et al.*, 2000). Extent of melting at the Southeast Indian Ridge 110-116º E is controlled by mantle temperature variations. The spreading rate at this site is approximately constant at 74-76 mm/yr (full rate) (*Shah and Sempére*, 1998). At the Northern Chile Ridge, these tectonic features are absent. There are no spreading rate variations or mantle temperature variations that might have a strong influence on the extent of melting.

The evidence discussed above suggests that at intermediate spreading rates, the thermal regimes controlling petrogenesis and crustal accretion are easily influenced by tectonic variables such as hotspots, small variations in spreading rate, and mantle

temperature variations. When comparing other ridges to the Northern Chile Ridge, it becomes clear how pervasive the influence of these variables is.

Influence of Segmentation and Transform Offsets on Petrogenesis

The shallow mantle at the Northern Chile Ridge is not being cooled by long-offset transforms in the crust, contrary to what *Bach et al*. (1996) had suggested. *Bach et al.* (1996) had pointed out that the Northern Chile Ridge has higher Na_2O contents than East Pacific Rise and Galapagos Spreading Center magmas, which reflects a lower extent of melting. They postulated that the lower extent of melting was due to cooler temperatures that were caused by the presence of the long-offset transforms. They noted that cooling could not extend very deep into the upper mantle, because the seismic tomography results of *Zhang and Tanimoto* (1993) do not show a cold anomaly in the sub-Chile Ridge mantle.

The difference in Na_2O contents at the Northern Chile Ridge does in fact occur, but it is completely explainable by differences in spreading rate. The Northern Chile Ridge has a normal extent of melting for its spreading rate, based on the global relationship found by *Niu and Hékinian* (1997), and a normal axial depth for its extent of melting, based on the global relationship found by *Klein and Langmuir* (1987) (Figure 35). Southern Chile Ridge segments S5-S7, which are axial-valley, transform-dominated ridge segments spreading at the same rate as the Northern Chile Ridge, similarly exhibit a normal mean extent of melting for their spreading rate and a normal mean axial depth for their extent

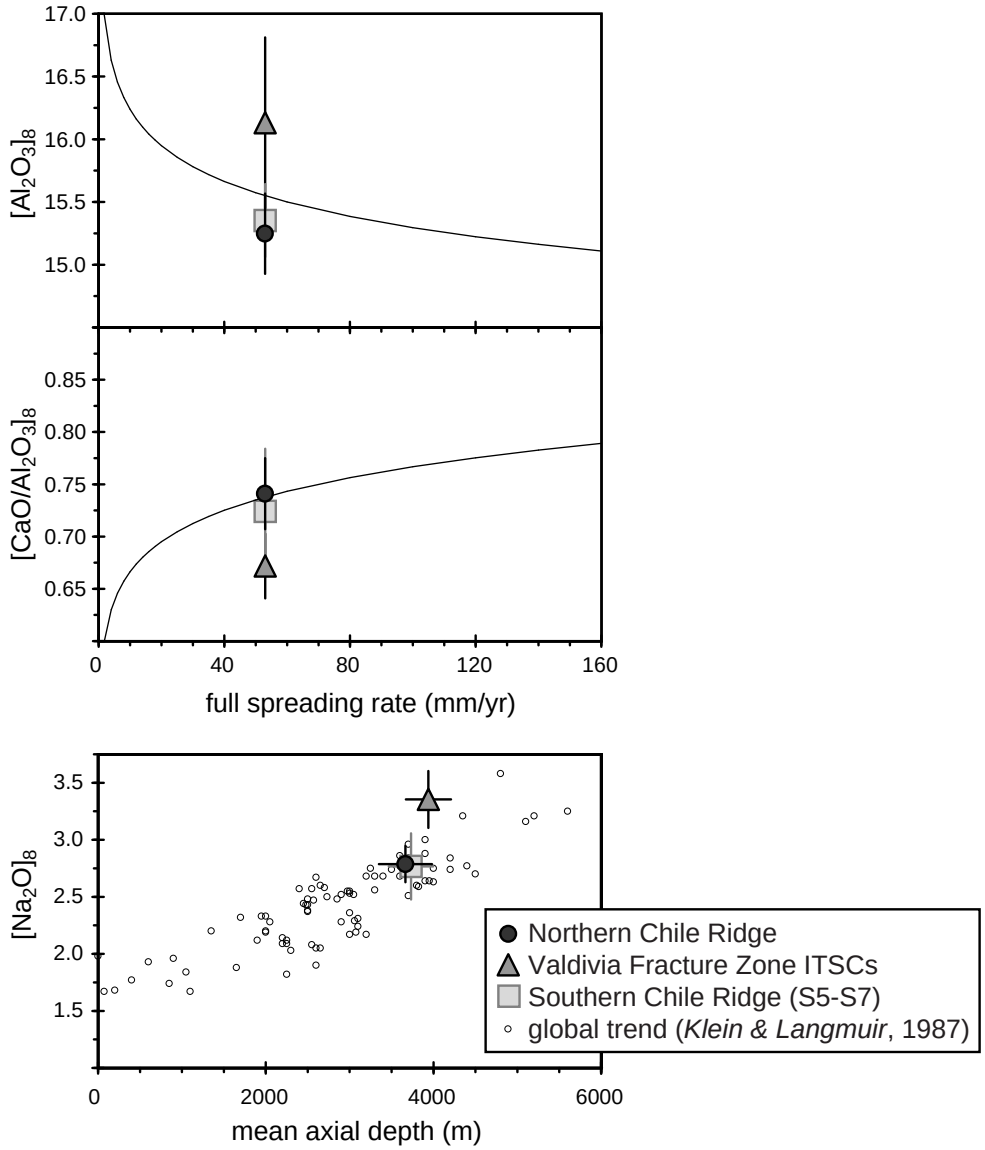

Figure 35: Comparison of mean MORB major element compositions from the Northern Chile Ridge, Valdivia Fracture Zone ITSCs, and Southern Chile Ridge segments S5-S7 to global systematics. The relationships with spreading rate are from *Niu and Hékinian* (1997): $[Al_2O_3]_8 = 17.241$ x [spreading rate]$^{-0.026}$, and $[CaO]_8/[Al_2O_3]_8 = 0.579$ x [spreading rate]$^{0.061}$. The global trend of regionally averaged $[Na_2O]_8$ vs. axial depth is from *Klein and Langmuir* (1987). Northern Chile Ridge values are $[Al_2O_3]_8 = 15.25 \pm 0.32$; $[CaO]_8/[Al_2O_3]_8 = 0.741 \pm 0.034$; $[Na_2O]_8 = 2.79 \pm 0.16$; and axial depth = 3660 ± 316. Valdivia Fracture Zone values are $[Al_2O_3]_8 = 16.13 \pm 0.68$; $[CaO]_8/[Al_2O_3]_8 = 0.672 \pm 0.031$; $[Na_2O]_8 = 3.35 \pm 0.25$; and axial depth = 3944 ± 269. Southern Chile Ridge values are $[Al_2O_3]_8 = 15.35 \pm 0.29$; $[CaO]_8/[Al_2O_3]_8 = 0.724 \pm 0.060$; $[Na_2O]_8 = 2.77 \pm 0.29$; and axial depth = 3737 ± 265. Spreading rate for all three regions is 53 km/My. Error bars show1 standard deviation among the population. Major elements were backtracked along the best-fit MELTS crystal fractionation model.

of melting. Therefore this region of the Southern Chile Ridge does not appear to be cooled by transforms either.

On the other hand, the Valdivia Fracture Zone lavas do seem to have an unusually low extent of melting, shown in high mean $[Al_2O_3]_8$ and low mean $[CaO/Al_2O_3]_8$ compared to global systematics (Figure 35). This section of the ridge has the same spreading rate as the Northern Chile Ridge and Southern Chile Ridge. The relationship between high $[Al_2O_3]_8$ and low extent of melting is verified by high $[Na_2O]_8$ in these samples also (Figure 8; high $[Al_2O_3]_8$ alone can also be due to differences in pressure of crystal fractionation, but high $[Na_2O]_8$ cannot).

Backtracking for the Valdivia Fracture Zone and Southern Chile Ridge lavas was done using the MELTS slope for the Northern Chile Ridge MORBs and the same MgO constraints (MgO = 7.93-8.87). This MgO constraint included 40% of the samples for the Valdivia Fracture Zone, and 49% of the samples for Southern Chile Ridge segments S5-S7. However, even using all the samples (*i.e.*, with no MgO constraint), the calculated means and standard deviations were not much different.

The Chile Ridge example indicates that in a normal mid-ocean ridge setting, even at an intermediate spreading rate and with no hotspots nearby, we should not expect the presence of long-offset transforms to affect the extent of melting in a large-scale sense. However, in the extreme case of ITSCs at a fracture zone system, extent of melting is in fact reduced. It is unclear whether this is due to an effect on mantle temperature or a tectonic effect.

There is no consensus on how transform offsets are expected to affect magma supply. Some workers have inferred that transforms cause a very local decrease in extent of melting of the mantle, extending only 15 km down the segment axis (*Langmuir and Bender*, 1984). There have been few interpretations of sites where transforms are thought to affect large-scale regional melting patterns over hundreds of km such as *Bach et al*. (1996) invoked.

In the Results section, it was shown that there are no regional-scale geographic variations at the Northern Chile Ridge, either in trace element content (distribution of enriched mantle blobs) or MgO content (extent of differentiation). Along-axis variations in extent of melting calculated from the equation of *Niu and Batiza* (1991) for the Northern Chile Ridge are shown in Figure 36. At the northern end of segment N5, high $[Na_2O]_8$ contents in the lavas cause the calculated extent of melting to be low. However, these high $[Na_2O]_8$ contents are probably due to mixing with the alkalic lavas and do not reflect real differences in extent of melting.

The predicted TFE, the effects of transforms on petrogenetic processes such as mantle melting and crystal fractionation at the ridge axis, are not seen in any kind of systematic way. The Northern Chile Ridge is an ideal site to look for a systematic TFE, since it overlies a relatively compositionally uniform mantle with no regional gradients in mantle composition or temperature, and has a segmentation geometry dominated by large-offset transforms of varying lengths. The absence of a clear signal at this site suggests that other factors beyond the transform offsets play a dominant role in controlling partial melting and fractionation, such as the effect of the proximity of a hotspot on the presence

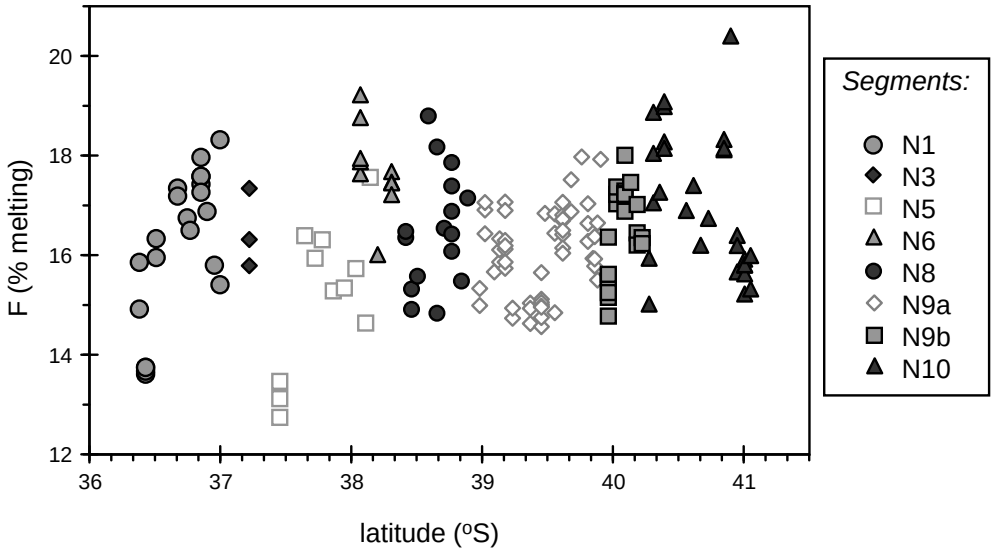

Figure 36: Latitudinal variations in extent of melting (*F*), calculated according to the equation $F = 19.202 - 5.175*[Na_2O]_8 + 15.537*[CaO]_8/[Al_2O_3]_8$ (*Niu and Batiza*, 1991). Each segment is shown with a different symbol. The low extents of melting at the northern end of segment N5 are probably not real; based on correlations with trace elements, high $[Na_2O]_8$ contents in this region appear to be due to mixing with small amounts of alkalic magmas. Excluding segment N5, the highest extent of melting at the ridge is $F = 20.40$ %, sample D50 at segment N10; the lowest extent of melting is $F = 13.60$ %, sample D111-1 at segment N1.

of long-lived magma chambers. This explains why the results elsewhere have been ambiguous.

There are some interesting examples of the influence of segmentation on the petrogenesis of lavas recovered at the Northern Chile Ridge. The onset of plagioclase crystallization appears to have been delayed in lavas from site D94 on segment N6. These samples are unique in that they contain only olivine and spinel phenocrysts, at MgO contents as low as 7.8 weight %. No plagioclase microlites were observed in these samples, indicating that the lavas really were not saturated in plagioclase, and plagioclase didn't separate out of the lavas mechanically. High Na_2O contents in a crystallizing magma can delay the onset of plagioclase crystallization (*Biggar and Humphries*, 1981). However, since D94 lavas don't have high Na_2O contents, a more likely explanation is that the crystallizing magmas had higher H_2O contents. A drastic increase in H_2O content in D94 lavas may have been through incorporation of meteoric H_2O from hydrothermal circulation in the crust. This is consistent with geological observations of pervasive hydrothermal alteration in a terrane just to the east of segments N5 and N6, that has been severely structurally disrupted by the tectonics associated with rift propagation (*Karsten et al.*, 1999). One possible mechanism by which this might occur is stoping of hydrothermally altered wallrock into a magma body.

Alkalic basalts occur at the broad inflated zone at the northern end of segment N5, both on-axis and at an off-axis seamount, as described previously. This inflated zone is characterized by shallow bathymetry, as well as a mantle Bouger anomaly low, which likely corresponds to thick crust. The southern end of this segment is the propagating

rift; *Phipps Morgan and Sandwell* (1994) found that nearly all propagating rifts south of 30º S are propagating down either a bathymetry or a gravity gradient. The alkalic basalts indicate the presence of a blob of enriched, fertile mantle under this location, which produces abnormally high volumes of melt. Mantle heterogeneity may be responsible for the thick crust at this site, and the thick crust may be responsible for rift propagation. In this way, a chemical mantle heterogeneity is controlling ridge segmentation at this site. Recent studies have found the same phenomenon at other sites (*Abelson and Agnon*, 2001; *Albers and Christensen*, 2001; *Georgen et al.*, 2001; *Michael et al.*, 1994; *Rabain et al.*, 2001).

CONCLUSIONS

The 1998 PANORAMA Expedition to the Northern Chile Ridge recovered MORBs that range from ultra-depleted N-MORBs to T-MORBs, as well as a few alkalic basalts. This is a much more petrologically and geochemically diverse suite of samples than had previously been reported for this region. It includes some of the few on-axis alkalic basalts in the Pacific not associated with a known hotspot.

Northern Chile Ridge MORBs constitute a cogenetic suite that experienced crystal fractionation at a pressure of approximately 2 kbar. Scatter around the crystal fractionation trends cannot be completely explained by crystallization effects (different pressures of crystallization or different H_2O contents in the parent magmas), and require variations in parent magma Na_2O content. Among the Northern Chile Ridge MORBs, incompatible trace element ratios correlate with long-lived radiogenic isotope ratios (Nd, Sr, and Pb) and not with major element indicators of extent of melting ($[Na_2O]_8$). For incompatible trace element ratios, quantitative models of mixing are robust, but models of melting are not.

Based on these observations, the following petrogenetic model is suggested. The magmas parental to the recovered Northern Chile Ridge lavas (prior to alteration by shallow-level crystal fractionation) were generated by mixing between primitive alkalic magmas with primitive depleted MORB magmas. The amount of alkalic magma in the mixture is < 5% for N-MORBs, 9-15% for T-MORBs. The primitive depleted MORB magmas were generated by 14-20% melting of a depleted mantle source that had a trace

element composition similar to that of sample D105-2, and an isotopic composition with high $^{143}Nd/^{144}Nd$ and low $^{87}Sr/^{86}Sr$, $^{206}Pb/^{204}Pb$, $^{207}Pb/^{204}Pb$, and $^{208}Pb/^{204}Pb$. The primitive alkalic magmas were generated by melting of a distinct fertile mantle source that was enriched in incompatible trace elements relative to the depleted mantle source, and is expected to have had an isotopic composition with low $^{143}Nd/^{144}Nd$ and high $^{87}Sr/^{86}Sr$, $^{206}Pb/^{204}Pb$, $^{207}Pb/^{204}Pb$, and $^{208}Pb/^{204}Pb$.

The amount of alkalic primitive magma in the mixture controls the incompatible trace element content (including K_2O and K/Ti), but doesn't significantly affect the major element content. Metasomatic addition of very small quantities of a fluid enriched only in the most highly incompatible trace elements (Cs, Rb, Ba, Th, U, Nb, and Ta) may also occur, since the wide variations in these elements are not correlated with variations in the rare earth elements and K/Ti.

A likely scenario in which the mixing described above might occur is melting of an upper mantle that contains ubiquitous heterogeneities of fertile mantle embedded in a depleted mantle matrix, similar to the "plum-pudding" mantle idea. The new detailed sampling program on the PANORAMA Expedition allowed the recovery of the alkalic samples that first indicated mixing was a possibility and which serve as a mixing end-member.

Applying the petrogenetic model to the Northern Chile Ridge sample suite yields the following inferences.

The Northern Chile Ridge mantle contains fewer blobs of enriched mantle than other southeast Pacific ridges, based on the observation that the population of NCR lavas has

lower K/Ti than other southeast Pacific ridge lavas. This may be because the Northern Chile Ridge is buffered from Pacific Superswell hotspot material by the East Pacific Rise/Pacific-Antarctic Ridge spreading center system. A previous episode of melt extraction, which had been suggested by *Bach et al.* (1996), is not required.

None of the subduction-related contamination that has been observed near the Chile Margin Triple Junction is found at the Northern Chile Ridge (this study), or at the Valdivia Fracture Zone or northernmost Southern Chile Ridge (*Sturm et al.*, 1999; *Klein et al.*, 2001). This suggests that chemical heterogeneities introduced into the upper mantle by subduction are small in geographic scale and are subordinate to larger regional patterns of mantle heterogeneity.

Northern Chile Ridge lavas are more primitive (higher Mg #) than lavas from the Galapagos Spreading Center and the Juan de Fuca Ridge, which are other intermediate spreading rate ridges located near hotspots. This suggests that at intermediate spreading rates, hotspots exert an important influence on the thermal budget controlling shallow crystallization and mechanisms of crustal accretion. Comparisons with recent data from other non-hotspot-influenced intermediate rate ridges, the Gorda Ridge and the Pacific-Antarctic Ridge near 60º S, support the new conclusion.

There are no obvious systematic segment-scale transform fault effects, either in crystallization processes, extent of partial melting, or distribution of mantle compositional heterogeneities.

The presence of long-offset transforms does not affect the regional extent of melting at the Chile Ridge, except near the Valdivia Fracture Zone, where the segment-transform

geometry approaches the extreme case of a fracture zone containing intra-transform spreading centers. The Northern Chile Ridge and Southern Chile Ridge have a normal extent of melting for their spreading rate and a normal axial depth for their extent of melting, based on comparing data from these ridges to global systematics found by *Niu and Hékinian* (1997) and *Klein and Langmuir* (1987).

REFERENCES

Abelson, M., and A. Agnon, Hotspot activity and plume pulses recorded by geometry of spreading axes, *Earth Planet. Sci. Lett.*, *189*, 31-47, 2001.

Albers, M., and U. R. Christensen, Channeling of plume flow beneath mid-ocean ridges, *Earth Planet. Sci. Lett.*, *187*, 207-220, 2001.

Allègre, C. J., and D. L. Turcotte, Implications of a two-component marble-cake mantle, *Nature*, *323*, 123-127, 1986.

Anderson, D. L., T. Tanimoto, and Y.-s. Zhang, Plate tectonics and hotspots: the third dimension, *Science*, *256*, 1645-1651, 1992.

Asimow, P. D., M. M. Hirschmann, and E. M. Stolper, Calculation of peridotite partial melting from thermodynamic models of minerals and melts, IV: Adiabatic decompression and mean properties of mid-ocean ridge basalts, *J. Petrology*, *42* (5), 963-998, 2001.

Bach, W., E. Hegner, J. Erzinger, and M. Satir, Chemical and isotopic variations along the superfast spreading East Pacific Ridge from 6º to 30º S, *Contrib. Mineral. Petrol.*, *116*, 365-380, 1994.

Bach, W., J. Erzinger, L. Dosso, C. Bollinger, H. Bougault, J. Etoubleau, and J. Sauerwein, Unusually large Nb-Ta depletions in North Chile Ridge basalts at 36º 50' to 38º 56' S: major element, trace element, and isotopic data, *Earth Planet. Sci. Lett.*, *142*, 223-240, 1996.

Biggar, G. M., and D. J. Humphries, The plagioclase, forsterite, diopside, liquid equilibrium in the system CaO-Na2O-MgO-Al2O3-SiO2, *Mineralogical Magazine*, *44*, 309-314, 1981.

Byerly, G. R., The nature of differentiation trends in some volcanic rocks dredged from the Galapagos Spreading Center, *J. Geophys. Res.*, *85*, 3797-3810, 1980.

Cande, S. C., E. M. Herron, and B. R. Hall, The early Cenozoic tectonic history of the southeast Pacific, *Earth Planet. Sci. Lett.*, *57*, 63-74, 1982.

Cande, S. C., R. B. Leslie, J. C. Parra, and M. Hobart, Interaction between the Chile ridge and Chile trench: Geophysical and geothermal evidence, *J. Geophys. Res.*, *92*, 495-520, 1987.

Cheatham, M. M., An examination of some of the causes of sensitivity change in ICP-MS analysis: Expansion changes, configuration, matrix complexity, and cone conditions: Can a correction always be made?, http://www.geochemistry.syr.edu/cheatham/papers/EAS_Symposium/EASpage1.HTML, 1995.

Cheatham, M. M., W. F. Sangrey, and W. M. White, Sources of error in external calibration ICP-MS analysis of geological samples and an improved non-linear drift correction procedure, *Spectrochimica Acta*, *48B* (3), E487-E506, 1993.

Chen, C. Y., and F. A. Frey, Trace element and isotopic geochemistry of lavas from Haleakala volcano, east Maui, Hawai'i: Implications for the origin of Hawaiian basalts, *J. Geophys. Res.*, *90* (B10), 8743-8768, 1985.

Chen, Y., and W. J. Morgan, Rift valley/no rift valley transition at mid-ocean ridges, *J. Geophys. Res.*, *95* (B11), 17,571-17,581, 1990.

Christie, D. M., and J. M. Sinton, Evolution of abyssal lavas along propagating segments of the Galapagos spreading center, *Earth Planet. Sci. Lett.*, *56*, 321-335, 1981.

Christie, D. M., and J. M. Sinton, Mantle processes in the generation of MORB from the 95° W Galapagos propagating rift area, *Contrib. Mineral. Petrol.*, *94*, 274-288, 1986.

Christie, D. M., I. S. E. Carmichael, and C. H. Langmuir, Oxidation states of mid-ocean ridge basalt glasses, *Earth Planet. Sci. Lett.*, *79*, 397-411, 1986.

Clague, D. A., and M. Holmes, Geology, petrology, and mineral potential of the Gorda Ridge, in *Geology and Resource Potential of the Continental Margin of Western North America and Adjacent Ocean Basins—Beaufort Sea to Baja California*, Circum-Pacific Council for Energy and Mineral Resources, Earth Sci. Series, edited by D. W. Scholl, A. Grantz, and J. G. Vedder, 1989.

Clague, D. A., F. A. Frey, G. Thompson, and S. J. Rindge, Minor and trace element geochemistry of volcanic rocks dredged from the Galapagos Spreading Center: Role of crystal fractionation and mantle inhomogeneity, *J. Geophys. Res.*, *86*, 9469-9482, 1981.

Clague, D. A., W. B. Friesen, P. Quinterno, M. Holmes, J. L. Morton, R. Bouse, L. Morgenson, and A. S. Davis, Preliminary geological, geophysical, and biological data from the Gorda Ridge, U. S. Geol. Survey Open File Rep., *84*, 364-, 1984.

Cohen, R. S., and R. K. O'Nions, The lead, neodymium and strontium isotopic structure of ocean ridge basalts, *J. Petrol.*, *23*, 299-324, 1982.

Cox, K. G., J. D. Bell, and R. J. Pankhurst, *The Interpretation of Igneous Rocks*. London: Allen and Unwin, 1979.

Danyushevsky, L. V., S. M. Eggins, T. J. Falloon, and D. M. Christie, H_2O abundance in depleted to moderately enriched mid-ocean ridge magmas; Part I: Incompatible behaviour, implications for mantle storage, and origin of regional variations, *J. Petrology*, *41* (8), 1329-1364, 2000.

Davis, A. S., and D. A. Clague, Geochemistry, mineralogy, and petrogenesis of basalt from the Gorda Ridge, *J. Geophys. Res.*, *92*, 10,476-10,483, 1987.

Davis, A. S., and D. A. Clague, Gabbroic xenoliths from the northern Gorda Ridge: Implications for magma chamber processes under slow spreading centers, *J. Geophys. Res.*, *95* (B7), 10,885-10,905, 1990.

Delaney, J. R., H. P. Johnson, and J. L. Karsten, The Juan de Fuca Ridge - hot spot – propagating rift system: New tectonic, geochemical and magnetic data, *J. Geophys. Res.*, *86*, 11747-11750, 1981.

Ewing, M., and B. C. Heezen, Some problems of Antarctic submarine geology, in *Antarctic in the International Geophysical Year*, Geophys. Monogr. Ser., vol. 1, edited by A. Crary et al., pp. 75-81, Am. Geophys. Union, Washington, D. C., 1956.

Ferguson, E. M., and E. M. Klein, Fresh basalts from the Pacific-Antarctic Ridge extend the Pacific geochemical province, *Nature*, *366*, 330-333, 1993.

Fornari, D. J., M. R. Perfit, A. Malahoff, and R. Embley, Geochemical studies of abyssal lavas recovered by DSRV ALVIN from eastern Galapagos Rift, Inca Transform and Ecuador Rift, 1, Major element variations in natural glasses and spatial distributions, *J. Geophys. Res.*, *88*, 10519-10529, 1983.

Frey, F. A., D. H. Green, and S. D. Roy, Integrated models of basalt petrogenesis: A study of quartz tholeiites to olivine melilitites from southeastern Australia utilizing geochemical and experimental petrological data, *J. Petrology*, *19* (3), 463-513, 1978.

Garbe-Schönberg, C.-D., Simultaneous determination of 37 trace elements in 28 international rock standards by ICP-MS, *Geostandards Newsletter*, *17* (1), 81-97, 1993.

Georgen, J. E., J. Lin, and H. J. B. Dick, Evidence from gravity anomalies for interactions of the Marion and Bouvet hotspots with the Southwest Indian Ridge: effects of transform offsets, *Earth Planet. Sci. Lett.*, *187*, 283-300, 2001.

Ghiorso, M. S., and R. O. Sack, Chemical mass transfer in magmatic processes IV: A revised and internally consistent thermodynamic model for the interpolation and extrapolation of liquid-solid equilibria in magmatic systems at elevated temperatures and pressures, *Contrib. Mineral. Petrol.*, *119*, 197-212, 1995.

Govindaraju, K., 1994 Compilation of working values and sample description for 383 geostandards, *Geostandards Newsletter*, *18* (Special Issue), 1-158, 1994.

Grove, T. L., R. J. Kinzler, and W. B. Bryan, Fractionation of mid-ocean ridge basalt (MORB), in *Mantle Flow and Melt Generation at Mid-Ocean Ridges*, American Geophys. Union Geophys. Monograph, vol. 71, edited by J. Phipps Morgan, D. K. Blackman, and J. M. Sinton, pp. 281-310, Am. Geophys. Union, Washington, D. C., 1992.

Hall, L. S., and J. M. Sinton, Geochemical diversity of the large lava field on the flank of the East Pacific Ridge at 8º 17' S, *Earth Planet. Sci. Lett.*, *142*, 241-251, 1996.

Handschumacher, D. W., Post-Eocene plate tectonics of the eastern Pacific, in *The Geophysics of the Pacific Ocean Basin and its Margin*, Geophys. Monogr. Ser., vol. 19, edited by G. H. Sutton et al., pp. 177-202, Am. Geophys. Union, Washington, D. C., 1976.

Hébert, R., R. D. Bideau, and R. Hékinian, Ultramafics and mafic rocks from the Garret Transform Fault near 13º 30' S on the East Pacific Rise: Igneous petrology, *Earth Planet. Sci. Lett.*, *65*, 107-125, 1983.

Hékinian, R., R. D. Bideau, M. Cannat, U. J. Francheteau, and R. Hébert, Volcanic activity and crust-mantle exposure in the ultrafast Garret Transform Fault near 13º 28' S in the Pacific, *Earth Planet. Sci. Lett.*, *108*, 259-275, 1992.

Hékinian, R., R. D. Bideau, R. Hébert, and Y. Niu, Magmatism in the Garret Transform Fault (East Pacific Rise near 13º 27' S), *J. Geophys. Res.*, *100*, 10,163-10,185, 1995.

Hékinian, R., P. Stoffers, C. W. Devey, D. Ackerman, C. Hémond, J. O'Connor, N. Binard, and M. Maia, Intraplate versus ridge volcanism on the Pacific-Antarctic Ridge near 37º S – 111º W, *J. Geophys. Res.*, *102* (B6), 12,265-12,286, 1997.

Hékinian, R., P. Stoffers, D. Ackerman, S. Révillon, M. Maia, and M. Bohn, Ridge hotspot interaction: The Pacific-Antarctic Ridge and the Foundation Seamounts, *Marine Geology*, *160*, 199-223, 1999.

Herron, E. M., Sea-floor spreading and the Cenozoic history of the east-central Pacific, *Geol. Soc. Am. Bull.*, *83*, 1671-1692, 1972.

Herron, E. M., and Hayes, D. E., A geophysical study of the Chile Ridge, *Earth Planet. Sci. Lett.*, *6*, 77-83, 1969.

Herron, E. M., S. C. Cande, and B. R. Hall, An active spreading center collides with a subduction zone: A geophysical survey of the Chile margin triple junction, in *Nazca Plate: Crustal Formation and Andean Convergence*, edited by L. D. Kulm et al., Mem. Geol. Soc. of Am., 154, 683-701, 1981.

Hess, P. C., Phase equilibria constraints on the origin of ocean floor basalts, in *Mantle Flow and Melt Generation at Mid-Ocean Ridges*, Am. Geophys. Union Geophys. Monograph, vol. 71, edited by J. Phipps Morgan, D. K. Blackman, and J. M. Sinton, pp. 67-102, Am. Geophys. Union, Washington, D. C., 1992.

Hey, R., A new class of "pseudofaults" and their bearing on plate tectonics: A propagating rift model, *Earth Planet. Sci. Lett.*, *37*, 321-325, 1978.

Hey, R., F. Duennebier, and W. J. Morgan, Propagating rifts on midocean ridges, *J. Geophys. Res.*, *85* (B7), 3647-3658, 1980.

Horn, I., S. F. Foley, S. E. Jackson, and G. A. Jenner, Experimentally determined partitioning of high field strength- and selected transition elements between spinel and basaltic melt, *Chemical Geology*, *117*, 193-218, 1994.

Jambon, A., B. Deruelle, G. Dreibus, and F. Pineau, Chlorine and bromine abundance in MORB: The contrasting behaviour of the Mid-Atlantic Ridge and East Pacific Rise and implications for chlorine geodynamic cycle, *Chem. Geol.*, *126*, 101-117, 1995.

Jochum, K. P., H. M. Seufert, and M. F. Thirlwall, Multi-element analysis of 15 international standard rocks by isotope-dilution spark source mass spectrometry, *Geostandards Newsletter*, *14* (3), 469-473, 1990.

Karsten, J. L., E. M. Klein, and S. B. Sherman, Subduction zone geochemical characteristics in ocean ridge basalts from the southern Chile Ridge: Implications of modern ridge subduction systems for the Archean, *Lithos*, *37*, 143-161, 1996.

Karsten, J. L., E. M. Klein, F. Martinez, R. Muhe, M. Sturm, T. Coleman, J. Hayasaka, D. Jung, G. Murray, R. Muse, A. Newsom, M. Stewart, S. Tougas, and J. Gallegos, The Northern Chile Ridge revealed: Preliminary cruise report of PANORAMA Expedition Leg 4, *InterRidge News*, *8*, 15-21, 1999.

Klein, E. M., and J. L. Karsten, Ocean-ridge basalts with convergent-margin geochemical affinities from the Chile Ridge, *Nature*, *374*, 52-57, 1995.

Klein, E. M., and C. H. Langmuir, Global correlations of ocean ridge basalt chemistry with axial depth and crustal thickness, *J. Geophys. Res.*, *92* (B8), 8089-8115, 1987.

Klein, E. M., M. A. Sturm, and J. L. Karsten, Isotope and trace element variations along the Southern Chile Ridge and Valdivia Fracture Zone system, *Eos, Trans. Am. Geophys. Union*, *82* (47), Fall Meet. Suppl., Abstract V51E-08, 2001.

Klitgord, K. D., J. D. Mudie, P. A. Larson, and J. A. Grow, Fast sea floor spreading on the Chile Ridge, *Earth Planet. Sci. Lett.*, *20*, 93-99, 1973.

Klöck, W., and H. Palme, Partitioning of siderophile and chalcophile elements between sulfide, olivine, and glass in a naturally reduced basalt from Disko Island, Greenland, *Lunar Planet. Sci.*, *18*, 471-483, 1988.

Kong, L. S., R. S. Detrick, P. J. Fox, L. A. Mayer, and W. B. F. Bryan, The morphology and tectonics of the MARK Area from SeaBeam and Sea MARK 1 observations (Mid-Atlantic Ridge 23° N), *Marine Geophys. Res.*, *10*, 59-90, 1988.

Koppers, A., Kd's Database, website http://www.earthref.org/GERM/bottom.htm, Geochemical Earth Reference Model (GERM).

Korotev, R. L., A self-consistent compilation of elemental concentration data for 93 geochemical reference samples, *Geostandards Newsletter*, *20*, 217-245, 1996.

Kuo, B.-Y., and D. W. Forsyth, Gravity anomalies of the ridge-transform system in the South Atlantic between 31 and 34.5º S: Upwelling centers and variations in crustal thickness, *Marine Geophys. Res.*, *10*, 205-232, 1988.

Langmuir, C. H., Geochemical consequences of in situ crystallization, *Nature*, *340*, 199-205, 1989.

Langmuir, C. H., and J. F. Bender, The geochemistry of oceanic basalts in the vicinity of transform faults: observations and implications, *Earth Planet. Sci. Lett.*, *69*, 107-127, 1984.

Langmuir, C. H., R. D. Vocke, Jr., G. N. Hanson, and S. R. Hart, A general mixing equation with applications to Icelandic basalts, *Earth Planet. Sci. Lett.*, *37*, 380-392, 1978.

Langmuir, C. H., E. M. Klein, and T. Planck, Petrological systematics of mid-ocean ridge basalts: Constraints on melt generation beneath ocean ridges, in *Mantle Flow and Melt Generation at Mid-Ocean Ridges*, Geophys. Monogr. Ser., vol. 71, edited by J. Phipps Morgan, D. K. Blackman, and J. M. Sinton, pp. 183-280, Am. Geophys. Union, Washington, D. C., 1992.

Lanphere, M. A., and F. A. Frey, Geochemical evolution of Kohala volcano, Hawai‘i, *Contrib. Mineralogy and Petrology*, *95*, 100-113, 1987.

Lawson, K., R. C. Searle, J. A. Pearce, P. Browning, and P. Kempton, Detailed volcanic geology of the MARNOK area, Mid-Atlantic Ridge north of Kane transform, in *Tectonic, Magmatic, Hydrothermal, and Biological segmentation of mid-ocean ridges*, Geol. Soc. Special Pub., no. 118, edited by C. J. MacLeod, P. A. Tyler, and C. L. Walker, pp. 61-102, 1996.

Macdonald, K. C., The crest of the Mid-Atlantic Ridge: Models for crustal generation processes and tectonics, in *The Western North Atlantic Region, The Geology of North America*, vol. M, edited by P. R. Vogt and B. E. Tucholke, pp. 51-68, 1986.

Martinez, F., J. L. Karsten, and E. M. Klein, Recent kinematics and tectonics of the Chile Ridge, *Eos, Trans. Am. Geophys. Union*, *79* (45), Fall Meet. Suppl., Abstract T12C-01, 1998.

McDonough, W. F., and S.-s. Sun, The composition of the Earth, *Chemical Geology*, *120*, 223-253, 1995.

Menard, H. W., T. E. Chase, and S. M. Smith, Galapagos Rise in the southeastern Pacific, *Deep Sea Res.*, *11*, 233, 1964.

Michael, P. J., The concentration, behavior, and storage of H_2O in the suboceanic upper mantle: Implications for mantle metasomatism, *Geochim. Cosmochim. Acta*, *52*, 555-566, 1988.

Michael, P. J., Regionally distinctive sources of depleted MORB: Evidence from trace elements and H_2O, *Earth and Planet. Sci. Lett.*, *131*, 301-320, 1995.

Michael, P. J., and R. L. Chase, The influence of primary magma composition, H_2O and pressure on mid-ocean ridge basalt differentiation, *Contrib. Mineral. Petrol.*, *96*, 245-263, 1987.

Michael, P. J., D. W. Forsyth, D. K. Blackman, P. J. Fox, B. B. Hanan, A. J. Harding, K. C. MacDonald, G. A. Neumann, J. A. Orcutt, M. Tolstoy, and C. M. Weiland, Mantle control of a dynamically evolving spreading center: Mid-Atlantic Ridge 31-34º S, *Earth Planet. Sci. Lett.*, *121*, 451-468, 1994.

Middlemost, E. A. K., The basalt clan, *Earth Sci. Rev.*, *11*, 337-364, 1975.
Montaser, A., *Inductively Coupled Plasma Mass Spectrometry*, J. Wiley, New York, 1998.
Naumann, T. R., and D. J. Geist, Generation of alkalic basalt by crystal fractionation of tholetiitic magma, *Geology*, *27* (5), 423-426, 1999.
Niedermann, S., and W. Bach, Anomalously nucleogenic neon in North Chile Ridge basalt glasses suggesting a previously degassed mantle source, *Earth Planet. Sci. Lett.*, *160*, 447-462, 1998.
Niu, Y., and R. Batiza, An empirical method for calculating melt compositions produced beneath mid-ocean ridges: application for axis and off-axis (seamounts) melting, *J. Geophys. Res.*, *96* (B13), 21,753-21,777, 1991.
Niu, Y., and R. Hékinian, Spreading-rate dependence of the extent of mantle melting beneath ocean ridges, *Nature*, *385* (23), 326-329, 1997.
Parmentier, E. M., and J. M. Sinton, State of science: Mid-ocean ridges, *FUMAGES (Future of Marine Geology and Geophysics) Workshop Report*, P. Baker and M. McNutt, eds. Proceedings of a workshop December 5-7, 1996, Consortium for Oceanographic Research and Education, National Science Foundation, pp. 89-121, 1998.
Perfit, M. R., D. J. Fornari, A. Malahoff, and R. Embley, Geochemical studies of abyssal lavas recovered by DSRV ALVIN from Eastern Galapagos Rift, Inca Transform, and Ecuador Rift, 3, Trace element abundances and petrogenesis, *J. Geophys. Res.*, *88*, 10551-10572, 1983.
Perfit, M. R., D. J. Fornari, M. C. Smith, J. F. Bender, C. H. Langmuir, and R. Haymon, Small-scale spatial and temporal variations in mid-ocean ridge crest magmatic processes, *Geology*, *22*, 375-379, 1994.
Philpotts, A. R., *Principles of Igneous and Metamorphic Petrology*, Prentice Hall, Englewood Cliffs, New Jersey, 1990.
Phipps Morgan, J., Thermodynamics of pressure release melting of a veined plum pudding mantle, *Geochemistry, Geophysics, Geosystems (G-Cubed)*, *2*, paper number 2000GC000049, 2001.
Phipps Morgan, J., and Y. J. Chen, Dependence of ridge-axis morphology on magma supply and spreading rate, *Nature*, *364*, 706-708, 1993.
Phipps Morgan, J., and D. W. Forsyth, Three-dimensional flow and temperature perturbations due to a transform offset: Effects on oceanic crustal and upper mantle structure, *J. Geophys. Res.*, *93* (B4), 2955-2966, 1988.
Phipps Morgan, J., and D. T. Sandwell, Systematics of ridge propagation south of 30º S, *Earth Planet. Sci. Lett.*, *121*, 245-258, 1994.
Pilger, R. H., Kinematics of the South American subduction zone from global plate reconstructions, in *Geodynamics of the Eastern Pacific Region, Caribbean and Scotia Arcs*, Geodyn. Ser., vol. 9, edited by R. Cabre, pp. 113-125, Am. Geophys. Union, Washington, D. C., 1983.
Press, W. H., S. A. Teukolsky, W. T. Vetterling, and B. P. Flannery, *Numerical Recipes in C: The Art of Scientific Computing*, Cambridge University Press, New York, 1995.

Puchelt, H., and R. Emmermann, Petrogenetic implications of tholeiitic basalt glasses from the East Pacific Rise and the Galapagos Spreading Center, *Chem. Geol.*, *38*, 39-56, 1983.

Rabain, A., M. Cannat, J. Escartín, G. Pouliquen, C. Deplus, and C. Rommevaux-Jestin, Focused volcanism and growth of a slow spreading segment (Mid-Atlantic Ridge, 35º N), *Earth Planet. Sci. Lett.*, *185*, 211-224, 2001.

Schiano, P., J. L. Birck, and C. J. Allègre, Osmium-strontium-neodymium-lead isotopic covariations in mid-ocean ridge basalt glasses and the heterogeneity of the upper mantle, *Earth Planet. Sci. Lett.*, *150*, 363-379, 1997.

Schilling, J.-G., Upper mantle heterogeneities and dynamics, *Nature*, *314*, 62-66, 1985.

Shah, A. K., and J.-C. Sempére, Morphology of the transition from an axial high to a rift valley at the Southeast Indian Ridge and the relation to variations in mantle temperature, *J. Geophys. Res.*, *103* (B3), 5203-5223, 1998.

Shen, Y., and D. W. Forsyth, Geochemical constraints on initial and final depths of melting beneath mid-ocean ridges, *J. Geophys. Res.*, *100* (B2), 2211-2237, 1995.

Sherman, S. B., *Influences of ridge subduction on mid-ocean ridge processes: Petrologic observations from the Southern Chile Ridge and the Woodlark Basin*, Ph. D. Thesis, University of Hawai‘i at Mānoa, 1998.

Sherman, S. B., J. L. Karsten, and E. M. Klein, Petrogenesis of axial lavas from the Southern Chile Ridge: Major element constraints, *J. Geophys. Res.*, *102* (B7), 14,963-14,990, 1997.

Sinton, J. M., R. S. Detrick, Mid-ocean ridge magma chambers, *J. Geophys. Res.*, *97* (B1), 197-216, 1992.

Sinton, J. M., D. S. Wilson, D. M. Christie, R. N. Hey, and J. R. Delaney, Petrologic consequences of rift propagation on oceanic spreading ridges, *Earth Planet. Sci. Lett.*, *62*, 193-207, 1983.

Sinton, J. M., S. M. Smaglik, J. J. Mahoney, and K. C. Macdonald, Magmatic processes at superfast spreading mid-ocean ridges: Glass compositional variations along the East Pacific Rise 13-23º S, *J. Geophys. Res.*, *96*, 6133-6155, 1991.

Skoog, D. A., and J. J. Leary, *Principles of Instrumental Analysis*, Saunders College Pub., Fort Worth, 1992.

Sleep, N. H., Tapping of magmas from ubiquitous mantle heterogeneities: An alternative to mantle plumes?, *J. Geophys. Res.*, *89* (B12), 10,029-10,041, 1984.

Small, C., Global systematics of mid-ocean ridge morphology, in *Faulting and Magmatism at Mid-Ocean Ridges*, Geophys. Monograph 106, pp. 1-25, Am. Geophys. Union, Washington, D. C., 1998.

Smith, W. H. F., and D. T. Sandwell, Global sea floor topography from satellite altimetry and ship depth soundings, *Science*, *277* (5334), 1956-1962, 1997.

Sparks, D. W., and E. M. Parmentier, Melt extraction from the mantle beneath spreading centers, *Earth Planet. Sci. Lett.*, *105*, 368-377, 1991.

Stolper, E., A phase diagram for mid-ocean ridge basalts: Preliminary results and implications for petrogenesis, *Contrib. Mineral. Petrol.*, *74*, 13-27, 1980.

Sturm, M. E., E. M. Klein, J. L. Karsten, and F. Martinez, Trace element variations in axial lavas from the Central Chile Ridge: Results from the 1998 Panorama 4

Expedition, *Eos, Trans. Am. Geophys. Union*, *79* (45), Fall Meet. Suppl., Abstract T12C-03, 1998.
Sturm, M. E., E. M. Klein, D. W. Graham, and J. L. Karsten, Age constraints on crustal recycling to the mantle beneath the southern Chile Ridge: He-Pb-Sr-Nd isotope systematics, *J. Geophys. Res.*, *104* (B3), 5097-5114, 1999.
Sun, S.-s., and W. F. McDonough, Chemical and isotopic systematics of oceanic basalts: implications for mantle composition and processes, in *Magmatism in the Ocean Basins*, Geological Society Special Pub. 42, edited by A. D. Saunders and M. J. Norry, pp. 313-345, Geol. Soc. Am., Boulder, Colorado, 1989.
Tebbens, S. F., and S. Cande, Southeast Pacific tectonic evolution from early Oligocene to Present, *J. Geophys. Res.*, *102* (B6), 12,061-12,084, 1997.
Tebbens, S. F., S. C. Cande, L. Kovacs, J. C. Parra, J. L. LaBrecque, and H. Vergara, The Chile Ridge: A tectonic framework. *J. Geophys. Res.*, *102* (B6), 12,035-12,059, 1997.
Tolstoy, M., A. J. Harding, and J. A. Orcutt, Crustal thickness on the Mid-Atlantic Ridge: Bull's-eye gravity anomalies and focused accretion, *Science*, *262*, 726-729, 1993.
Tucholke, B. E., J. Lin, and M. C. Kleinrock, Megamullions and mullion structure defining oceanic metamorphic core complexes on the Mid-Atlantic Ridge, *J. Geophys. Res.*, *103* (B5), 9857-9866, 1998.
Villemant, B., Trace element evolution in the Plegrean Fields, Central Italy: Fractional crystallization and selective enrichment, *Contrib. Mineral. Petrol.*, *98*, 169-183, 1988.
Villemant, B., H. Jaffrezic, J.-L. Joran, and M. Treuil, Distribution coefficients of major and trace elements: Fractional crystallization in the alkali basalt series of Chaine des Puys (Massif Central, France), *Geochim. Cosmochim. Acta*, *45*, 1997-2016, 1981.
Vlastélic, I., D. Aslanian, L. Dosso, H. Bougault, J. L. Olivet, and L. Géli, Large-scale chemical and thermal division of the Pacific mantle, *Nature*, *399*, 345-350, 1999.
Vlastélic, I., L. Dosso, H. Bougault, D. Aslanian, L. Geli, J. Etoubleau, M. Bohn, J.-L. Joron, and C. Bollinger, Chemical systematics of an intermediate spreading ridge: The Pacific-Antarctic Ridge between 56º S and 66º S, *J. Geophys. Res.*, *105*, 2915-2936, 2000.
Wessel, P., and W. H. F. Smith, New, improved version of Generic Mapping Tools released, *Eos, Trans. Amer. Geophys. U.*, *79* (47), 579, 1998.
White, W., A. W. Hofmann, and H. Puchelt, Isotope geochemistry of Pacific mid-ocean ridge basalt, *J. Geophys. Res.*, *92* (B6), 4881-4893, 1987.
Zhang, Y. S., and T. Tanimoto, High-resolution global upper mantle structure and plate tectonics, *J. Geophys. Res.*, *98* (B6), 9793-9823, 1993.